ABSTRACT

Title of Dissertation: MULTI-CHANNEL SCANNING SQUID MICROSCOPY

Su-Young Lee, Doctor of Philosophy, 2004

Dissertation directed by: Professor Frederick C. Wellstood
Department of Physics

I designed, fabricated, assembled, and tested an 8-channel high-T_c scanning SQUID system. I started by modifying an existing single-channel 77 K high-T_c scanning SQUID microscope into a multi-channel system with the goal of reducing the scanning time and improving the spatial resolution by increasing the signal-to-noise ratio S/N. I modified the window assembly, SQUID chip assembly, cold-finger, and vacuum connector. The main concerns for the multi-channel system design were to reduce interaction between channels, to optimize the use of the inside space of the dewar for more than 50 shielded wires, and to achieve good spatial resolution.

In the completed system, I obtained the transfer function and the dynamic range ($\Phi_{max} \sim 11\Phi_0$) for each SQUID. At 1kHz, the slew rate is about 3000 Φ_0/s. I also found

that the white noise level varies from 5 $\mu\Phi_0$ /Hz$^{1/2}$ to 20 $\mu\Phi_0$ /Hz$^{1/2}$ depending on the SQUID. A new data acquisition program was written that triggered on position and collects data from up to eight SQUIDs. To generate a single image from the multi-channel system, I calibrated the tilt of the *xy*-stage and *z*-stage manually, rearranged the scanned data by cutting overlapping parts, and determined the applied field by multiplying by the mutual inductance matrix. I found that I could reduce scanning time and improve the image quality by doing so.

In addition, I have analyzed and observed the effect of position noise on magnetic field images and used these results to find the position noise in my scanning SQUID microscope. My analysis reveals the relationship between spatial resolution and position noise and that my system was dominated by position noise under typical operating conditions. I found that the smaller the sensor-sample separation, the greater the effect of position noise is on the total effective magnetic field noise and on spatial resolution. By averaging several scans, I found that I could reduce position noise and that the spatial resolution can be improved somewhat.

Using a current injection technique with an *x*-SQUID, and (i) subtracting high-frequency data from low-frequency data, or (ii) taking the derivative of magnetic field B_x with respect to *x*, I show that I can find defects in superconducting MRI wires.

MULTI-CHANNEL SCANNING SQUID MICROSCOPY

by

Su-Young Lee

Thesis submitted to the Faculty of the Graduate School of the
University of Maryland, College Park in partial fulfillment
of the requirements for the degree of
Doctor of Philosophy
2004

Advisory Committee:

Professor Frederick C. Wellstood, Chair/Advisor
Professor James R. Anderson
Professor Richard L. Greene
Professor Christopher J. Lobb
Professor Colin Philips

DEDICATION

To my parents

ACKNOWLEDGEMENTS

This dissertation would not have been possible without the help and patience of many people.

I wish to thank my advisor, Professor Frederick C. Wellstood for support, guidance and patience during my research. Not only his dedication and passion to physics but also his advice for my private life always inspired me. When I had to stop my project and leave to Korea suddenly, he showed me patience and gave me lots of advices for my life. In the circumstance of his extremely busy schedule as an associate chair for undergraduate education, he always cared about students, opened his door, listened and answered my silly questions.

I would like to thank the committee, Professors James R. Anderson, Richard L. Greene, Christopher J. Lobb, and Colins Philips for being my committee and spending time to review my thesis.

I thank the Professors in the CSR, Christopher J. Lobb for generous conversation and not hesitating over my troublesome requests, Professor Richard L. Greene for instructing the CSR seminar and stimulating discussions, Professor Richard Webb for allowing for me to use his equipment, and Professor Steven M. Anlage for his lectures on Superconductivity.

I would like to thank Professor In-Sang Yang at Ewha Womans University for his initial guidance in physics and his support and concern. I thank Professor Sung-Ik

Lee at Pohang University of Science and Technology for showing enthusiasm towards physics and constant attention to me. I also thank Professor Zheong G. Khim at Seoul National University for his support and warm conversations while I worked at SNU.

I thank Dr. Sojiphong Chatraphorn for instructing me in everything from fabricating SQUIDs to building scanning SQUID microscopes. Even after he left, I learned a lot from his neatly written records. I also thank Dr. Erin F. Fleet for showing me how to operate the cryo-cooled SQUID microscope. I learned a lot from both Erin and Guy during my 1st year of lab life. I also want to thank Jan Gaudesrad for being a good lab partner and for his positive thinking and diligence.

I would like to thank Dr. John Matthews for taking care of my multi-channel SQUID microscope in my absence, correcting my poor English in this thesis, and his knowledge of the magnetic inverse technique. I also want to thank Dr. Roberto C. Ramos for being so nice and always ready to help me and everyone else in the lab.

I am indebted to my colleagues in the subbasement. I thank Dr. Andrew Berkeley for his friendship and advice on physics and electronics, even though his smartness depressed me sometimes. I am thankful to David Tobias for discussions about my experiment, offering warm chats and sneaking-up on me so I would not feel lonely in my corner of the lab. I am grateful to Hanhee Paik for her friendship and helping me understand SETs and hysteretic SQUIDs. I would like to thank Huizhong Xu for showing his enthusiasm and knowledge toward physics and helping me distinguish between Korean green tea and Chinese green tea. I want to thank Sudeep

Dutta for showing interest in my experiment, reading Fred's illegible handwriting for me, and making the lab-atmosphere warm by just his existence. I thank Gus Vlahacos for good conversation and work on building the next generation of SQUID microscopes. I thank Felipe Busko for helping to order the new translation stage from Newport. I would like to thank Matt Kenyon, Anders Gilbertson, Mark Gubrud, Soun Pil Kwon, and Vijay Viswanathan for many good conversations and helpful advice. I wish they all obtain great results for their experiments.

I am thankful to all my colleagues in the Center for Superconductivity Research. I thank Dr. Matthew Sullivan and Dr. Sheng-Chiang Lee for providing scrupulous information about writing a thesis and encouraging my writing. I thank Dr. Bin Ming for initial instructions for YBCO film fabrication.

I would like to thank Doug Bensen and Brian Straughn for not only their technical help but also for many warm conversations. I want to thank the staff in CSR, Brian Barnaby, Belta Pollard, Grace Sewlall, and Cleopatra White for being nice and taking care of all the paperwork.

I would like to thank Jane Hessing in the Physics Department's Office of Student Services for warm conversations and for taking care of all the paperwork from my starting to finishing as a graduate student. I thank Jesse Anderson in Z-order and Al N. Godinez in Physics Receiving for giving me warm smiles and chatting when I ask to fill the liquid nitrogen dewar.

At Necocera, I thank Dr. Lee Knauss for his collaboration, reviewing my position noise paper, and encouraging my work. I want to thank Jeonggoo Kim for his constant help and advice while I was struggling with making YBCO thin films. I thank Antonio Orozco and Harsh for many helpful comments.

I would like to thank Robin Cantor, president of Star cryo-electronics, Inc., for his quick replies and advice when I set up my SQUID system with his SQUID electronics. I thank Marilyn Kushner at U.C. Berkeley Microlab for making photolithographic masks for my SQUID chips.

I want to thank my many classmates at the University of Maryland including Kyu-yong Lee for his sincere and steady effort and Jae-Woong Hyun for friendship and concern for me. I also want to thank Jong-Won Kim, Seok-Hwan Chung, Winson, and Ynggwei for their friendship and many discussions.

I would like to thank all the members in the Superconductivity group at SNU in Korea who helped me when I visited the group for 1 year. I want to thank Dr. Jaewan Hong for showing diligence and enthusiasm on his SPM system, Seung Hyun Moon and Yonuk Chong for sharing their knowledge and interest towards physics, Ungwhan Pi for friendship and helping my soldering, Seunghee Jeon for helping me with lots of problems I had, and Burm Baek for helping me understand SQUIDs better. I am grateful to Su-Youn Lee, Jonghun Kim, Joonsung Lee, Jongho Baek, Seongjin Yun, Soohyon Phark, Bongwoo Ryu, Insu Jeon, YongSeung Kim for helping me have a good time.

I would like to thank Maria Aronova for being my best friend, classmate, partner, roommate, my relative in the United States, a singer in my wedding, and an aunt for my baby. I don't know how to fully appreciate her, but I can say my life in this foreign country was happy because of her. I want to thank Young-Chan Kim for being a model physicist and humanist. I thank him for helping me while living in the U.S., answering lots of my questions, and giving theoretical comments.

Especially, I would like to thank my parents in law in Korea for supporting and encouraging me to finish my Ph. D. I am grateful to my loving daughter Woo-Jin for being my reason to live. I thank her for her health and being a nice girl even though I could not spend as much time with her as I wanted to. I want to thank Woojin's nanny for taking care of my baby with great love.

I would like to thank my special friend and husband, Jae-Oh Cheong for his great support and patience, for not hesitating to live alone in Korea for more than 1 year, and for being my mental center. His encouragement leads me on.

I want to thank my brothers Seok Lee for his prayers and sacrifice and Hyun-sung Lee and his family for being strong supporters and showing their enthusiasm as doctors, and my sweet sister Seojin for showing faith toward me and giving me warm memories of my childhood. Finally, I thank my father Hong-ha Lee, and my mother Bok-young Seo for showing belief in their daughter and endless love and support for 32 years. I could not be here without their sacrifice and support. The words "thank you"

are not enough for their love. I promise that I will not disappoint them by being a sincere physicist.

TABLE OF CONTENTS

LIST OF FIGURES

LIST OF TABLES

Chapter 1

Introduction

1.1 A Brief History of SQUIDs

Superconductivity remains one of the last great frontiers of scientific research. The first superconductor (mercury) was discovered by Heike Kamerlingh Onnes in 1911 [1] when he noticed that its resistance vanished suddenly just below 4.2 K. About 20 years later, Walter Meissner and Robert Ochsenfeld found another phenomenon, that superconductors repel or expel magnetic fields. This property of superconductors is called the “Meissner Effect” [2]. In 1950, F. London proposed that flux would be quantized in a superconducting ring [3]. The first widely-accepted theoretical understanding of superconductivity (BCS theory) was advanced in 1957 by J. Bardeen, L. Cooper, and J. R. Schrieffer [4]. The fact that it took 46 years from discovery to understanding, and also required the development of quantum mechanics, gives some indication of the difficulty of the problem. In 1962, Brian D. Josephson predicted that electrons would "tunnel" through a narrow non-superconducting region [5], and that this would produce some surprising phenomena which we now call the dc and ac “Josephson effects”. The Josephson effects were soon used by Jaklevic, Lambe, Silver, and Mercereau to develop the first SQUID (Superconducting QUantum Interference Device)[6].

SQUIDs are a relatively well-known application of superconductivity. They are electrical devices that are capable of detecting extremely weak magnetic fields. There are two kinds of SQUIDs. The dc SQUID consists of two Josephson junctions in a loop, and this was the type first made by Jaklevic *et al.* [6]. The other type is the rf SQUID, which consists of a single Josephson junction in a loop and is operated with radio-frequency flux bias. The first rf SQUIDs were developed by Zimmerman *et al*., Mercereau *et al*., and Nisenoff *et al*. [7,8].

It turns out that, with the proper circuits, SQUIDs can be used as magnetic flux meters, magnetometers, gradiometers, voltmeters, susceptometers, rf amplifiers, current comparators, and even quantum bits. The main difference between these applications is in the nature of the input signal and the input circuit that is used to couple the input signal to the SQUID. The most important merit of the SQUID in an application is that it can have extremely high sensitivity or low noise. Depending on the application, a specific circuit optimization is required to achieve the best performance (highest signal-to-noise ratio). Needless to say, the main difficulty has been the need to cool devices to cryogenic temperatures, since materials only become superconducting below a critical temperature (T_c) that is ordinarily quite low compared to room temperature. This difficulty has lessened since the discovery of high-T_c superconductivity in 1986 by Bednorz and Muller [9]. Nevertheless high-T_c still means low temperature (typically 77K) operation.

1.2 History of scanning SQUID microscopy

Many techniques have been used for imaging magnetic fields, including Hall bar microscopy [10], scanning magnetoresistive microscopy [11], magnetic force microscopy [12], magneto-optical imaging [13], and electron beam holography. Since SQUIDs are small and extremely sensitive to magnetic field, SQUIDs are potentially a very powerful tool for imaging magnetic fields from a sample.

Scanning SQUID microscopes with truly "microscopic" resolution were first developed in the early 1990s. In the first SQUID microscopes, the sample and the SQUID were cooled with liquid cryogens [14,15,16] in a vacuum environment. Using some of these systems, properties of the superconducting order parameters in high-T_c materials [17] and vortices [18] were studied. In addition some of these microscopes were used to demonstrate nondestructive evaluation (NDE) in metallic structures [19,20]. In fact, there is a long history of using SQUIDs for imaging NDE samples at the mm and cm scale, and the microscopes fit into this history. To overcome the limitation of the sample and difficulties of the sample loading, R. Black, Y. Gim, and F. Wellstood built the first "room temperature" scanning SQUID microscope in the mid-1990's [21]. In this system, the sample was in air at room temperature, and the SQUID was at 77 K in vacuum. To keep the sample hot and the SQUID cold, the SQUID and sample were separated by a 25 μm thick sapphire window [22,23], resulting in a minimum sensor-to-sample distance of about 50 μm (see Ch.5). A patent for the idea and technology of the scanning SQUID microscope was granted to Wellstood, Gim, and Black [21].

Since these first systems, several other groups have developed their own SQUID microscopes. L. N. Morgan *et al*. built a high-T_c (HTS) SQUID system for room

temperature NDE [24, 25]. J. Clarke *et al*. built a HTS SQUID system with a SiN window for bio-magnetic samples [26]. Wikswo *et al*. [27] and Decert *et al*. [28] have built low-T_c (LTS) SQUID systems for room temperature NDE of samples.

In addition, the Maryland patent was licensed by Neocera, Inc., which proceeded to commercialize the scanning SQUID microscope. In collaboration with our group, they modified the cooling system to use closed-cycle refrigeration rather than liquid nitrogen, and made numerous other improvements to make the system more user friendly. Figure 1.1 shows one of their early MAGMA-C1 systems. Neocera's commercial scanning SQUID microscope was specially built for failure analysis (see Ch. 9) and fault isolation in integrated circuits and multi-chip modules [29,30] and have been sold to semiconductor manufacturers.

1.3 Motivation

This thesis concerns the development of a multi-channel SQUID microscope. There are several factors that motivate this research. Although the sensitivity of a SQUID is very high, the spatial resolution of a room temperature scanning SQUID microscope is limited. The main factors limiting the spatial resolution are the size of the sensor and the sensor-to-sample distance *z*. Since real samples often have intervening layers of material, there is often little choice about reducing z. For example, many computer chips are mounted in "flip-chip" configuration, which means that the active current elements are buried under 100-200 μm of silicon. Much recent research on room temperature SQUID microscopy has focused on improving the spatial resolution *s* achieved under typical operating conditions [31,32] despite the obvious difficulty of

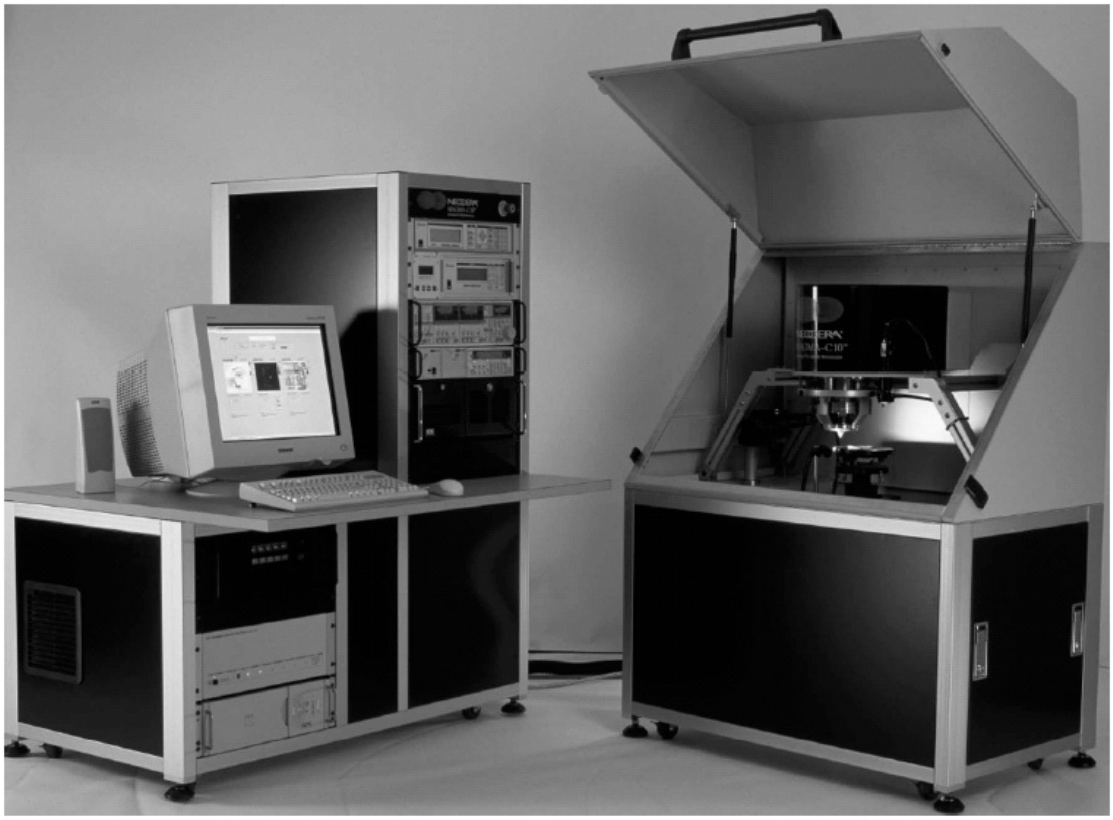

Figure 1.1: Photograph of commercial scanning SQUID microscope, MAGMA-C10 (reproduced from Ref. [33])

these real-world constraints. For example, Chatraphorn *et al.* showed that by using a magnetic inverse technique, one could obtain a spatial resolution in the resulting current density image that was about 10 times better than the raw magnetic field image, and up to about 5 times better than the senor-to-sample separation z [22]. Ultimately, this improvement is limited by the S/N ratio.

Another limitation of scanning SQUID microscopy is the lengthy scanning time. For a commercial SQUID system, the elapsed time is very important. For example, if one wants to find defects in an MRI wire that is 1 km long, one better not be scanning at 1mm/sec.

A multi-channel SQUID system is one possible solution to these deficiencies. With a multi-channel SQUID system, it should be possible to improve the spatial resolution by increasing the S/N ratio because more "signals" are available. Alternatively, a multi-channel SQUID system should be able to complete scans more rapidly with the same S/N in each pixel. Thus, a properly configured 8-channel SQUID system can reduce the elapsed time by a factor of 8 compared with a single-channel SQUID (see Fig. 1.2).

1.4 Organization of the thesis

The remainder of my thesis is organized as follows. In Chapter 2, I discuss Josephson junctions, the dc SQUID and noise in SQUIDs. I also discuss the different sources of 1/f noise and white noise and how they can be reduced. I finish with a brief description of some applications of SQUIDs.

In Chapter 3, I describe why I use high-T_c SQUIDs, and discuss the detailed design of my multi-channel SQUID chip. I also discuss the possible problem of multi-

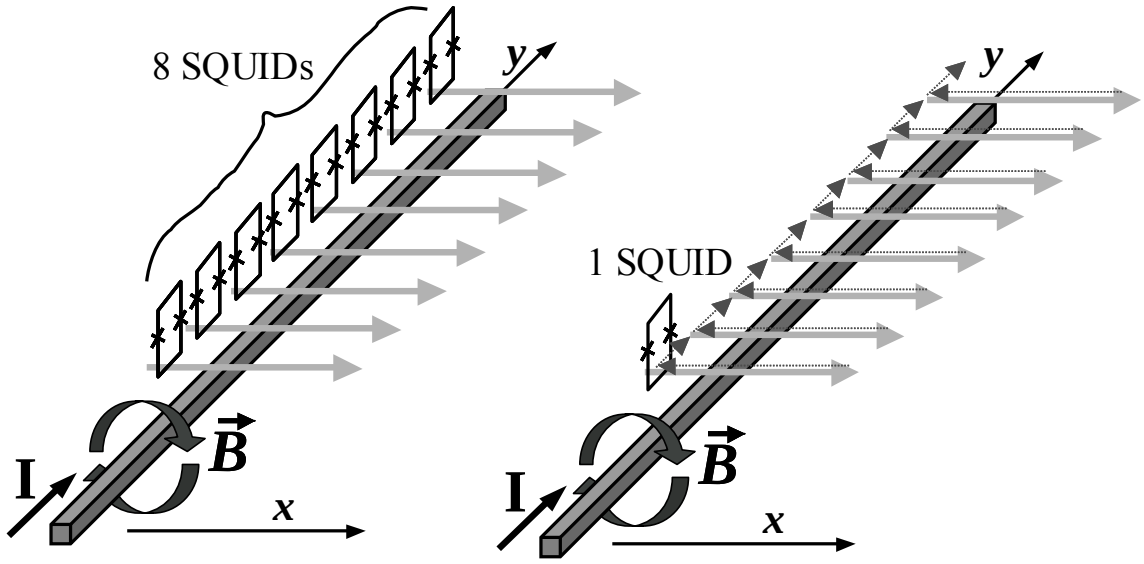

Figure 1.2 (a) Eight x-SQUIDs simultaneously scanning a wire, (b) single SQUID raster scanning a wire.

channel SQUID "crosstalk" and its solution. Given the design of the SQUID chip, I then calculate the mutual inductance between each SQUID and its modulation line, and the mutual inductance between a SQUID and its neighboring modulation lines. From this calculation, I estimate the crosstalk between SQUIDs and describe how the output from the multi-channel system is related to the actual magnetic field.

In Chapter 4, I describe how I fabricated multi-channel SQUID chips. I introduce the $YBa_2Cu_3O_{7-x}$(YBCO) thin film fabrication process using pulsed laser deposition (PLD) and photolithography. I finish with measurements of the SQUIDs in my 8-SQUID chip.

In Chapters 5 and 6, I describe how I modified an existing single-channel high-T_c SQUID microscope into a multi-channel SQUID system. I briefly describe the previous system, and the difference between the new and the old systems. In Chapter 5, I focus on modifications to the microscope body. In Chapter 6, I introduce the multi-channel electronics and its characteristics. In addition, I describe the new *xy*-translation stage and the data acquisition program. Finally, I demonstrate how I generate a single image from the multi-channel system and explain how I calibrate the system.

In Chapter 7, I describe how uncertainty in the position at which the field is measured affects a magnetic image. I show that stage jitter or limited resolution of the position encoder can cause error in position. I find that even small amounts of position noise during scanning can significantly degrade the images. I show that the effect of position noise is largest where the magnetic field gradients are strongest and that the position noise can be reduced by averaging several scans. In addition, I calculate what

criteria must be satisfied to minimize the effect of position noise on the magnetic images. In particular, I find a minimum criteria for the accuracy of the translation stage.

In Chapter 8, I discuss how position noise affects the spatial resolution if one takes a magnetic image and converts it to an image of the source currents. I derive an analytical relationship between spatial resolution and position noise. I find that the closer the sample is to the sensor, the greater the effect of the position noise is on the spatial resolution. I identify a critical separation z_0, below which position noise dominates the total system noise. I also show how much the spatial resolution can be improved by reducing the position noise.

In Chapter 9, I will introduce different methods to find defects in superconducting wires using a SQUID microscope. Nb-Ti superconducting wire is used to wind superconducting magnets for magnetic resonance imaging (MRI) systems. If the Nb-Ti filaments are broken inside the wire, this reduces the current carrying capacity and can make the magnet useless for MRI. Finding hidden, interior breaks, or other defects is not easy. One way is to wind a magnet, cool it down and see if it works. However, if the magnet does not work, then the whole system is scrapped, which is expensive. That is why accurate detection of defects before winding is important.

Chapter 2

dc SQUID Overview

In this chapter, I introduce the theory of Josephson junctions and dc SQUIDs. I also discuss noise in SQUIDs, including white noise and 1/f noise, as well as the main applications of SQUIDs.

2.1 Theory of Josephson junctions

2.1.1 Equations of motion for a Josephson junction

An ideal Josephson tunnel junction [1] consists of two weakly coupled superconducting electrodes separated by a thin insulating layer through which Cooper pairs can tunnel. Many characteristics of Josephson junctions can be explained by the resistively and capacitively shunted junction (RCSJ) model [2,3]. Figure. 2.1 shows the basic components of this model: an ideal junction, an ideal current source, a shunting capacitor and a shunting resistor.

We can find the equations of motion of an RCSJ by considering the current flow in each arm of the circuit. Current I_c through (or into) the capacitance C is given by,

$$I_c = C\frac{dV}{dt} \tag{2.1}$$

where C = εA/a is the parallel plate capacitance of a junction with an insulating barrier of thickness a, an area A, and permittivity ε. The current through the resistor R is given

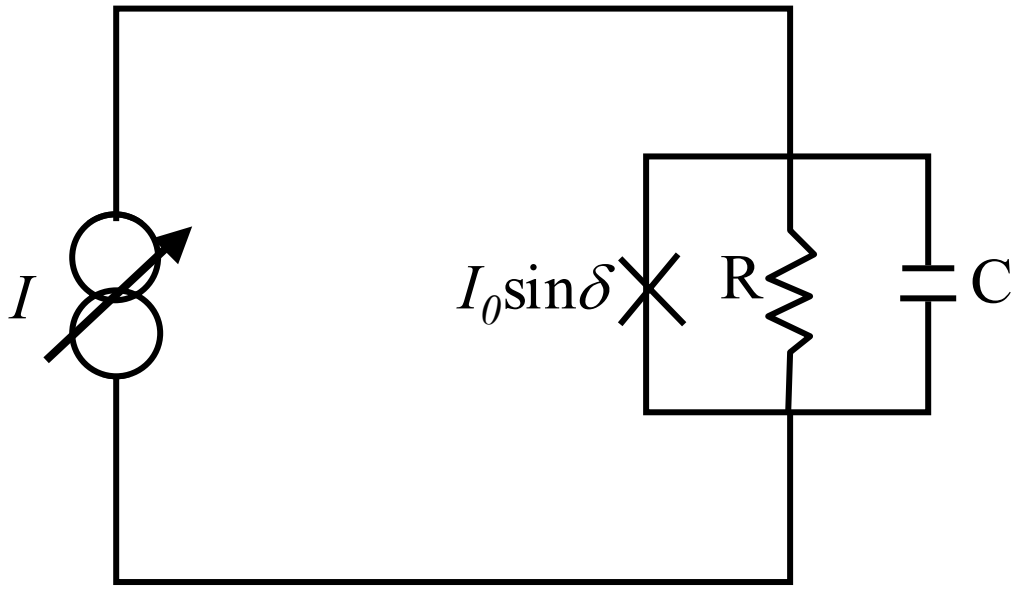

Figure 2.1: RCSJ model of a Josephson junction connected to a current source.

by,

$$I_r = \frac{V}{R} \tag{2.2}$$

Also, the ac Josephson relation tells us that [4]:

$$V = \frac{\Phi_0}{2\pi}\frac{d\delta}{dt} \tag{2.3}$$

where $\Phi_0 \equiv h/2e = 2.07\times10^{-15}$ T·m^2 is the flux quantum. Finally, the current through the junction is given by the dc Josephson relation,

$$I_j = I_0 \sin\delta, \tag{2.4}$$

where δ is the gauge-invariant superconducting phase difference between the two superconducting electrodes and I_0 is the critical current of the junction. Using current conservation, the total current I flowing through the three arms of the resistively and capatively shunted junction will be,

$$I = \frac{C\Phi_0}{2\pi}\frac{d^2\delta}{dt^2} + \frac{\Phi_0}{2\pi R}\frac{d\delta}{dt} + I_0 \sin\delta. \tag{2.5}$$

Equation (2.4) can also be written in dimensionless form:

$$i = \beta_c\ddot{\delta} + \dot{\delta} + \sin\delta, \tag{2.6}$$

where the dimensionless parameters are defined as

$$\tau \equiv 2\pi R I_0 t/\Phi_0,$$

$$i \equiv I/I_0, \tag{2.7}$$

$$\beta_c \equiv 2\pi C I_0 R^2/\Phi_0,$$

and " $\cdot$ " represents a derivative with respect to τ.

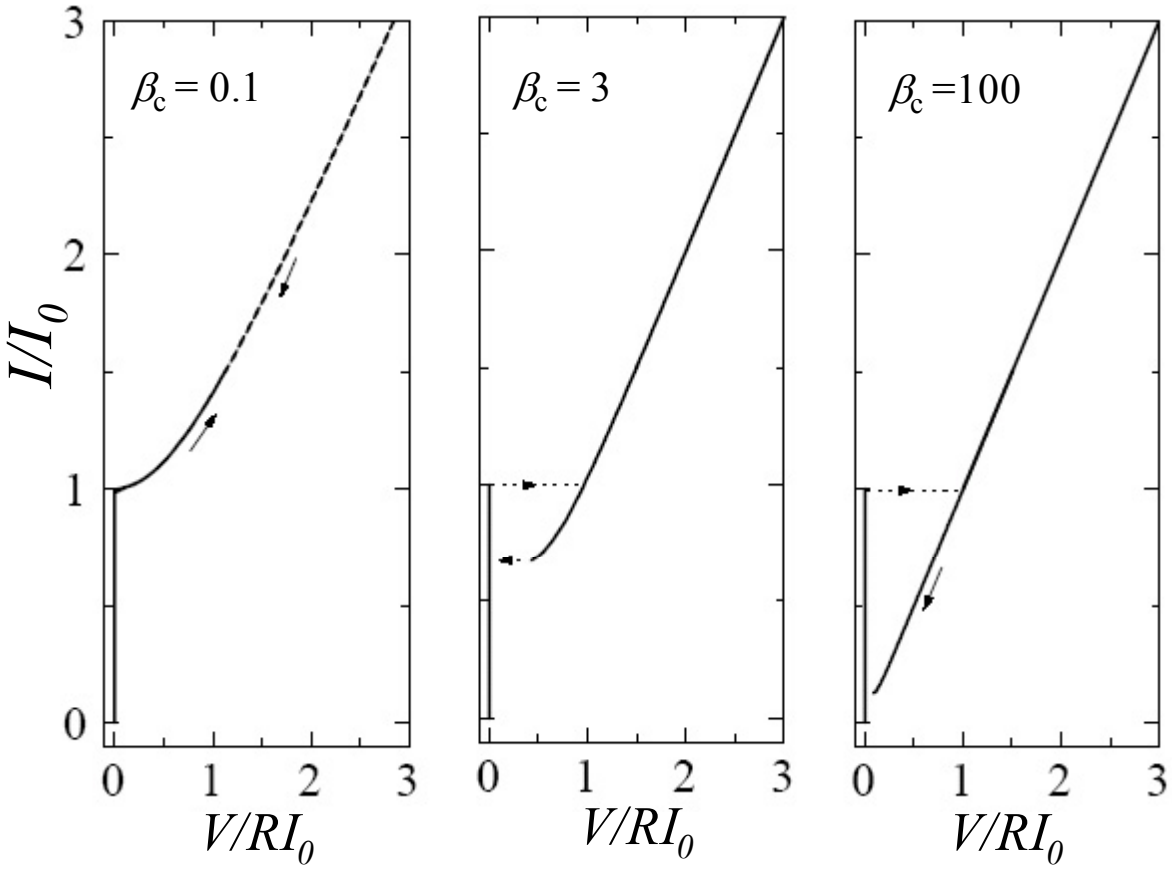

Figure 2.2: I-V characteristics of an ideal RCSJ Josephson junction at T = 0 for β_c =0.1, 3, and 100. (reproduced from ref. [5])

The parameter β_c is the "Stewart-McCumber damping parameter" [2, 3]. As shown in Fig. 2.2, if β_c >1 then the I-V curve becomes hysteretic, while for β_c <1 the IV is nonhysteretic.

2.1.2 Josephson junction with $\beta_c \ll 1$ (Non-hysteretic I-V curve)

When $\beta_c \ll 1$, the dynamics of the junction are determined simply by the Josephson junction and the shunting resistance. The dimensionless Eq. (2.6) becomes:

$$i = \dot{\delta} + \sin\delta. \tag{2.8}$$

If $I < I_0$, then all the current I flows through the junction and the voltage is zero. Thus the dimensionless voltage v across the junction is

$$v \equiv \frac{V}{I_0 R} = \dot{\delta} = 0 \qquad \text{for} \quad I \le I_0 \tag{2.9}$$

If $I > I_0$, then current flows through the Josephson junction and the resistor. Equation (2.8) can then be rewritten as

$$d\tau = \frac{d\delta}{i - \sin\delta}. \tag{2.10}$$

Integrating both sides yields : [6]

$$\tau = \frac{2}{\sqrt{i^2 - 1}} \tan^{-1}\left(\frac{-1 + i\tan\frac{\delta}{2}}{\sqrt{i^2 - 1}} \right) \tag{2.11}$$

Thus, the phase difference δ as a function of dimensionless time τ is

$$\delta(\tau) = 2\tan^{-1}\left[\left\{ 1 + \sqrt{i^2 - 1}\tan\left(\frac{\tau\sqrt{i^2 - 1}}{2} \right) \right\} \Big/ i \right] \tag{2.12}$$

To proceed, note that Eq. (2.12) is a periodic function with period τ_p,

$$\tau_p = \frac{2\pi}{\sqrt{i^2 - 1}} \tag{2.13}$$

The dc component of voltage is the time average of the voltage over the period. Therefore, the time-averaged dimensionless voltage is given by,

$$\langle v \rangle = \frac{1}{\tau_p} \int_{-\tau_p/2}^{\tau_p/2} \dot{\delta}\, d\tau = \frac{1}{\tau_p} \left[\delta(\frac{\tau_p}{2}) - \delta(-\frac{\tau_p}{2}) \right] = \frac{2\pi}{\tau_p} = \sqrt{i^2 - 1}\,. \tag{2.14}$$

Then using $V = \langle v \rangle I_0 R$, the relation between I and V is just,

$$V = I_0 R \sqrt{i^2 - 1} = R\sqrt{I^2 - I_0^2} \qquad \text{for } I > I_0. \tag{2.15}$$

Combining Eq. (2.9) and Eq. (2.15), we get the full I-V characteristics for $\beta_c \ll 1$ (see Fig.2.3). For the limit $I \gg I_0$, one finds ohmic behavior. In particular, I note that the I-V curve is non-hysteric since the effect of capacitance is negligible in this limit.

2.1.3 **Josephson junction with $\beta_c \gg 1$ (Hysteretic I-V curve)**

For $\beta_c \gg 1$, which can be thought of as the large capacitance limit, one might think that the junction can be treated as a parallel resistor and capacitor. For such an *RC* circuit, the averaged voltage is just *IR*. However, we have to be careful because of the non-linear relation between current and phase due to the junction. In fact, there are also several resistances that may be present. Thus there is shunt resistance R_s (due to any added shunts), a subgap resistance R_{sg}, which might exist for $V < 2\Delta/e$, and a normal resistance R_n of the junction. Of course R_n only exists for $V > 2\Delta/e$. and the dissipation increases very rapidly at the gap. Among these resistances, the smallest one will dominate Eq. (2.5) in the appropriate voltage range.

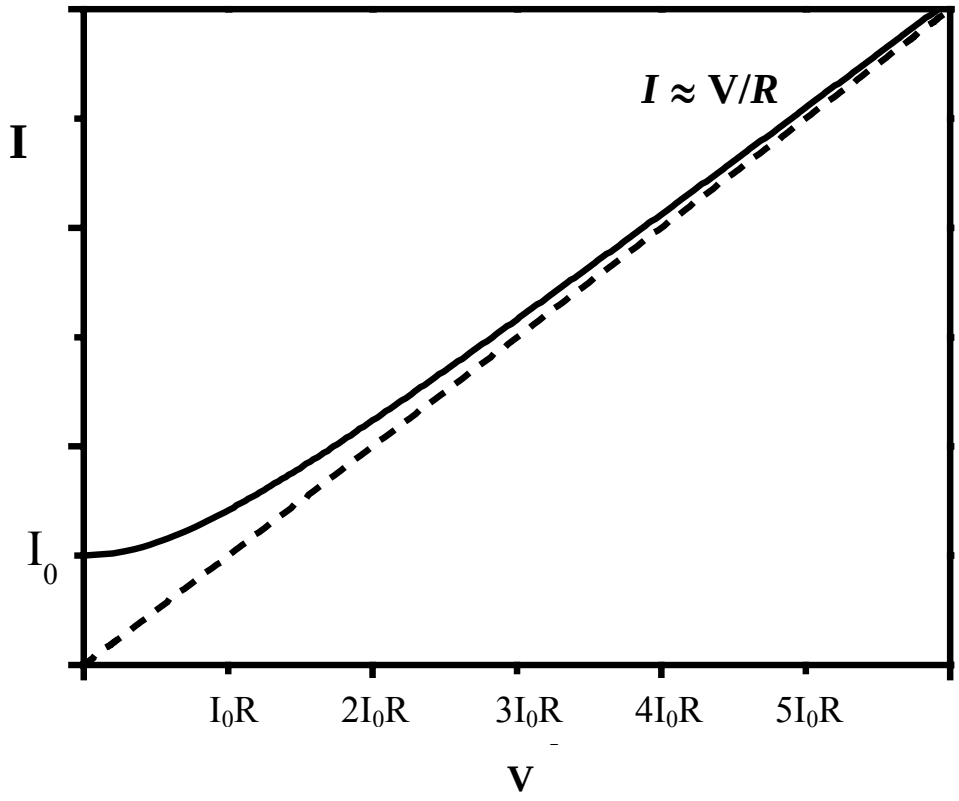

Figure 2.3: Calculated I-V characteristic of a shunted junction with $\beta_c \ll 1$. The solid line is from Eq. (2.9) and Eq. (2.15). The dashed line is $I = V/R$.

Let's first consider the situation where we start with $I = 0$, V = 0 and then increase I, but not too much, so that $I < I_0$. In this case, current can be driven through the Josephson junction with constant phase (it is also possible to have $I < I_0$ and the phase not constant, as described below.) If the phase is constant, the voltage across the junction will be zero. When $I \geq I_0$, a voltage is present and one sees quasi-ohmic behavior because the currents starts to flow through the resistance. This behavior can be explained by the motion of a ball moving on a tilted washboard potential [2,3] (see Fig. 2.4). The tilt is proportional to the applied bias current and the time derivative of phase corresponds to the voltage. When the tilt of the washboard is small and in the increasing direction (I increasing), the ball is confined in a well and the time average of $\dot{\delta}(t)$ is zero (voltage is zero). When the washboard tilt is enough for the ball to roll out, the time average of $\dot{\delta}(t)$ is nonzero (voltage is not zero). The critical tilt corresponds to I_0. This behavior corresponds to the I-V along the upper line in Fig 2.5(a).

Next consider the case when $I \gg I_0$, V > 0 and we start to decrease I. When $I \geq I_0$, the phase evolves in time and thus there is a voltage. However, when $I \leq I_0$, if the phase is evolving, it will tend to continue to evolve because of the capacitance. The corresponding section of the I-V curve is shown in Fig. 2.5(a) as a dashed curve.

This behavior can be understood from the washboard model. Suppose the ball is rolling down the tilted potential and we start to decrease the tilt so that $I < I_0$. At this tilt, there will be local minimum in the potential. But since the ball already has the kinetic energy, even if the angle of the washboard is well below the critical angle, the ball still has enough energy to roll over the bumps. Therefore, the ball will keep rolling and the voltage will not be zero. If the subgap resistance R_{sg} is smaller than the shunting

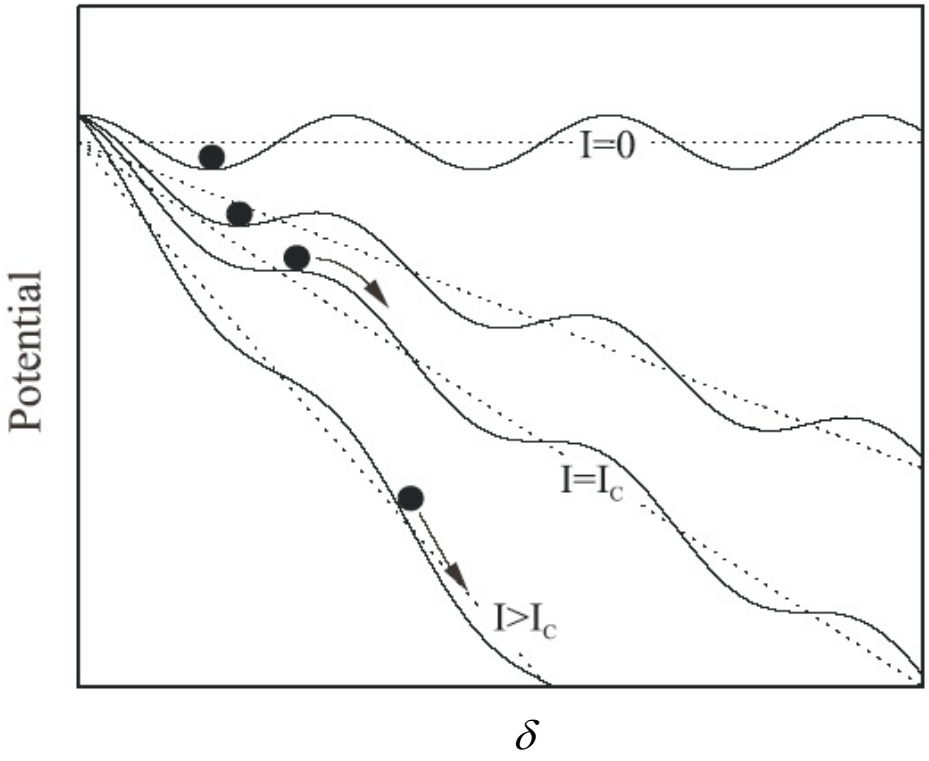

Figure 2.4: Massive particle moving in a tilted washboard potential is analogous to behavior of a RCSJ (reproduced from reference [5]).

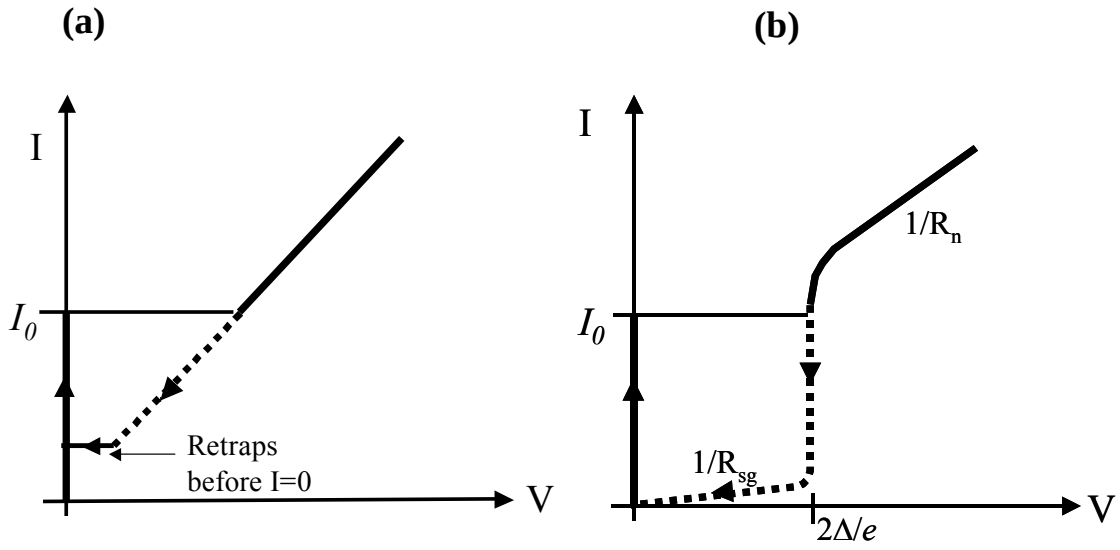

Figure 2.5: Hysteretic I-V curve (a) with small R_{sg}, (b) with large R_{sg}.

resistance R_s, then, for $V < 2\Delta/e$ the dominant resistance in Eq.(2.5) is R_{sg} Since the normal resistance R_n exists only above I_0, the slope of I-V curve changes from $1/R_n$ to $1/R_{sg}$ at $I \approx I_0$ (voltage gap = $2\Delta/e$) as shown in Fig.2.5(b). This kind of hysteretic Josephson junction is used for digital circuits and in quantum computation with superconducting devices [7].

2.2 dc SQUID

A dc SQUID consists of a superconducting loop which is broken by two Josephson junctions (see Fig. 2.6(a)). When the Josephson junctions are non-hysteretic ($\beta_c \ll 1$), the capacitance can be neglected and the total current flowing through the SQUID is the sum of the currents flowing through each junction and each parallel shunting resistor. From Eq. (2.5), the total current I is given by,

$$I = I_1(t) + I_2(t) = I_0 \sin\delta_1 + I_0 \sin\delta_2 + \frac{\Phi_0}{2\pi R_1}\frac{d\delta_1}{dt} + \frac{\Phi_0}{2\pi R_2}\frac{d\delta_2}{dt}, \quad (2.16)$$

where i = 1, 2 represent the left and right arm of the SQUID respectively and each junction has critical current I_0. The circulating current $J(t)$ that flows around the loop is then just [8]:

$$J(t) = (I_2(t) - I_1(t))/2. \quad (2.17)$$

The flux-phase relation tells us furthermore that the total flux in the loop is related to the junction phase by [9]:

$$\delta_1 - \delta_2 = 2\pi(\Phi_a + LJ)/\Phi_0, \quad (2.18)$$

where L is the total loop inductance and Φ_a is the external applied flux. The term ($\Phi_a + LJ$) = Φ_T is the total flux threading the superconducting ring.

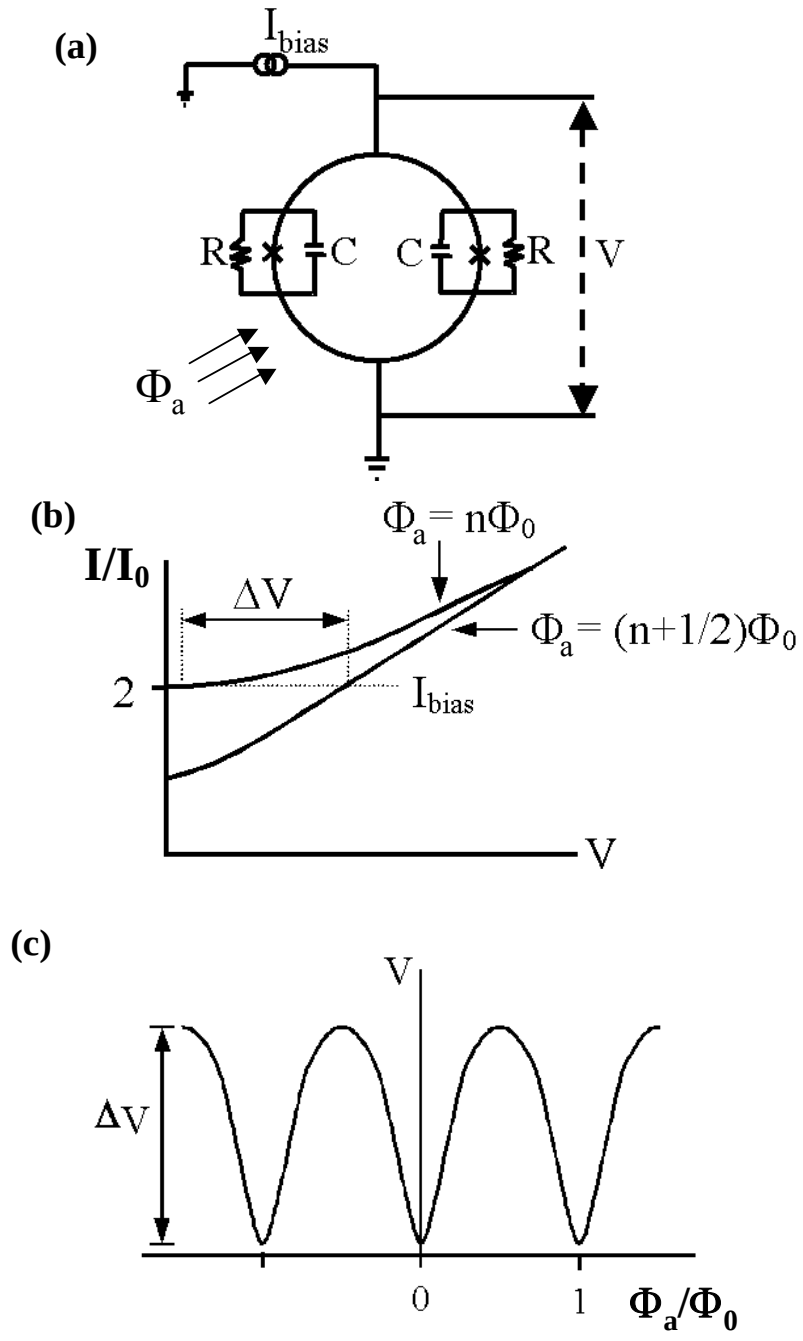

Figure 2.6: (a) Schematic of dc SQUID. (b) I-V characteristic curve of $\beta = 1$ SQUID. (c) Periodic relation between V and Φ_a/Φ_0 at a fixed bias current I_{bias}.

For convenience, we assume that the two junctions, two resistances, and two arm inductances are identical. Introducing the dimensionless quantities used in section 2.1, we can obtain,

$$v = (\dot{\delta}_1 + \dot{\delta}_2)/2, \tag{2.19}$$

$$i = \dot{\delta}_1 + \dot{\delta}_2 + \sin\delta_1 + \sin\delta_2, \tag{2.20}$$

$$j = (\sin\delta_2 - \sin\delta_1)/2, \tag{2.21}$$

$$\delta_1 = \delta_2 + 2\pi(\phi_a + \beta\, j/2), \tag{2.22}$$

where the parameters are defined as $v \equiv V/I_0R$, $2\pi RI_0/\Phi_0 \equiv \tau$, $i \equiv I/I_0$, $j \equiv J/I_0$, $\phi_a \equiv \Phi_a/\Phi_0$, $\beta_c = 2\pi I_0R^2C/\Phi_0$, $\beta = 2LI_0/\Phi_0$ and " $\cdot$ " represents a derivative with respect to τ [9].

From Eq. 2.19~2.22, we can show that

$$i = 2\dot{\delta}_2 + 2\cos\left(\pi(\phi_a + \beta j/2)\right)\cdot\sin\left(\delta_2 + \pi(\phi_a + \beta j/2)\right). \tag{2.23}$$

If I define $\delta \equiv \delta_2 + \pi(\phi_a + \beta j/2)$ and assume the time derivative of the circulating current j and applied flux ϕ_a is negligible, then this reduce to:

$$i = 2\dot{\delta} + a\cdot\sin(\delta), \tag{2.24}$$

where $a \equiv 2\cos(\pi(\phi_a + \beta j/2))$. This is very similar in form to the dimensionless equation for a single Josephson junction (see Eq.(2.8)). Following the same procedure, the time averaged voltage is just:

$$V = \frac{IR}{2}\sqrt{1 - \left[\frac{2I_0}{I}\cos\left(\pi\left(\frac{\Phi_a}{\Phi_0} + \beta j/2\right)\right)\right]^2} \tag{2.25}$$

Of course we would also need to solve for j to use this equation. Nevertheless, it is clear that the I-V curve depends on the applied flux, the circulating current j, and β. The modulation parameter $\beta = 2I_0L/\Phi_0$ is determined during the fabrication process. For, $\beta \ll 1$, the effect of j can clearly be neglected, and we sees that V is periodic in ϕ_a. This is the most important property of a dc SQUID. As flux is applied, the I-V curve will modulate between the curve at integer external field ($\Phi_a = n\Phi_0$) and that at half-integer external field ($\Phi_a=(n+1/2)\Phi_0$). For β not small compared to 1, the equation for the I-V curve is not simple because of the circulating current J term, but the relation between the voltage and the applied flux will still be periodic.

When $I = 2I_0$, the modulation of voltage is a maximum. At this current, the relation between voltage and external flux is shown schematically in Fig. 2.6(b). In particular, the response is periodic. However, I note that this non-linear response to flux makes a SQUID somewhat difficult to use as a measuring device because the response is very sensitive to the operating point. To get around this problem, it is standard practice to use a negative feedback loop or "flux-locked loop" to linearize the response, as will be explained in detail in Chapter 6.

2.3 Noise in the dc SQUID

The ability of a SQUID to detect small magnetic fluxes or fields is ultimately limited by the noise in the SQUID itself. We can separate this noise into two distinct types. One is called "white noise" or "broad-band" noise that arises from the resistive shunts in the SQUID. This noise does not depend on frequency, hence the term "white". The other is called "1/f noise", or excess low-frequency noise, which increases with

decreasing frequency. Typically 1/f noise in SQUIDs is only visible below 10 to 10^3 Hz. In this section, I discuss briefly the mechanisms that are known to generate noise in SQUIDs and how the noise may be removed or minimized.

2.3.1 1/f noise in low-T_c SQUID

The study of 1/f noise in SQUIDs is important because many applications (biomagnetism, NDE, corrosion and geophysics) require high sensitivity at low frequencies, often below 10 Hz. A large number of experiments over the last 20 years have shown that there are two dominant sources of 1/f noise in SQUIDs: (1) critical current fluctuations, and (2) vortex hopping. For many SQUIDs, both sources are important.

As explained in Ref. [9], critical current fluctuations occur because of microscopic physical processes within each junction. For example, if a single electron is trapped by a defect in the junction's insulating barrier, this causes the tunneling barrier to raise locally, thus reducing the critical current. As an electron is trapped or released, the critical current will fluctuate, producing a random telegraph signal. A similar situation occurs if a charged ion moves in the insulating barrier.

For a single trap, the noise spectral density $S(f)$ of this fluctuating critical current will be a Lorentzian [10]

$$S_{I_0}(f) \propto \frac{\alpha\, t_{\mathrm{p}}}{1+(2f\pi\tau)^2}, \tag{2.26}$$

where t_p is related to the life time of the trap. In most instances, the trapping is activated by temperature, so t_p is temperature dependent and we can write $t_p = t_0 \exp(E/k_B T)$ where E is the energetic height of the trap's barrier. If many traps are active in the junction, and each has its own t_p, the spectral density becomes [11]

$$S(f) \propto \int_0^\infty dE \left[\frac{t_0 \exp(E/k_B T)}{1 + (2f\pi t_0)^2 \exp(2E/k_B T)} \right] D(E) \ , \qquad (2.27)$$

where $D(E)$ is the distribution of activation energies for the traps. By carrying out this integral with the assumption that $D(E)$ is broad with respect to $k_B T$, we can get [9]

$$S(f) \propto \frac{k_B T}{f\pi} D(\bar{E}) \qquad (2.28)$$

where $\bar{E}$ is $k_B T \ ln(1/2\pi f\tau_0)$. We note that Eq. (2.28) predicts a 1/f - dependent spectral density for critical current fluctuations.

Remarkably, it turns out that one can reduce the noise from critical current fluctuations by various methods [10,12,13]. When the critical currents of both junctions increase together, this is called an "in-phase" fluctuation and otherwise, an "out-of-phase" fluctuation [14]. An in-phase fluctuation in the SQUID critical currents causes the V-Φ curve to shrink or stretch along the voltage-axis. In fact, the standard flux locked loop (described in Chapter 6) eliminates the effect of in-phase fluctuations. On the other hand, for an out-of-phase fluctuation, the I_0 of each junction is different, and this causes the circulating current J to change in the SQUID. This additional circulating current generates a flux LJ in the SQUID, which looks a lot like an applied flux. That is, the effect of out-of-phase fluctuations is to make the periodic modulation curve shift along the flux axis. This shift cannot be eliminated by just using an ordinary flux modulation scheme. However, a variation on this scheme can be used to reduce out-of-phase critical current noise. For example, Koch *et al.* [10] used a "bias reversal scheme". The basic idea is to reverse the SQUID bias current regularly, so that the additional circulating current from the critical current fluctuation switches back and forth and is effectively canceled out [14]. This same scheme, with slight modifications,

has been used for years in commercial SQUID electronics systems. Thus, for example, the Star Cryoelectronics I use has an optional bias reversal feature.

In addition to critical current fluctuations, flux motion can also cause 1/f noise. When SQUIDs are cooled in a magnetic field B_0, flux vortices can be trapped in the superconducting regions. If the vortices are strongly pinned at defects, there is no problem. However if the pinning sites are not too strong, then thermal activation can cause the vortices to hop randomly between pinning sites. This random motion can cause 1/f flux noise. The effect of this hopping on the noise in a SQUID can be analyzed using ideas that are similar to those I used to explain I_0 fluctuations. In particular, we can use Eq. (2.25), but now τ is a temperature-dependent hopping time, instead of the mean time trap lifetime, and the proportionality constants are different. Again, the superposition of many different hops can also yield a *1/f* spectral density [15].

After recognizing that it is possible to eliminate 1/f noise from critical current fluctuations, it is natural to ask if we can reduce the effect of vortex hopping noise using a similar scheme. Unfortunately, we cannot reduce it with an electronic biasing scheme since it actually is flux that is changing and this is what the SQUID senses. However, the noise is affected by the SQUID design, the cooling method, and the film quality.

The most practical method of eliminating vortex hopping is to use a SQUID design that does not allow flux vortices to enter. For example, Dantsker *et al*. [16] made noise measurements on films of various widths. The noise level in a 30 μm wide SQUID is much lower than that in a 500μm wide SQUID. This is because few or no

vortices will be present if the SQUID has a much smaller area than $A_0=\Phi_0/ B_0$ where B_0 is the field the SQUID is cooled in.

Another practical approach is to cool the SQUID in B = 0, since then vortices will not be trapped and thus they cannot cause noise. For example, Miklich *et al*. [17] showed that the flux noise $S_\Phi(f)$ is proportional to the cooling field, B_0. This means that $S_\Phi(f)$ is proportional to the number of vortices, as expected. Therefore, a good strategy is to keep B_0 very small when the SQUID is cooled through T_c.

Finally, depending on film quality, the flux noise can change dramatically, from 10^{-5} $\Phi_0/Hz^{1/2}$ to 10^{-2} $\Phi_0/Hz^{1/2}$ at 1 Hz and 77K in HTS SQUIDs [18, 19]. Also, Shaw *et al*. showed that artificial pinning sites reduce noise. These pinning site may be produced by proton or heavy-ion irradiation or by punching many small holes in the film [16]. Thus for lower noise, high-quality epitaxial YBCO thin films with many strong pinning sites are essential.

2.3.2 **White noise in low-T_c SQUID**

Above the 1/f noise region, the noise in a SQUID is frequency independent or white. This white noise is called “intrinsic noise” because it arises from the SQUID itself, assuming that the performance is not limited by the amplifiers used to read out the SQUID signal. To understand this noise, we first consider the situation for one junction.

If a junction is shunted by a normal resistor with resistance R, the Nyquist current noise power spectral density and voltage noise power spectral density from this resistance are, respectively,

$$S_I^{\,0}(f) = \frac{4k_BT}{R} \quad \text{and} \quad S_V^{\,0}(f) = 4k_BTR \ . \tag{2.29}$$

We can account for this noise by adding a random Nyquist noise current term $I_N(t)$ into Eq. (2.4) to obtain a Langevin equation,

$$I + I_N(t) = \frac{C\Phi_0}{2\pi}\frac{\partial^2\delta}{\partial t^2} + \frac{\Phi_0}{2\pi R}\frac{\partial\delta}{\partial t} + I_0 \sin\delta. \tag{2.30}$$

Using the tilted washboard model, we can set $I - I_0 \sin\delta = -4\pi e / h(\partial U / \partial\delta)$, where U is an effective potential energy as a function of δ [20]. The addition of the noise term $I_N(t)$ causes random tilting of the potential and leads to the I-V characteristic curve becoming rounded. This happens because the phase oscillates within the valleys of the washboard and also makes transition between the valleys due to the random tilting [8]. Phenomenologically, the voltage noise power spectral density across the junction can then be written as [9]:

$$S_V^{\,1}(f) = 4\gamma_0\, k_BTR \ . \tag{2.31}$$

where γ_0 is a dimensionless number which is greater than one for $I > I_0$.

To determine γ_0 for a junction, one can show that the voltage noise arises from two sources. One is the Nyquist voltage noise directly from the shunt, while the other is noise from the resistor that was generated at high frequency and mixed down to low frequency by the non-linearity in the junction [9]. These two terms are lumped into γ_0.

I next consider a bare SQUID (a SQUID without an input circuit), which consists of two Josephson junctions. The voltage noise power spectral density across the SQUID can be written as,

$$S_V(f) = 4\gamma_V\, k_BT\left(\frac{R}{2}\right) = 2\gamma_V\, k_BTR \ , \tag{2.32}$$

where γ_V can be found only by digital simulation. For a SQUID with β_c=0, β =1, at sufficiently low temperature and biased properly Tesche *et al.*and Bruines *et al*. found $\gamma_v \sim 9$ [17,21].

If $S_V(f)$ is known, the corresponding effective flux noise power spectral density $S_\Phi(f)$ is then

$$S_\Phi(f) = \frac{S_V(f)}{V_\Phi^{\,2}} \ , \tag{2.33}$$

where $V_\Phi = \partial V / \partial \Phi_a$ is the flux to voltage transfer function. Taking the derivative of Eq.(2.24) with respect of Φ at $I \approx 2I_0$ and $\Phi \approx (1/4)\,\Phi_0$ for $\beta \approx 1$ and $\beta_c \ll 1$ gives:

$$V_\Phi = \frac{\partial V}{\partial \Phi_a} \approx \frac{R}{L} \ , \tag{2.34}$$

where L is the inductance of the SQUID's loop. Plugging Eq.(2.32) and Eq. (2.34) back into Eq.(2.33), Tesche *et al.* and Bruines *et al*. found $S_\Phi(f) \cong 18 k_B T L^2/R$. Thus we see that low noise operation is possible by using a low inductance SQUID at low temperature, and it is best to keep the resistance R high.

2.3.3 **Noise in high-T_c SQUIDs**

Tesche *et al.* showed theoretically that the minimal white noise in low-T_c SQUIDs is obtained for $\beta \approx 1$ [8]. However it is now known that this white noise result cannot be applied accurately to high-T_c SQUIDs. While the underlying physics and equations are the same, the SQUID parameters for high-T_c devices tend to push the behavior into a different regime.

The behavior of 1/f noise in high-T_c SQUIDs is similar to that in low-T_c SQUIDs. Again the sources are the fluctuations of the critical current and vortex motion. This excess noise can be reduced in the same way as for low-T_c SQUIDs (see section 2.3.1).

For the white noise, the behavior is somewhat different. The I-V curve in Eq.(2.25) is only slightly temperature-dependent near 4.2 K for Nb SQUIDs with typical parameters. Thus the transfer function V_Φ (= $dV/d\Phi$) in typical low-T_c SQUIDs does not depend strongly on temperature. However, for high-T_c SQUIDs, the effect of temperature is not negligible. Enpuku *et al.* found the characteristics and transfer function for relatively high temperature operation [22]. From their analysis, they found the SQUID transfer function V_Φ is given by:

$$V_\Phi = \frac{4I_0R_0}{\Phi_0(1+\beta)}\exp\left(-\frac{3.5\pi^2 k_B TL}{{\Phi_0}^2}\right) \tag{2.35}$$

where k_B = 1.38×10^{-23} J/K is the Boltzman constant. The white flux noise power spectral density is given by,

$$S_\Phi = \left[1+\exp\left(1.23-4.82\frac{2\pi k_B T}{I_0\Phi_0}\right)\right]\cdot L^2\,\frac{2k_BT}{R_0}\cdot\left[1+\left(\frac{R_0}{LV_\Phi}\right)^2\right] \tag{2.36}$$

From this expression, we can see that the flux noise increases when the self-inductance increases. Also for fixed self-inductance, the effect of I_0 is weak. While this expression is complicated, one can still see that the white noise can be reduced by using low inductance SQUID design.

2.4 SQUID applications

2.4.1 Non-Destructive Evaluation

SQUIDs can detect weak magnetic fields without requiring any electrical or mechanical connection to a sample. These characteristic make them potentially very useful for Non-Destructive Evaluation (NDE) of metal parts and electrical circuits. For many industrial application, NDE is a very important technique. SQUIDs have been used for several kinds of NDE including the localization of shorts in integrated circuits, the detection of defects in superconducting wires, and the examination of corrosion and other subsurface damage in metallic structures.

For integrated circuit manufacturing, "failure analysis" means the localization of a defect in a computer chip or multi-chip module (MCM). Finding defects has become progressively harder as the size of transistors has gotten smaller. Since SQUIDs are small and currents produce magnetic fields, it is perhaps natural to think of using a SQUID microscope to locate defects in computer chips. Also, one can apply magnetic inverse techniques [23] to produce current density images that reveal the location of the current carrying wires. For examples, Fig. 2.7(a) shows a magnetic field image taken by S. Chatraphorn using our single-channel high-T_c scanning SQUID microscope [24]. Figure 2.7(b) is the current density image found using the magnetic inversion technique. Figure 2.7(c) is the CAD layout of the wires in the MCM. The CAD design shows that one of the wires on the fourth layer (4F) is not supposed to connect to a wire in the third layer (3F), but the SQUID results show that the two are shorted at a specific location.

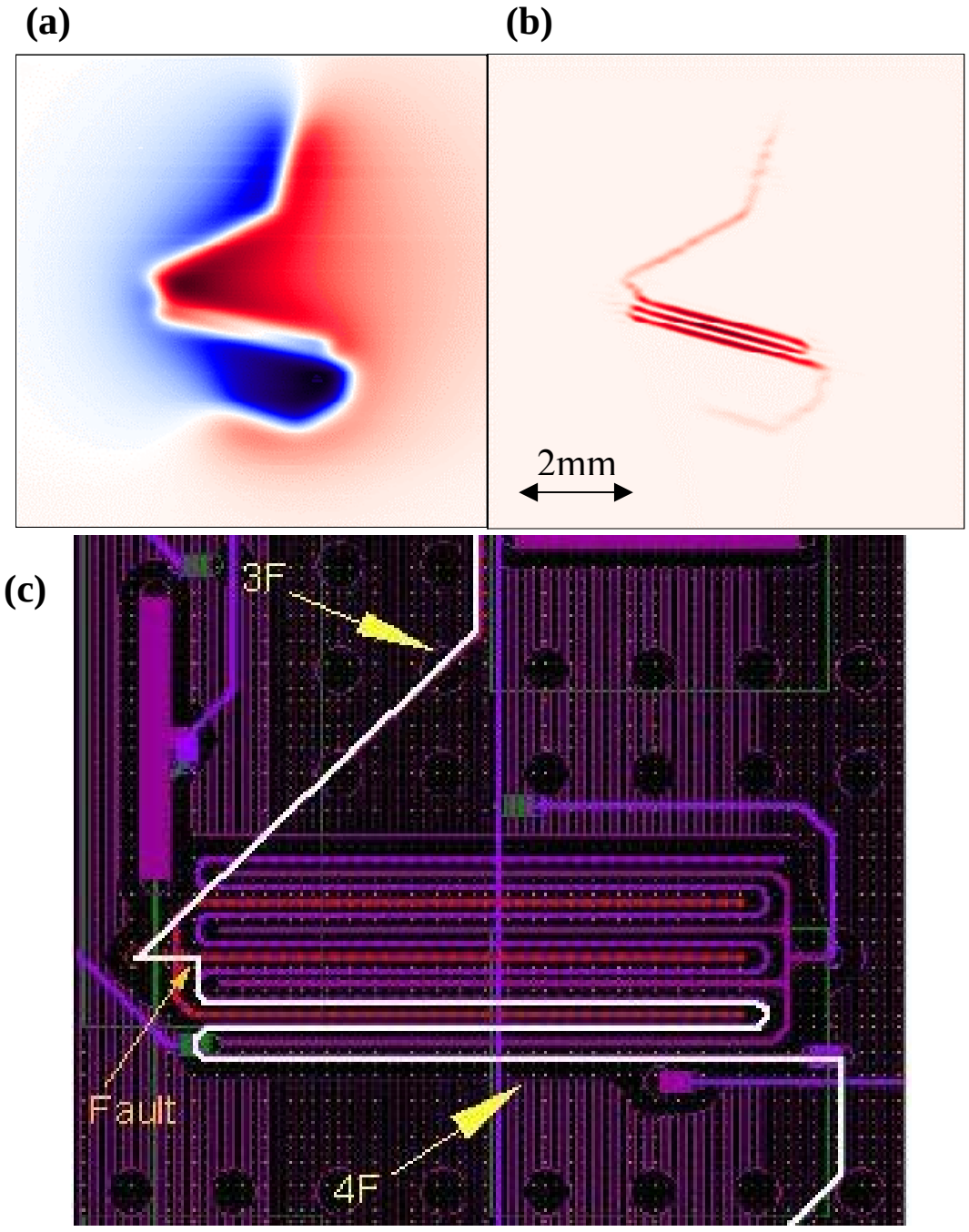

Figure 2.7: Magnetic image of a multi-chip module (MCM) over a "hot spot". (a) Magnetic field B_z (red and blue indicate ± 50 nT) (b) Current density image calculated from (a), (c) CAD layout of circuit. The line in (c) indicates the current path obtained from SQUID (reproduced from Ref. [24]).

One of the largest applications of superconductors is for magnets for Magnetic Resonance Imaging (MRI) systems. These wires are composites in which NbTi filaments are embedded in copper. It is hard to find defects inside the wire that could disrupt the flow of supercurrent. In Chapter 9, I show that SQUIDs have the potential for doing this type of NDE.

Corrosion has been studied for many decades because many structures are made of metal and serious accidents can occur if the metal is weakened by corrosion. Wikswo *et al*. demonstrated that SQUIDs can be used to detect very weak magnetic fields from hidden, active corrosion [25].

In our lab, corrosion currents (current flow from chemical reaction in corrosion) were measured by J. O. Gaudestad using our single channel high-T_c scanning z-SQUID microscope [26]. Figures 2.8(a)~(d) show how the magnetic field changes while the aluminum sample undergoes pitting corrosion in a solution. In these images, the magnetic field tends to be stronger at the edges than at the center of the sample. Also, the sequence of images shows that the intensity of the magnetic field increased and then decreased after several hours, presumably because the corrosion pits will slowly close off.

The current flow between source pits and drain pits appears to act as a finite current lead or "current-dipole". In these images, the SQUID is detecting the magnetic field from current-dipoles formed during the corrosion. Therefore vertical pitting corrosion induces an x or y component of magnetic field and horizontal pitting corrosion induces a z-component of magnetic field. Since the SQUID was oriented to

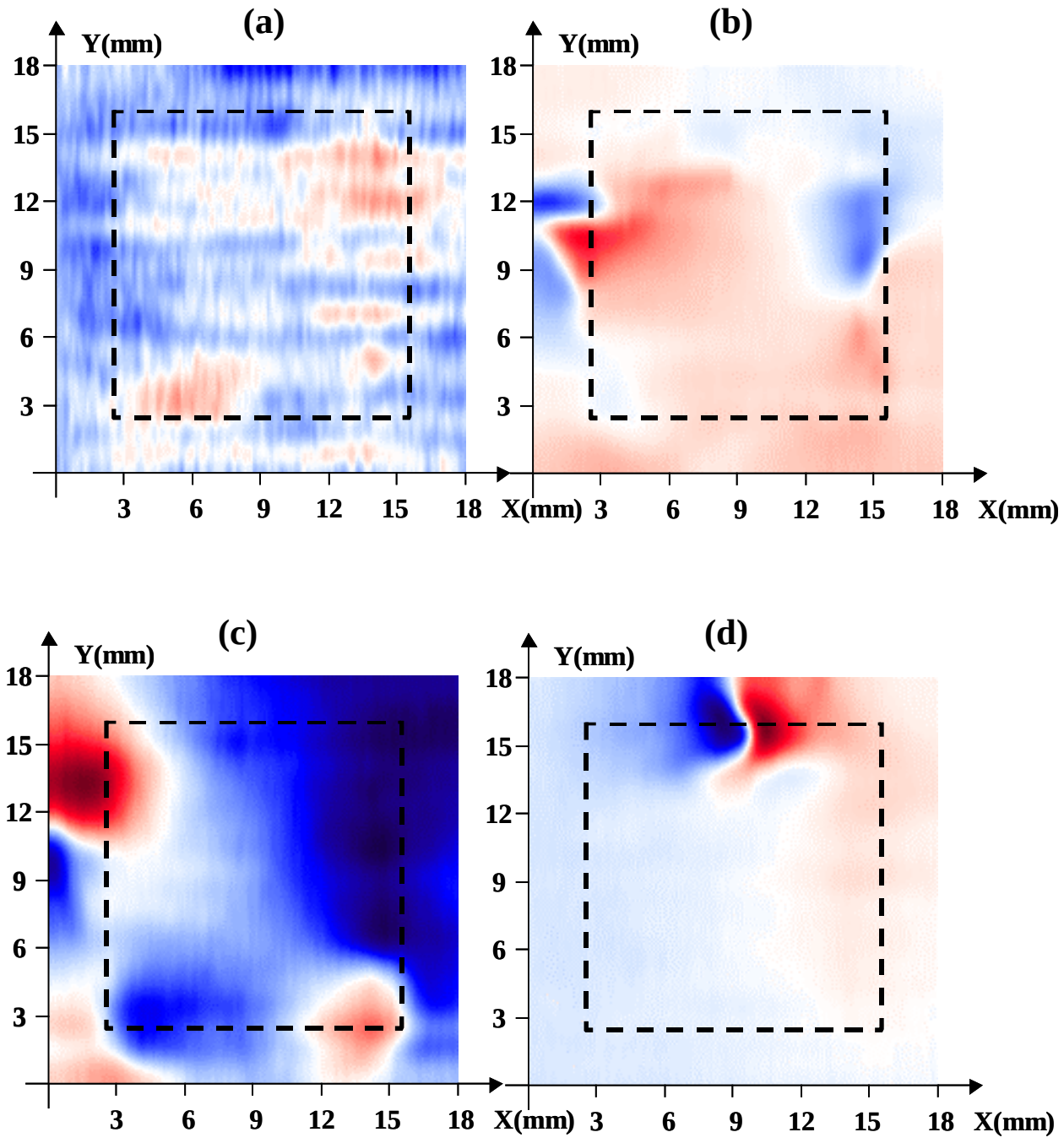

Figure 2.8: Magnetic imaging of active pitting corrosion of Al in a NaCl solution during (a) 6~43 min with B_{pp} = 16 nT, (b) 92~128 min with 188 nT, (c) 134~179 min with 79 nT, and (d) 304~340 min with 176 nT. Red and blue indicate maximum and minimum of magnetic field, respectively (reproduced from ref. [26] by J. O. Gaudestad *et al*.).

detect B_z (z-SQUID configuration) and horizontal pitting will occur mainly on the edges of the plate, more signal was detected at the edges.

2.4.2 **Biomagnetic studies**

Another outstanding application of SQUIDs is biomagnetic studies. Properly designed low-T_c SQUID are sensitive enough to detect magnetic fields produced by currents generated when neurons are active in the human brain. Magnetoencephalography (MEG) has merit because the magnetic fields from cortical neurons are not distorted by bone and tissue. This allows fairly accurate localization of sources in the brain. MEG research can be used for presurgical mapping of tumors [27], neurocognitive perception [28], and linguistic studies [29]. Commercial MEG systems typically use 100 SQUID channels or more, arranged in a helmet-shaped apparatus that fits closely to the head.

Compared with the field generated by the brain (pT to fT), the signal from a beating heart is much stronger (pT to nT). Magnetocardiographs (MCG) can be used for diagnosis of ischemic or fetal heart disease and localization of the region of arrhythmia [30]. As with MEG, the magnetic signal can be combined with electrical measurements to produce additional information [31].

2.4.3 **Geophysics**

SQUIDs have also been used for geophysics. By measuring the magnetic field from layers of rock, the geological history of a region can be understood. Also, by applying low-frequency electromagnetic fields to the ground, the conductivity vs. depth

of an area can be determined. Thus Clarke *et al.* measured the surface impedance of the ground as a function of frequency, and found the resistivity as a function of position and depth. The resulting resistivity can yield important information on the existence of sedimentary basins, geothermal sources, and oil deposits and earthquakes [32]. As another example, Prof H. Paik developed a superconducting gravity gradiometer (SGG) that uses a SQUID as an amplifier to detect variations in g, the local gravitational acceleration [33].

2.5 Conclusion

In this chapter, I described the equations of motions and behavior of Josephson junctions and SQUIDs. I discussed the I-V curves in two limits. A dc SQUID consists of two Josephson junctions in a loop. I described 1/f noise that arises from critical current fluctuations and vortex hopping. I noted that bias current reversal techniques help to reduce the 1/f noise from critical current fluctuations. For eliminating 1/f noise from vortex hopping, zero-field cooling and good quality thin films with strong pinning sites are essential. Nyquist noise arises in the resistive shunts in the SQUID, and causes white noise in the SQUID. However, we can minimize this noise by optimizing the SQUID design. A few applications of SQUIDs were discussed. Using a scanning SQUID microscope, we can measure the magnetic field from samples or circuits without electrical or physical contact. SQUIDs are also used for biomagnetic and geophysical measurements.

Chapter 3

Design of a Multi-channel High-T_c SQUID Chip

In this chapter, I describe the main issues affecting the design of SQUID chip for a multi-channel SQUID microscope. In particular, I discuss why I chose to use high-T_c SQUIDs and how I chose the orientation of the SQUID. I also describe in detail the design of my multi-channel SQUID chip. Given this design I then calculate the mutual inductance between a SQUID and its modulation line, and the mutual inductance between a SQUID and neighboring modulation lines. From this calculation, I found the crosstalk between SQUIDs and discuss how to correct for it.

3.1 High-T_c SQUID chip

The ultimate limiting source of noise in SQUIDs is the intrinsic, or Nyquist noise, from the resistors shunting the junctions. Since this noise scales with the temperature, this would suggest using a low-T_c SQUID. In addition, low-T_c superconducting materials can be made into wires, or patterned into complex multi-layer structures. However, it is hard to beat the attraction of high-T_c SQUIDs. High-T_c SQUIDs can be operated in liquid nitrogen at 77 K. Liquid nitrogen is cheap, readily available, and will last a long time in a dewar because of its high latent heat. In addition, it turns out that the sensitivity of high-T_c SQUID is good enough (~$10\mu\Phi_0/\mathrm{Hz}^{1/2}$) for many purposes. Thus finding electrical shorts in integrated circuits, or NDE of

superconducting wires samples is within the capability of high-T_c SQUIDs. For these reasons, I chose a high-T_c SQUID as a sensor.

There are several ways to fabricate Josephson junctions for a high-T_c SQUID. The most common devices are step-edge Josephson junctions and bicrystal grain boundary junctions. A step edge junction is made using the following procedure: A step is first fabricated by Ar^+ ion-milling a photoresist-masked $SrTiO_3$ substrate to produce a step with a step angle of 65-75° (see Fig. 3.1). An HTS film is then deposited over this step and patterned into a line, forming a junction where the line goes over the step (see Fig 3.1(a)[1]). By using standard photolithography and ion-milling, the step edge can be placed anywhere. This can be advantageous when making gradiometers [2] or multiple devices.

A bicrystal grain boundary junction is produced by growing an HTS films on a specially manufactured bicrystal substrate - two pieces of substrate are fused together with an in-plane misalignment as shown in Fig 3.1(b) [1]. Junctions form only along this fused line, which restricts design freedom. However, fabrication is very straightforward and reliable. In addition, SQUIDs made with bicrystal junctions show relatively good noise properties. Therefore, I chose to use bicrystal grain boundary junctions for my multi-channel SQUID chip.

Common angles of misorientation for the grain boundary are 24° and 30°. To increase the SQUID sensitivity, the product of the critical current (I_c) and junction resistance (R_N) should be large [3]. Ludwig *et al.* found the magnetic field noise of a magnetometer made with a 30° bicrystal was significantly lower than that for 24°. The reason was that the I_cR_N product for the 30° magnetometer was twice as large as that for

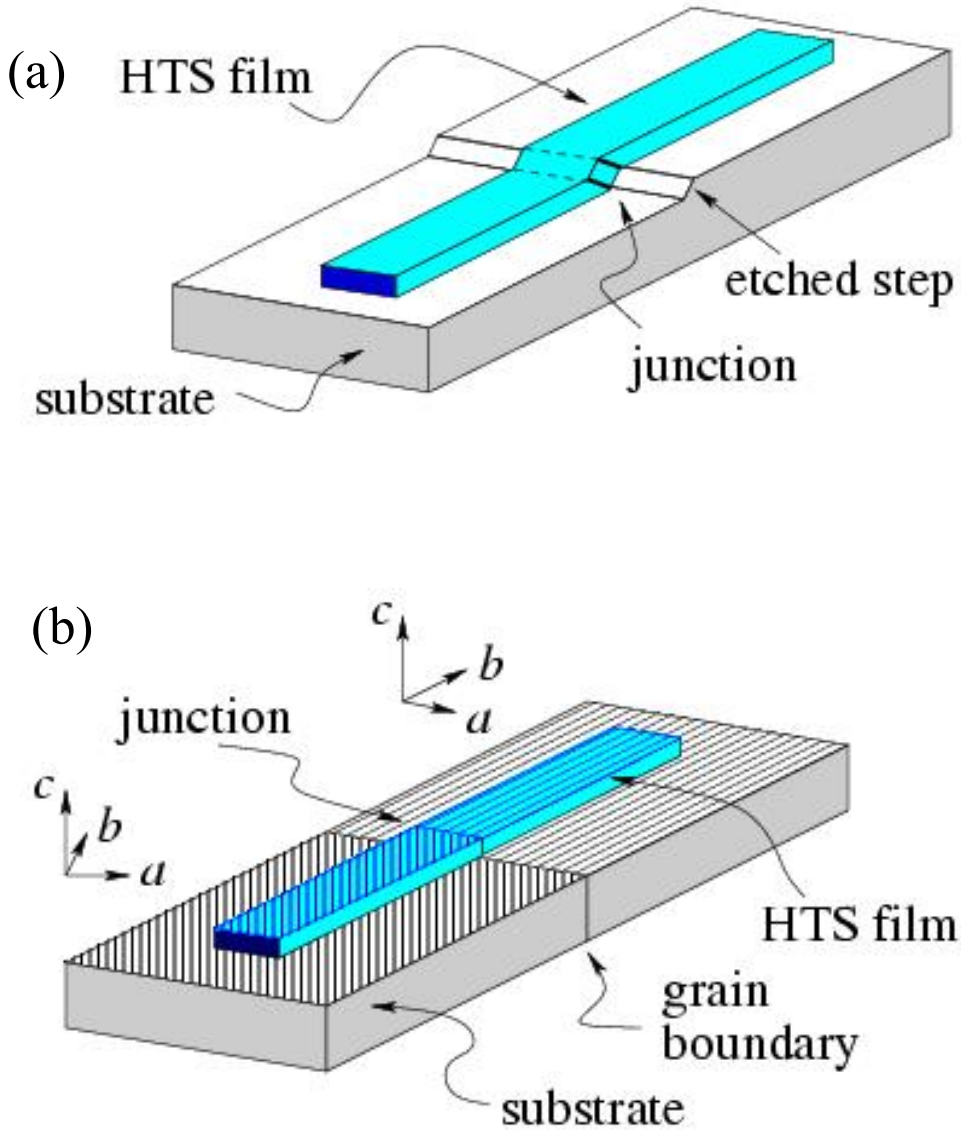

Figure 3.1: (a) Step edge grain boundary Josephson junction, (b) Bicrystal grain boundary Josephson junction (reproduced from Ref. [1])

the 24° [4]. For this reason, 30° bicrystals are now commonly used for SQUID fabrication.

3.2 Bare SQUID vs. coupled SQUID

In many applications of SQUIDs, the SQUID is coupled to a separate pickup loop to enhance its sensitivity. SQUID microscopy is the notable exception. In fact, fro microscopy, a bare SQUID is preferable. To understand why pickup coils are often used for other applications, I note that a typical value for the inductance of a SQUID is about 100 pH or less, which is quite low. Since inductance scales with length, this means that typical SQUID are quite small (< 1mm) and thus the effective pickup area of a bare SQUID is small, resulting in a low magnetic field sensitivity for many applications. To solve this problem, a separate pickup coil with large area is introduced. To ensure good inductive coupling to the SQUID, Ketchen and Jacox introduced the idea of using a spiral thin-film input coil on a SQUID in a square washer configuration [5]. The input coil is separated from the SQUID by an insulating layer. This design can also be used for high-T_c SQUIDs.

Unlike other applications, scanning microscopy requires high spatial resolution in addition to sensitivity. This means we should not have a large area pickup coil since it will average the magnetic field over a large area. Therefore, although there are advantages to using a pickup coil, it is not helpful for our purpose. In addition, the fabrication of a bare SQUID sensor is much more convenient for HTS. The sensitivity of a bare high-T_c SQUID (~10μ Φ_0/Hz$^{1/2}$) is good enough when the sample is very close to the sensor, typically below 200 μm. Fig 3.2(a)-(b) shows simple diagrams of a bare

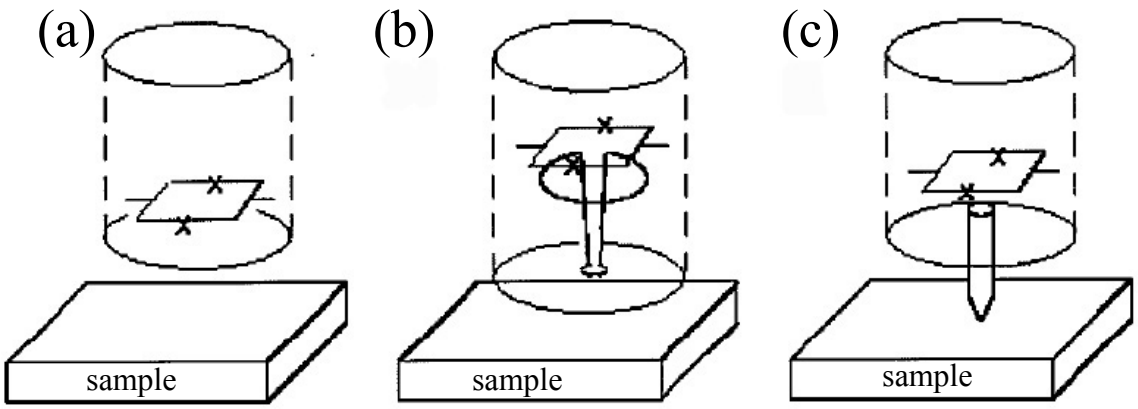

Figure 3.2: Various schemes for arranging the SQUID for microscopy of room temperature samples (a) bare z-SQUID, (b) SQUID inductively coupled to superconducting pickup coil, (c) SQUID coupled to 300 K flux guide (figure is reproduced from [6]).

SQUID system (like my system) and a coupled SQUID system. Fig 3.2(c) shows a recently developed method using a magnetic flux guide made of high permeability material, which gives extremely small spatial resolution, in principle if one can get close to the sample, although with significant degradation of the sensitivity [7]. We also note that if one could build a system like Fig. 3.2 (b) then one could also probably just build a bare SQUID of the same size as the pickup coil, and use it instead. The resulting bare SQUID system would have superior flux and field sensitivity.

Figure 3.3(a) shows the layout I adopted for my 8-channel SQUID chip. Each bare SQUID is a vertically oriented rectangular loop with outer dimensions 30 μm by 60 μm and inner dimensions 10 μm by 40 μm, as shown in Fig. 3.3(b). The calculated effective area is approximately $\sqrt{30 \cdot 10} \times \sqrt{60 \cdot 40}\,\mu\text{m}^2$ which is 17×49 μm^2 and self-inductance L ~ 70 pH. For a given magnetic flux sensitivity, a large SQUID size tends to give a better sensitivity while the spatial resolution is degraded. I note that this is only roughly true for an "*x*-SQUID" such as I describe here. We chose 17 μm as the effective width of the SQUID since it is roughly equal to the present limit of the spatial resolution if we are 100 μm from the sample. This limit comes by applying an appropriately filtered magnetic inverse technique [8,9], which yields a spatial resolution of the source current density of about z/5, where z is the distance between the sample and the sensor. It is difficult to operate our SQUID microscope with a z smaller than about 100 μm, leading to a spatial resolution limit of about 20 μm. Therefore, the SQUID width is appropriate for our system. The vertical effective length of the SQUID, 49 μm, is longer than the horizontal width of the SQUID in order to improve

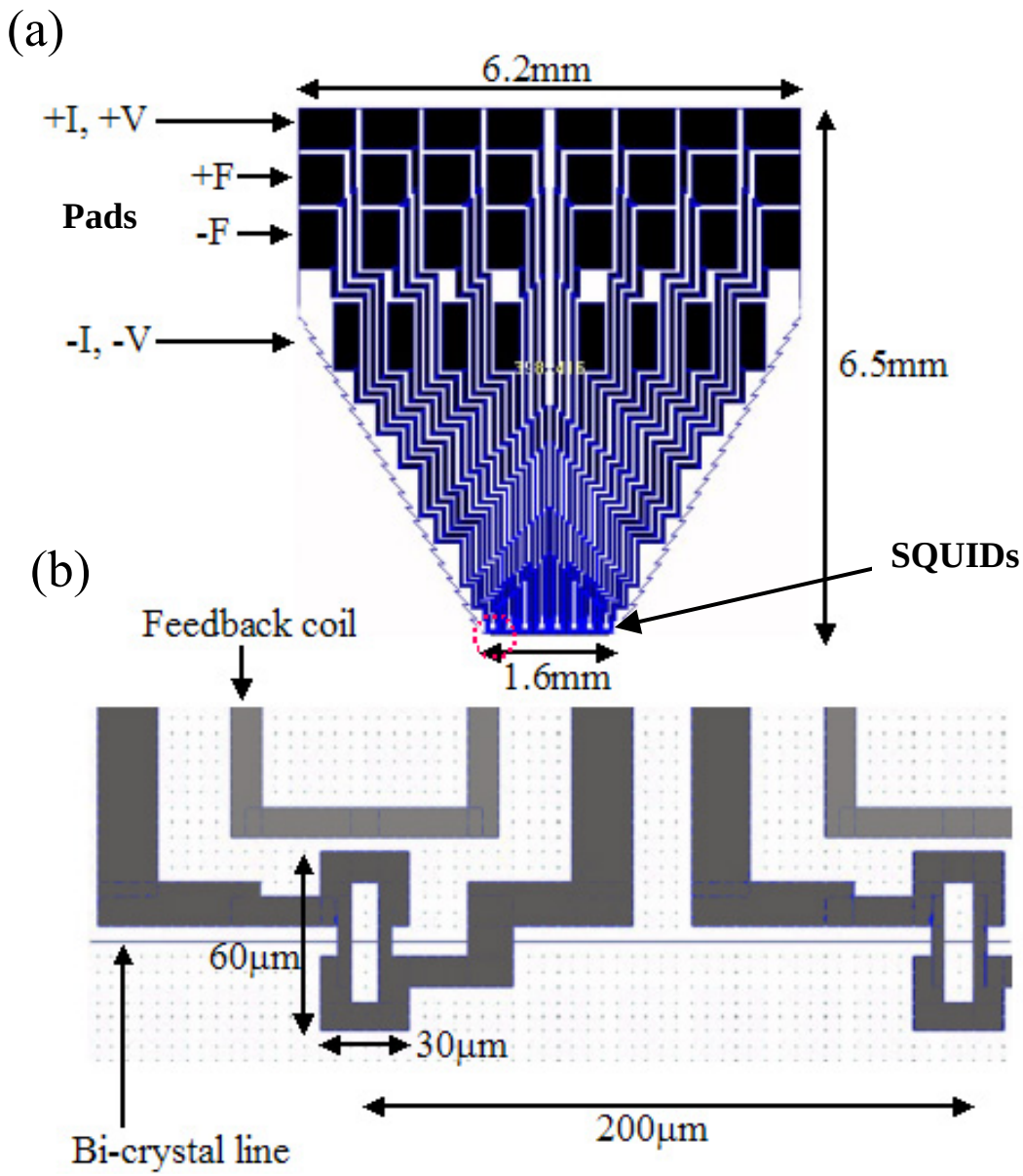

Figure 3.3: (a) Design of my 8-channel high-T_c SQUID chip (overall size 6.2 mm×6.5 mm). Current, voltage, and flux pads are labeled. The SQUIDs are along the bottom of the chip. (b) Magnified view of an individual SQUID with outer area 30 μm×60 μm.

the sensitivity. In fact, this dimension has little effect on spatial resolution for an *x*-SQUID configuration.

In my design, the flux feedback line and ac flux modulation line are shared. I designed the distance between each SQUID and its feedback line to be 10 μm. In principle, the closer the better the coupling, however, when I tried to reduce it below 5 μm I had difficulty patterning the chip. From mutual inductance calculations (see section 3.4 for detail), I find that mutual inductance between a SQUID and its feedback line is about 2.39 pH. In fact, we had run an earlier single *x*-configuration SQUID with a very similar design (see Fig. 3.4). For this earlier system we measured the mutual inductance to be

$$M_F \cong \frac{R_F}{C_\Phi} = \frac{1000\Omega}{0.1V/\Phi_0} = 2.07pH \qquad (3.1)$$

where M_F is the mutual inductance between the SQUID and its feedback line, R_F is the feedback resistance, and C_Φ is the feedback loop's voltage-to-flux transfer function.

3.3 SQUID orientation

A key aspect of the design of my multi-channel SQUID chip is the orientation of the SQUID loops. Figure 3.4 shows the two most common orientations used in SQUID microscopy. In Fig 3.4(a) the SQUID loop is parallel to the sample plane. We call this a *z*-SQUID configuration. In Fig 3.4(b) the SQUID loop is perpendicular to the sample plane. We call this an *x*-SQUID configuration. While the z-SQUID is sensitive to the z-component of magnetic field, the *x*-SQUID is sensitive to the *x*-component of magnetic field, which is also the main scanning direction when raster scanning a sample. The different configurations are useful for different applications. For the *x*-SQUID

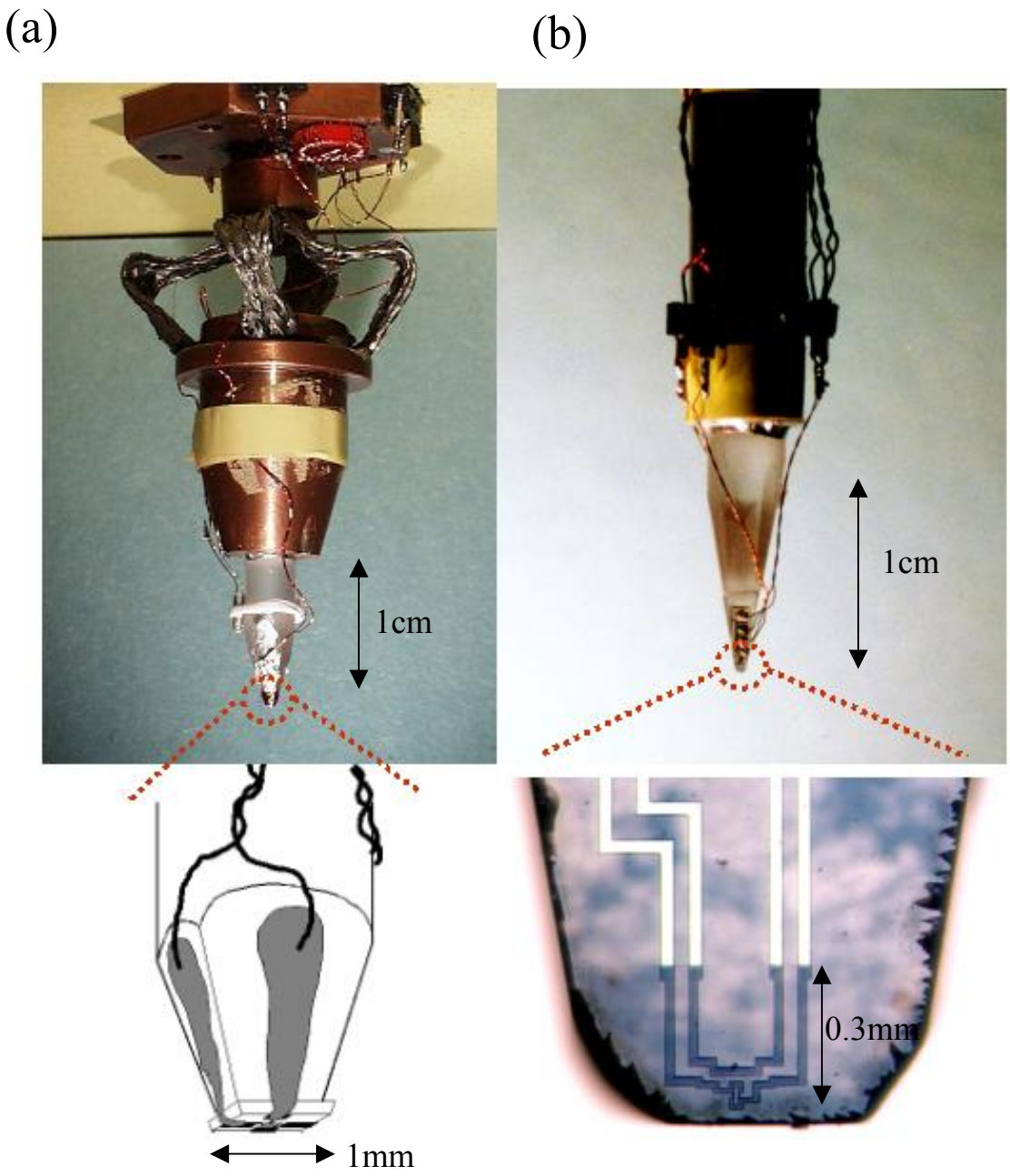

Figure 3.4: Cold-finger and sapphire rod for (a) single *z*-SQUID, (b) single *x*-SQUID.

configuration, there are some additional advantages. In particular, it is easy to make a multi-channel SQUID by simply placing the SQUIDs next to each other in a line on one side of the chip. Electrical connections can then be made to the other end of the chip, where there is no shortage of space. However, in the case of the *z*-SQUID, the configuration complicates the wiring of the modulation lines and I-V lines since everything will end up being pushed close to the sample surface. Therefore, I chose the *x*-SQUID configuration for my multi-channel SQUID chip.

Thus my multi-channel SQUID chip consists of 8 equally separated *x*-SQUIDs in a single array on the same plane. I chose 8 because typically a DAQ board has 8 differential channels, and also because of the availability of a commercial 8-channel SQUID feedback electronics and controller [10].

3.4 Crosstalk between SQUIDs and its calibration

In my design the distance between the center of a SQUID and the center of the next SQUID is 200 μm, and the 8 SQUID array is arranged at the bottom of the chip with a total length of 1.6 mm (see Fig. 3.3(a)). 200 μm is somewhat large, but reducing the separation would increase crosstalk between the SQUIDs and neighboring modulation lines. Increasing the separation beyond 200 μm would make the width at the bottom of the chip larger, which we will see in Chapter 5 would mean the window would also have to be larger, making it harder to bring the window close to sample.

The issue of crosstalk is important for any multi-channel SQUID design. Ideally, one wants each SQUID to read only the magnetic field from the sample and couple only to its own feedback line. But each SQUID can also pick up signals from neighboring

feedback lines as shown in Fig. 3.5. When I designed the SQUID chip, I had to consider how large this effect would be by finding the mutual inductance between a SQUID and a neighboring SQUID's modulation line.

The mutual inductance M_{12} can be defined as the proportionality between the magnetic flux generated in the second coil to the current in the first coil which produced it. In my SQUID chip, the flux in a SQUID loop is generated by a current in all of the feedback lines. The mutual inductance between a SQUID and a modulation line is given by,

$$M = \frac{\mu_0}{4\pi} \int \oint \frac{d\vec{l}_1 \cdot d\vec{l}_2}{r} \qquad (3.2)$$

where the closed loop integration dl_1 is over the SQUID loop, the open loop integration dl_2 is along the feedback line, and r is the distance between the SQUID loop and the feedback line (see Fig 3.6). For my design, the mutual inductance then becomes

$$M = \frac{\mu_0}{4\pi}\left(\int_{d_1}^{d_2} dy_2 \hat{y} + \int_{c_1}^{c_2} dx_2 \hat{x} - \int_{d_2}^{d_1} dy_2 \hat{y}\right) \cdot \left(\int_{a_1}^{a_2} \frac{dx_1}{r_1} \hat{x} + \int_{b_1}^{b_2} \frac{dy_1}{r_2} \hat{y} - \int_{a_2}^{a_1} \frac{dx_1}{r_3} \hat{x} - \int_{b_2}^{b_1} \frac{dy_2}{r_4} \hat{y}\right) \qquad (3.3)$$

where (a_1, b_1) is the bottom-left corner position of the rectangular SQUID loop, (a_2, b_2) is the top-right corner SQUID position, (c_1, d_1) is the bottom-left corner of the feedback line, and (c_2,d_2) is the top-right corner of the feedback line (see Fig 3.6). Using the numerical values from my design, I can then calculate the mutual inductance.

The calculated mutual inductance between SQUID 1 and it's own modulation line, M_{11} is 2.39pH, and the calculated mutual inductance between SQUID 2 and SQUID 1's modulation line, M_{12} is 0.143pH. Thus the calculated crosstalk of a SQUID

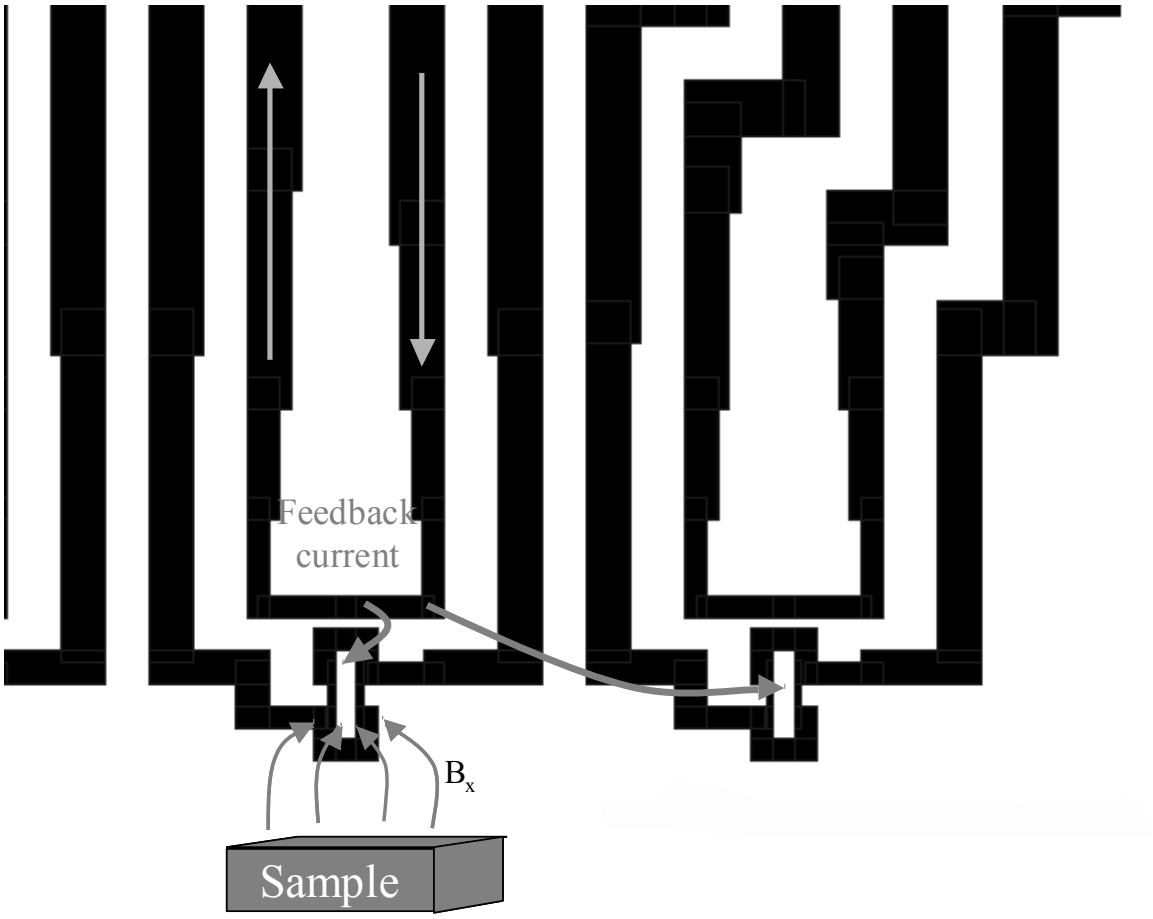

Figure 3.5: Diagram illustrating crosstalk between a SQUID and a neighboring SQUID's modulation line.

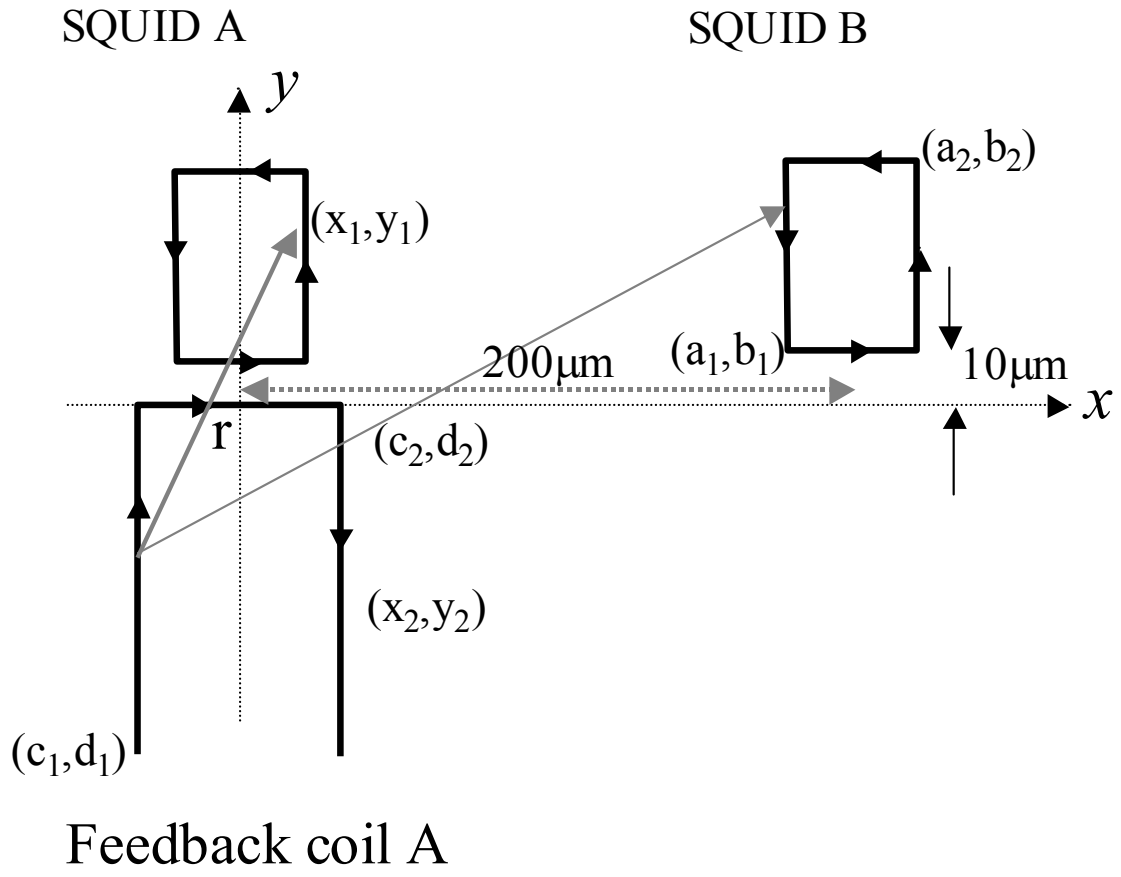

Figure 3.6: Diagram showing parameters needed to calculate the mutual inductances between a SQUID and feedback coils.

with its neighboring modulation line is about 6%. While the crosstalk is not negligible, it is low enough that the design should function well.

I note that even if the actual crosstalk is not negligible, there is a way to correct for it. When a SQUID is operated in a flux-locked loop (see Chapter 6) the feedback flux $M_f I_f$ cancels the applied flux Φ_a and the error flux Φ_e will be the difference between the feedback flux and the applied flux Φ_a,

$$\Phi_e = \Phi_a - M_f I_f = \Phi_a - M_f \frac{V_{out}}{R_f} \qquad (3.4)$$

where the output voltage from the feedback loop is $V_{out} = I_f R_f$. If the feedback electronics works well, we expect Φ_e to be about zero. Then, Eq. (3.4) becomes,

$$\Phi_a = \frac{M_f}{R_f} V_{out} \qquad (3.5)$$

If I apply these same considerations to my 8-channel SQUID chip, Eq. (3.4) is replaced by a set of equations,

$$\begin{aligned}
\Phi_{1e} &= \Phi_{1a} - M_{11f} I_{1f} - M_{12f} I_{2f} - M_{12f} I_{3f} \cdots - M_{18f} I_{8f} \\
\Phi_{2e} &= \Phi_{2a} - M_{21f} I_{1f} - M_{22f} I_{2f} - M_{22f} I_{3f} \cdots - M_{28f} I_{8f} \\
\Phi_{3e} &= \Phi_{3a} - M_{31f} I_{1f} - M_{32f} I_{2f} - M_{32f} I_{3f} \cdots - M_{38f} I_{8f} \qquad (3.6) \\
&\cdots \\
\Phi_{8e} &= \Phi_{8a} - M_{81f} I_{1f} - M_{82f} I_{2f} - M_{82f} I_{3f} \cdots - M_{88f} I_{8f}
\end{aligned}$$

The feedback will work to keep each error flux equal to zero and $V_{out} = I_f R_f$ for each SQUID. Eq. (3.6) can be expressed simply in matrix form

$$\begin{pmatrix} \Phi_{1a} \\ \Phi_{2a} \\ \Phi_{3a} \\ .. \\ \Phi_{8a} \end{pmatrix} = \frac{\overline{\overline{M}}}{R_f} \begin{pmatrix} V_{1out} \\ V_{2out} \\ V_{3out} \\ .. \\ V_{8out} \end{pmatrix} \qquad (3.7)$$

where $\overline{\overline{M}}$ is a mutual inductance matrix between the SQUIDs and the feedback lines. The implication of Eq. (3.7) is that if I know the mutual inductance matrix $\overline{\overline{M}}$, then I can find the flux at each SQUID from the outputs voltages I measure.

I note that while a 6 % correction may seem small, the matrix relationship between Φ and V_{out} is not so simple and even small inaccuracies can destroy the possibility of applying a magnetic inverse technique to the data.

3.5 Other concerns for design

Our group has made high-T_c SQUIDs for many years with junction widths of about 3 μm. This junction width gives about 50 μA as the critical current I_0 when the thickness of the $YBa_2Cu_3O_{7-\delta}$ (YBCO) thin film is 200nm. These values are chosen for low noise performance (see Chapter 4). Of course the 3 μm junction line must cross the bicrystal line in order to be a weak link. As Fig. 3.3(b) shows, one bias current lead also crosses the bicrystal line. To prevent another weak link, the lead was designed to have a thicker width, 15 μm in my design. This means that the feedback line should be able to carry about 250 μA before exceeding its critical current.

Each SQUID has its own feedback line so I can control them separately. Each SQUID also has 4 pads on top of the chip; 2 are for the bias current, and 2 are for the feedback current. The current and voltage pads are common on the SQUID chip and are split in the next step of wiring. The total number of pads on one chip is 32.

The overall size of the multi-channel SQUID chip is about 6.2×6.5 mm^2, but the bottom of the chip narrows down to 1.6 mm in order to fit into the aperture of the

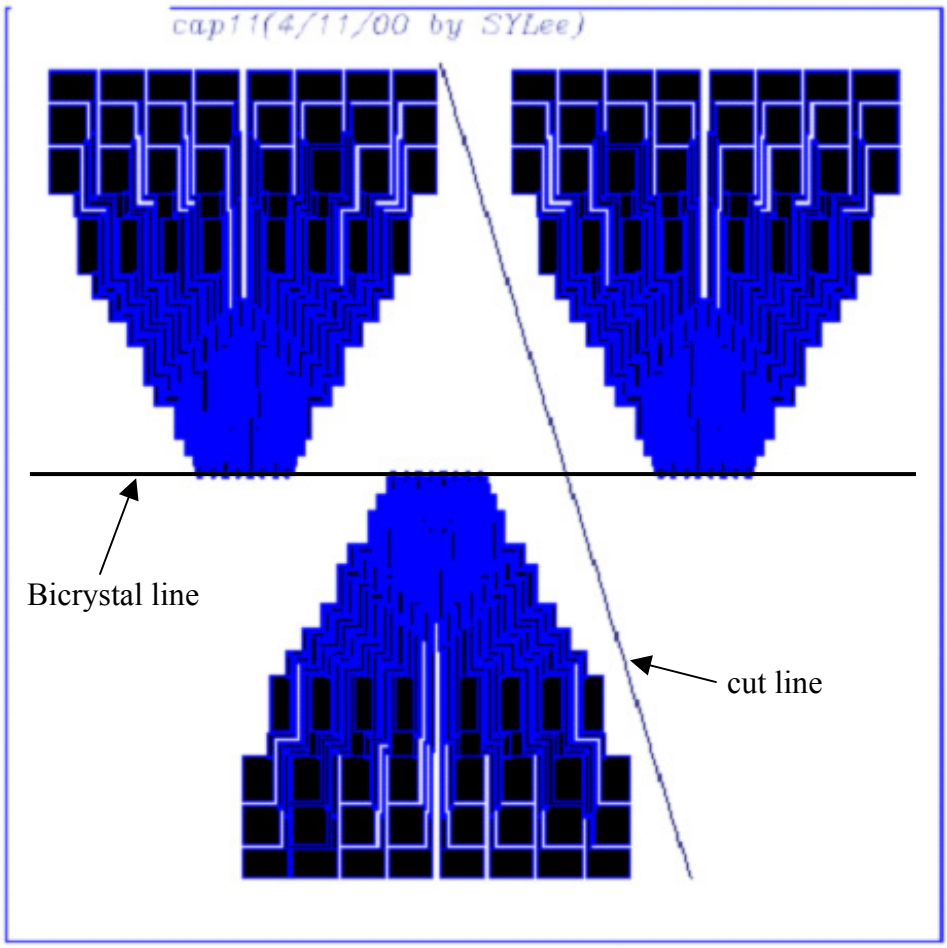

Figure 3.7: Total mask design for a 15 mm×15 mm substrate. Three multi-channel SQUID chips fit into one bicrystal substrate. The diagonal line indicates the first cut line for dicing.

microscope's window (see Chapter 5). Since the size of the bicrystal substrate is 15 mm×15 mm, three multi-channel chips can fit on a single substrate, as shown in Fig. 3.7, and the chip is diced after patterning (see Chapter 5).

3.6 Conclusion

My multi-channel high-T_c SQUID chip consists of an array of 8 SQUIDs in the x-SQUID orientation. Each SQUID has a 30 μm × 60 μm outer area and the distance between SQUIDs is 200 μm. The distance between a SQUID and its feedback line is 5 μm. Based on this design, the calculated crosstalk between a SQUID and a neighboring modulation line is about 6%.

Chapter 4

Chip Fabrication and Testing

In this chapter, I describe how I fabricated multi-channel SQUID chips. I introduce the YBCO thin film fabrication process and describe how I patterned the films using photolithography. Finally, I show measurements on a completed 8-channel SQUID chip.

4.1 YBCO thin film fabrication

4.1.1 Deposition of YBCO and Au thin films using Pulsed Laser Deposition

There are several methods that have been used to grow high-T_c superconducting thin films. Popular methods include evaporation, pulsed laser deposition (PLD), metal-organic chemical vapour deposition (MOCVD), and sputtering. For my SQUID fabrication, the PLD method was used. PLD is relatively simple and tends to have a high success rate compared to other growth techniques, making it ideal for prototyping new materials [1]. Another merit of PLD is that it works well with complex multi-component materials. By adjusting the laser energy density, gas pressure, focusing, etc., a thin film can be optimized comparatively easily. In addition, PLD allows the growth of multiple layers of thin films without breaking vacuum (*in situ*) by using a multi-target carousel. The main down-side of this technique is that only a small area gets uniform coverage. Fortunately my substrate is small enough to be covered uniformly.

Here is the procedure and optimization I used for YBCO and Au deposition on an STO substrate. This process was modified slightly from Chatraphorn's [2].

For growing my films, I used one-side polished bicrystal $SrTiO_3$(STO) substrate [3] that was 15 mm × 15 mm in size and had a 30° grain boundary mismatch. Before deposition, the substrate needs to be cleaned using Acetone and Methanol in an ultrasonic bath for 5 minutes. The STO substrate is then attached to a heater stage using silver paint, and is shielded by a shutter. The amount of silver paint is important because either too thick or too thin silver paint can give a non-uniform and inaccurate substrate temperature (2~3 drops of silver paint is enough for my substrate size). To bond the chip to the heater, I increase temperature slowly to 100 °C at 5 °C per minute with the heater in air. While I wait for the silver paint to dry, I mount the gold target and polished YBCO target on the carousel. I then optimize the energy density and spot size by adjusting the laser intensity and lens position. The height of the Au target needs to be the same as the YBCO target, or else one has to optimize separately. For PLD I use a Lamda Physik KrF excimer laser [4] that emits 248 nm UV light with about 150mJ per pulse. Figure 4.1 shows a top view of the PLD chamber, which is maintained by Neocera, Inc. [5].

After the silver paint is dried and the adjustment of the energy density is finished, I close the chamber with the heater flange and pump the chamber. While it is pumping, I start the programmable temperature controller. I increase substrate temperature at a rate of 30 °C per minute up to the optimized YBCO deposition temperature (790~810 °C) and keep the temperature fixed after that.

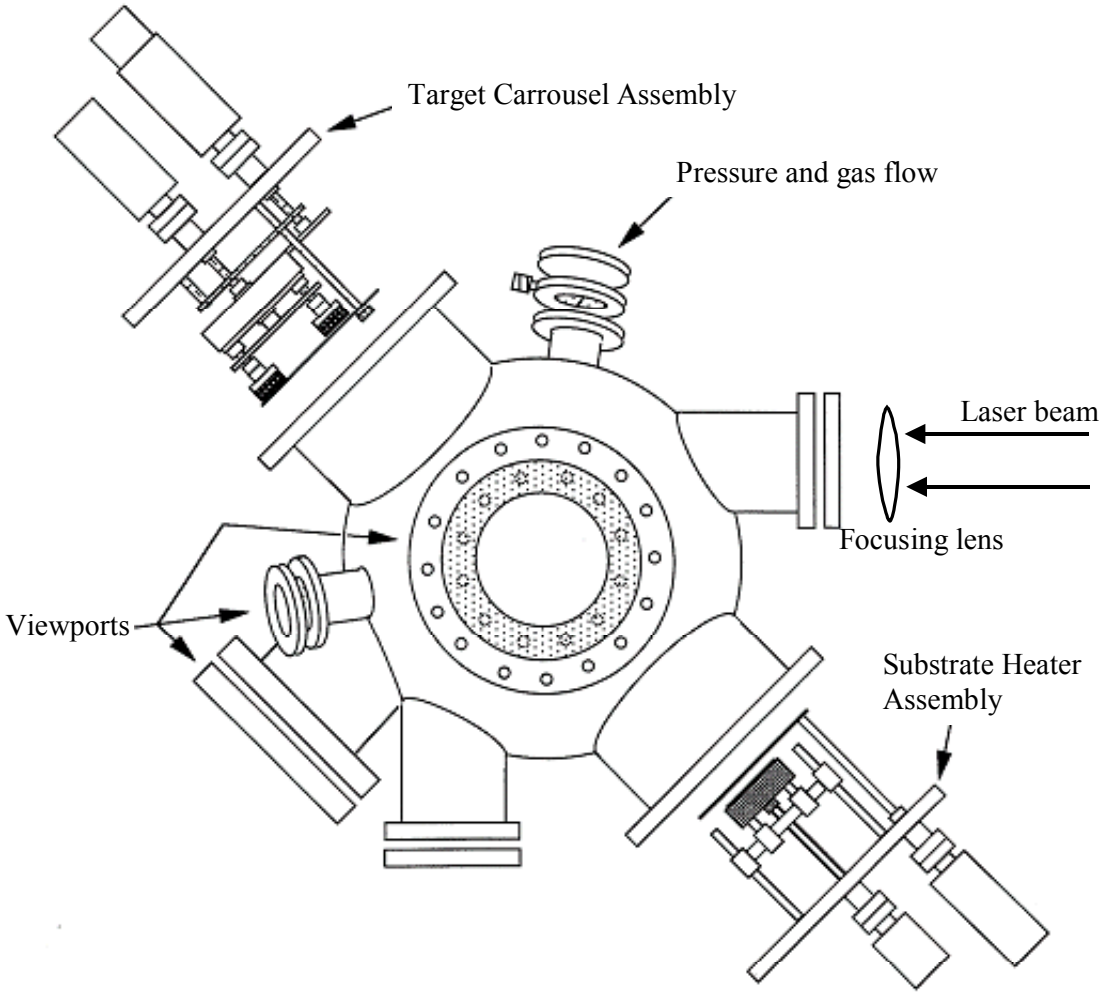

Figure 4.1: Top view of pulsed laser deposition chamber (taken from Neocera catalog [5]).

Once the base pressure is below 10^{-5} mTorr, I pre-ablate the YBCO target at a 10 Hz pulse rate for 3 minutes, keeping the shutter in front of the substrate. This procedure cleans the surface of the YBCO target. Next, I open the fine control pressure valve to make a 200 mTorr O_2 atmosphere for YBCO deposition. When the pressure is stable, I deposit YBCO using a 10 Hz pulse repetition rate for 8 minutes to give a film about 200 nm in thickness. The pulse energy is about 167mJ. Immediately after I turn off the laser, I cool the film as fast as possible by switching off the heater. While it is cooling, I close the fine valve and open the main oxygen valve to fill the chamber with 500 Torr of O_2 and then close the valve. After the YBCO film is cooled down below 100 °C, I pump the chamber to at least 1 mTorr and deposit Au. I use the same laser alignment and energy density for the Au deposition. I use a pre-ablation time of 1 minute and deposition time of 12 minutes to produce a 150 nm thick Au layer.

In order to get good films, we must optimize the deposition conditions, so I started by growing films on a test STO substrate. I faced two main problems while trying to make the films. First, I tended to get two transition temperatures for the YBCO thin film. This means that there are two phases of YBCO. To make a single phase is important because the presence of two phases implies poor film quality, which tends to be associated with extra noise. We found that this problem was caused by the test STO substrates, which had surface that were not purely (100) orientation, resulting in two phases. Another problem I encountered was that the temperature was not right because silver paint that was holding the thermometer to the heater stage was flaking off over time. To avoid this problem, I checked the temperature using a portable infrared

temperature meter. Even though the error of the temperature meter is relatively large, this was helpful if the temperature difference was more than 20 °C.

4.1.2 **Testing YBCO films**

After deposition, there are several tools that can be used to see if the YBCO film has grown well. The most powerful diagnostic is a measurement of the transition temperature. Another useful check is to look through an optical microscope with reflected light and direct light. X-ray diffraction is also useful for checking crystal structure. Since my deposition conditions were closely optimized by Chatraphorn [2], I usually use just the first 2 methods.

To measure T_c, I use non-contact AC susceptometery. As the insets to Fig. 4.2 show, a small current is applied to a coil below the film. This produces a magnetic field that induces current in the sample. A pickup coil on the surface of the film detects any response. When the film is above T_c, the HTS acts as a normal metal, field penetrates through the film, and the pickup coil detects a strong signal. When the film is below T_c, the YBCO film is in the superconducting state. It then acts as a perfect diamagnetic material, and the induced magnetic field is shielded from the pickup coil [6].

Figure 4.3 show measurements on one of my Au-coated bicrystal YBCO thin films. The dashed lines in Fig 4.2 and Fig 4.3 are the imaginary part of the response and the solid lines indicate the real part. Fig 4.3(a) shows the response when I measure to the left side of the bicrystal. The most important thing is how sharply the transition temperature changes. If the change of the transition temperature is within 0.5 °C, it is considered good enough to make a SQUID. In Fig. 4.3(a), the T_c (onset is 87.75 K) is

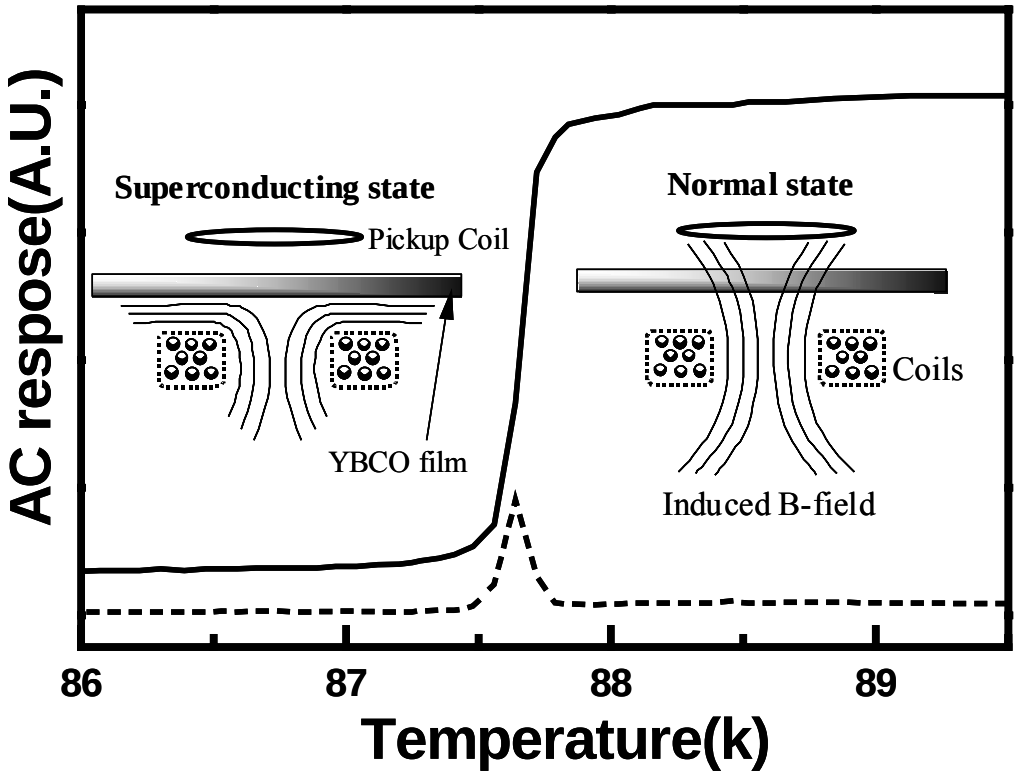

Figure 4.2: Change in ac susceptometry response of a YBCO thin film between superconducting state and normal state. Solid line shows in-phase output of pickup coil, dashed line shows out of-phase response (modified from Ref. [6]).

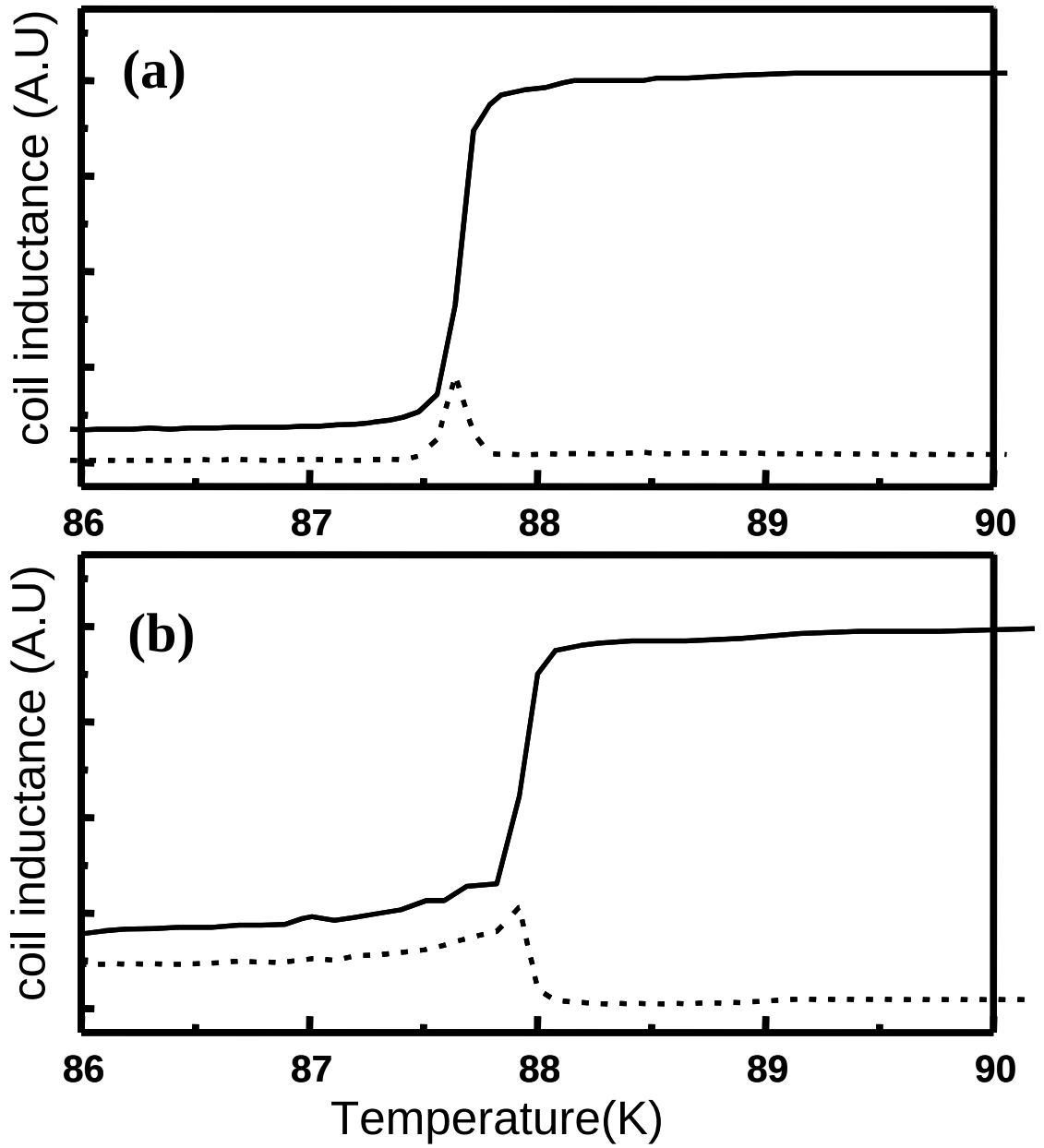

Figure 4.3: Susceptibility response v.s. temperature of bicrystal YBCO film at (a) left of bicrystal line and (b) center of bicrystal line.

lower than ideal (about 90 K), but the width of T_c is below 0.5 °C, so it can be used for SQUIDs. Figure 4.3(b) shows the response when I measure across the bicrystal line. As shown in Fig 4.3(b), there is a tail in the response. This occurs because there is some leakage of magnetic field through the weak link in the grain boundary.

By using an optical microscope with direct light and reflected light, I can check the surface of the film and whether the film has a lot of outgrowths, ab-axis growth, or melt-drops from the PLD. For example, when the temperature controller was not working properly, reading a lower temperature than the actual temperature, I found a lot of melt-drops on my film. On the other hand, a low deposition temperature can cause ab-axis growth.

4.2 Photolithography

I use standard photolithography to make SQUIDs from my YBCO films. Photolithography is the process of transferring patterns on a mask to the surface of a film. There are two main types of photoresist, positive and negative. With positive resist, the area exposed to UV is removed. Negative resists behave in just the opposite manner. Positive resists are more widely used because they offer better process controllability for small features. I use Shipley's 1813 positive resist for my patterning and do all my processing in a clean room. I note that I made minor modification from the procedure optimized by Chatraphorn and Knauss [2, 5].

The first step in the photolithographic process is to clean the surface of the YBCO coated STO substrate (see Fig. 4.4). I use acetone, followed by methanol and DI water, and then dry with nitrogen gas. I then put the substrate on the resist spinner,

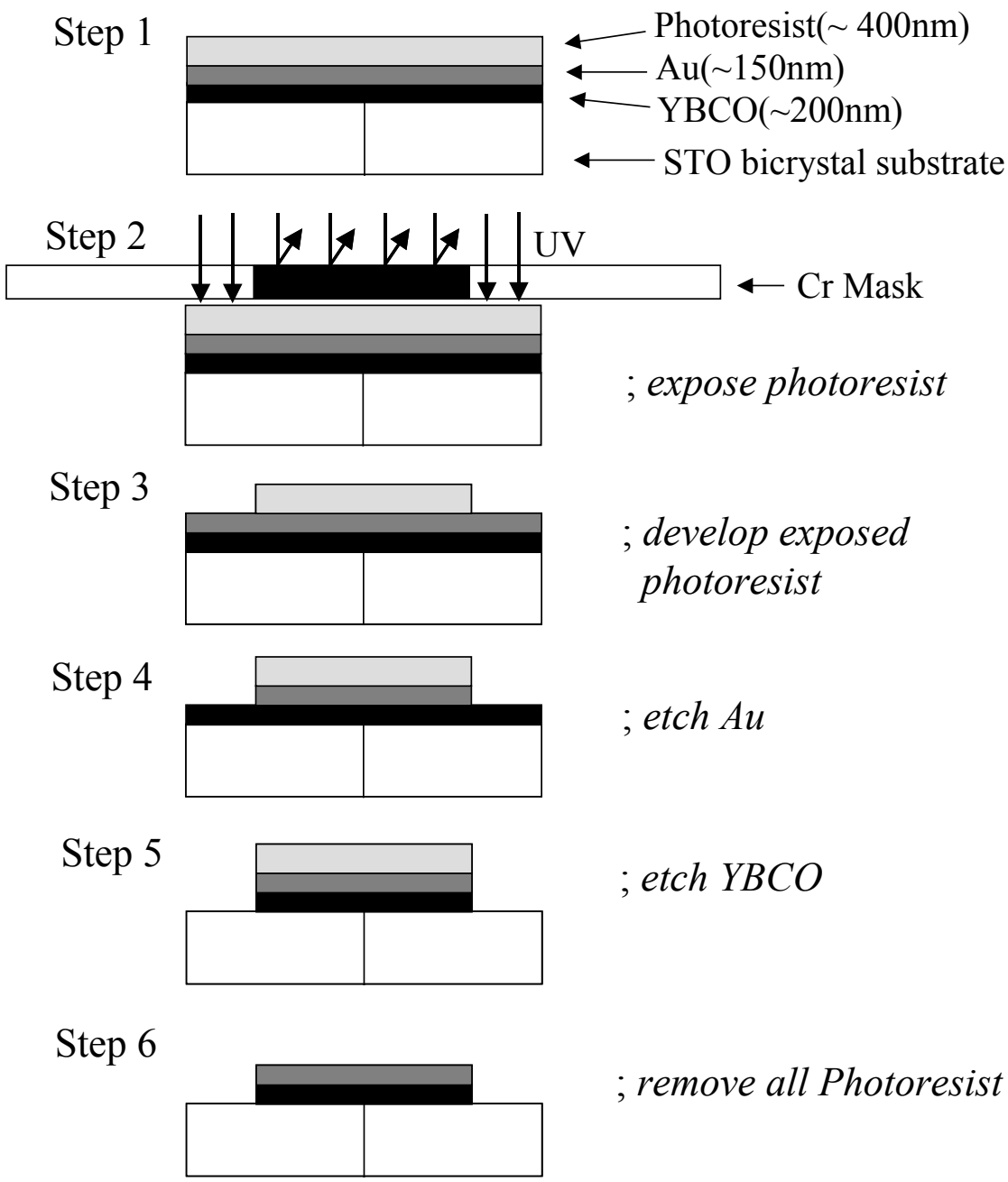

Figure 4.4: Single mask photolithographic procedure.

apply photoresist, and spin at 4000 RPM for 30 seconds. This technique produces a thin uniform layer of photoresist on the surface. To dry the photoresist, I bake in an oven at 110 °C for 7 minutes (or 2 minutes on the hotplate at 100 °C). The baking time has to be optimized carefully because under-baked photoresist can be attacked in a later step by the resist developer in non-exposed area, while over-baked photoresist will degrade the photosensitivity.

The second step is mask alignment and exposing the photoresist. I used a Cr-mask for positive resist. Since the SQUID design has 3 μm width junctions, the alignment is very important. I use a contact method with an exposure time of 40 seconds on a Karl Suss MJB3 mask aligner.

The third step is developing the exposed photoresist. To do this, I dip the film in the developer for 40 seconds and rinse with DI water. I use 15 °C Shipley's Microposit MF 319 diluted with DI water for the developer.

The fourth step is removing the exposed regions of Au using Au etchant. The Au etchant is made of a solution of 4g Potassium Iodine (KI) and 1g Iodine(I) in 80 ml of DI water. I dip the film for 60 seconds.

The fifth step is removing exposed regions of YBCO using 0.5% phosphoric acid (by volume). Depending on film quality, the etching time varies. Therefore, I had to check the process of the etch using an optical microscope after 30 seconds, and then decide to dip longer or not. The range of etching time was about 30~60 seconds. I also note that the fourth and fifth steps should be carried out at an acid fume bench for contamination and safety reason.

The sixth step is cleaning away residual photoresist. After I bake the resist and dip the chip in acid, it is hard to get rid of all the photoresist. This procedure is very important though since I have to repeat the entire process for three different masks, as discussed below. If the resist is not cleaned completely, then the residual resist affects other steps. I clean the resist by dipping the film in acetone in an ultrasonic bath for more than 5 minutes.

For SQUID fabrication, I have to repeat these six basic steps three times because I have 3 different masks. Figure 4.4 shows the 6 steps for the first mask. Fig. 4.5 illustrate the whole procedure for patterning with three masks. The first mask used in Fig. 4.5(b) is to clean the edges of the chip of YBCO in order to see the bi-crystal line. Since the resist at the edge of the substrate is thicker than at the center, a longer exposure time (45sec) is required. The second mask used in Fig. 4.5(c) is for removing Au from the YBCO where the SQUIDs will be, but keeping Au everywhere else. Therefore, in this procedure, I have to skip the fifth step in order to keep the YBCO. The mask used in Fig 4.5(d) is a most delicate and important mask. Through the optical microscope in the mask aligner, I have to find the bicrystal line and align this very accurately so that the bicrystal line is within the 3 μm junction areas of all the SQUID patterns. The final step is covering the SQUID chip with photoresist in order to protect the YBCO from water and prevent O_2 from escaping the YBCO. Figure 4.6 shows a completed multi-channel SQUID chip.

Since I have 24 SQUIDs on one substrate, it was hard to etch all the SQUIDs and modulation lines at the same time. Figure 4.7 shows, some problems I encountered. In Fig. 4.7(a), leftover resist interrupted the YBCO etch. To solve this problem,

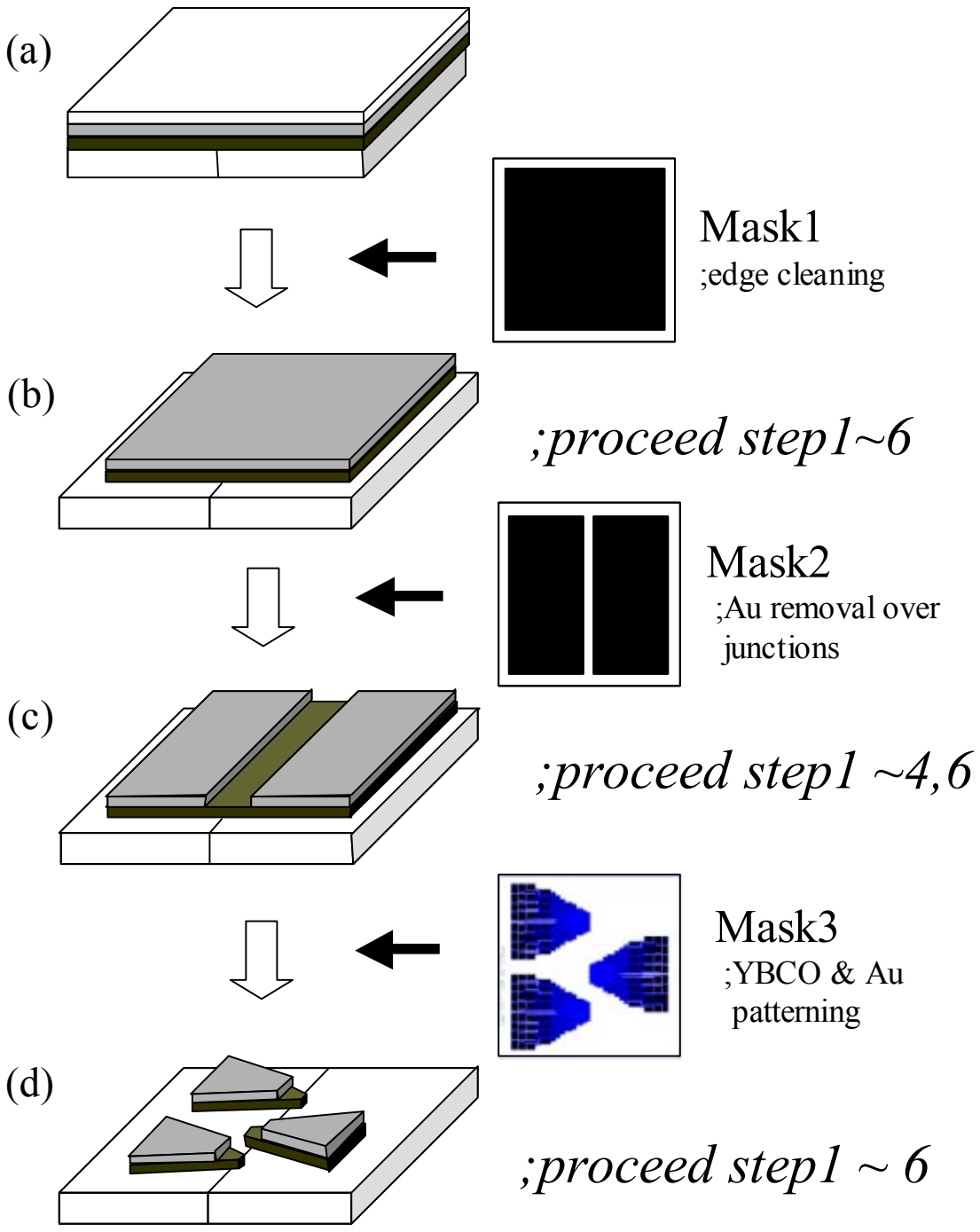

Figure 4.5: Total photolithographic procedure using three masks for making the multi-channel SQUID chip.

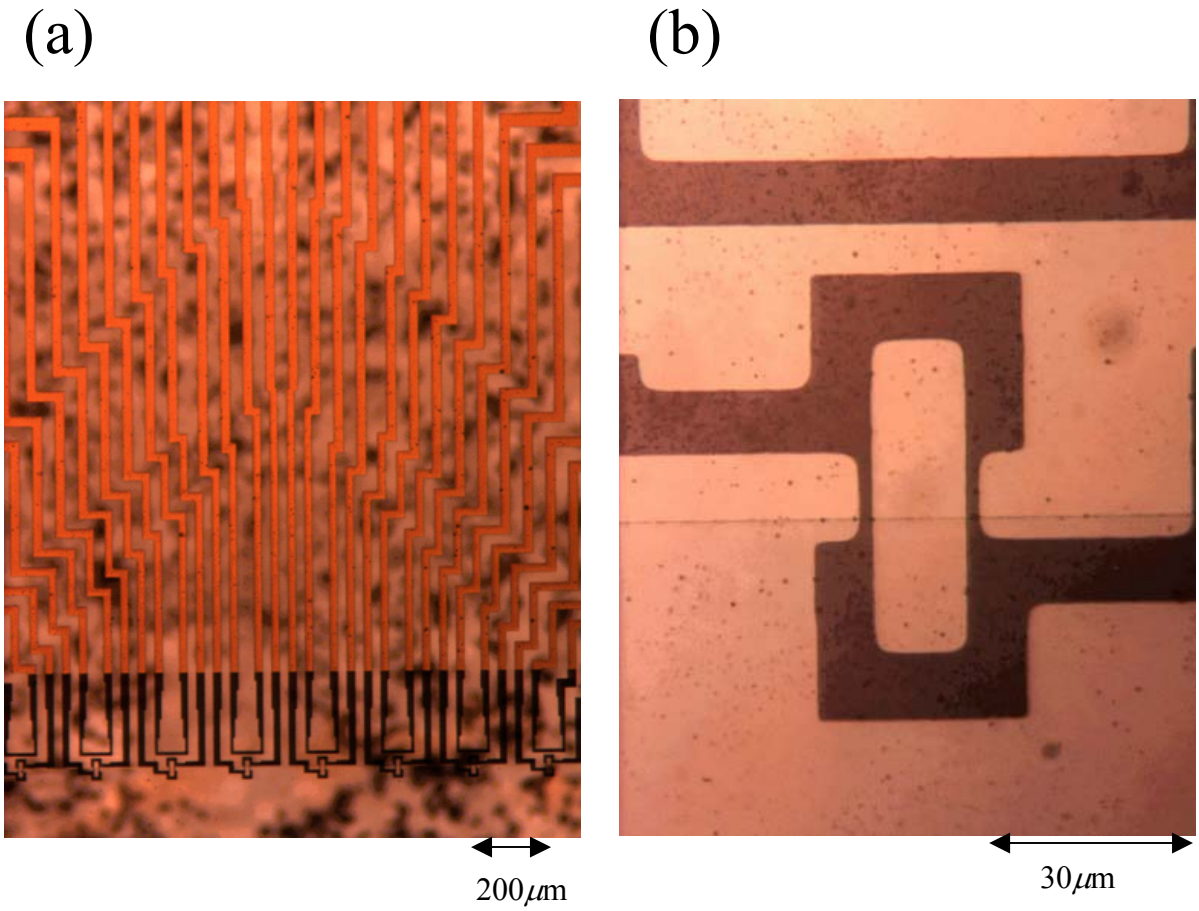

Figure 4.6: (a) Picture of successful 8-channel SQUID chip. (b) Magnified multi-channel SQUID chip near SQUID junction. Mottled pattern in (a) is silver paint on back side of STO chip.

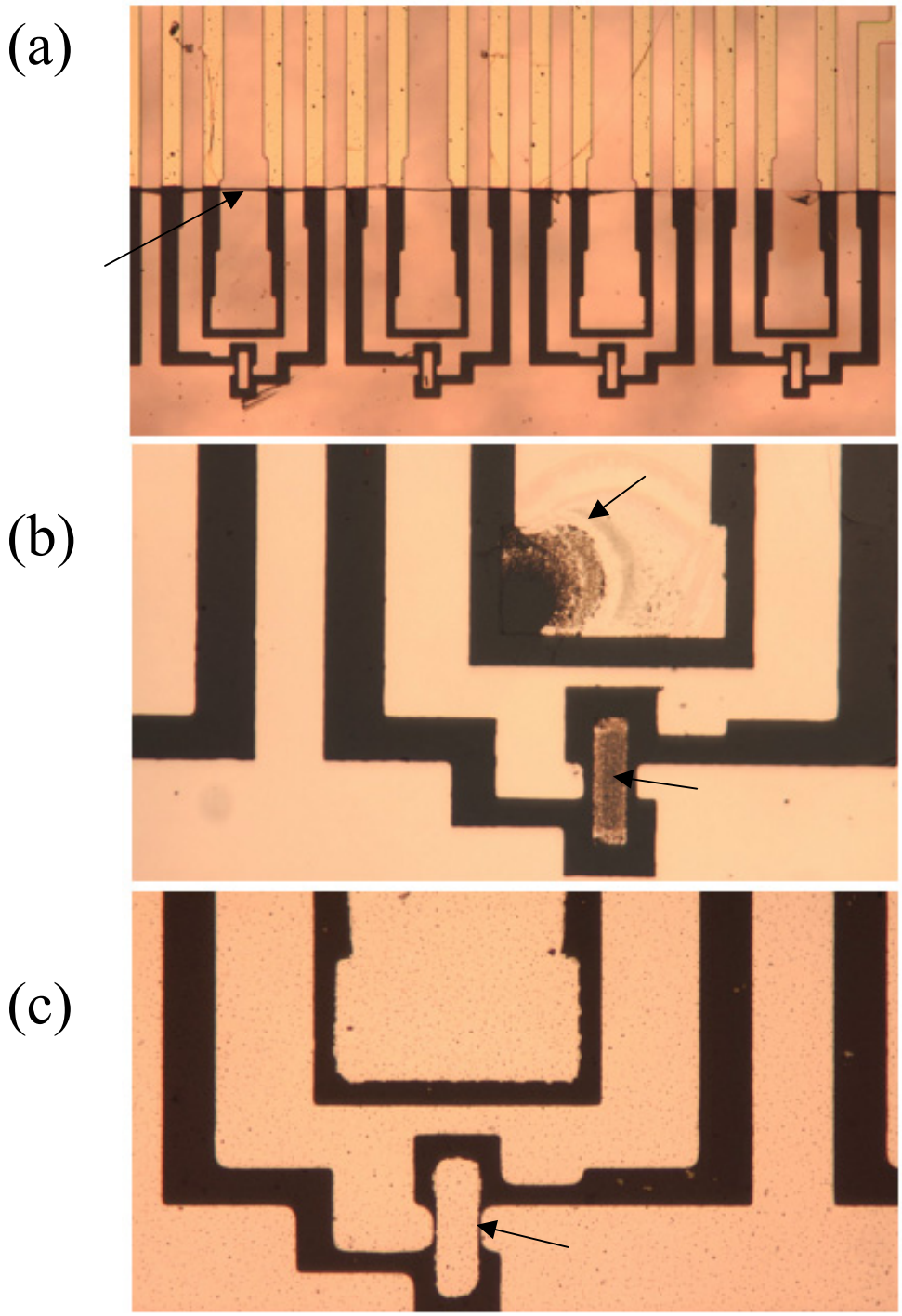

Figure 4.7: Examples of failed photolithography for multi-channel SQUID chip. (a) Failed because of thick Au, (b) failed because of short YBCO etching time, and (c) failed because of too long etching time.

reduced the Au thickness and cleaned the photoresist thoroughly using an ultrasonic bath. Fig 4.7(b) and (c) shows the result when the etching time is too short or too long, respectively. A longer etching time could be used to remove from one device, but it tends to overetch other devices. Therefore, uniform thin film deposition is important for getting everything to work.

Needless to say, it is important to use clean beakers, pure chemicals, and fresh photoresist. The photoresist should be kept in a safe and cold place at all times and used before the expiration date.

4.3 Measurements of 8 SQUIDs on a Chip

4.3.1 I-V characteristics

A powerful method to check the quality of a SQUID is to measure the I-V characteristics. As I explained in Chapter 2, the junctions of high-T_c SQUIDs are resistively and capacitively shunted, and the I-V curve is non-hysteretic. When external flux is changed continuously, the I-V curve should modulate periodically. I use a standard 4-point probe I-V measurement with an 8-channel dip probe. Each channel has 4 leads, with 2 leads for ± current and 2 leads for ± voltage. I use a function generator and 1 kΩ resistor to supply current to one SQUID at a time.

For testing an 8-channel SQUID chip, I made wire-bonds from the SQUID chip to a custom-made SQUID pc board (see Chapter 5). I built a custom dip probe into which I could plug the pc board and which allowed me to test 8 SQUIDs just by changing BNC cables, channel by channel, without warming the chip up. After I finish the wiring as shown in Fig. 4.8, I sweep the current in order to obtain the I-V curve at

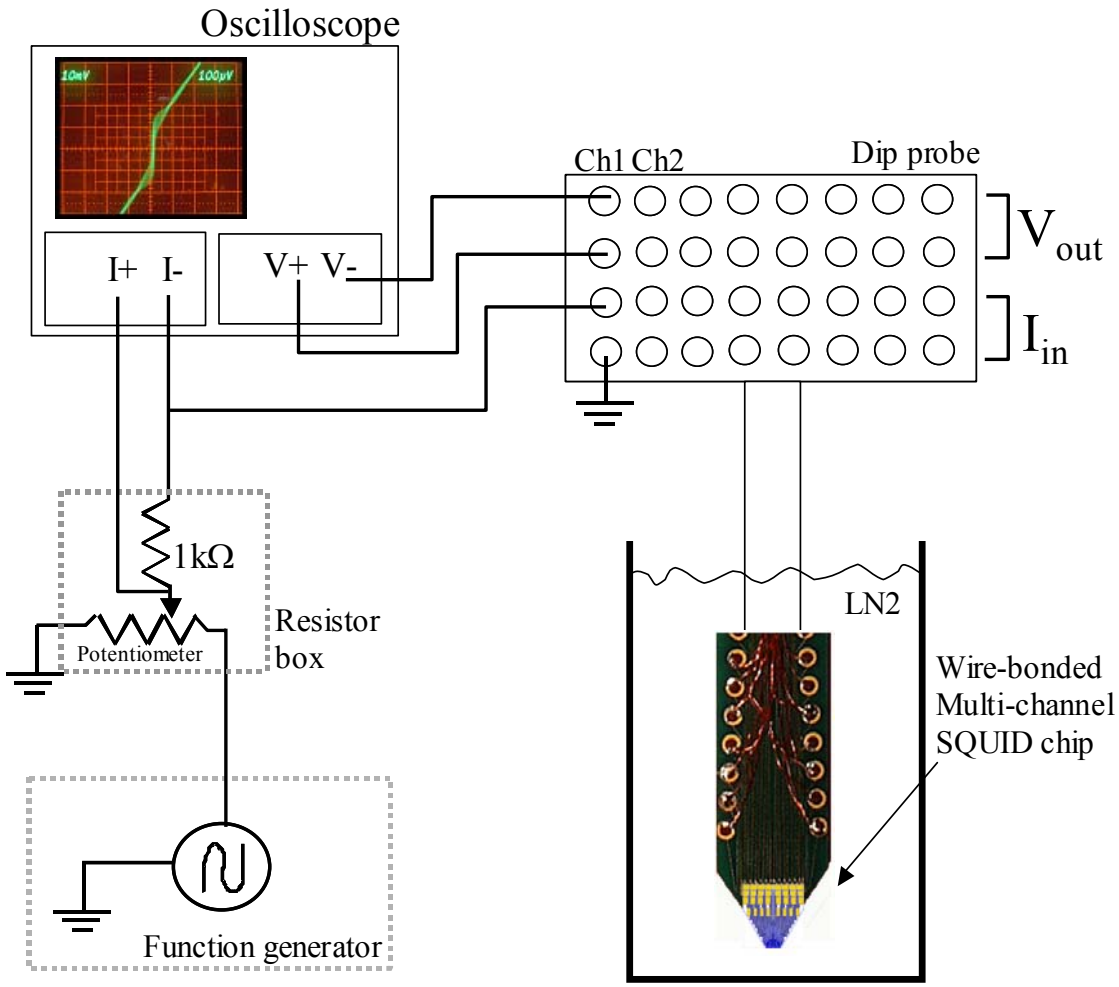

Figure 4.8: Measurement setup for I-V characteristics for 8-channel SQUID chip.

room temperature. When I dip the SQUID chip into liquid nitrogen, a fast slope change is seen when T falls below T_c. I then adjust the range of the oscilloscope to see the I-V curve.

Figure 4.9 shows SQUID I-V characteristic curves for all 8 SQUIDs on the 3rd chip I tested. All of the devices are working, as shown. When I approach with a magnet, the I-V curves oscillate (the picture was exposed while I was approaching with the magnet and all showed modulation).

I note that I built and tested two other chips. For the first chip, 6 out of 8 devices worked, while for the second chip, 7 out of 8 worked. In these earlier chips, I lost the some SQUIDs because of static electricity. A SQUID that has been destroyed by static electricity can be distinguished by optical microscopy (the junction is blown up). Therefore, my yield of working SQUIDs was surprisingly good, although care must be taken in handling the chips and making connections to the SQUIDs.

4.3.2 **The parameters of SQUIDs from the I-V curves**

From the I-V curve, I can find the critical current, junction resistance, and voltage modulation depth of each SQUID. Although this is not accurate, even rough numbers are very useful. Figure 4.10 gives one example of how I get these values. The critical current I_c shown in Fig. 4.10 is about 30μA. The junction resistance R_J, which is the slope of the curve is about 3.85 Ω. The voltage modulation ΔV at maximum is about 50 μV (see Fig 2.6(c) also).

Table 4.1 shows the parameters for all 8 SQUIDs on the third chip. I note that the critical currents of the SQUIDs varies from 15~80 μA, R_J varies from 3.75~7.14 Ω,

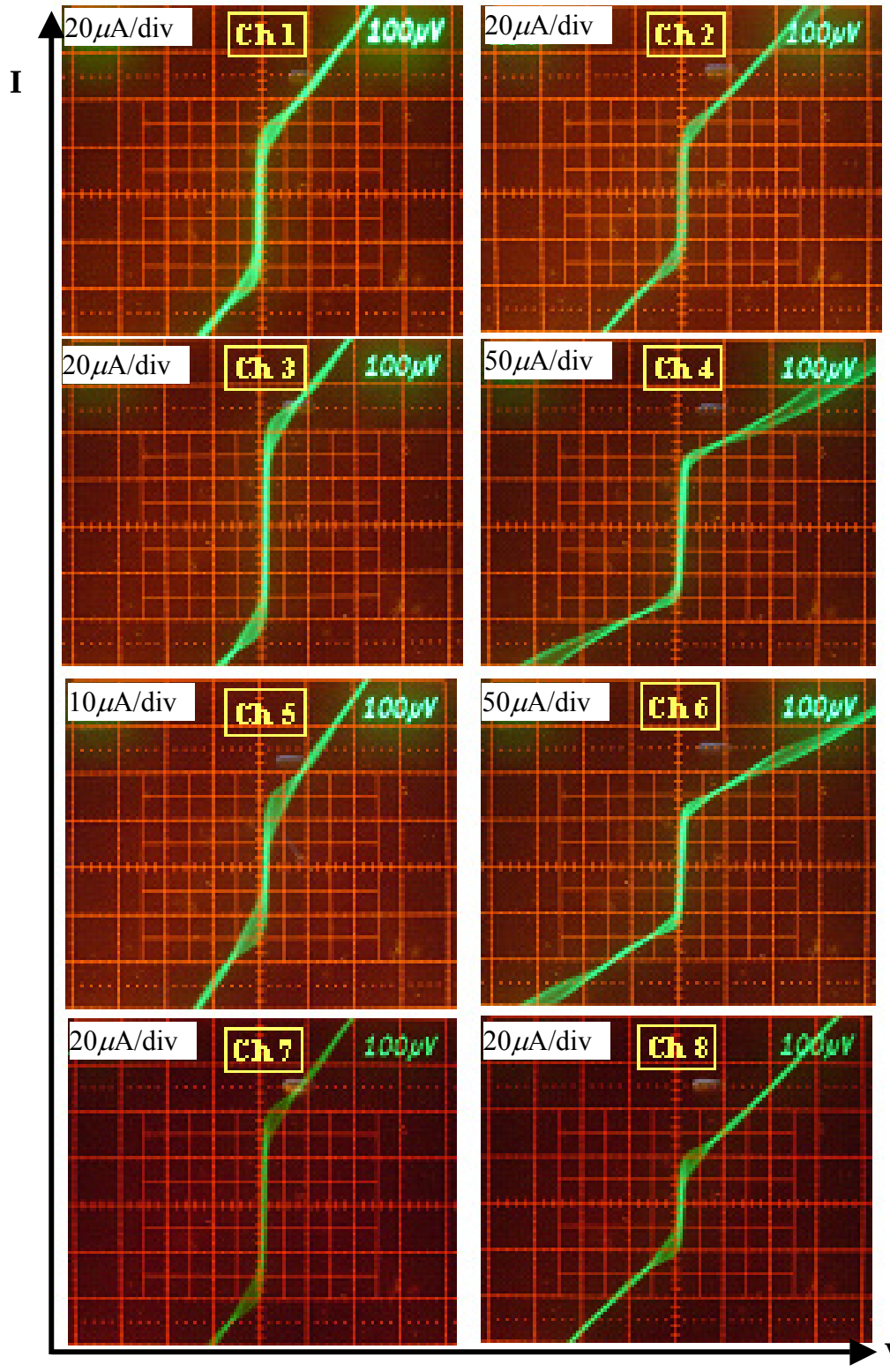

Figure 4.9: I-V characteristic curves for 8 working SQUIDs on one chip, measured at 77K. *x*-axis is 100 μV per large division and *y*-axis is labeled on left-top in each curve (division refers to large division).

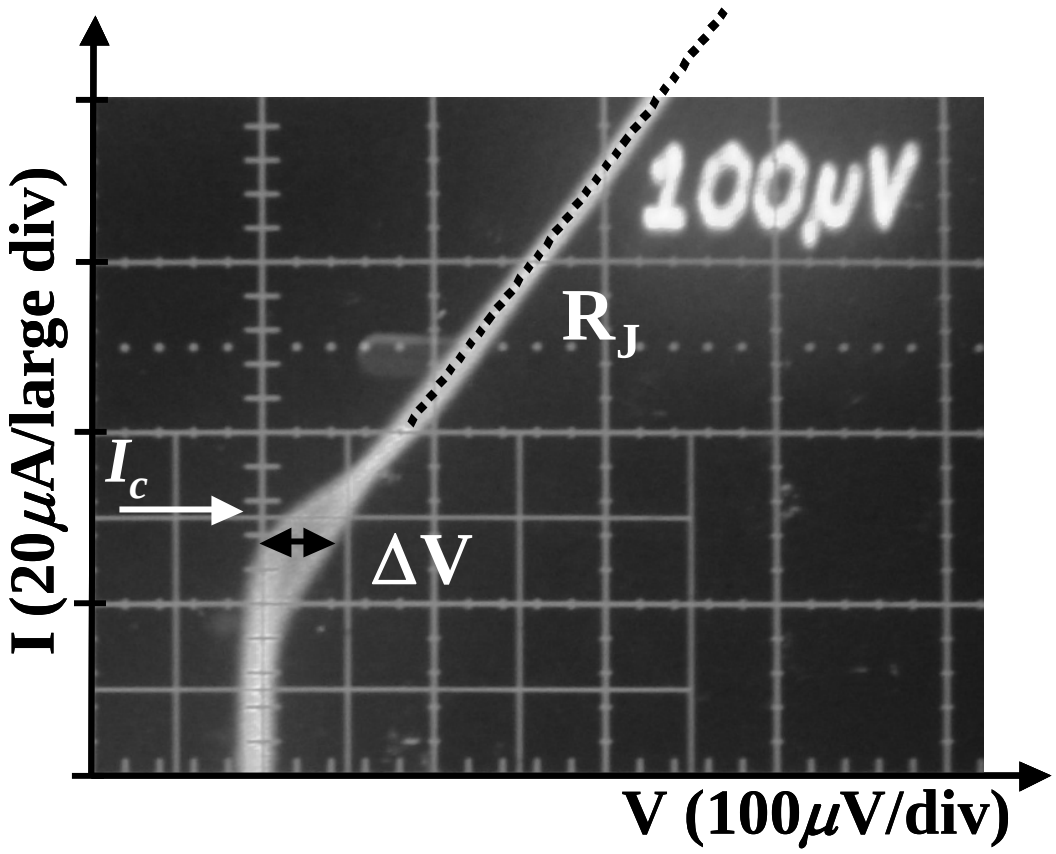

Figure 4.10: I-V characteristic curve of channel 1 SQUID showing how to find the SQUID characteristic parameters: The critical current I_c (= $2I_0$) ~ 30 μA, junction resistance $R_J \sim 4\Omega$, and voltage modulation depth $\Delta V \sim 50$ μV.

Table 4.1: SQUID parameters, I_c, R_J, ΔV, and $\beta = 2I_0L/\Phi_0$ for 8 SQUIDs on chip, measured at 77K. L ~ 70 pH.

	$2I_0$ (μA)	ΔV(μV)	R_J(Ω)	β ($2I_0L/\Phi_0$)
Ch 1	30	50	3.85	1.05
Ch 2	30	40	4.55	1.05
Ch 3	46	45	4.17	1.61
Ch 4	80	40	3.75	2.80
Ch 5	15	50	7.14	0.53
Ch 6	65	40	4.00	2.28
Ch 7	40	40	3.85	1.40
Ch 8	21	50	5.00	0.74
Average	41	44	4.54	1.43

and ΔV varies from 40~50 μV, even though all fabrication conditions of the chip are same. Since I have separate feedback electronics for each channel, each SQUID can be optimized separately, so the difference in critical currents is not a serious problem.

However, if the difference is too large (larger than ~200 μA), I have to change bias resistors in the SQUID electronics for a specific channel. Therefore, it is better to have a narrower range of critical currents.

4.3.3 **Evaluation of multi-channel SQUID chip**

A good SQUID means a low noise SQUID. One concern is that the variation in I_0 and R might cause poor performance. The flux noise S_Φ in SQUIDs is affected by the junction shunting resistance R_J and the modulation parameter $\beta \equiv 2LI_0/\Phi_0$. A theoretical expression for flux noise for low-T_c SQUID has been obtained and it has been proved that the flux noise is optimal for $\beta \approx 1$ [7]. However it is known that this low-T_c result cannot be applied accurately to high-T_c SQUIDs. In fact the magnetic flux noise in high-T_c SQUIDs is not understood fully, as I mentioned in Chapter 2. Enpuku *et al.* found that [8]

$$V_\Phi = \frac{8I_0R_J}{\Phi_0(1+\beta)}\exp\left(-\frac{3.5\pi^2 k_B TL}{\Phi_0}\right) \tag{4.1}$$

$$S_\Phi = \left[1+\exp\left(1.23-4.82\frac{2\pi k_B T}{I_0\Phi_0}\right)\right]\cdot L^2\frac{k_B T}{R_J}\cdot\left[1+\left(\frac{2R_J}{LV_\Phi}\right)^2\right] \tag{4.2}$$

where $k_B = 1.38\times10^{-23}$ J/K is Boltzman constant.

Figure 4.11 shows that the expected flux noise increases when the self-inductance increases and at fixed self-inductance the effect of different I_0 is weak. However, low I_0 is desirable because it leads to a larger R_J which gives low flux noise.

The weak influence of critical current on flux noise is good for a multi-channel SQUID system. Since my eight SQUIDs have the same size, I can assume the self-inductance is fixed at L ~ 70 pH. Therefore, even though the critical currents vary from 13 to 80 μA, the flux noise in the different SQUIDs should not vary too much, at least in principle. As we will see in Chapter 6, the measured noise does vary, but not from I_0 and R_J.

4.4 Conclusion

I fabricated SQUIDs out of YBCO thin films that I deposited on 1.5cm×1.5cm bi-crystal STO substrates using PLD. Using standard photolithography, I patterned the YBCO film. When I measured the I-V characteristics of the 8 SQUIDs, I found critical currents with range of 15~80 μA, voltage modulation depths from 40~50 μV, and modulation parameter β from 0.3~1.6. These parameters were acceptable for using the SQUIDs in my multi-channel system.

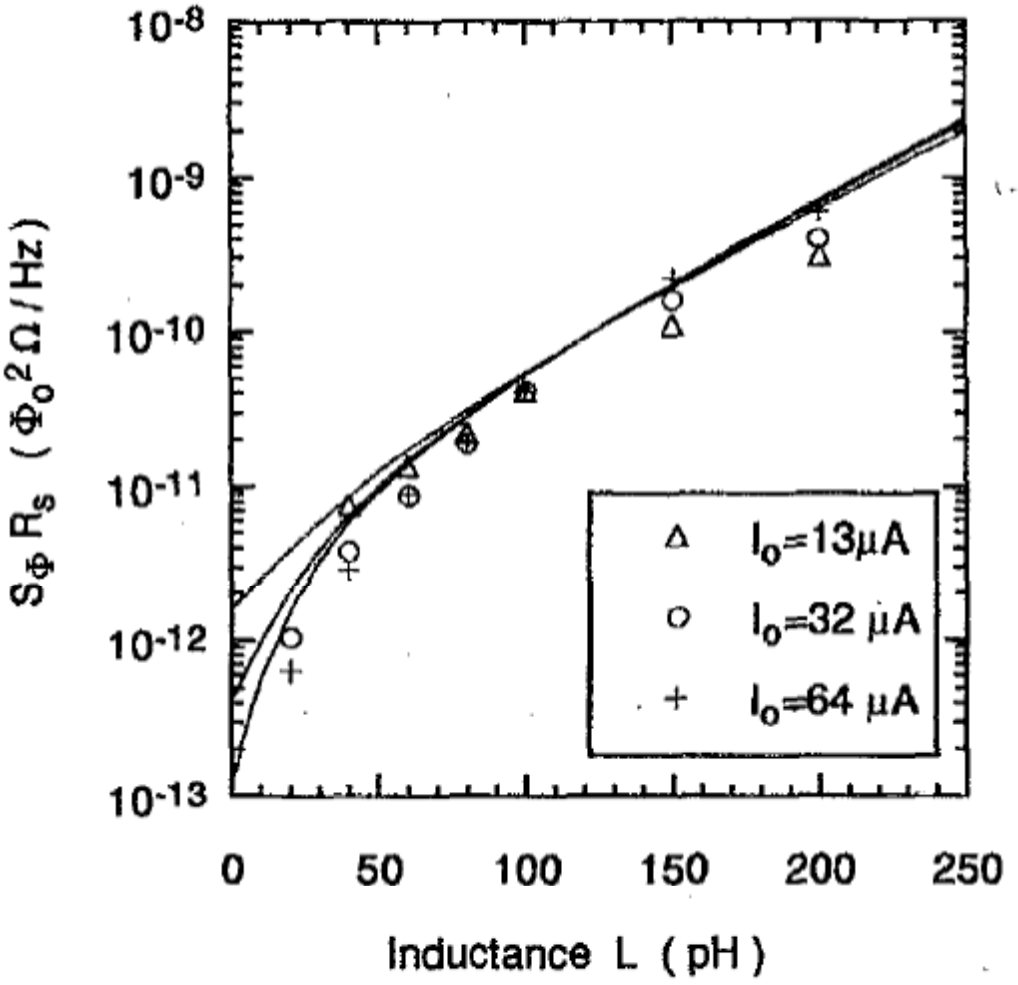

Figure 4.11: Inductance and critical current dependence of SQUID flux noise. The solid line are calculated from Eq. (4.1)-(4.2) [8] and symbols represent simulations from Ref. [9]. The top, middle, and bottom lines show the calculated results for I_0 =13, 32, and 64 μA, respectively (figure taken from Ref. [8]).

Chapter 5

Scanning SQUID Microscope Design and Construction

In this chapter I describe how I converted an existing single-channel high-T_c SQUID microscope into a multi-channel SQUID system. I begin by discussing the previous system and then focus on the modification I made to the microscope body.

5.1 The old high-T_c single-channel SQUID microscope

In the earliest scanning SQUID microscopes, the sample was at the same temperature as the SQUID (4 K or 77 K). This restricted the kinds of samples which could be imaged. In addition, the sample could not be easily modified or replaced, since this required warming up the SQUID also. To overcome these problems, "room temperature" SQUID systems were developed. The first room temperature scanning SQUID microscopes was built by Randy Black and Yongyu Gim [1, 2]. In a room temperature scanning SQUID system, the SQUID is cold (at 77K), but the sample is in air at atmospheric pressure at 300 K. Vacuum and a thin window separate the sample from the cryogenic environment of the SQUID.

The second generation room temperature system was designed by S. Chartrophorn and E. F. Fleet [3, 4]. They kept the same liquid nitrogen dewar to cool the SQUID, but redesigned the SQUID tip assembly, cold-finger, and the window. In addition, they built another SQUID microscope that used a cryo-cooler to cool the

SQUID instead of liquid nitrogen. It was this cryo-cooled design that was adapted to the commercial market by Neocera. Figures 5.1 and 5.2 show a diagram and photograph, of the second generation room-temperature LN_2-cooled SQUID microscope. Since I modified this system to build my multi-channel SQUID microscope, I will describe it in some detail.

5.1.1 **Vacuum window**

In the room-temperature LN_2-cooled SQUID microscope, the SQUID chip is mounted on the bottom of a sapphire tip just above a thin window (see Fig 5.1,). Since the spatial resolution of the SQUID system is strongly dependent on the sample-to-sensor separation, it is important to keep the window as thin as possible. Of course the window must not be too thin, or it will not survive atmospheric pressure. For the window assembly, Chatraphorn and Fleet used a 1 mm thick sapphire disc with a 1mm hole in it to support a 25 μm thick sapphire window, which covered the hole. The sapphire tip and SQUID could be lowered into the hole, to allow a sensor-to-sample separation of 100 μm or less.

5.1.2 **SQUID chip assembly**

In the 1st and 2nd generation design, the SQUID was mounted in a z-SQUID configuration (see Fig. 3.4(a)). An 800×800 μm^2 SQUID chip was glued to the bottom of a bullet-shaped sapphire rod that had a flattened square (2nd generation) or circular (1st generation) tip. This configuration put the plane of the SQUID loop parallel to the *xy*-plane (sample plane). For an *x*-SQUID configuration, a rectangular SQUID chip is

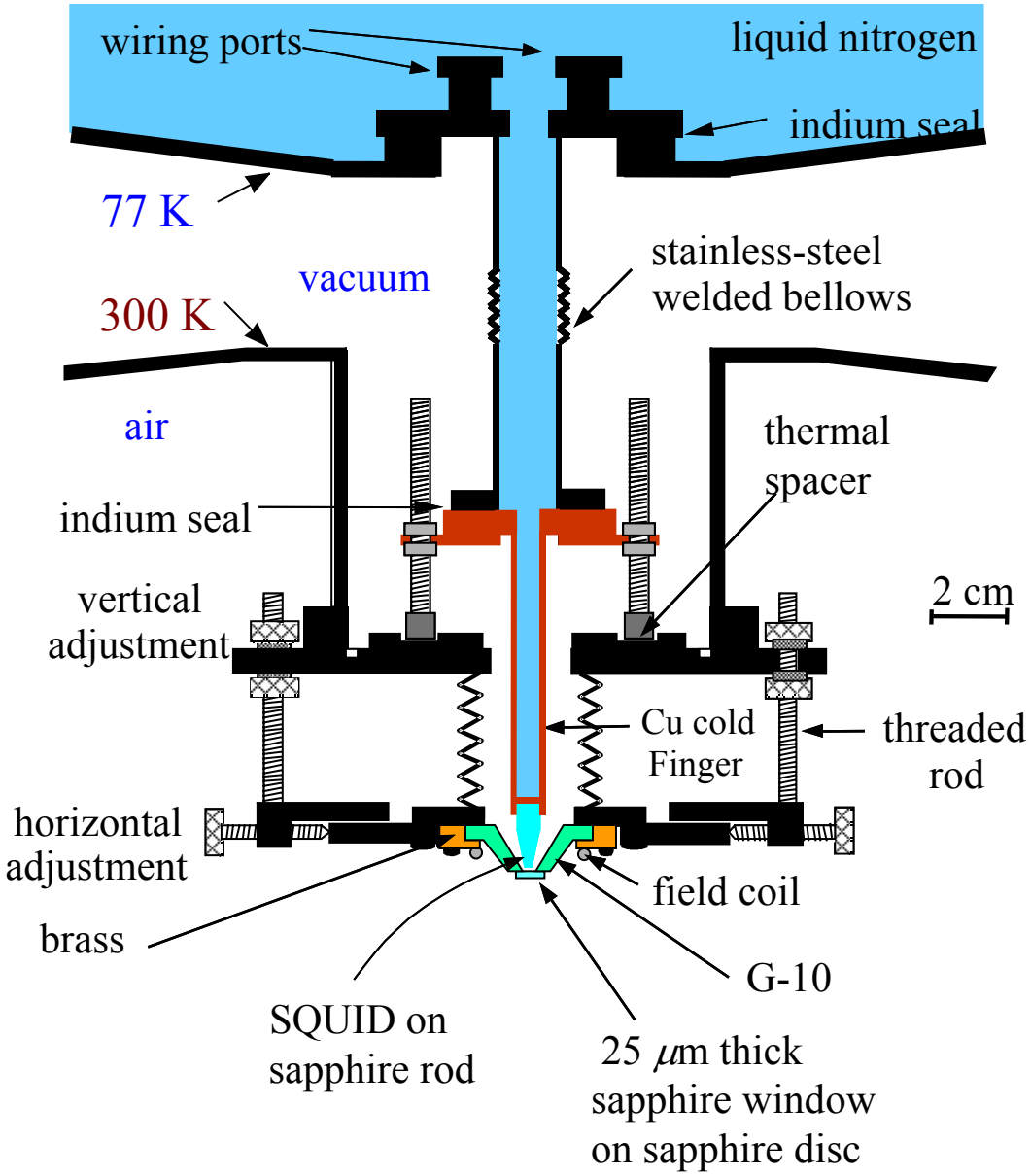

Figure 5.1: Schematic of 2nd generation room-temperature SQUID microscope design. Asterisks denote changes in material or design from 1st generation SQUID system (reproduced from Ref. [3]).

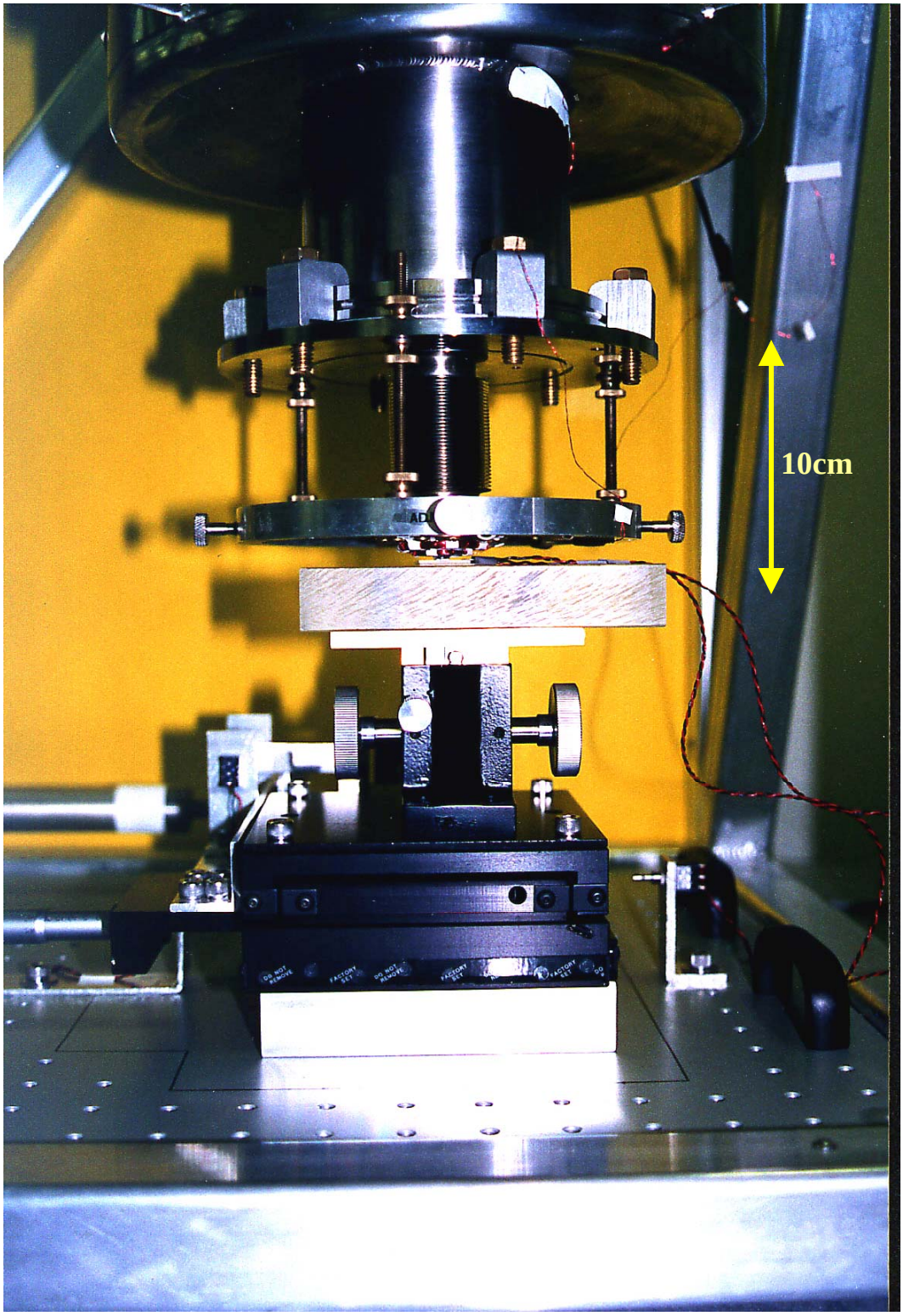

Figure 5.2: Photograph of the lower exterior section of the 2nd generation SQUID microscope with sample stage mounted on home-built scanning table (reproduced from Ref. [3]).

glued to the end of the sapphire rod as shown in Fig 3.4(b), making the SQUID loop plane perpendicular to the *xy*-plane.

5.1.3 **Cold-finger**

The SQUID chip is attached to the end of the cold-finger. The most important role of the cold-finger is to transfer the liquid nitrogen temperature (77K) to the SQUID chip. As shown in Fig 5.1, the copper portion of cold-finger has a hole drilled along its length (but not all the way through), to allow liquid nitrogen to almost reach the SQUID chip. The red color in Fig 5.1 indicates that part of the cold-finger is copper. The 1st and 2nd generation systems used silver paint to attach the SQUID chip assembly (chip and sapphire bullet) to the copper cold-finger. After filling with liquid nitrogen, the equilibrium temperature of the sapphire tip was about 78K. In addition, to keep the cold-finger from moving, the cold-finger has a flange which is supported by the outside of the window manipulator. For thermal isolation, a spacer made of nylon is used to separate the flange, which is at 77 K, from the case, which is at room temperature.

5.1.4 **Window manipulator**

Since thermal contraction of the cold finger, or the outer window assembly will occur, it is essential to be able to move the window and bring it very close to the SQUID. To control the window so that it can be brought close to the SQUID, we need a manipulator. Figures 5.1 and 5.2 show the basic arrangement. A very flexible vacuum-tight bellows allows the window flange and window to be moved in *x, y* and z. There are 3 knobs for making vertical window adjustments, and 4 knobs for horizontal

window adjustments. The SQUID tip must fit closely into a 1mm aperture in the support for the thin window. Although the purpose of the design is to allow alignment of the SQUID tip to the center of the window, in practice it is hard to be very precise and one must be very careful when bringing the tip close to the window. This is one reason why it is difficult to operate with the SQUID very close to the sample.

5.1.5 **Wiring and dewar**

As shown in Fig. 5.1, the wires to the SQUID are submerged in liquid nitrogen. This minimize heat flow down the wires from room temperature to the SQUID. The dewar used for the system started life as a conventional 77 K bucket dewar. This dewar was modified by the shop, which welded on a custom tail flange for the window manipulator assembly and cold finger. During this process, all the super-insulation was removed, so that the LN_2 hold time is only a couple of days.

5.2 Modifications for multi-channel SQUID microscope

To construct the multi-channel SQUID microscope, I modified the window assembly, SQUID chip assembly, cold-finger, and vacuum connector and also built a new SQUID chip. I retained the entire outside of the dewar and manipulator as shown in Fig 5.3. I also changed the *xy* translation stage, as I discuss in Chapter 6.

One of the big concerns for the multi-channel SQUID system design was to reduce interaction between different SQUID channels. Another requirement was the need to optimize the use of the available space inside the dewar, since I had to fit 8 times as many wires as for the single-channel system. Finally, the design needed to

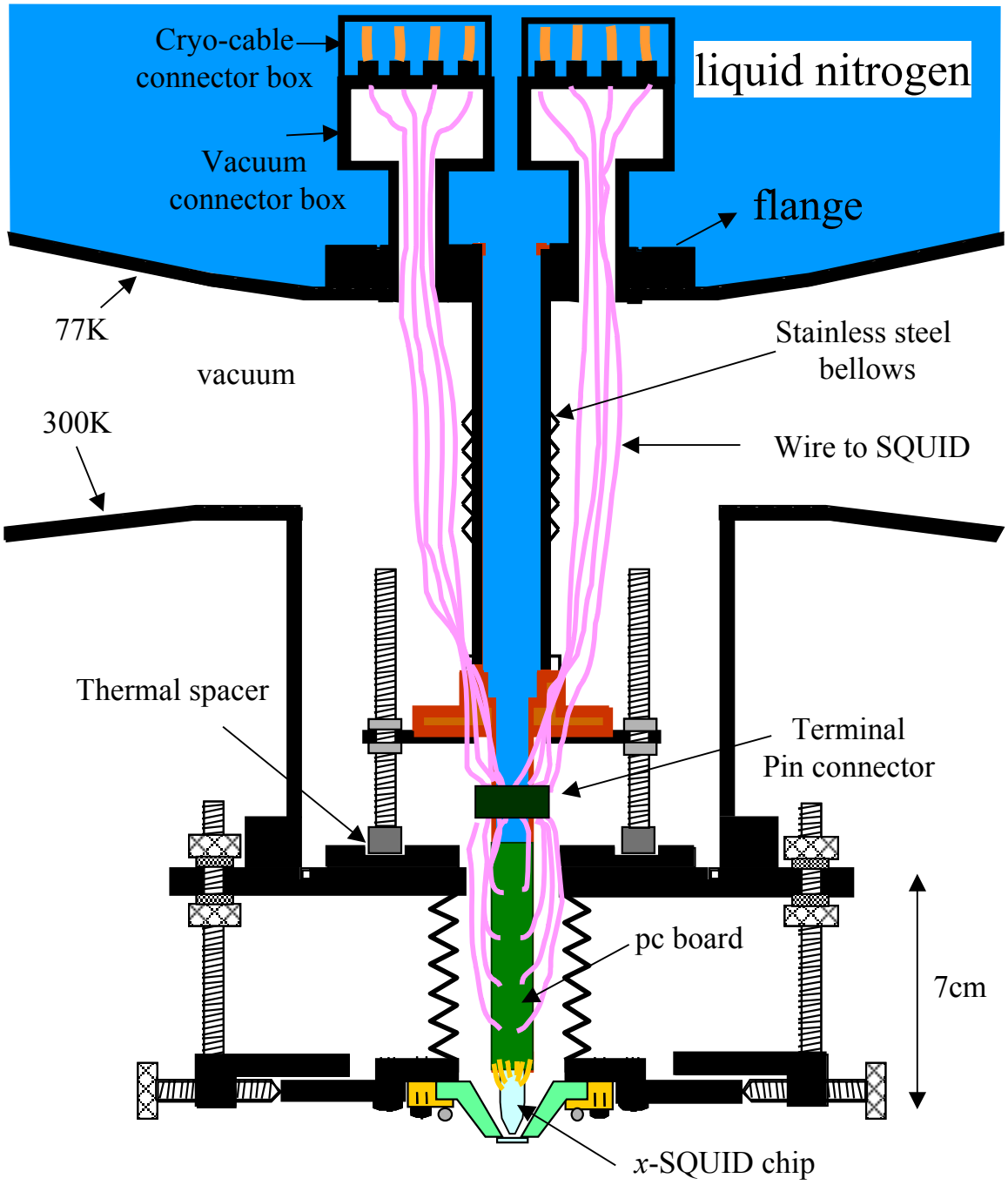

Figure 5.3: Schematic of lower section of multi-channel SQUID system.

ensure that the distance between the sample and the SQUIDs was similar or smaller than with the single SQUID microscope, in order to achieve good spatial resolution.

5.3 Vacuum window

5.3.1 Window and nose cone (window assembly)

As I explained in section 5.1, a very thin window is required in the microscope, since otherwise the thickness of the window would limit the spatial resolution. In addition to this requirement, the window should be stiff enough not to flex under atmospheric pressure. The window also must be vacuum tight, non-magnetic, non-conducting, and preferably transparent to allow easy visual alignment of the tip. Sapphire and diamond are probably the best choices, although very thin SiN windows are also available [5].

I used a commercially available 5 mm diameter, 25 μm thick sapphire disk as my window. Single crystal sapphire is a very hard material. However, a 25 μm thick sapphire window can easily break because of differential thermal contraction of the thin sapphire and the G10 (plastic) nose cone if the outside of the system changes temperature. As in the previous design, to prevent breaking, yet keep the window as thin as possible, I added a window support interlayer made from a 1mm thick sapphire disk with a small tapered hole into which the SQUID chip assembly can fit (see Fig. 5.4(a)). This thick sapphire disk can endure force by thermal contraction of the flange that holds it, and it is thermally matched to the thin window, so no forces are placed on the window itself.

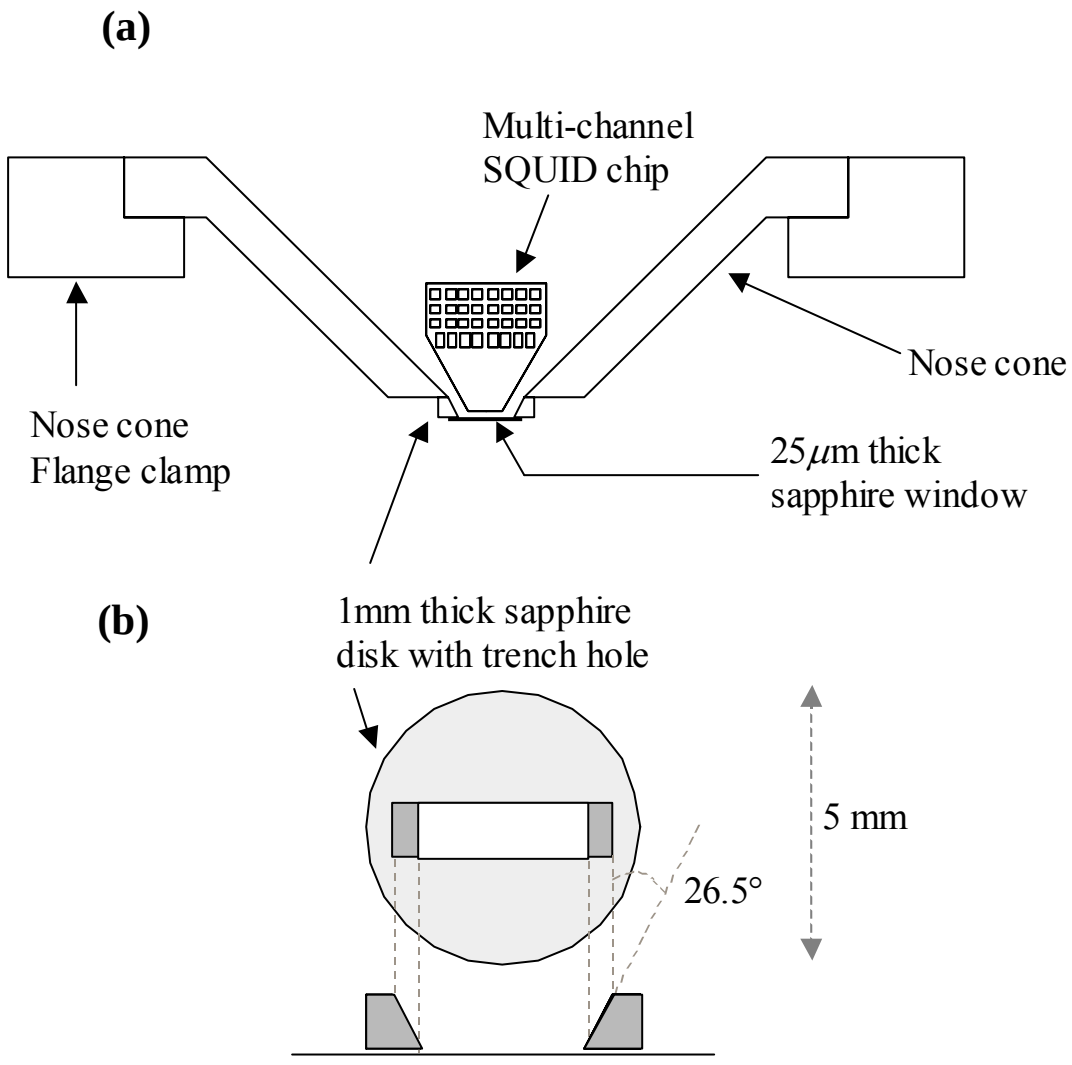

Figure 5.4: (a) Side view of modified window assembly and multi-channel SQUID chip. (b) Design of 1 mm thick sapphire window support disk with trench hole.

Since the 25 μm thick sapphire window must withstand atmospheric pressure, the hole in the thick sapphire disk should be made as small as possible. Figure 5.4(b) shows the "trench" design that I developed for the window and support. I needed to use a rectangular trench, instead of the circular hole used in earlier designs because the multi-SQUID chip is about 1.6 mm long at its base and the thickness is 0.5 mm. Therefore, I set the size at the bottom of the trench hole to be 2.2×1 mm^2 to include marginal space. The size at the top of the trench hole is designed to 3×1 m m^2 to allow easier access of the SQUIDs. With this design I found that the 25 μm thick sapphire window with area 2.2×1 mm^2 could withstand atmospheric pressure.

5.3.2 Calculation of bending of thin window

The trench window I developed was significantly larger than the previous design (which had a 1mm diameter hole). In addition to making sure it could withstand atmospheric pressure, I also needed to check how much it would bend. I estimated the amount of bending by applying Hooke's law to a bending beam [6]. As shown in Fig. 5.5(a), the effect of bending along line A is smaller than that of bending along line B. Therefore, I can simplify the problem to 1-D by assuming the bending is only along line B. The bending depth δz is given by (see Appendix A),

$$\delta z = \frac{1}{YI} \int dx \int m dx \qquad (5.1)$$

where Y is Young's modulus, I is the center of mass, and m is the bending moment. The center of mass I contains information about the cross-section of the bending line. I calculate the bending depth for two cases, one when the force is only at the center, the other when the force is uniform along the beam.

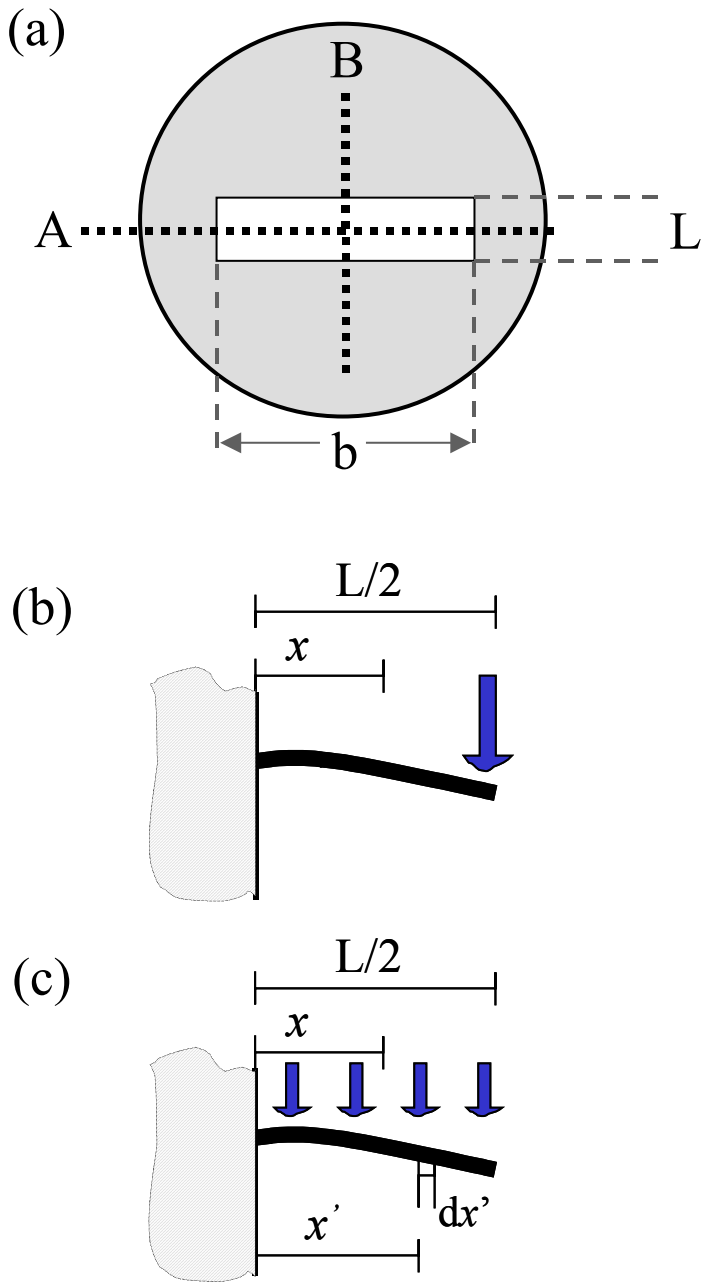

Figure 5.5: (a) Bottom view of the thick sapphire disk with a trench hole of area L×b. (b) Bending beam with external force only at the end and (c) with uniformly distributed external force.

(i) Force at the center: Figure 5.5(b) shows a 1-dimensional rod with applied force only at the center. The moment m at a distance x from the edge of the window is given by

$$m = \left[\frac{L}{2} - x\right]F \ . \tag{5.2}$$

Using Eq. (5.1), the bending depth at x = L/2 is

$$\delta z(L/2) = \frac{1}{YI}\int_0^{L/2} F\left(\frac{Lx}{2} - \frac{x^2}{2}\right)dx = \frac{FL^3}{4Y\,t^3 b} \ , \tag{5.3}$$

where $I = t^3 b/12$ and t is the thickness of the window. The force can be expressed in terms of the pressure, $F = PbL/2$. Then the bending due to a single force at the center is

$$\delta z(L/2) = \frac{PL^4}{4Y\,t^3} \ . \tag{5.4}$$

The Young's modulus for single crystal sapphire is Y = 50×10^6 psi, atmosphere pressure P = 15 psi (1.01×10^5 pa), L = 1 mm, and t = 25 μm. For these parameters, Eq. (5.4) gives a bending depth z ~ 4.8 μm.

(ii) For a uniformly distributed force as shown in Fig. 5.5(c), the moment m at a distance x from the center is,

$$m = \int_0^{L/2} \mathrm{d}F(x'-x) = \int_0^{L/2} Pb\mathrm{d}x'(x'-x) = \frac{PbL}{2}\left(\frac{L}{4} - x\right) \quad . \tag{5.5}$$

Using Eq. (5.1), the moment is obtained as

$$\delta z(L/2) = \frac{PL^4}{16Y\,t^3} \ . \tag{5.6}$$

Equation (5.6) yields a bending depth δz = 1.2 μm for my window. Since atmosphere pressure is uniform, the second model should be a better model for my

system. A bending depth of 1.2 μm is relatively small compared to the thickness of the sapphire, 25 μm and the 1 mm width of the window, which also suggests that the window should not break. While there is no 100 % guarantee that it will not break under the pressure, this is a good number to start from.

5.3.3 Assembling the nose cone and vacuum window

The sapphire disk window support with its trench hole is epoxied to the microscope nose cone (see Fig. 5.6). The nose cone is made from G10 fiberglass, which is non-magnetic, stiff, and machinable. However it is somewhat porous, so to ensure vacuum integrity I sprayed the surface with DATAKOAT [7] and then baked it for 1 hour at 65.5 °C.

To make the trench hole in the 1 mm thick sapphire disk window support, I started with a commercially available 5 mm diameter, 1 mm thick, sapphire disk with a 1mm diameter hole in the center. Using a diamond drill with a drill bit smaller than 1mm on a drill press, I drilled a 50 μm deep shallow layer and milled the layer to a width of 4mm. I drilled successively narrower 50 μm steps and milled each layer. As shown in my design (see Fig. 5.4(b)), the trench hole becomes narrower as I drill deeper. Needless to say, this required some care, as sapphire is quite brittle.

Once the nose cone and sapphire disk with trench hole were completed, I glued the 1 mm thick sapphire disk on to the nose cone using flexible epoxy [8]. After the epoxy dried (after 24 hr), I cleaned the surface with acetone, followed by methanol. I painted the epoxy around the trench hole and then attached the 25 μm sapphire window over the trench using flexible epoxy. If too little epoxy is used, one does not get a good

vacuum seal, and if too much epoxy is used, the window will become thicker than 25 μm, so care and patience is required. Figures 5.6 (a)-(c) show an overview, top view, and side view of a finished vacuum window assembly.

After curing an additional 24 hr, I tested the vacuum window assembly for leaks using a homebuilt window test assembly. It was very convenient to have a window test assembly because this eliminated the need to assemble the whole system just to leak test the window. In addition, it is handy for checking spare windows since the vacuum window can fail for many reasons, for example, such as when the SQUID sensor touches it.

5.4 SQUID chip assembly

5.4.1 SQUID chip preparation

The design and fabrication of the multi-channel SQUID chip was described in Chapters 3 and 4. After the SQUID chip is patterned (see Chapter 4), I used a diamond dicing saw [9] to dice the 15×15 mm^2 chip into three 8-SQUID chips. Figure 3.7 shows one of the cutting lines for the 15×15 mm^2 SQUID chip. After separating the three multi-channel chips, I used the dicing saw to cut more precisely along the boundary of the pattern, allowing for a total cut width of about 200 μm. Without this additional space, the jagged edge left by the saw could reach the patterned wires and destroy them. The width of this jagged edge depends on the speed of the dicing saw, the angle of the cut, and the growth direction of the thin film. Therefore, before cutting close to the SQUIDs, it is important to do a test cut to estimate the width. Specifically, bicrystal

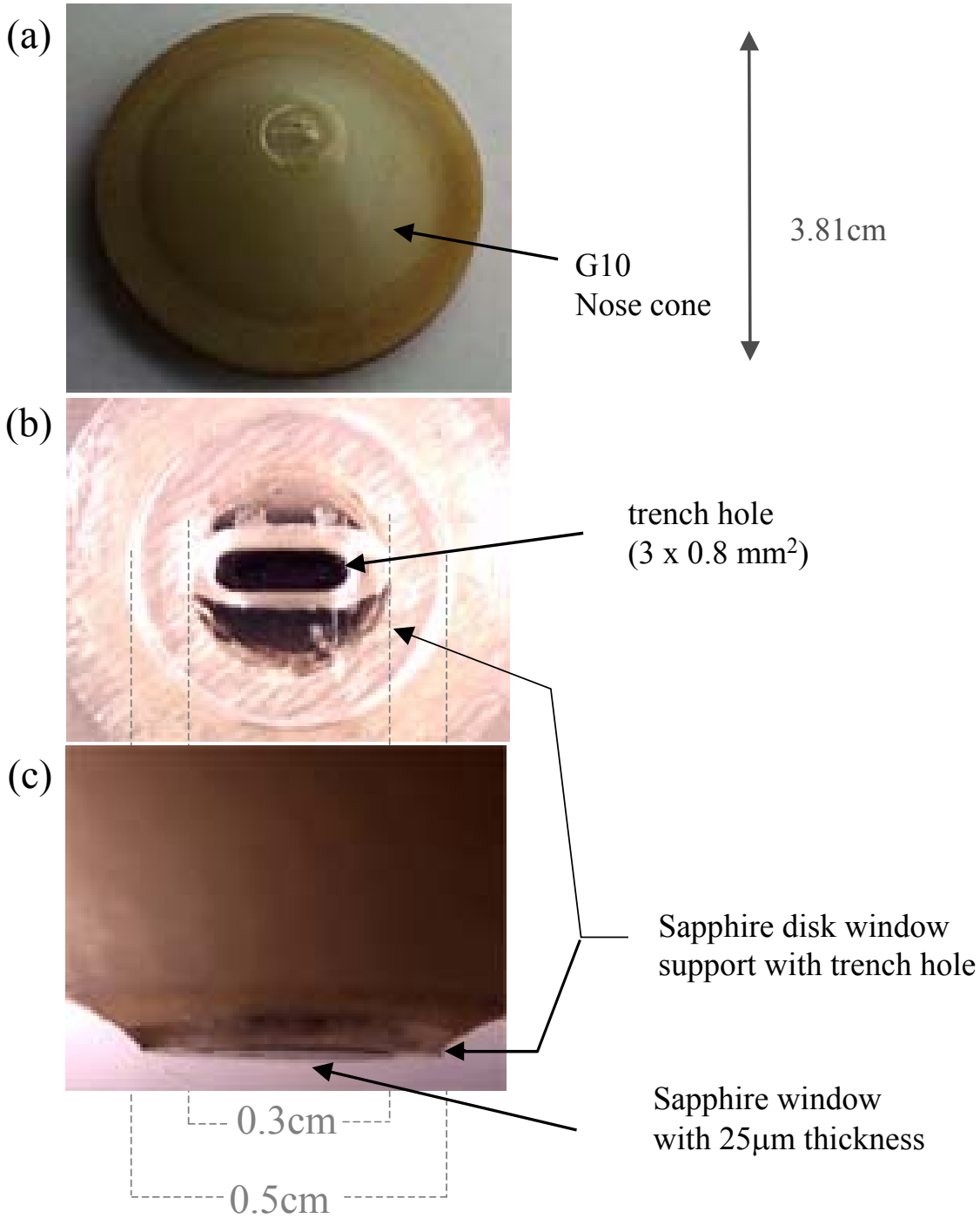

Figure 5.6: (a) Overview, (b) top view, and (c) side view of window assembly.

substrates tend to have more jagged edges. In my multi-channel SQUID chip, the bottom of the chip is the most delicate part since there are eight SQUIDs placed at the bottom in an array. To reduce the risk of losing any of the SQUIDs, I kept a margin of about 200 μm. I used a cutting speed of 10 ~ 50 mil/sec.

After cutting with the diamond saw, I used sand paper to trim the edge towards the SQUID loop. In the beginning, I used rough sand paper (#600) and kept checking the progress using an optical microscope. To finish it, I used very fine polish, typically used for optical lenses [10]. Since there are 8 SQUIDs, there is a high risk of a crack invading one of them. Even using the optical lens sand paper, the surface can crack. One crack was very close to one of the 8 SQUIDs as shown in Fig. 5.7, so at that point I stopped polishing. The distance between the center of the SQUID loop and the bottom of the chip is about 150 μm. Since the height of the SQUID loop is known to be 60 μm, this left about 90 μm between the edge of the chip and the SQUID. I note that Neocera, Inc., has worked on this polishing process and figured out how to get a very smooth edge, with SQUIDs just a few microns from the edge [11].

5.4.2 **SQUID chip assembly**

The SQUID chip assembly consists of the multi-channel SQUID chip, a small pc-board, and terminal pins, as shown in Fig. 5.8. Since the multi-channel SQUID chip has 32 pads in a small area, wire-bonding is required for the wiring. I designed a pc-board to accept the wire-bonds and connect to hard-wired lines. On the SQUID chip, the current and voltage pads for a given SQUID are in common, while they are separate on the pc-board. Since each SQUID requires a pair of wires for current, a pair for voltage,

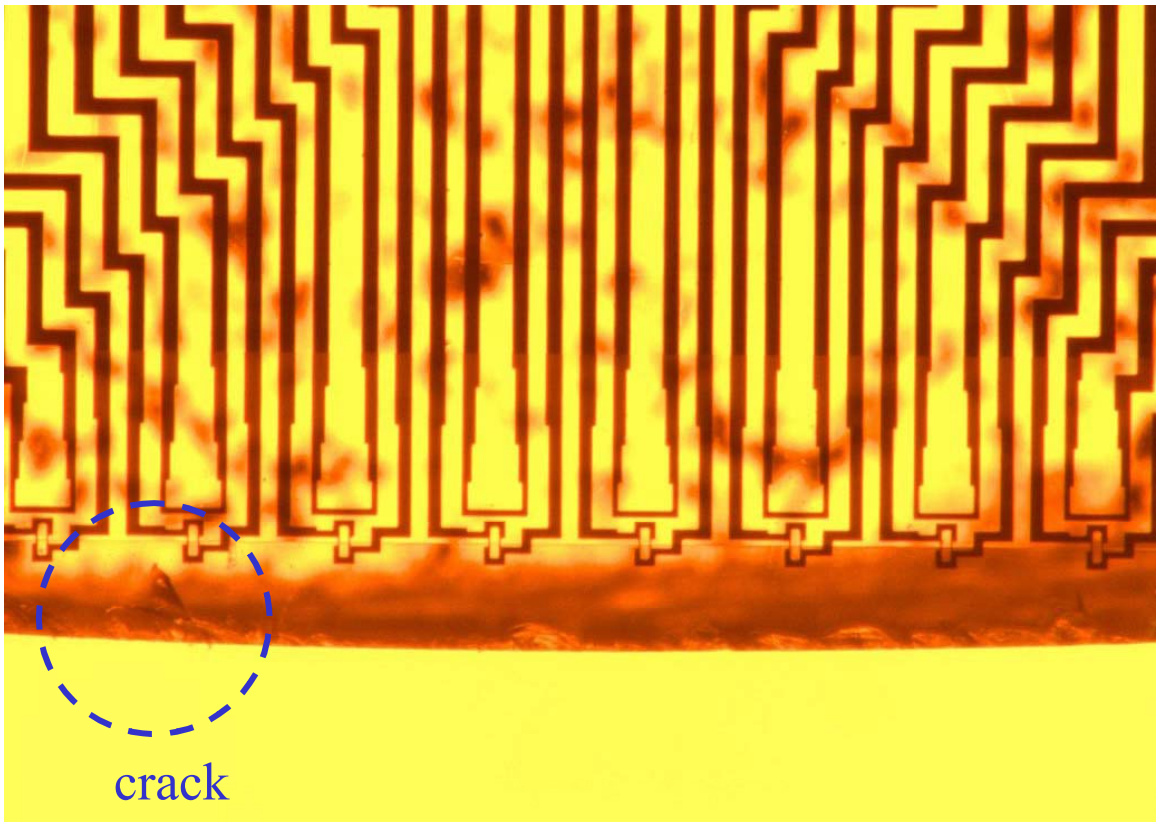

Figure 5.7: Multi-SQUID chip after dicing and polishing, showing small crack near the second SQUID loop.

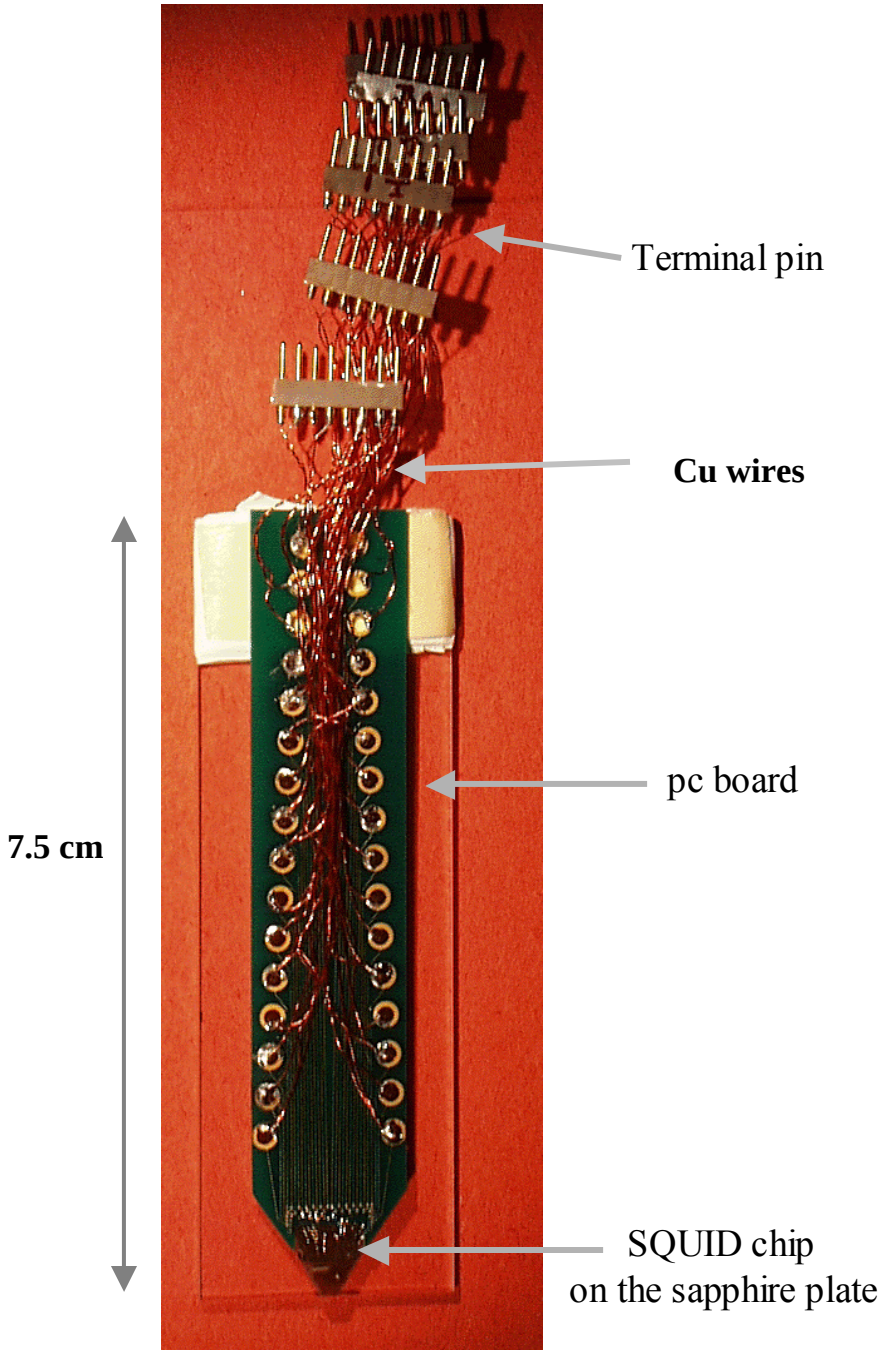

Figure 5.8: Multi-channel SQUID chip assembly, including SQUID chip, pc board, and 48 terminal pins. The assembly is resting on a glass slide.

and a pair for feedback flux, this gives 48 wires connected to the pc-board (6 wires×8 channels). On the opposite end of the pc-board, Cu wire was connected by soldering. The Cu wires are connected to terminal pins for ease in connecting the board and to protect the SQUIDs from heat during soldering.

Figure 5.9(b) shows a side view of the bottom part of the SQUID chip assembly. Since the pc board is not thermally conducting, I mounted the chip on a sapphire plate that was epoxied to the cold-finger. The main reason for using sapphire is that single crystal sapphire has a large thermal conductivity at 77K. My aim was to keep the multi-channel SQUID chip as far from the Cu cold-finger as possible, while still maintaining good thermal contact. This was important because eddy currents will be induced in the metal from the modulation current (or other applied fields), and these eddy currents can affect the SQUID signal. I glued the SQUID chip and part of the pc board to the sapphire board using epoxy [8].

Before I performed the wire-bonding, I had to solder the copper wires between the pc board and terminal pins. If the wire-bonding is performed first, then the heat from the soldering can destroy the SQUID junctions. After soldering, I performed the wire-bonding [12]. In the beginning, it took me 14 hrs to finish 32 wires but with practice I reduced this to 3~4 hrs. Figure 5.9(a) shows a finished wire-bonded SQUID chip. I note that the Au wire I used for wirebonding was more stable than Al wire (with 1% Si); the Al wire came off easily when I dip-tested the chip in liquid nitrogen. After I finished testing the SQUID chip assembly, I attached a Pt-sensor thermometer [13] to the back of the SQUID chip to monitor the temperature of the SQUID.

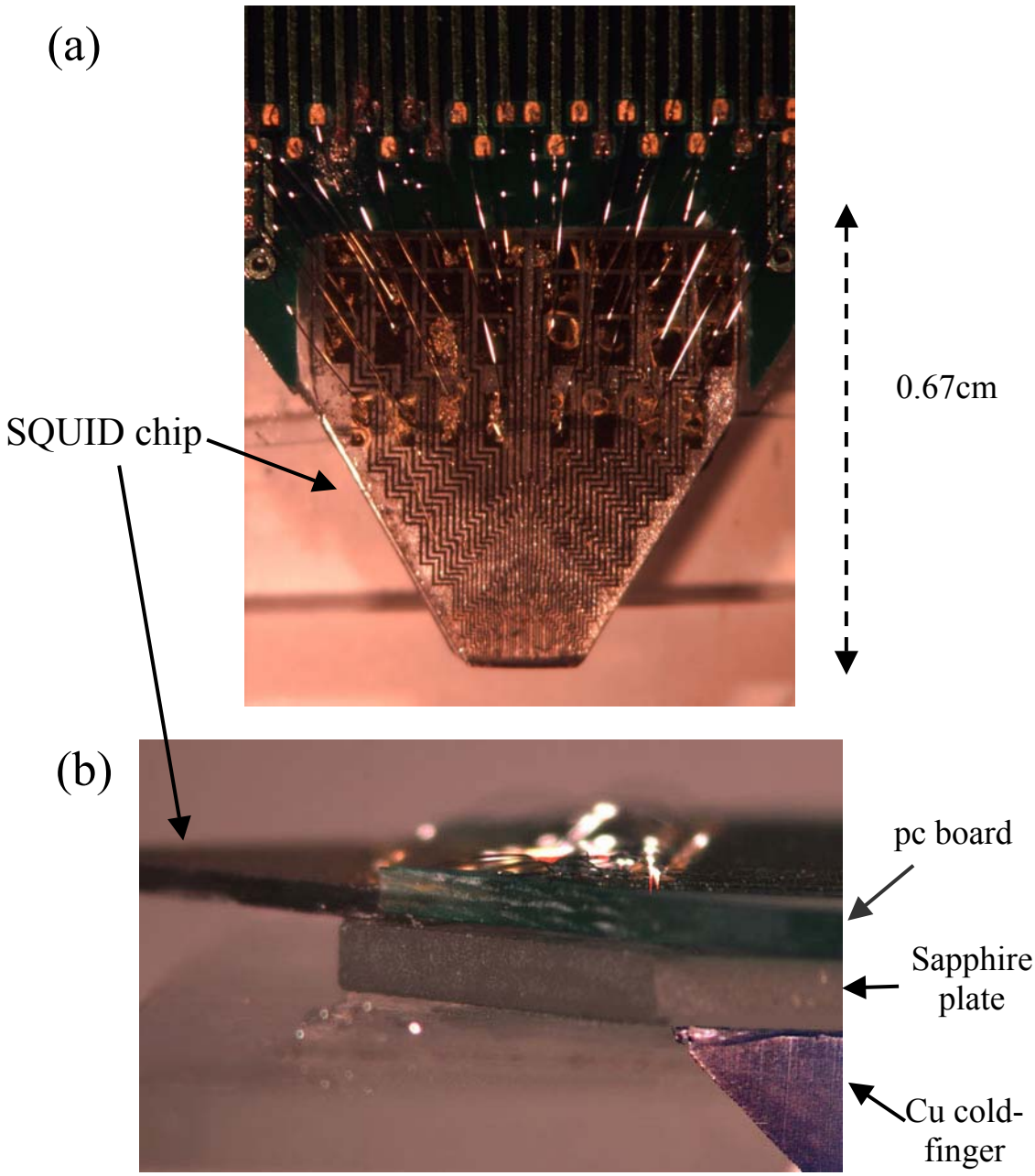

Figure 5.9: (a) SQUID chip after wire-bonding, (b) side view of SQUID chip assembly with sapphire board sitting on Cu cold-finger.

5.5 Cold-finger and connector box

5.5.1 Design of cold-finger

The main role of the cold-finger is to keep the SQUID chip at 77K. The cold-finger consists essentially of two parts. One part is made of Cu, and it is this part that the SQUID chip assembly will be attached to. The other part is made of stainless steel and is connected to the liquid nitrogen bath in the stainless steel dewar. These two parts are vacuum-sealed with an Indium seal. Both have a center hole to allow liquid nitrogen to flow to the bottom of the cold-finger.

The main reason I had to modify the original single-channel cold-finger was that there was not enough space for 48 wires. To make space for so many wires, I designed the copper part to be a half cylinder. In addition, I increased the diameter to allow more liquid nitrogen down the center. Figures 5.10(a)-(b) show a cross-section of the side view and front view of the Cu part of the cold-finger. I kept the same design for the stainless steel bellows (see Fig. 5.11). The purpose of the bellows is to compensate for thermal contraction of the inside of the dewar when it is filled with liquid nitrogen.

5.5.2 Design of connector box

To prevent electrical coupling between the different SQUID channels, I intended to use separate cryogenic vacuum electrical feedthroughs for each channel. In the previous system, the vacuum connector was placed on the main cold-finger flange of the stainless steel cold-finger (see Fig. 5.11). This flange sat in the liquid nitrogen at the bottom of the dewar and was vacuum-sealed with Indium. Therefore, the flange is at the

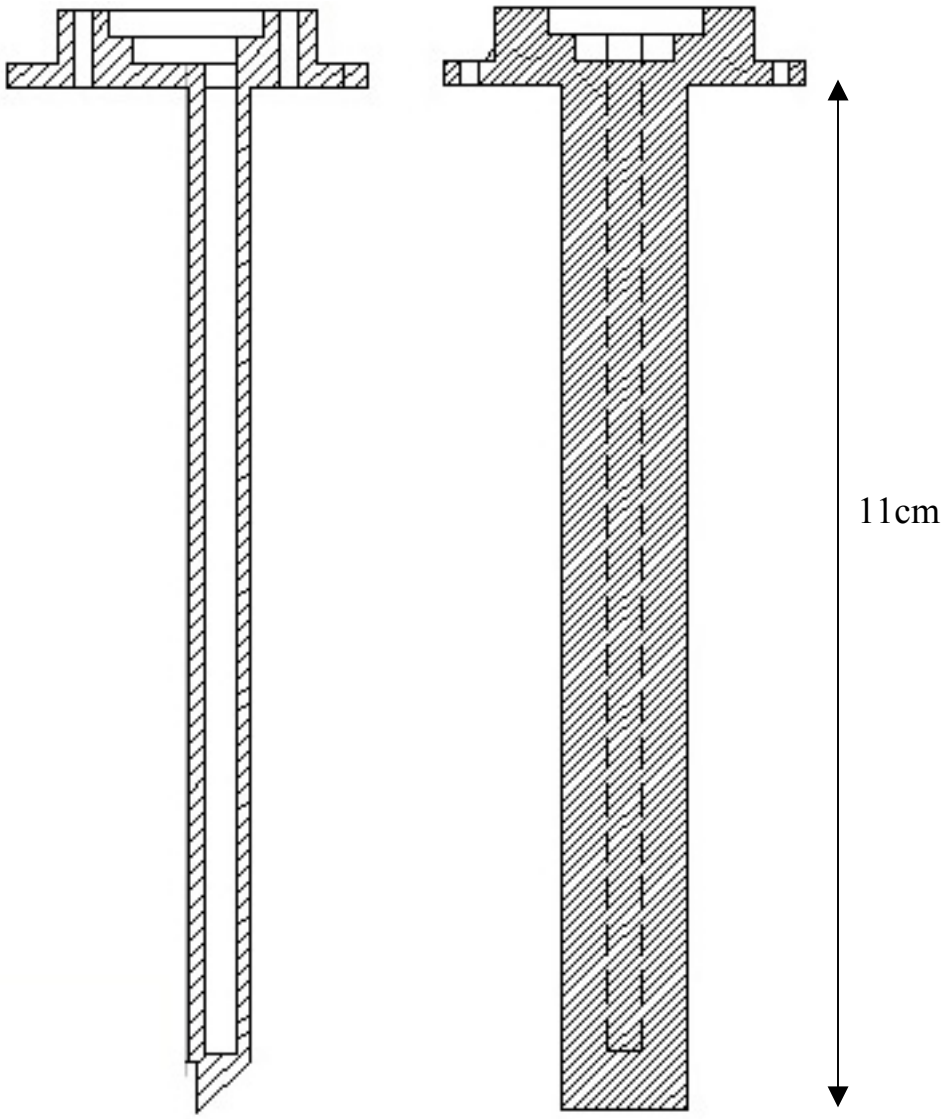

Figure 5.10: (a) Side view, (b) front view of design of hollow Cu part of cold-finger.

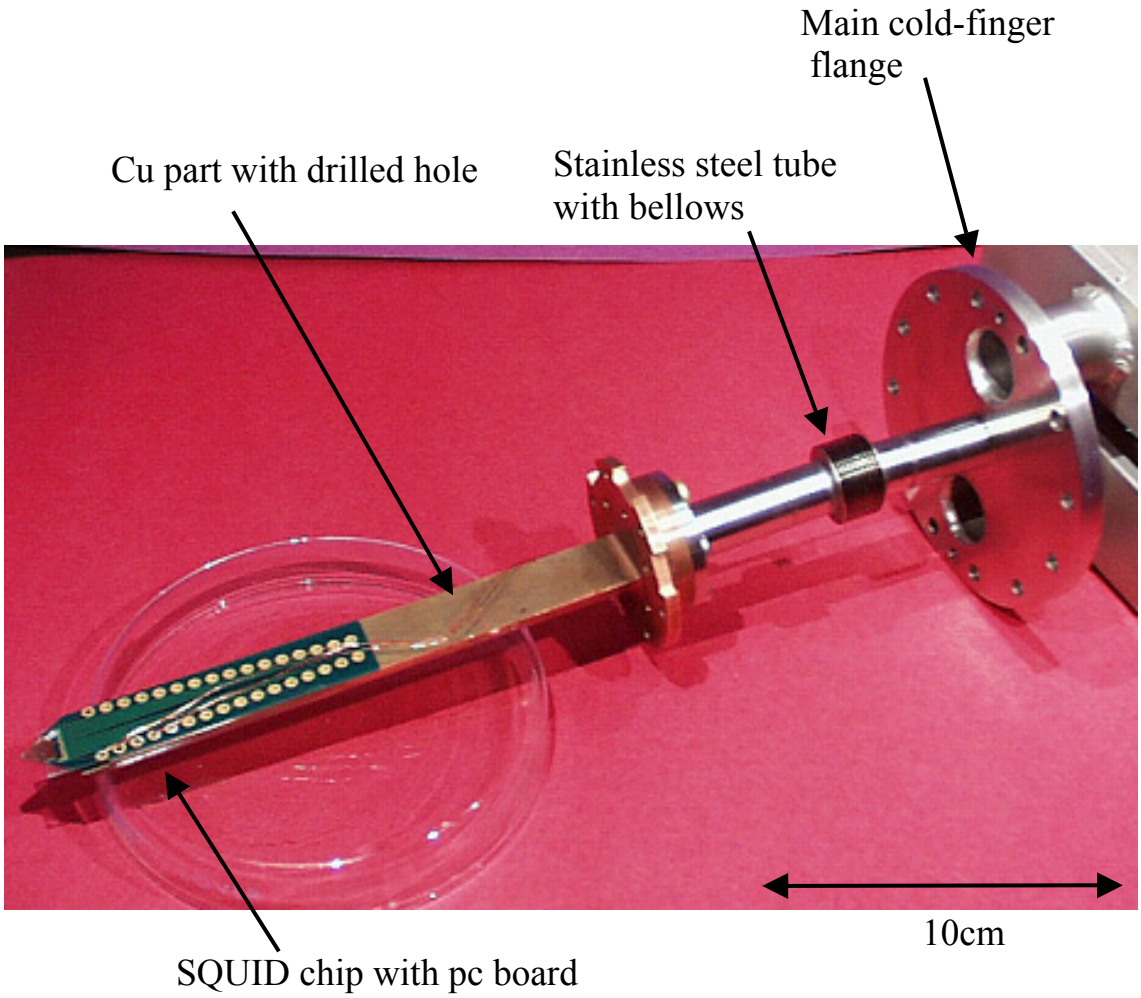

Figure 5.11: Cold-finger assembly, which consists of a hollowed-out Cu part and a stainless steel part with flexible bellows.

boundary between vacuum and liquid nitrogen. However, since the cold-finger flange should match the dewar flange, I could not modify the size of the main cold-finger flange to create space for more wires.

The flange only allowed enough space for 2 connectors. To make more space for connectors, two connector boxes were required. In my design, each connector box contains 4 vacuum connectors on the top cover, and is connected to the main cold-finger flange with a welded stainless steel tube (see Fig. 5.12). The connector box has a top cover for the connectors and a side cover to easily check the wiring. These covers were also vacuum-sealed with Indium, and the final assembly sits directly in liquid nitrogen.

5.5.3 **Assembly including wiring**

While the cold-finger and the connector box based on my design were being machined in the shop, I prepared the 48 wires coming from the SQUID chip assembly to the connector boxes (see Fig 5.12). I twisted pairs of Cu wires and inserted them into Teflon tubes, and then inserted the tube into a Cu braid. I would have preferred a stainless steel tube instead of Cu braid for shielding, but it was not flexible, making it hard to fit into the limited space available. This shielding procedure is also designed to prevent interaction between channels and protect from radio-frequency interference. The thickness of one complete braid with wires was about 2-3 mm.

When the connector box was machined, I put the cryogenic vacuum connectors onto the top cover of the connector box. I used eight Oxford 10-pin cryogenic vacuum connectors [14]. For the vacuum seal, I used soft soldering with wood's metal

(Cerrolow-117 Alloy) using acid liquid flux. First, I put two metal blocks on a hot plate and laid the connector box top cover on the metal block, setting the temperature to about 200 °C. When the top cover was hot, I applied acid flux around the hole for each connector with a Q-tip. Immediately after that, I inserted a vacuum connector into each hole and applied a small amount of Wood's metal (size of a ball with 3 mm radius). When the Wood's metal started to melt, I spread the liquid wood's metal around the connector using a Q-tip to cover the gap between the connector and the top. I note that after soldering it is important to wash the top cover to get rid of acid residue since it is very corrosive. Also this procedure should be performed under a ventilation hood because the vapors are harmful if inhaled.

After putting 8 vacuum connectors onto the top covers of the connector boxes, I soldered 48 wires to the connectors, and soldered the other ends to eight female 6-pin terminals. Since the wire is thin and only soldered in terminal pin, it can easily become disconnected even when treated gently. Applying DATAKOAT [15] on the peeled wire helps a little. This was one of the weak points in the design.

At this point, there were a few steps to complete the SQUID chip assembly, cold-finger, connector boxes, and wiring. Before I laid the SQUID chip assembly on the flat Cu cold-finger, I attached Mylar tape to the back of the pc-board and used silver paint to attach the sapphire board to the cold-finger (see Fig. 5.9(b)). I then wrapped the cold-finger and SQUID chip assembly with Teflon tape, and taped down the wires from the cold-finger assembly using Teflon tape. Figure 5.12 shows the finished cold-finger, including the SQUID chip assembly and vacuum connector box (this entire part is the cold-finger assembly). In Fig. 5.12, one can see an additional box above the connector

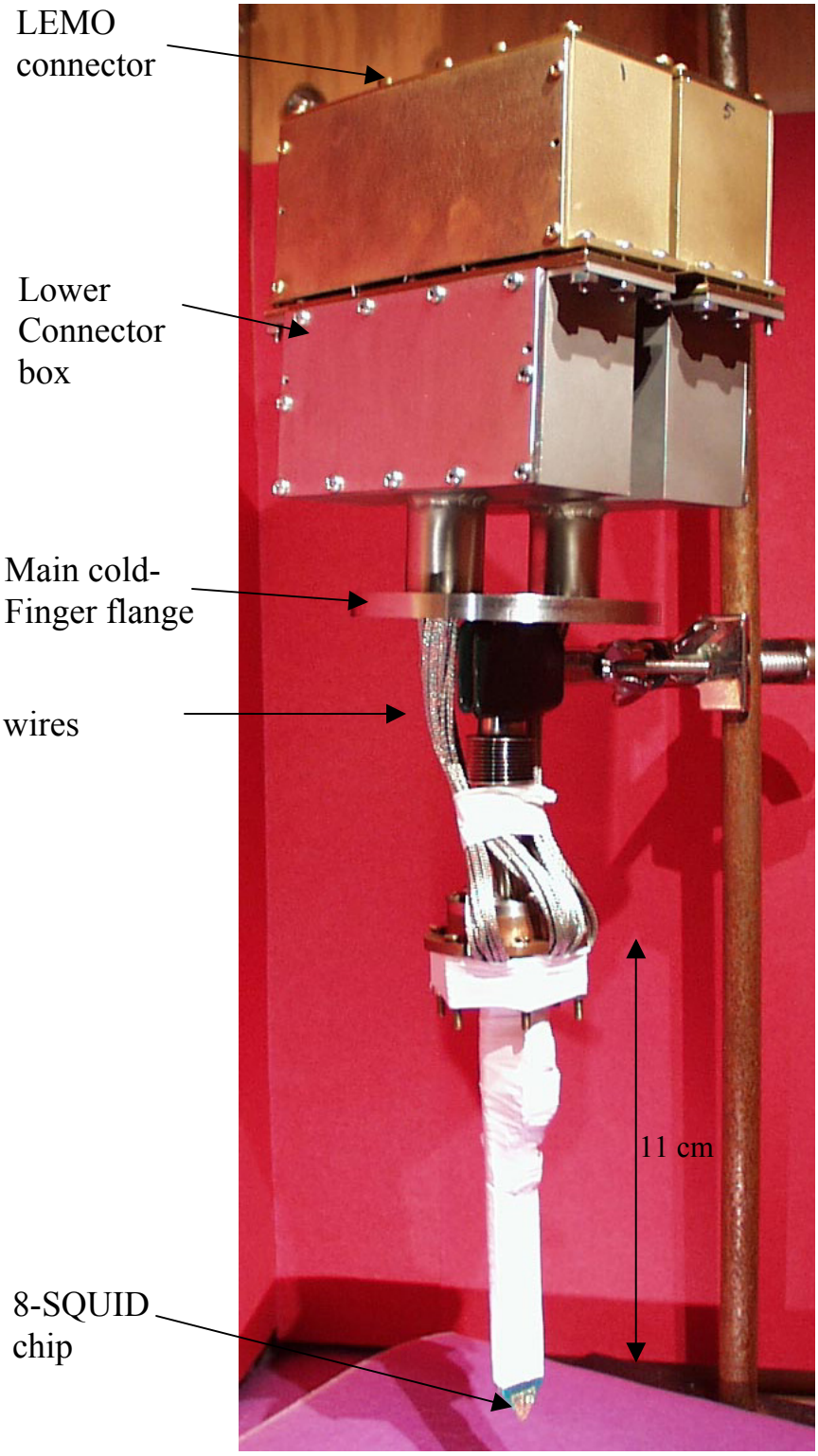

Figure 5.12: Completed multi-SQUID cold-finger assembly, including SQUID chip assembly, cold-finger, wiring, and connector boxes.

box. This is used to simply change from the vacuum connector feedthroughs to LEMO connectors that plug into commercial cryo-cable from the SQUID electronics [16].

5.6 Leak check

Since the working temperature of high-T_c SQUIDs is generally below 80 K, the system must maintain good vacuum to ensure thermal isolation. The cold-finger assembly for the multi-channel system has many parts, vacuum sealed with Indium or Wood's metal. These things can be potential sources of leaks.

I already noted the convenience of a leak test kit for individual parts in section 5.3.3. Previous members of the lab had already made a leak test kit for the window and nose cone, and I could use these to leak-test the nose cone and modified window for the multi-channel SQUID system. However, when I first assembled everything into the dewar and leak-tested, I could hear a faint hissing sound indicating the presence of a large leak. After taking the system apart and reassembling it several times, I was still having trouble finding the leak because I could not use the leak detector for such a large leak and the cold-finger assembly is deep inside the dewar, as shown in Fig. 5.13. In addition, it was very hard to manually tighten the screws that attach the cold-finger assembly to the dewar, partly due to the depth of the dewar, and partly because of the lack of space with the two-stage connector box filling the case of the dewar (see Fig. 5.13). Because of this, I made a leak test kit for the cold-finger assembly. I note that I also lost connections to several SQUIDs during the repeated disassembling and reassembling process.

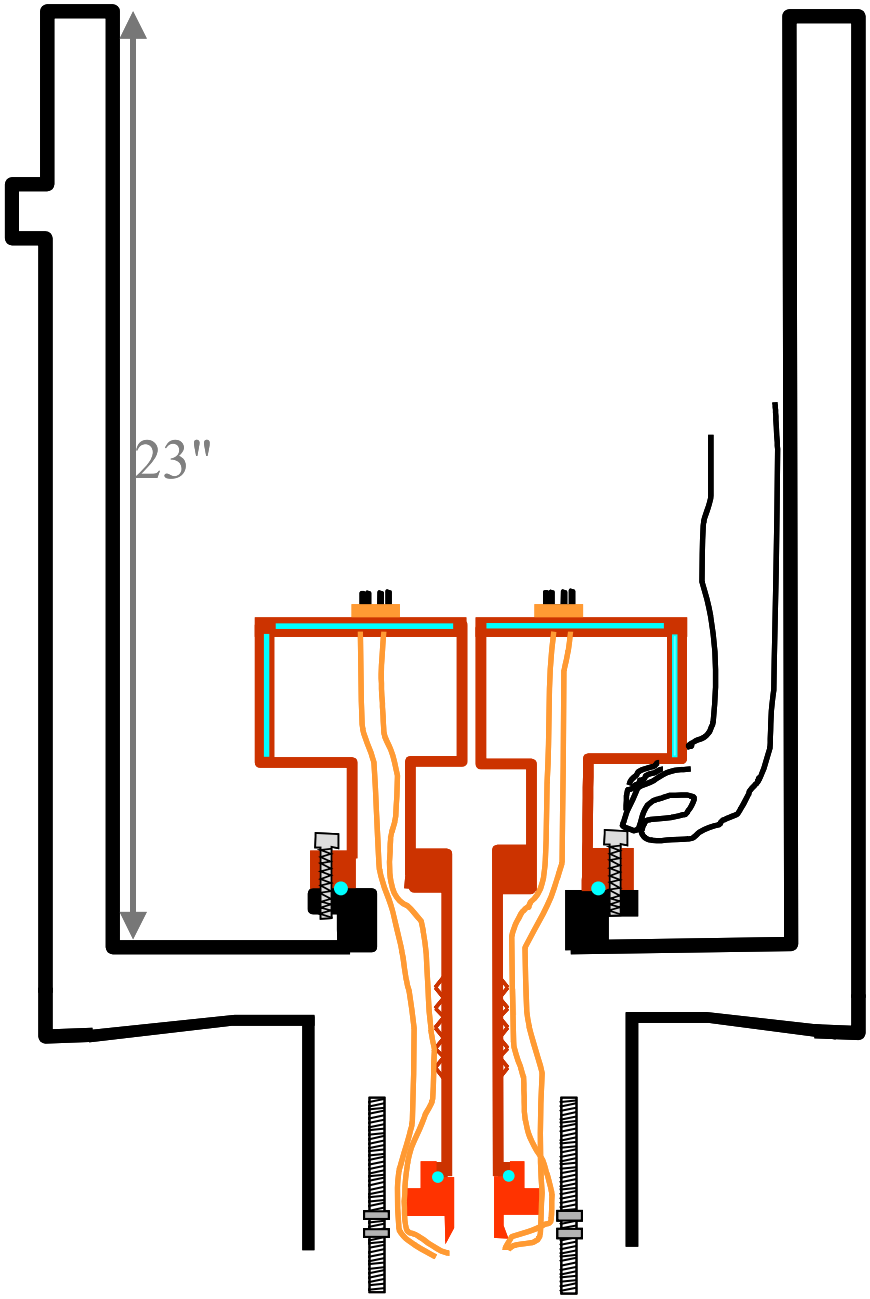

Figure 5.13: Diagram of liquid nitrogen dewar illustrating some of the difficulties of assembly. It is hard to localize leaks deep inside the dewar and the space is very limited, making it hard to tighten the screws or assemble and disassemble the main cold-finger flange.

Using the leak test assembly, I easily found the main leak in the cold-finger assembly. It turned out that a screw hole in the front cover of the connector box had been made as a through-hole when it was not supposed to be. After having the shop weld the hole closed, I used the helium detector to again check the assembly. I found a second leak in a wood's metal seal on top of the vacuum connector box, as shown in Fig. 5.14. I could see a very fine crack in the Wood's metal which was the likely cause.

It is possible that the torque from screwing down the top cover may have caused the crack. To solve this problem, I changed the top cover material from 1/8" thick brass to 1/4" thick stainless steel and used washers. After that, there was no leak at room temperature.

However, when I filled the dewar with liquid nitrogen, the reading on the vacuum gauge increased suddenly as the liquid nitrogen level reached near the top cover of the vacuum connector box. This could be due to the thermal contraction difference between wood's metal and stainless steel in the vacuum connector box. Also, wood's metal is very weak. This leak was hard to fix, so instead I added charcoal to the vacuum connector box. The charcoal can absorb the gas, and if the leak is small enough, it will extend the lifetime of the vacuum. Because the leak was weak, the pressure in the multi-channel SQUID system could remain low enough for over 9 months. Clearly, the feedthroughs were a weak part of the design, although the problems were manageable.

5.7 Conclusion

Modifying the existing single-SQUID system to accommodate 8-channels was easier than starting from scratch. However, there were some disadvantages, for example,

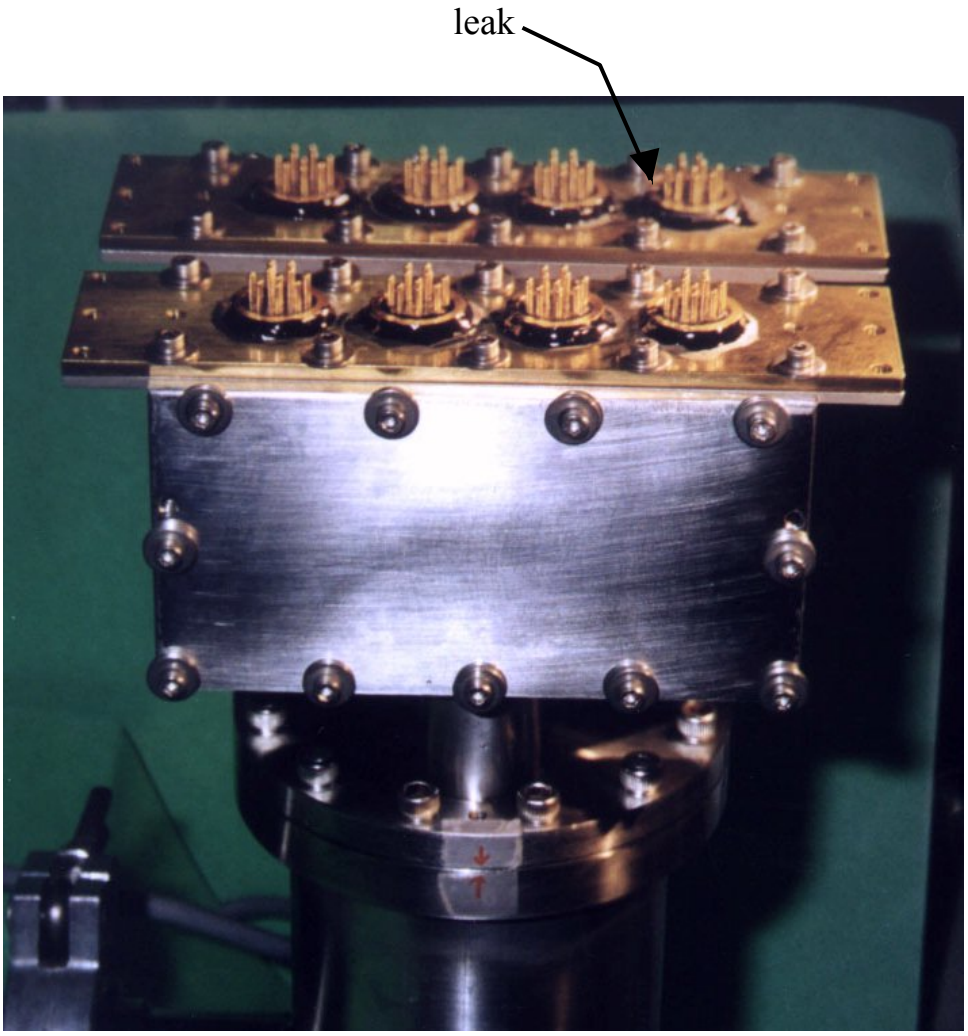

Figure 5.14: Assembled connector box showing location of leak in the wood's metal around one of the cryogenic vacuum connectors.

lack of space. Modifications included making a multi-SQUID chip and changing the window support to a trench hole configuration in order to fit the multi-channel chip into it. I also made space for 48 wires by redesigning the cold-finger with a half-cylinder shape. By adding a vacuum connector box, I could use separate vacuum connectors for each channel. After I assembled these modified parts, I found and fixed some large leaks. Even though a weak leak still remained, the pressure inside the multi-channel SQUID system stayed below 1 mTorr for more than 9 months.

Chapter 6

Multi-Channel SQUID Electronics and Data Acquisition

In Chapter 5, I described the modifications I made to the existing single channel system in order to construct the multi-channel SQUID microscope. In this chapter, I will discuss the new electronics required for the multi-channel system. In addition I describe the new *xy* scanning stage and the data acquisition program I wrote to run the system. Finally, I demonstrate that I can combine the different channels in the multi-channel SQUID system to generate a single image.

6.1 Overall measurement scheme for 8-channel SQUID system

A typical scanning SQUID microscope consists of the SQUID itself, the microscope assembly, the SQUID electronics, an ac current source and Lock-In amplifier, and a data acquisition and control system. For the multi-channel SQUID system, for the most part, I used the same equipment as for the single-channel system. However I needed a set of SQUID electronics and Lock-In amplifier for each of the 8 channels, and I needed to expand the data acquisition program to accommodate 8 channels.

Figure 6.1 shows a schematic of the 8-channel SQUID system. For imaging circuits, I apply an audio frequency current to the sample, which is placed on the *xy*-stage at room temperature. The current generates a magnetic field that is detected by the

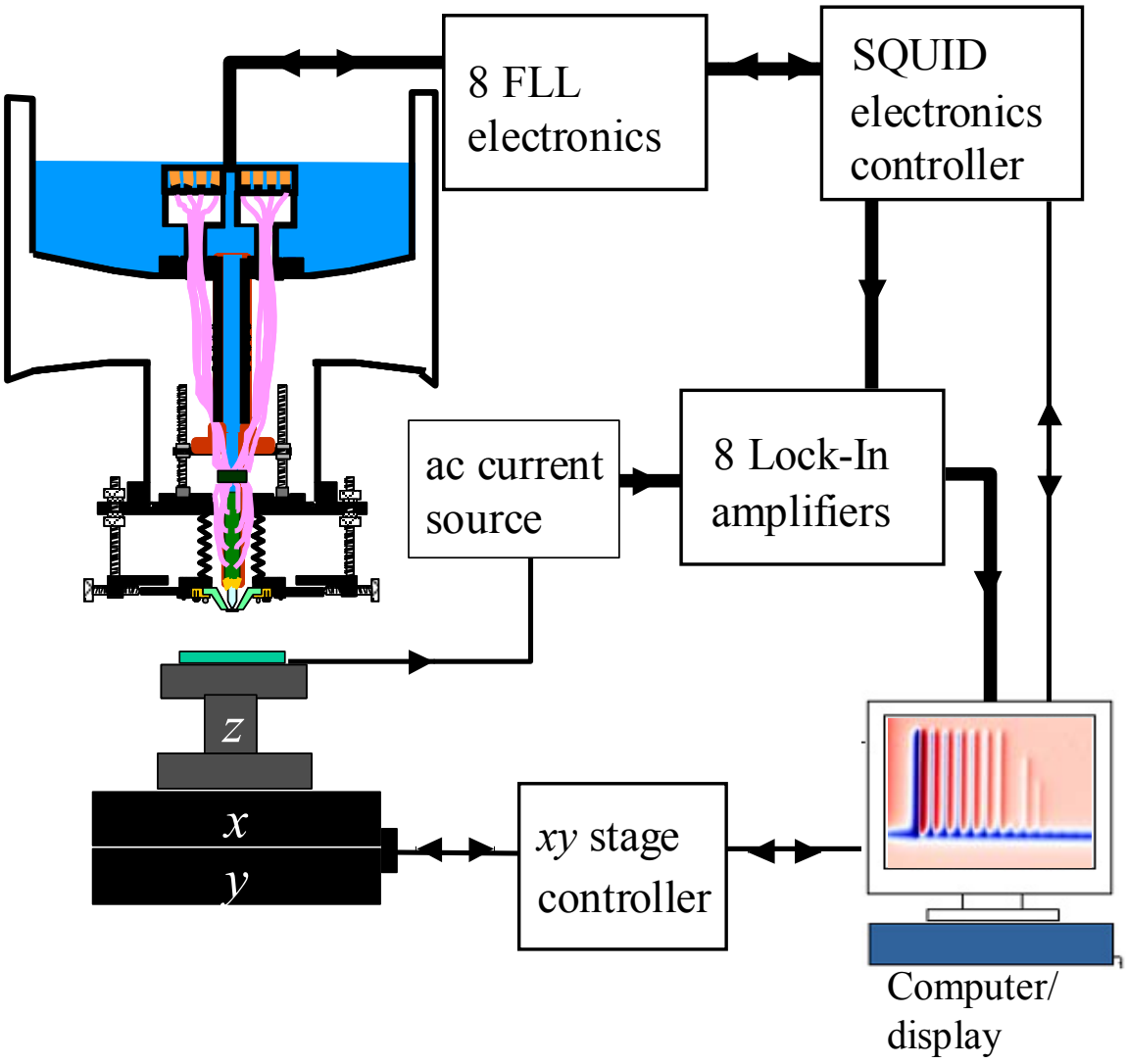

Figure 6.1: Block diagram showing overall measurement technique for using the 8-channel scanning SQUID microscope to image current flowing in a sample.

SQUIDs. The flux-locked loop SQUID electronics linearlizes the response of each SQUID and produces calibrated voltage outputs V_{out} that are proportional to the flux sensed by each SQUID. Each ac voltage output is fed to a lock-in amplifier. The output of each lock-in is read by an A/D board and computer as the sample position is changed, to produce a 2-dimensional image of the magnetic field from the sample.

6.2 SQUID Electronics and its performance

6.2.1 Flux locked loop SQUID electronics

The relation between the SQUIDs voltage and the applied flux is periodic, and thus non-linear. This is very inconvenient if we want to accurately monitor the flux. To fix this problem, the SQUID electronics linearizes the response of the dc SQUID by using negative feedback to form a "Flux locked loop" (FLL).

Figure 6.2 summarizes the basic operation of the FLL electronics. The idea is that when a modulation flux with frequency f_m and amplitude of $\Phi_0/4$ is applied to the SQUID, the voltage across the SQUID varies depending on the external flux (applied flux). If the applied flux (Φ_a) is zero, then the frequency of the SQUID voltage will be mainly at twice the modulation frequency (i.e. it will be at $2f_m$) as shown in Fig. 6.2 (b). In the mixer, the voltage output is multiplied by the reference modulation signal producing a mixer output at f_m and $3f_m$. Integration of the mixer output gives zero (or constant) since an integrator is essentially a low pass filter. On the other hand, if Φ_a is changed by $\Delta\Phi$ ($\Delta\Phi \ll \Phi_0$), then the voltage across the SQUID is as shown in Fig.6.2(d).

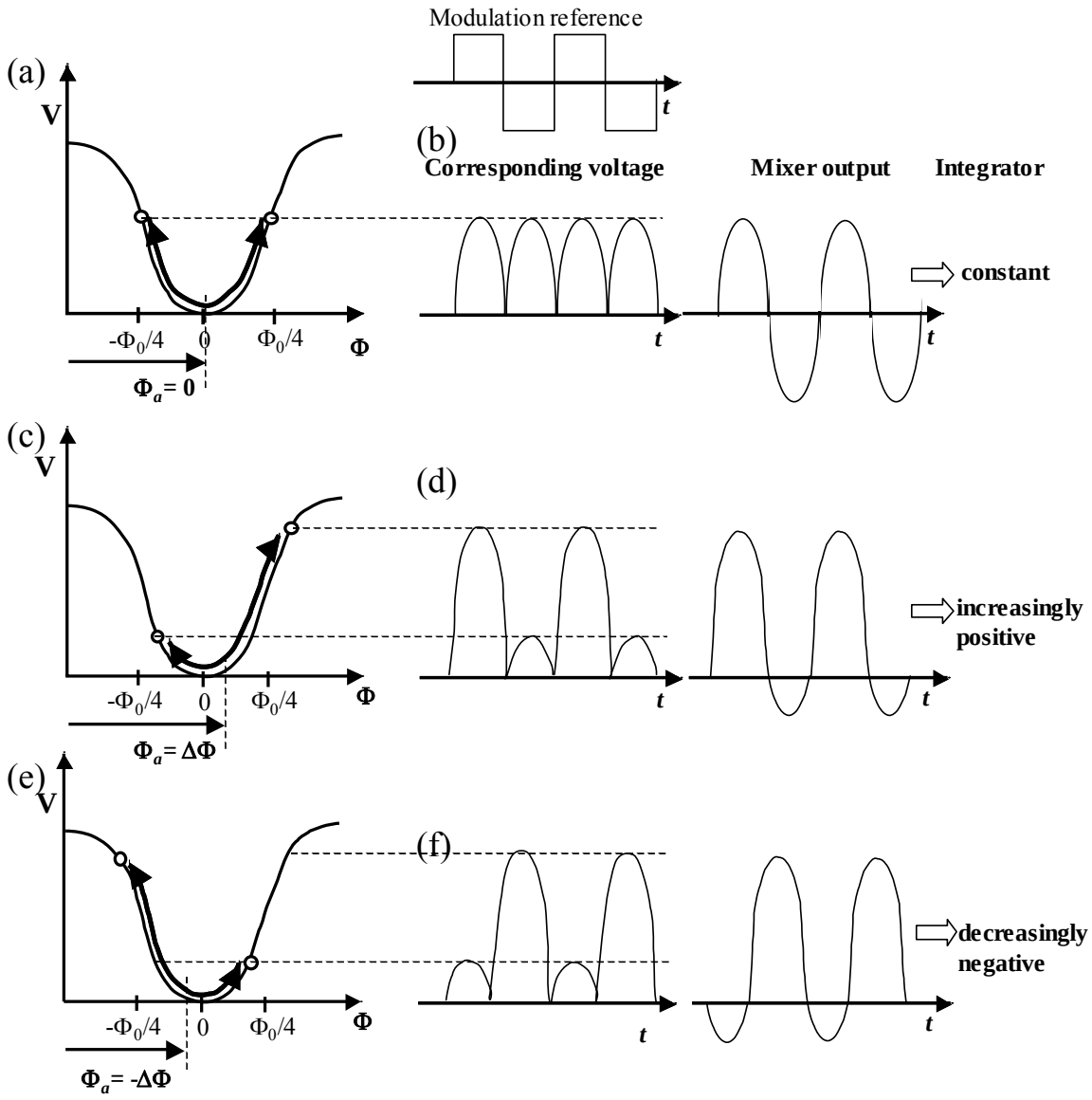

Figure 6.2: Operation of the flux-locked loop (FLL). The V(Φ) and V(t) for (a)-(b) zero mixer output, (c)-(d) positive mixer output, and (e)-(f) negative output.

In this case there is a component at frequency f_m, so that the mixer will generate an output at dc, and this will be integrated to produce a steadily increasing signal. Similarly,

if Φ_a is changed to -$\Delta\Phi$($\Delta\Phi \ll \Phi_0$), then the integrated mixer output is negative and steadily decreasing. Therefore, for a small change in flux $\Delta\Phi$, feeding back the negative of the output from the mixer will tend to oppose the original applied flux change (negative feedback).

Figure 6.3 shows a block diagram of the "Berkeley-box" FLL feedback electronics that we used for many years in the single channel system. In this system, the integrated mixer output is used to drive feedback current I_f in the feedback coil. This current generates a feedback correction flux $M_f I_f$ in the SQUID, where the M_f is the mutual inductance between the feedback coil and the SQUID loop. This feedback flux acts to null out the flux change $\Delta\Phi$, so that the integrator output stops increasing. When the magnetic flux in the dc SQUID is cancelled out by the feedback flux, then we say the SQUID is "Locked". If the FFL feedback electronics is locked, then, up to a sign, we can set

$$\Phi_a = M_f I_f \tag{6.1}$$

The voltage output (V_{out}) from the integrator is given by,

$$V_{out} = I_f R_f = \left(\frac{R_f}{M_f} \right) \Phi_a \tag{6.2}$$

where the "calibration" or transfer function is defined as M_f/R_f. From Eq. (6.2), it is obvious that the voltage output from the FLL is proportional to the applied flux. I note that the feedback coil is used for applying both the modulation current at frequency f_m and the feedback correction current I_f. Also, because the SQUID characteristic is periodic, in general we can lock at different values of total flux. Thus in general

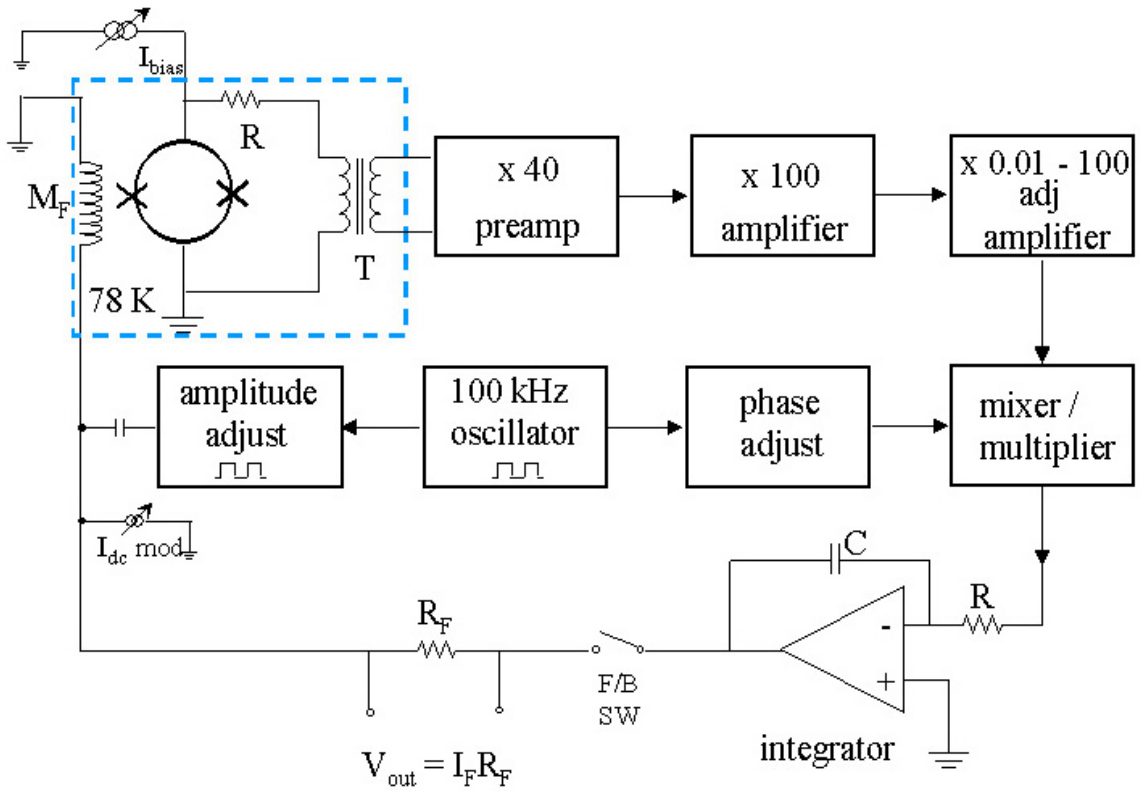

Figure 6.3: Schematic of the flux locked loop circuit for the Berkeley-box (reproduced from reference [1]).

$$V_{out} = \frac{R_f}{M_f}\left(\Phi_a - n\Phi_0\right) + V_{offset} \tag{6.3}$$

where n is an integer and V_{offset} takes into account that there can be an offset voltage from the buffer amplifier and other effects.

For the multi-channel SQUID system, I used an 8-channel 256 kHz commercial SQUID electronics set from Star Cryoelectronics [2]. Previous versions of the SQUID electronics were made by the Physics Department Electronics Development Group [3], based on the circuit design by J. Clarke's group at U. C. Berkeley (the "Berkeley box"). The Berkeley box is easy to modify and control but bulky, and expensive for a multi-channel system. Compared to the Berkeley box, the commercial version is small (wallet sized), and it is easy to run using a software-controlled interface. I optimized the SQUID electronics as described below. The details of this box are somewhat different than the Berkeley box, but the overall principles are the same.

The modulation frequency of the commercial SQUID electronics is 256 kHz. For tuning, I send a low frequency test signal to the modulation coil to sweep out V(Φ). Figure 6.4 shows the front panel of the software for the SQUID electronics with my typical tuning parameters [4]. First I have to optimize the test signal amplitude, feedback resistance, and integrator's capacitance of each SQUID in TUNE mode. Depending on the mutual inductance between the SQUID loop and the feedback coil, the test input and test signal amplitude are changed. The calculated mutual inductance between the SQUID and its modulation coil is approximately 2 pH (see Chapter 3). This

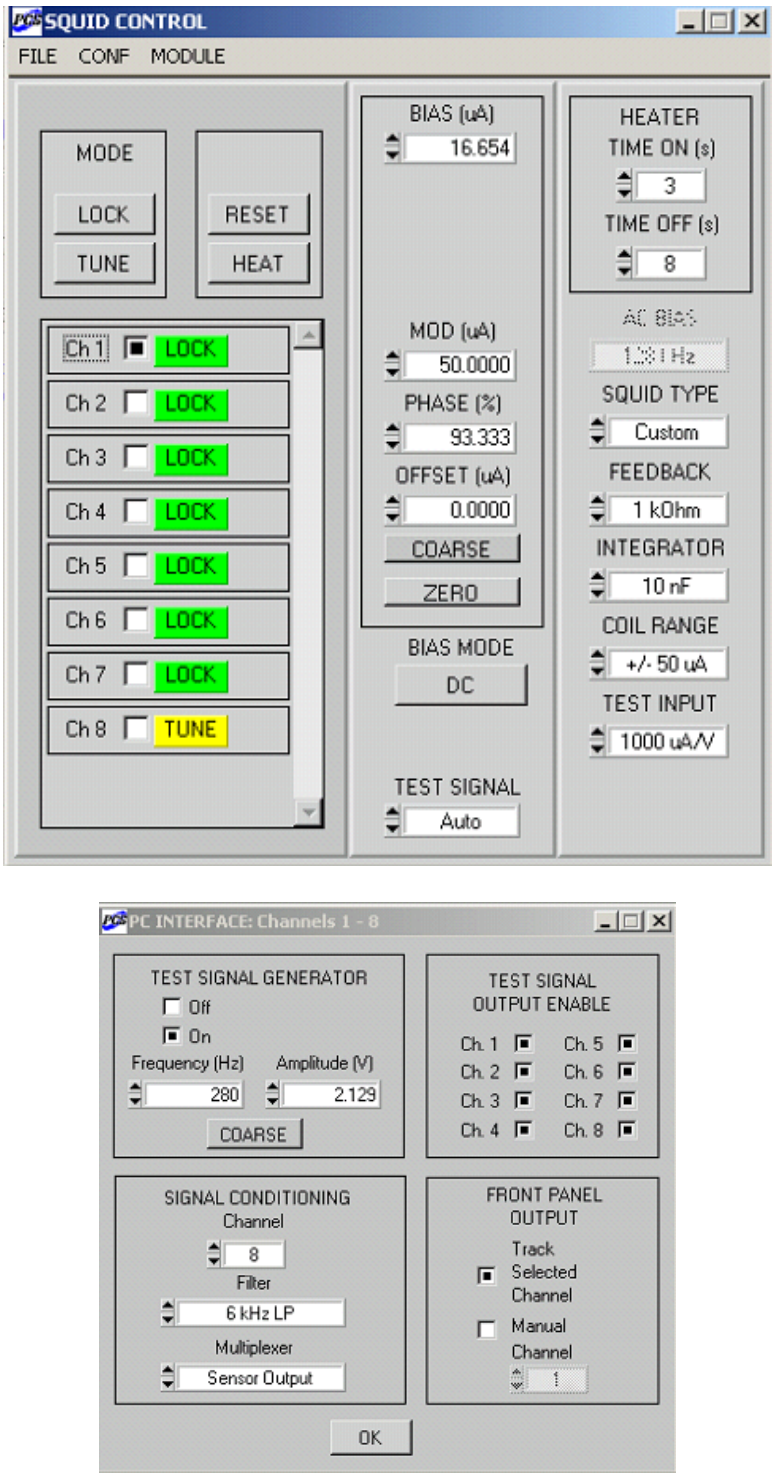

Figure 6.4: Software control panel for the Star Cryoelectronics 8-channel SQUID electronics.

corresponds to a modulation coupling of about $1\,\mathrm{m}A/\Phi_0$. The manual recommends a test input for my coupling of 1000 μA/V [4]. The amplitude of the test signal can be calculated by,

$$\text{Test Signal}[V] = \frac{(1[\Phi_0])(\text{Modulation coupling}[\mu A/\Phi_0])}{(\text{Test input}[\mu A/V])} = 1V\,. \qquad (6.4)$$

Thus about 1V is enough to sweep 1 flux quantum.

To optimize the feedback resistance and the integrator's capacitance, there are a few options that can be selected using the software interface: R_f = 1 kΩ, 10 kΩ, 100 kΩ, or 1 MΩ for the resistor and C = 1 nF, 10 nF, or 100 nF for the capacitor. For my multi-channel SQUID system, a feedback resistance of 1 kΩ and an integrator capacitance of 10nF were chosen for each channel. Once I set the test input, the test signal amplitude and frequency, the feedback resistance, and the integrator's capacitance (these parameters are the same for all the SQUIDs), I optimized the critical current, the ac modulation amplitude, and the phase for each channel, by finding the maximum of the SQUID signal output.

6.2.2 **The transfer function M_f/R_f**

For each channel the voltage output from the SQUID electronics depends linearly on the applied flux. To obtain the applied flux from the voltage output, I have to measure the transfer function (M_f/R_f) for each SQUID. The key to find M_f/R_f is to note that what the SQUID electronics measures is not the absolute value of magnetic flux, but rather a relative value. Figure 6.5 shows the idea. The straight lines in Fig. 6.5 are the linearized voltage output from the flux-locked loop corresponding to flux being

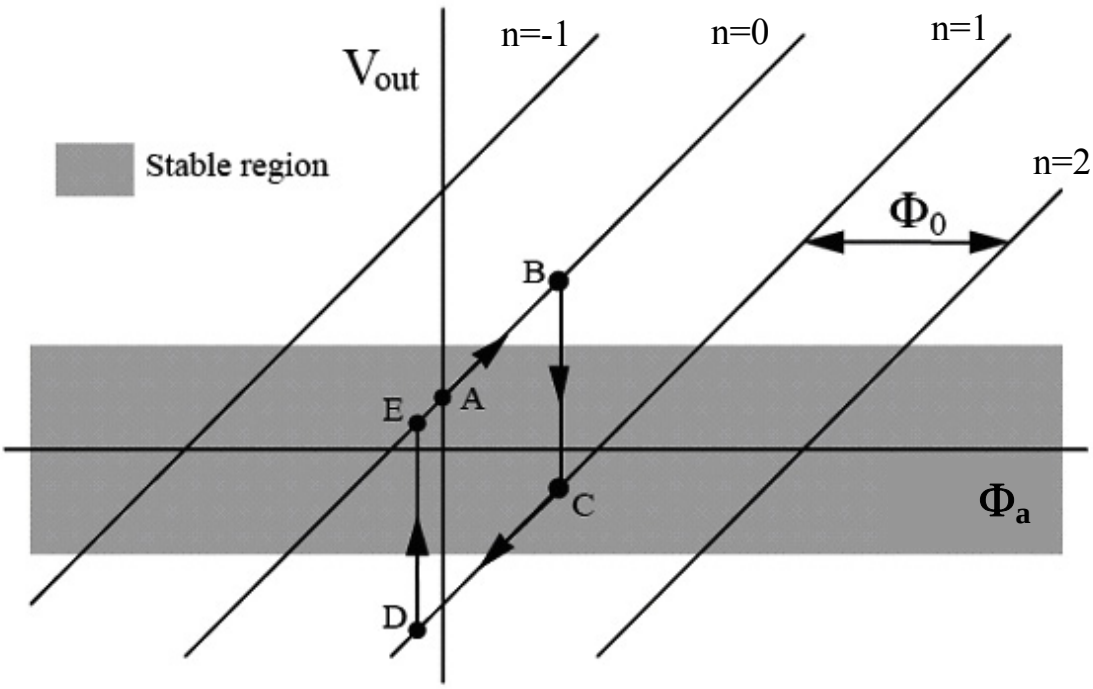

Figure 6.5: Voltage output vs. offset flux showing the transfer function (reproduced from reference [4])

fixed at different total flux $n\Phi_0$, where n is an integer. Therefore the flux difference between the lines is Φ_0, the voltage difference between lines is $(R_f/M_f)\Phi_0$, and one over the slope is M_f/R_f.

To measure the transfer function, I use the RESET and OFFSET buttons in LOCK mode. Pressing the RESET button temporarily opens the feedback loop and discharges the capacitor in the integrator. With the integrator discharged, once the reset button is released, the FLL electronics start tracking the applied signal starting with a voltage value as close to zero as possible. Suppose I start at A in Fig. 6.5. I can then reach point B by increasing the DC OFFSET in LOCK mode; this just applies external flux. At point B, I read the voltage output, press RESET, and then read the voltage output again. The voltage difference from before and after the RESET is just $(R_f/M_f)\cdot\Phi_0$ and dividing Φ_0 by this voltage reveals the transfer function M_f/R_f.

Table 6.1 lists the transfer functions I measured using this technique for the multi-channel SQUID system. The values for each channel lie in a narrow range between 1.072 Φ_0/V and 1.107 Φ_0/V. The small differences are probably due to slight difference in M_f in different channels.

6.2.3 **Dynamic range**

The voltage output from the integrator in the SQUID electronics is limited to ±10 V. Therefore, the maximum magnetic flux Φ_{max} that can be fed back (the dynamic range) is limited to,

$$\Phi_{max} = \frac{M_f V_{max}}{R_f + R_w} \tag{6.5}$$

Table 6.1: Transfer functions and mutual inductances for 7 working channels in the multi-channel SQUID system. $R_f = 1k\Omega$.

Channel	M_f/R_f(Φ_0/V)	B_a/V_{out}(T/V)	M_f(pH)
Ch1	1.087	1.605E-06	2.23
Ch2	1.072	1.584E-06	2.20
Ch3	1.091	1.611E-06	2.24
Ch4	1.107	1.634E-06	2.27
Ch5	1.101	1.626E-06	2.26
Ch6	1.072	1.584E-06	2.20
Ch7	1.084	1.601E-06	2.22
Average	1.088	1.606E-06	2.23

where M_f is the mutual inductance, R_f is the feedback resistance and R_w is the feedback wire resistance. The mutual inductance can be calculated from the transfer function as,

$$M_f = R_f \cdot \left[\frac{M_f}{R_f}\right] \cong 1000\Omega \cdot \left[1.1\Phi_0 / V\right] = 2.23\,pH \qquad (6.6)$$

as shown in Table 6.1. Since the feedback resistance is $R_f \gg R_w$, the dynamic range for my SQUID is

$$\Phi_{\max} \cong \frac{M_f V_{\max}}{R_f} = \frac{2.23[pH]10[V]}{1000[\Omega]} \cong 11\Phi_0 \qquad (6.7)$$

Therefore, the SQUID electronics cannot hold lock if more than 11 flux quanta are applied, which corresponds to a magnetic field of B ≅ 23.5 μT.

6.2.4 **Slew rate**

Another restriction of the SQUID FLL electronics is related to the frequency or bandwidth. If a large amount of magnetic flux is applied to the SQUID suddenly, the feedback electronics cannot follow the change, and the SQUID electronics can jump lock. The FLL electronics tries to keep the SQUID at a fixed total flux ($n\Phi_0$), but a sudden change in magnetic flux can cause it to jump to another value of the total flux ($n'\Phi_0$). The slew rate is the maximum rate at which the FLL electronics can track an applied flux without jumping lock.

In a FLL, the error flux Φ_e is the difference between the applied flux Φ_a and the feedback flux Φ_f,

$$\Phi_e = \Phi_a - \Phi_f . \qquad (6.8)$$

At the same time, the feedback flux is the product of the entire system gain G_0 (also called the open loop gain) and the error flux,

$$\Phi_f = G_0(\omega) \cdot \Phi_e . \tag{6.9}$$

If the error flux exceeds about $\Phi_0/4$, then the FLL can jump lock. Therefore, the maximum allowable error flux is about $\Phi_0/4$. The maximum feedback flux is thus $\Phi_f^{max} = G_0(\omega) \cdot \Phi_0/4$. Then, the slew rate $\omega \cdot \Phi_f^{max}$ is given by,

$$\frac{d\Phi_f^{max}}{dt} = \omega \cdot \Phi_f^{max} \cong \omega G(\omega) \cdot \frac{\Phi_0}{4} \tag{6.10}$$

For a 1-pole integrator, $G_0(\omega)$ is proportional to $1/\omega$, and the slew rate will be constant.

Figure 6.6(a) shows the maximum feedback flux versus sample frequency. Below 200Hz, I could not apply more current because of the limitations of the function generator used to apply flux. At 200 Hz, the feedback flux met the dynamic range limit (11 Φ_0). Even if I could apply more current below 200 Hz, I would still expect a constant feedback flux of 11 Φ_0. Above 10kHz, the maximum allowed feedback flux stops decreasing. Without a better understanding of the commercial SQUID electronics it is difficult to determine the reason for this. Figure 6.6(b) shows the slew rate versus frequency. As expected from Eq. 6.10, the slew rate is almost constant over the 200 Hz~10kHz range. At a typical frequency for the injected current (~1kHz), the slew rate is about 3000 Φ_0/s.

6.2.5 **Flux noise measurement**

I also used a spectrum analyzer to measure the flux noise of the SQUIDs in the LOCK mode of the SQUID electronics (see Fig. 6.7(a)). I note that the SQUIDs were

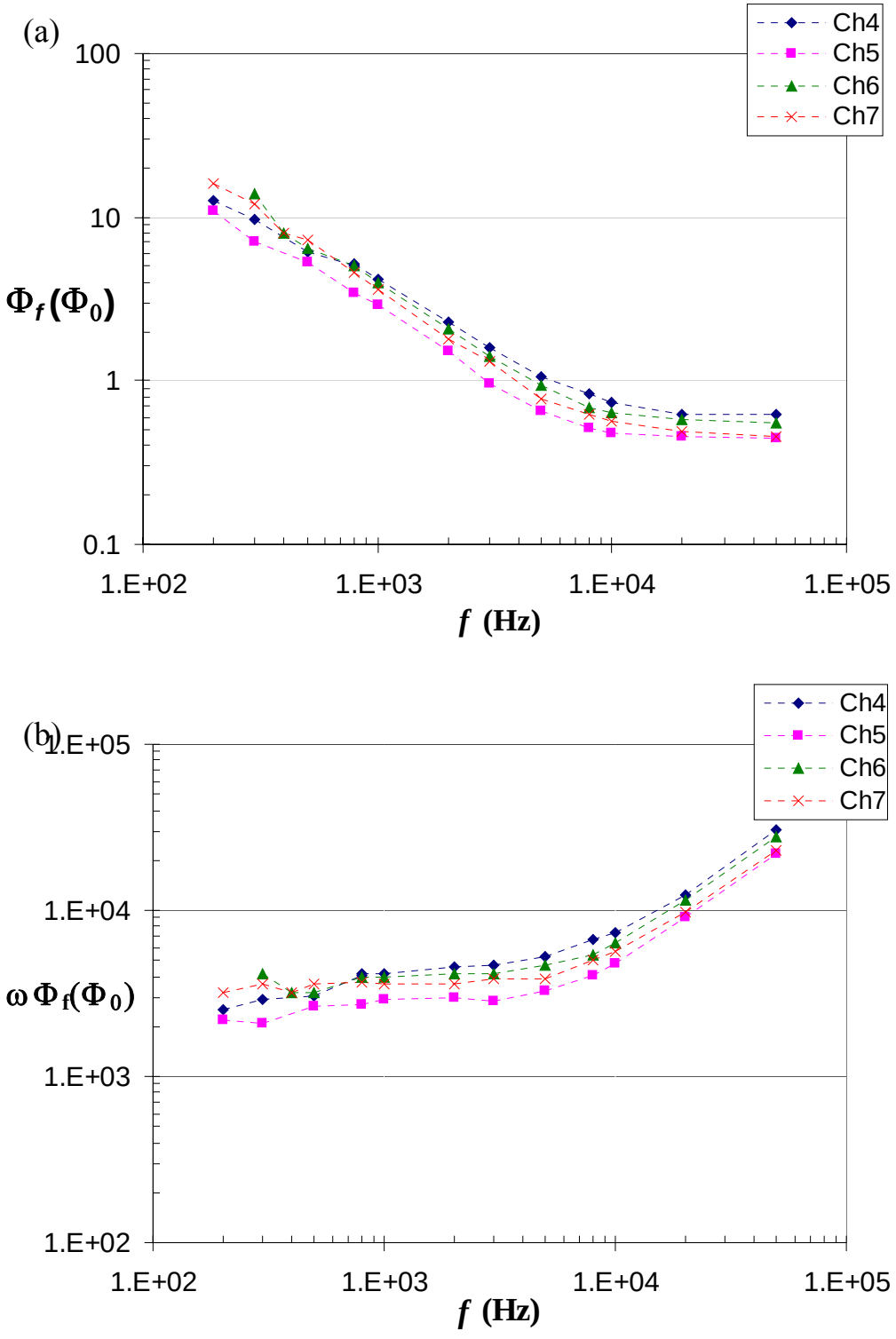

Figure 6.6: (a) Maximum feedback flux vs. frequency. (b) Slew rate vs. frequency.

(a)

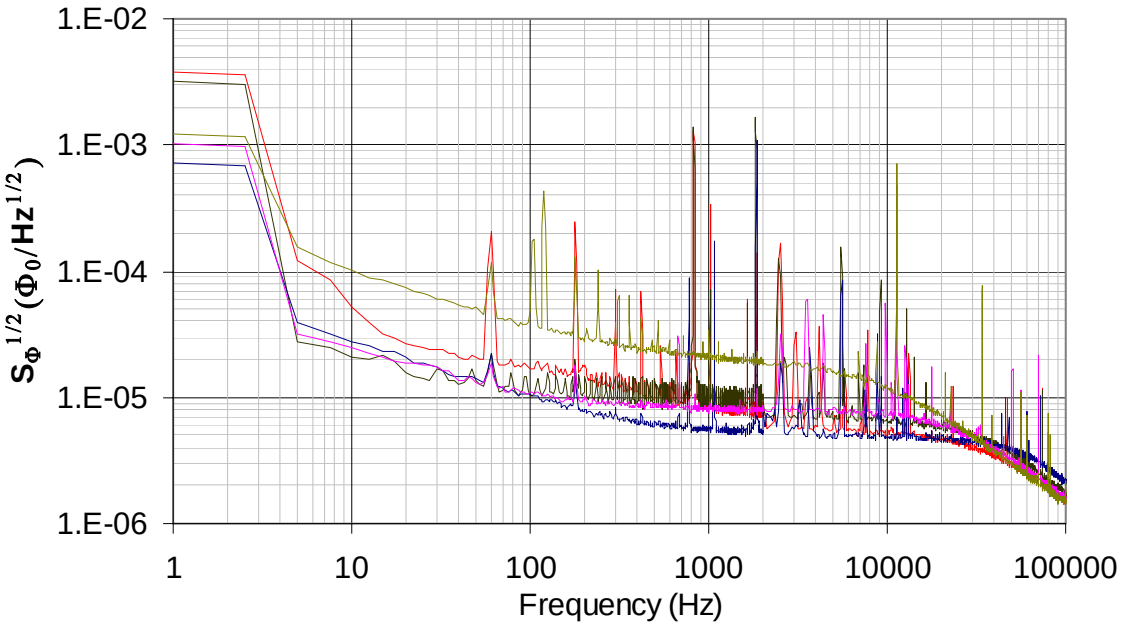

(b)

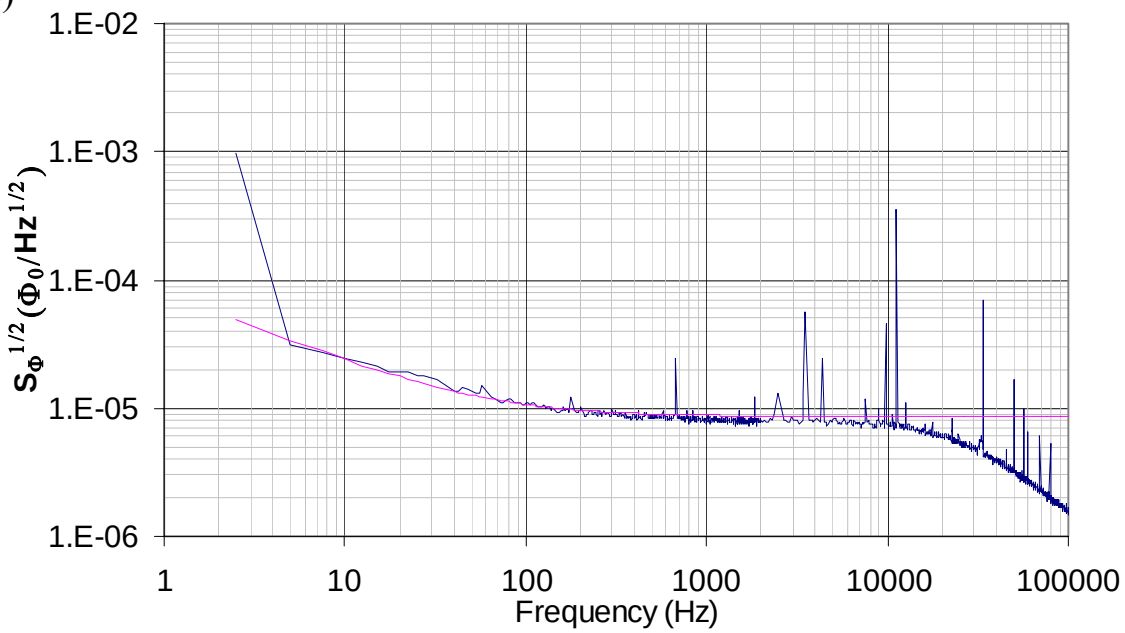

Figure 6.7 (a) Spectral density of the multi-channel SQUID. Channel 2,3,4,7,8 are orange, black, blue, pink, green, respectively. (b) Spectral density of the 7th SQUID and the result of the fit. Channel 7 is blue and the fit is pink.

not magnetically shielded for these measurements. The noise in each channel is somewhat different (note logarithmic scale). Below 500Hz, 1/f noise is clearly visible, while below 5 Hz, one sees drift. I note that the noise in the different SQUIDs at 10 Hz varies from 20 $\mu\Phi_0/\mathrm{Hz}^{1/2}$ to 100 $\mu\Phi_0/\mathrm{Hz}^{1/2}$. 1/f noise would be important if we want to measure dc fields from a sample, such as a biological specimen or corrosion sample. The pink curve in Fig. 6.7(b) shows the noise data for channel 7 with a fit to $\left(af^{-n}+b\right)^{1/2}$. I obtained for the fit parameters a = 6.3×10^{-9}, b = 7.4×10^{-11} Φ_0^2/Hz, and n = 1.1. As expected, n ~ 1 so the spectral density follows 1/f noise at low frequencies. I note that the Star cryoelectronics SQUID electronics can use current bias modulation to reduce 1/*f* noise in the SQUID [5], but I didn't use this option.

White noise is also clearly visible in the spectrum. From Fig. 6.7, we can see that the white noise varies from about 5 $\mu\Phi_0/\mathrm{Hz}^{1/2}$ to 20 $\mu\Phi_0/\mathrm{Hz}^{1/2}$. In particular, the noise in channel 8 is the largest at 20 $\mu\Phi_0/\mathrm{Hz}^{1/2}$. However, I note that the variation between individual noise measurements was quite large, sometimes as much as 10 $\mu\Phi_0/\mathrm{Hz}^{1/2}$ for the same channel. Considering the effective area of the SQUID of 17×50 $\mu\mathrm{m}^2$, the magnetic sensitivity of the SQUID for an average flux noise 10 $\mu\Phi_0/\mathrm{Hz}^{1/2}$ is 23.5 $\mathrm{pT/Hz}^{1/2}$. From Eq. (2.36), I can obtain a theoretical estimate for the flux noise for high-T_c SQUIDs. Using the parameters in Table 4.1, the estimated flux noise is 1.23 $\mu\Phi_0/\mathrm{Hz}^{1/2}$ and $V_\Phi=9.33\times10^{10}\mathrm{V}/\Phi_0$. This is 5 times smaller than the smallest flux noise I measured. However, unlike low-T_c SQUID, it is known that the flux noise level for high-T_c SQUIDs is not so accurately accounted for, and one typically see a larger flux noise than one would expect.

6.2.6 **Crosstalk**

In the multi-channel design, one important concern was to prevent crosstalk between channels. I calculated the mutual inductance between a SQUID and its neighboring modulation line in Chapter 3. In section 6.2.2, I obtained the mutual inductance between a SQUID and its modulation line by measuring the transfer function. In this section I describe how I measured the mutual inductance between a SQUID and the modulation line of its neighboring SQUIDs.

Let's assume there are only 2 SQUIDs. When current is applied to the modulation lines of both SQUIDs, the total flux at the first SQUID will be,

$$\Phi_1 = I_{1f}\mathrm{M}_{11} + I_{2f}\mathrm{M}_{12} + \Phi_{1a}\,, \tag{6.11}$$

where I_{1f} and I_{2f} are the feedback currents for the 1st and 2nd SQUIDs, respectively, M_{11} is the mutual inductance between the 1st SQUID and its modulation line, M_{12} is the mutual inductance between the 1st SQUID and the neighboring modulation line, and Φ_{1a} is the flux applied by any other source. If the SQUID is held at fixed flux in a flux-locked loop, then Φ_1 will be kept constant. For simplicity we will assume that this constant is zero and also that $\Phi_{1a} = 0$. Thus the voltage output of the 1st SQUID will be

$$V_{1out} = R_{1f} I_{1f} = -\frac{\mathrm{M}_{12}}{\mathrm{M}_{11}} R_{1f} I_{2f}\,. \tag{6.12}$$

To find M_{12}/M_{11}, I turned on only two SQUIDs at a time and measured the mutual inductance between a SQUID and its neighboring modulation line. In the remaining SQUIDs and modulation lines, no current is applied. As shown in Fig. 6.8, I locked the 1st SQUID in feedback, and set the 2nd SQUID in TUNE mode to apply a dc offset to the modulation line. I then increased or decreased the dc offset in the

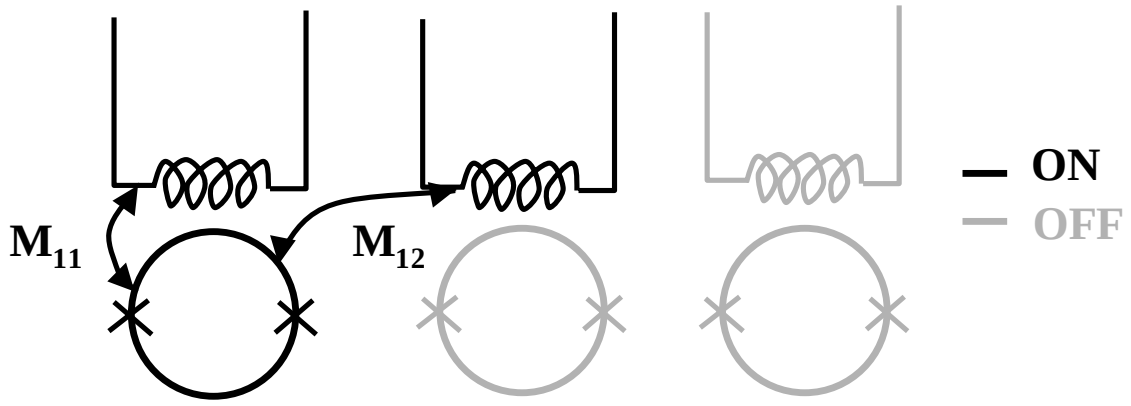

Figure 6.8 Schematic of multi-channel SQUIDs showing the mutual inductance M_{11} between the 1st SQUID and its modulation line and M_{12} between the 1st SQUID and a neighboring modulation line.

modulation line of the 2nd SQUID, and measured the voltage output of the 1st SQUID. Since the parameters M_{11} and R_{1f} are known to be 2.23 *p*H and 1kΩ, respectively, (see sections 6.2.3 and 6.2.4), Eq. (6.12) can be used to find M_{11}.

Figure 6.9 shows a sample data set, for which I found $M_{12} = 0.253$ *p*H. Similarly I obtained $M_{21} = 0.256$ *p*H by setting the 1st SQUID to TUNE mode and the 2nd SQUID to LOCK mode and applying a dc offset (see section 6.5.3 for other channels). As expected, these values of M_{12} and M_{21} are very similar because the shapes of SQUID and modulation line are almost identical. The relative ratio of coupling M_{12}/M_{11} is 11%. I note that this ratio is higher than the ratio of 6 % that I calculated in Ch.3.

6.3 New *xy* translation stage

The old (original) stage for the single SQUID microscope consisted of two stepper motors, motor controllers [6], aluminum drive shaft, and an aluminum *x*-*y*-*z* stage. To prevent magnetic flux noise from the motor, the motor was located 40 cm away from the stage with the connection between the two being made by means of rotating aluminum drive shafts. The stage position was determined by reading an analog voltage, produced by a position counter that summed the pulses from the motor controller. An A/D converter in the PC, then read the voltage to infer the position. However, the software synchronized the motor controller only at the beginning of a scan. Therefore, moving the stage and taking data were independently controlled.

After many years of use, the stage developed some problems. After scanning the *x*-direction it did not always return to exactly the same starting position because the

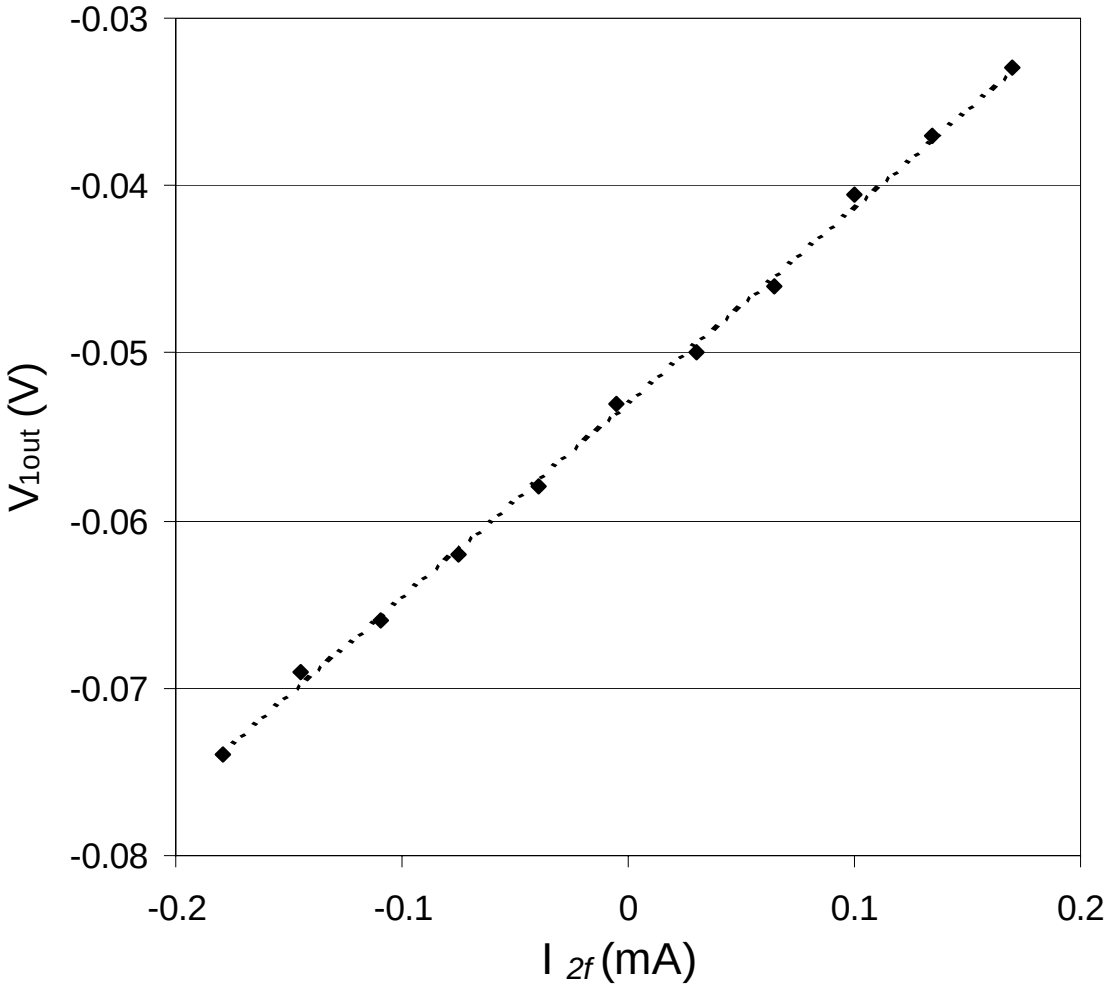

Figure 6.9 Graph of voltage output from the FLL of SQUID1 found by varying the dc offset current in the modulation line of SQUID2. The slope times M_{11}/R_f gives the mutual inductance M_{12} between the 1st SQUID and its neighboring modulation line.

position counter would pick up stray voltage pulses. Another problem was that the motor could no longer move faster than about 0.5 mm/sec (lubrication did not help). In addition, the motor controller did not have a position encoder or allow position feedback to the stage. In practice, we assumed the scanning speed was constant and took data with a constant sampling rate, but in fact the speed was not constant. The variation in scanning speed affects the resulting image because it creates errors in the reported position. Using a motor controller with a position encoder can solve this problem by synchronizing the stage and software at every data point, and ensuring the data collection is triggered by position (rather than by time). For these reasons we decide to change the stage, motor controller, and control software.

The new stage assembly consists of a Newport TSP 150 stage with a ESP 6000 UNIdrive 6000 motion controller [7]. We selected this stage because Neocera had experience with this type of stage and knew that they tended to have low magnetic noise and good scanning capabilities. Figure 6.10 shows the multi-channel SQUID system with the new stage. This scan stage has a total range of 15 cm and the manufacturer's quoted precision of the stage and motor controller is 0.1 μm. A PID (proportional-integral-derivative) feedback loop controls the position of the stage during scanning. When I first got the stage, I tried using the manufacturer's default PID parameters. However, I soon found that the speed of the stage was not constant. As Fig. 6.11(a) shows, the error between the desired speed and the actual speed was almost 40 %.

To solve this problem, I changed the PID gain factors. A schematic of the PID servo loop is shown in Fig. 6.12. The feedback signal F that is used to correct errors in the position is given by,

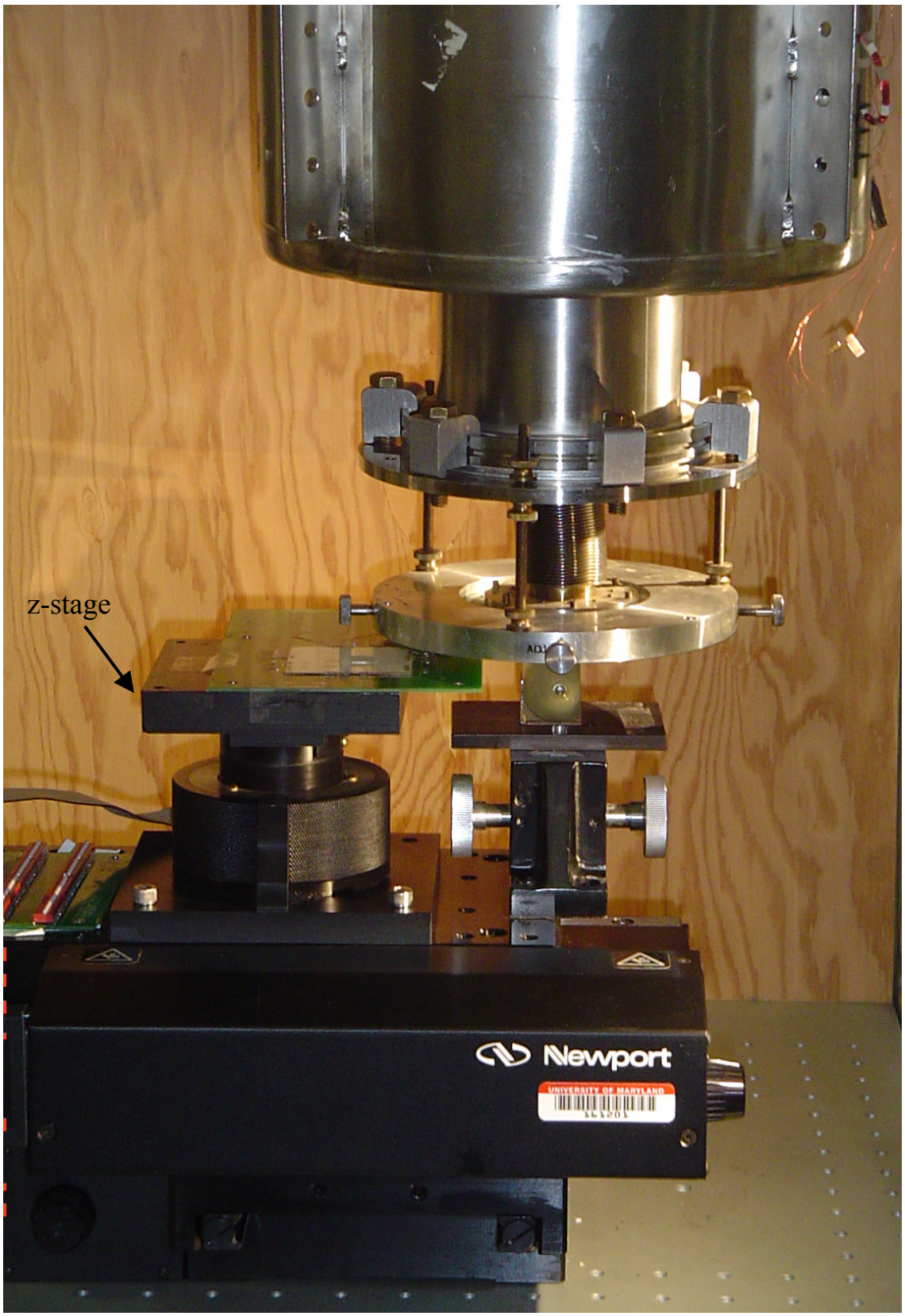

Figure 6.10: Photograph of multi-channel SQUID system with the new stage.

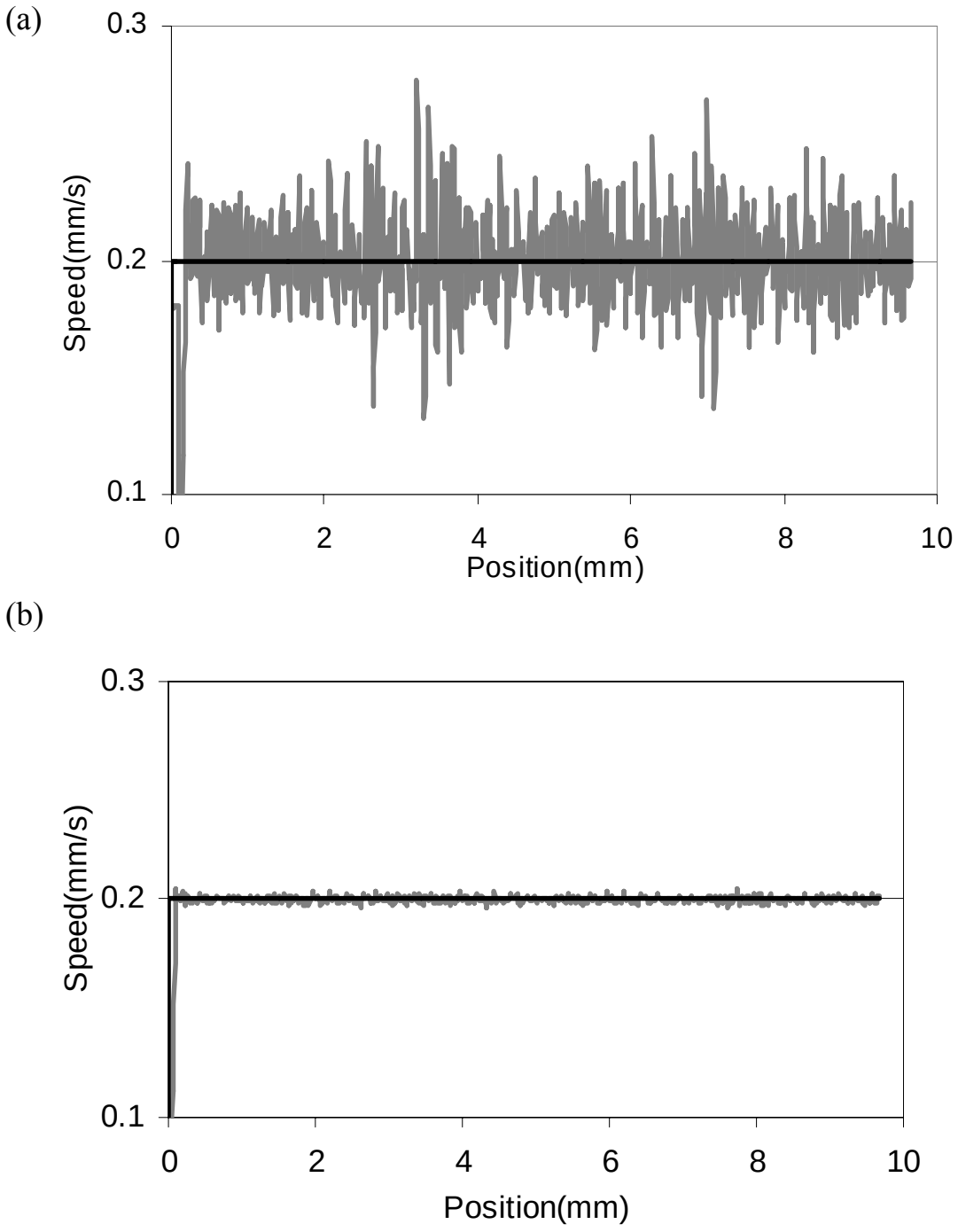

Figure 6.11 Speed performance of new stage using (a) default PID parameters and (b) optimized PID parameters (gray line). In both cases the programmed speed was 0.2 mm/s (black line).

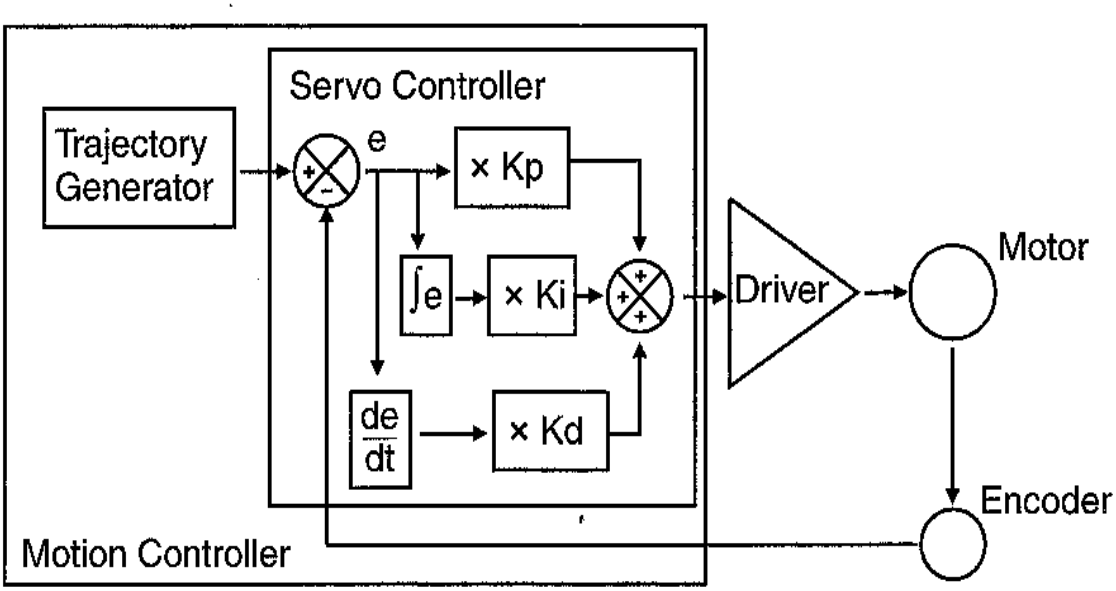

Figure 6.12 Schematic of PID Servo controller (reproduced from reference [8]).

$$F = K_p \cdot e + K_I \cdot \int e dt + K_d \cdot \frac{de}{dt}, \qquad (6.13)$$

where K_p is the proportional gain factor, K_I is the integral gain factor, K_d is the derivative gain factor, and e is the instantaneous following position error.

The first term in Eq. (6.13) (the proportional controller) amplifies the error between the desired setpoint and feedback output and drives the system actuator to bring the output to the setpoint. But the proportional controller cannot reduce steady-state errors. The next term (the integral controller) integrates the error over time and hence will correct any constant offset. However, the integral controller can cause large overshoots if the error is too large and fast. This is taken cared of by the last term, the derivative controller.

To tune the PID gain factors, I used a trial and error method. I started from the default values K_p = 15, K_I = 40, and K_d = 60 and varied them until reaching optimal PID values of K_p = 100, K_I = 300, and K_d = 250. Figure 6.11(b) shows the desired speed and the actual speed after the optimization. I note that the optimized values produced a dramatic improvement compared with the default values (compare Fig. 6.11(a) with Fig. 6.11(b)).

6.4 Data Acquisition program

6.4.1 Software for controlling the multi-channel system and collecting data

Generating a SQUID microscope image typically involves collecting high resolution magnetic values at ~10^5 accurately located positions. This process has been done automatically since the first version of the SQUID microscope when R. Black wrote a scanning program using Visual Basic v. 3 [9]. This program (called

"Runtime401") was well made and was used for more than 7 years with very little modification. A slightly modified version was also used for scanning microwave microscopy [10]. The program communicated with a motor controller board to control the stepper motors for the positioning and used a DAQ board to take data from the SQUID.

For the multi-channel SQUID system, I had to write new software. First, I needed to take data from several SQUIDs. I tried modifying the Runtime401 program, but it started to give errors because it overwrote an input buffer while previous data still occupied the buffer. Since the computer used the Win 3.1 operation system, it was hard to cure this memory problem. Second, I wanted the software to trigger on position, not on time. But the existing motor controller could not feed back to the stage and could only take data at constant time intervals (typically 30 ms). Triggering on time can cause accumulated position error (see Ch. 7 for detail) and I wanted to avoid this.

The new Newport motor controller and stage came with a LabVIEW package for controlling the scanning. Since LabVIEW is relatively user-friendly, I decided to use LabVIEW for writing the new scanning program [11]. The two most important concerns were that I needed to take data from several SQUIDs at the same time and I needed to trigger on position. I used a National Instruments DAQ 6052E data acquisition board for the 8-channel data acquisition [12]. The 6052E can scan multiple channels at a maximum rate of 333,000 samples/s [13]. I used the differential input modes for the 8-channel analog signals.

To trigger on position, the motor controller has a "pc" (position compare output triggering) command. This command makes the controller generate a TTL pulse every

time the stage advances by a set specified distance. I feed this pulse to the DAQ analogue trigger input, enabling the program to collect data at the specified position. The new scanning program, called "scanv11", functions well and does not generate errors.

6.4.2 Time trigger vs. position triggering

To show the difference between triggering on time and on position, I made several scans of a long wire carrying current. Each *x*-scan was taken at the same value of *y*. Figure 6.13(a) shows the difference between the averaged magnetic field from several scans and the individual scans at z = 1.5 mm with the "old" motor controller and "old" software. The difference in Fig. 6.13(a) is due to accumulated position error (see Ch.7 for details). The speed of the old motor was not perfectly constant, and data was taken every 30 ms (triggering in time), so the position error accumulates and causes the position of the peak magnetic field to shift left or right in each scan.

For the same conditions, I scanned the wire with the new stage and new software. As shown in Fig. 6.13(b), I was able to eliminate accumulated position error with the new system.

6.5 Demonstration of multi-channel system

Once the multi-channel SQUID microscope, data acquisition program, and new stage were ready, I began to test the complete system. Unfortunately, whenever I took apart and reassembled the system, I lost some wiring contacts. Also, I needed one lock-in for each SQUID. Since I only had 4 lock-ins, I used the first 4 out of 8 SQUIDs for

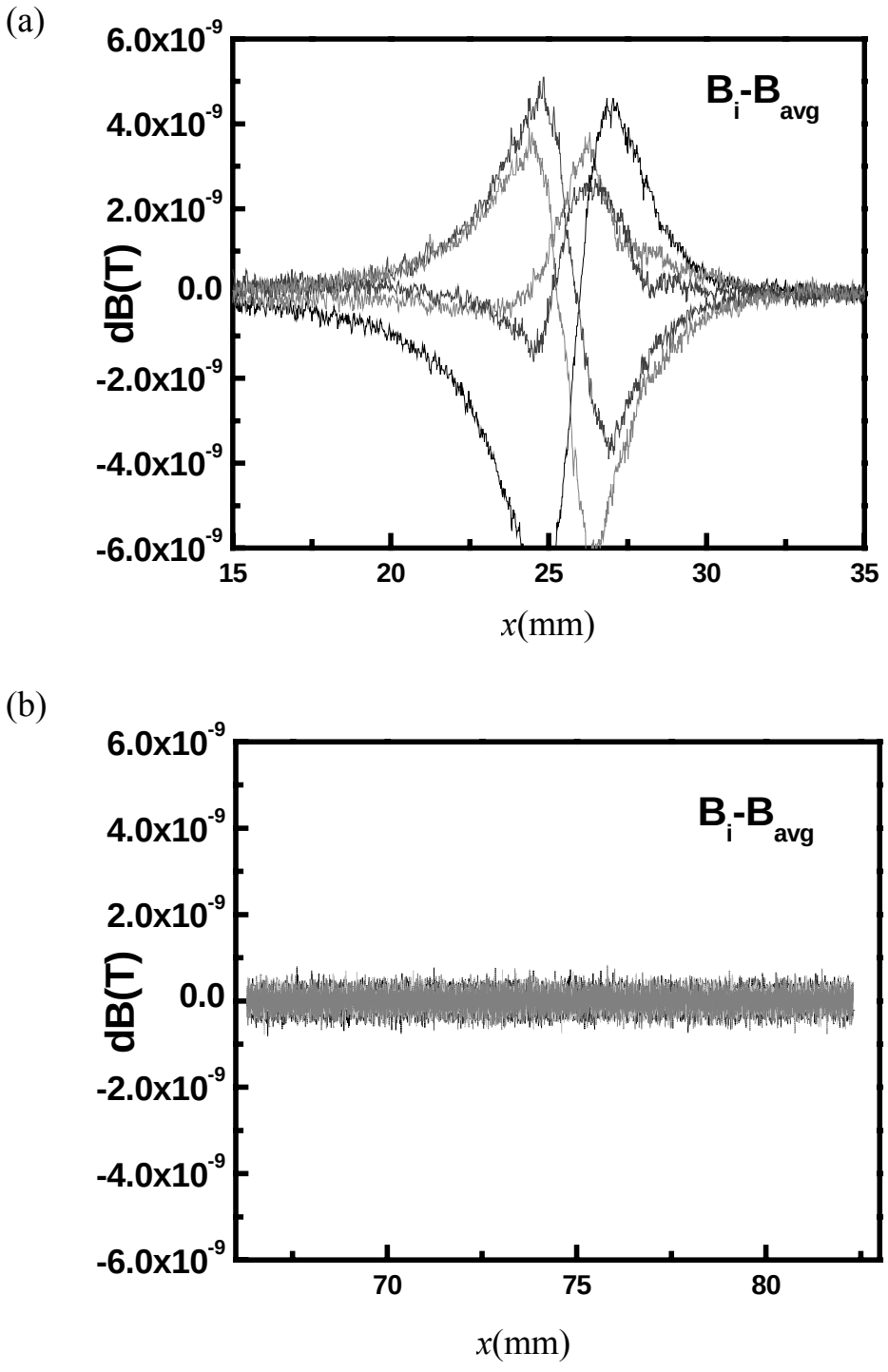

Figure 6.13 Difference between averaged magnetic field scan and individual magnetic field scans for a straight wire carrying current I ≈ 1 mA at z = 1.6 mm with (a) old software triggered on time and (b) new software triggered on position.

scanning. The test sample was a straight wire carrying an ac current. To construct an image I used 4 SQUIDs. However the array of SQUIDs is not aligned exactly with the *y*-scan direction (ϕ-calibration) and also not with the sample plane (height calibration). Therefore, I needed to calibrate the system, as explained in detail below.

6.5.1 **Height alignment**

When I use multiple SQUIDs to generate a single image, if the sample-to-sensor distances (z) of each channel is different, then the magnetic field image will be affected since $B_x \sim z/(x^2+z^2)$. When I attached the SQUID chip to the sapphire plate, the SQUID chip could be tilted which would make some SQUIDs closer than others. To solve this problem, I have to make the SQUID array parallel to the sample stage. Since the SQUID microscope body is hard to tilt, I corrected the height by adjusting the tilt of the z-stage and the *xy*-stage.

Figure 6.14 shows the left side of the multi-channel SQUID microscope and stage. θ_1 is the tilt angle between the SQUID array and the *xy*-stage scanning direction. θ_2 is the tilt angle between the SQUID array and the sample plane. To calibrate the height error, I scanned a straight wire with the 1st and 7th SQUID at different *y* positions with step size $\Delta y = 2$ mm. The angle θ_2 is obtained by,

$$\theta_2 = \tan^{-1}\left(\frac{z_{1ch7} - z_{1ch1}}{\Delta_{ch}}\right) \qquad (6.14)$$

where Δ_{ch} is the distance between channel 1 and channel 7, and z_{1ch1} and z_{1ch7} is the fitted result of sample-to-sensor distances at $y = y_1$ (channel 1 and channel 7, respectively). To get the fitted z, I fitted the measured magnetic field data to the

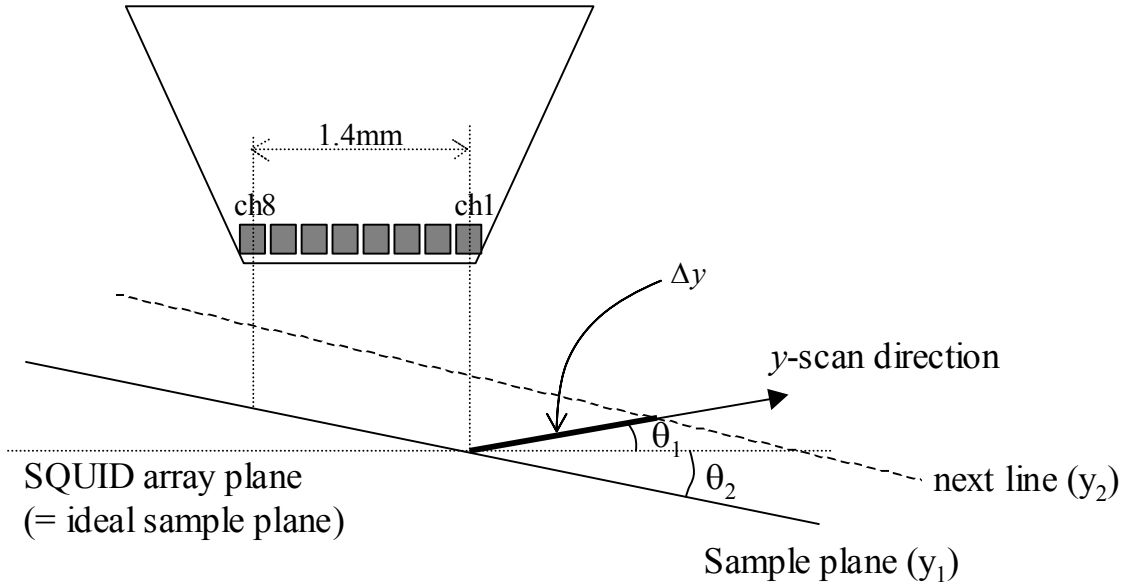

Figure 6.14 Side view of multi-channel SQUID microscope showing tilt of SQUID array, sample plane, and *xy*-stage.

theoretical magnetic field equation. The fit parameters were the sample current I, sample to sensor distance z, center position of wire x_c, *etc.,* including the SQUID area and contribution of any B_z component (see section 7.3 for details).

Using the θ_2 and fitted result at different y positions, I can obtain a relation between z at different y positions and θ_1,

$$z_{1ch1} - z_{2ch1} = \tan\theta_2 \left(\Delta y \cdot \cos\theta_1\right) + \Delta y \cdot \sin\theta_1 , \qquad (6.15)$$

where Δy is the y step size and z_{1ch1} and z_{2ch1} are the fitted distance between the 1st SQUID and the sample at $y = y_1$ and $y = y_2 = y_1+\Delta y$, respectively. I note that Eq. (6.15) is an implicit function of θ_1. To find θ_1, I plot Eq. (6.15) and find solutions graphically. I then adjust the *xy*-stage angle to compensate the tilt and check again. When (z_{1ch1} - z_{1ch4}) reaches a few micron difference, I make a fine adjustment of the z-stage by tightening or releasing the screws holding the z-stage to the *xy*-stage. Table 6.2 shows an example for z before and after the adjustment. With this techniques, I could reduce the angle differences by a factor of 10, as shown in Table 6.2.

6.5.2 ϕ-calibration

I reduced the height error between channels by adjusting the tilt of the stage. Another error factor is the angle between the y-scan direction and the SQUID array. Although I designed the SQUID array to be parallel to the y-scan direction, it was hard to align. After finding the SQUID chip tilt angles, I correct for it using a software method because it is hard to rotate the SQUID microscope body and *xy*-stage.

Figure 6.15 shows a front top view of the multi-channel SQUID microscope. ϕ_1 is the angle between the y-scan direction and the wire, ϕ_2 is the angle between the

Table 6.2 Sample-to-sensor distance z found by fitting the magnetic flux data from two SQUIDs for varying y position, before and after making z-adjustment. The angles are obtained from Eqs. (6.14) and (6.15).

	channel	$z(\mu m)$ at y_1	$z(\mu m)$ at $(y_1+\Delta y)$	$z(\mu m)$ at $(y_1+2\Delta y)$	Angles and counter plan
Before adjustment	Ch1	417.7	418.9	420.2	$\theta_1 = -0.074°$, $\theta_2 = 0.038°$; need to raise front of stage
	Ch7	416.9	418.1	419.3	
After adjustment	Ch1	401.4	401.4	402.3	$\theta_1 = -0.006°$, $\theta_2 = -0.005°$
	Ch7	401.5	401.3	401.7	

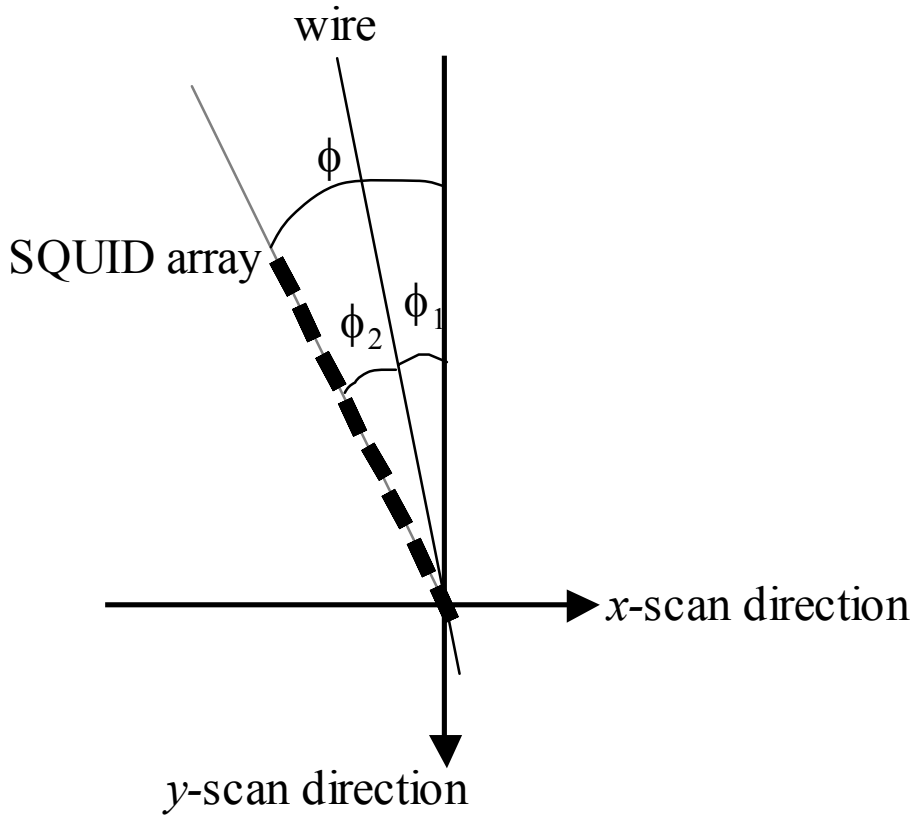

Figure 6.15: Top view of multi-channel SQUID system showing the angle between SQUID array, wire, and y-scan direction.

wire and the SQUID array, and ϕ is the angle between the SQUID array and the y-scan direction. I use the same dataset as described in section 6.5.1 (a scan of a straight wire), in order to obtain ϕ_1 and ϕ_2. To find ϕ_1 and ϕ_2, I find the x center position of the wire for two different y values. The angle ϕ_1 is given by,

$$\phi_1 = \tan^{-1}\left(\frac{x_{1ch1} - x_{2ch1}}{\Delta y}\right) \tag{6.16}$$

where Δy is the y-step size and x_{1ch1} and x_{2ch1} are the fitted results for the center position of the 1st SQUID at y_1 and y_2, respectively. Using ϕ_1 from Eq. (6.16), the angle ϕ_2 is obtained by,

$$\phi_2 = \sin^{-1}\left[\left(\frac{x_{1ch1} - x_{1ch7}}{\Delta_{ch}}\right)\cdot\cos\phi_1\right] \tag{6.17}$$

Adding ϕ_1 and ϕ_2, I found the angle $\phi = 7.98°$ between the SQUID array and the y-scan direction.

Figure 6.16 shows the scanning profile I used to generate a single image using four SQUIDs. To combine data from four SQUIDs, I have to choose specific scanning step sizes in x and y, given by:

$$\Delta y = \frac{\Delta_{ch}\cos\phi}{n}, \quad \Delta x = \frac{\Delta_{ch}\cos\phi}{m} \tag{6.18}$$

where n and m are integers. For Fig. 6.16, the integer n = 2, so the y-stage will move by "2·(# of SQUID –1)·Δy + Δy" after 2 lines of y-step.

As is also shown in Fig. 6.16, the tilt angle causes unused data at the ends of each scan. I cut out this data and rearrange the dataset using my LabVIEW program. Figure 6.17 shows the combined image after height alignment but without cutting the edge and Fig. 6.18 show the image after cutting. I note

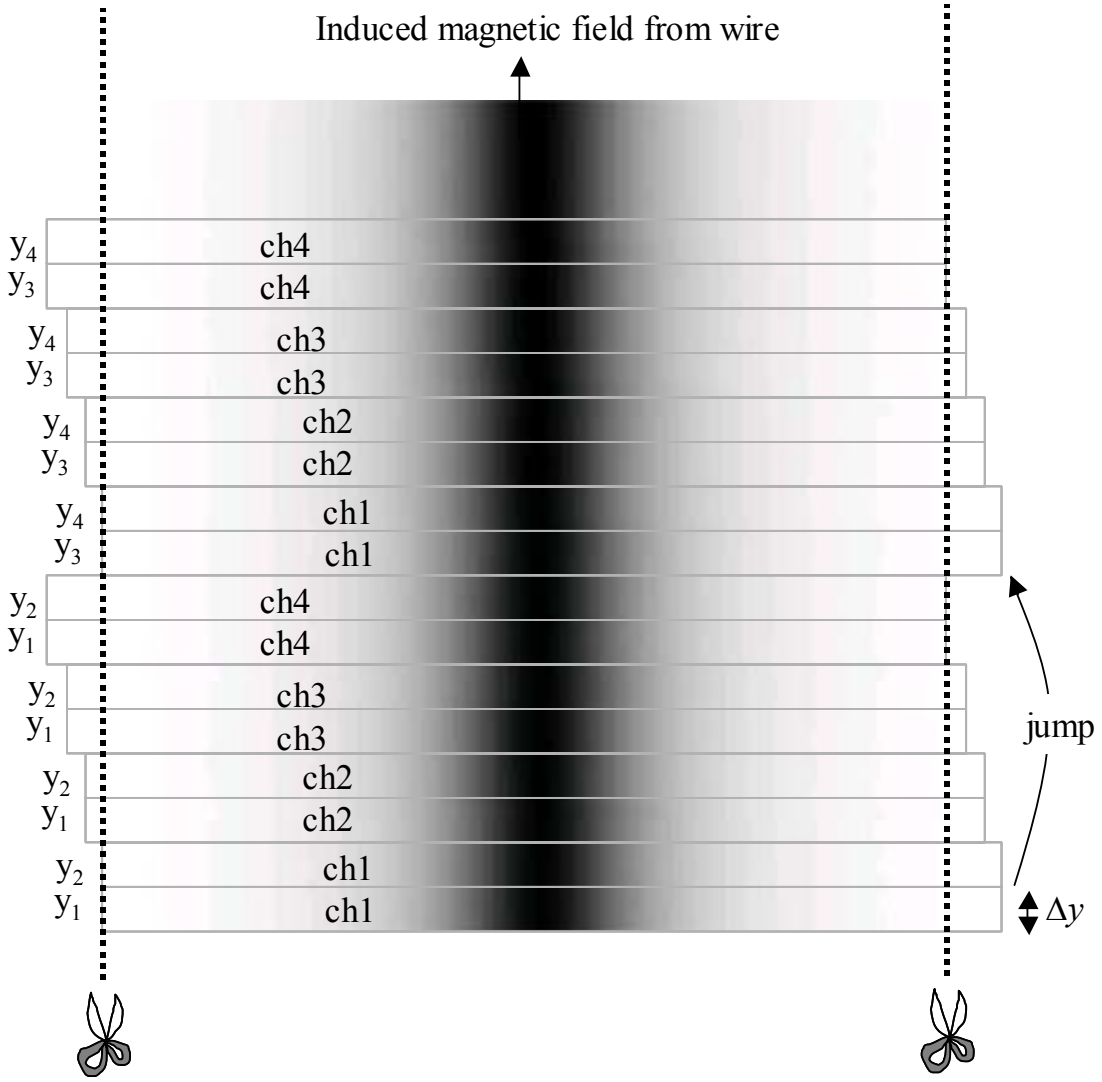

Figure 6.16: Scanning profile to generate single image with 4 SQUIDs. The dashed lines indicate where the data set should be cut.

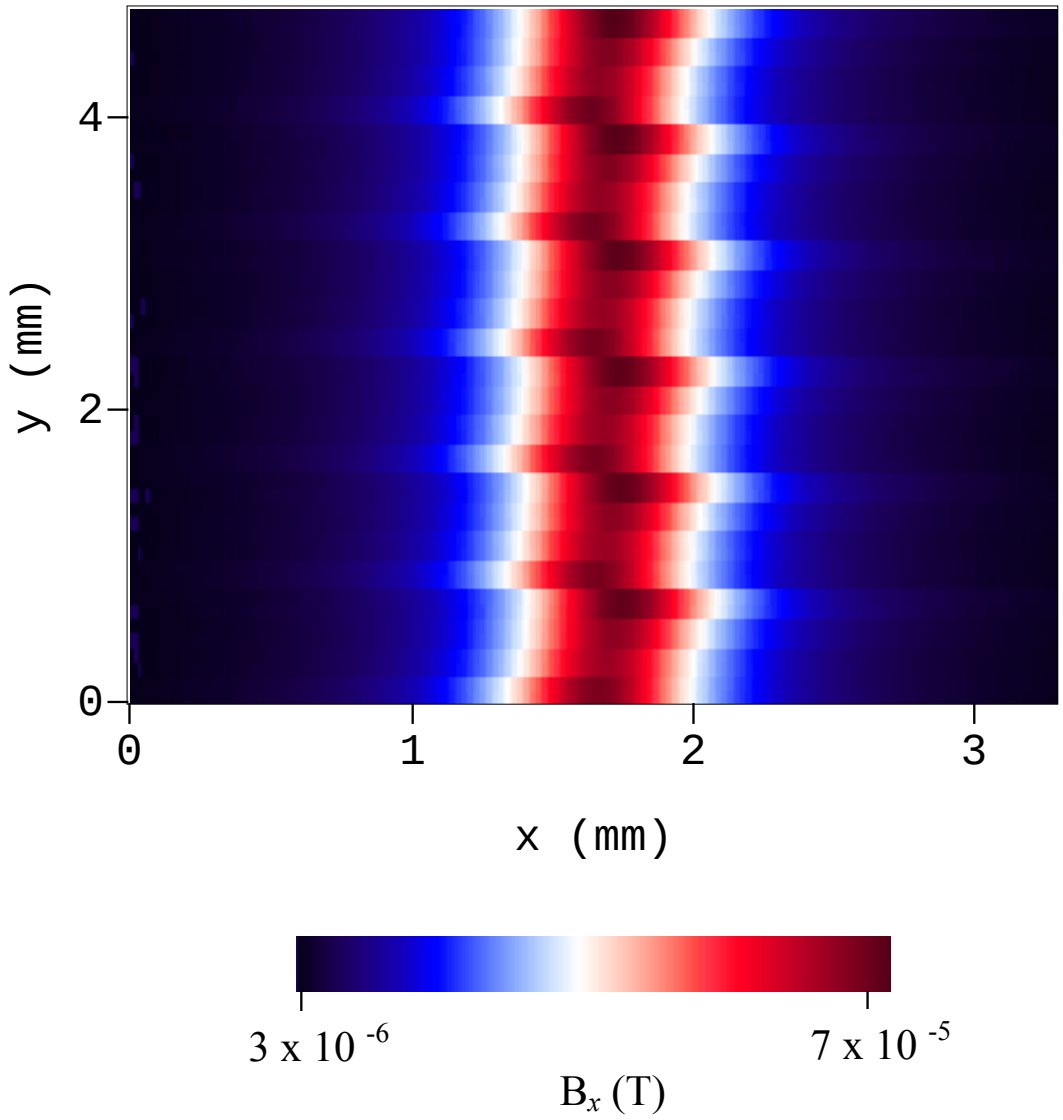

Figure 6.17: Combined magnetic image of straight wire carrying current I = 3.8 mA at z = 337 μm taken using four SQUIDs after height calibration (raw data: *m022807_0~3*, combined data: *m022807_no.hdf*).

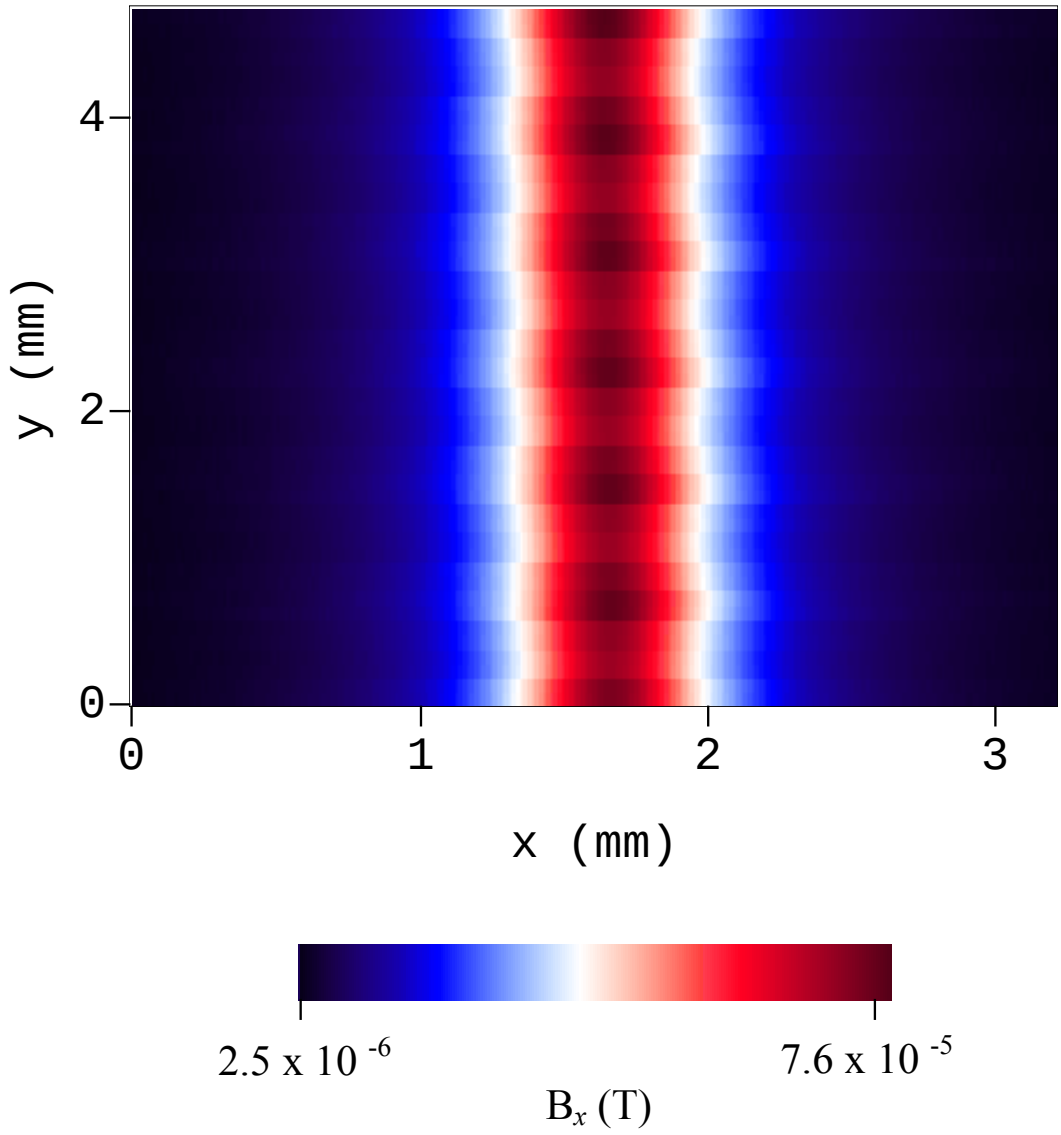

Figure 6.18: Combined magnetic image of straight wire carrying current I = 3.8 mA at z = 337 μm taken using four SQUIDs after height calibration and ϕ-calibration (raw data: *m022807_0~3*, combined data: *m022807_angle.hdf*).

that after the cutting the strongest signal in the image is aligned in the center, but the intensity of each channel is different. This is caused by crosstalk, as described in the next section.

6.5.3 **Crosstalk correction**

In Chapter 3.4 I described how I could calibrate the applied field and correct for crosstalk between the channels. Recalling Eq. (3.6), the applied flux is related to the output voltage by the mutual inductance between the SQUIDs and the modulation lines:

$$\begin{pmatrix} \Phi_{1a} \\ \Phi_{2a} \\ \Phi_{3a} \\ \Phi_{4a} \\ \cdots \end{pmatrix} = \frac{\overline{\overline{M}}}{R_f} \begin{pmatrix} V_{1out} \\ V_{2out} \\ V_{3out} \\ V_{4out} \\ \cdots \end{pmatrix}, \tag{6.19}$$

where $\overline{\overline{M}}$ is matrix of the mutual inductance between the SQUIDs and the different lines, and R_f is the feedback resistance assuming same for all channels. I found $\overline{\overline{M}}$ for channels 1 to 4 using the technique I described in section 6.2.6. I found:

$$\overline{\overline{M}} = \begin{pmatrix} 2.31 & 0.23 & 0.077 & 0.03 \\ 0.23 & 2.23 & 0.23 & 0.07 \\ 0.07 & 0.23 & 2.22 & 0.23 \\ 0.03 & 0.07 & 0.23 & 2.32 \end{pmatrix}. \tag{6.20}$$

where all values are in units of pH.

As shown in Fig. 6.18, without considering crosstalk, the signals from channels 2 and 3 were weaker than that from channels 1 and 4 because the voltage outputs of channel 2 and 3 were coupled to nearby SQUIDs on both sides. After I multiply the

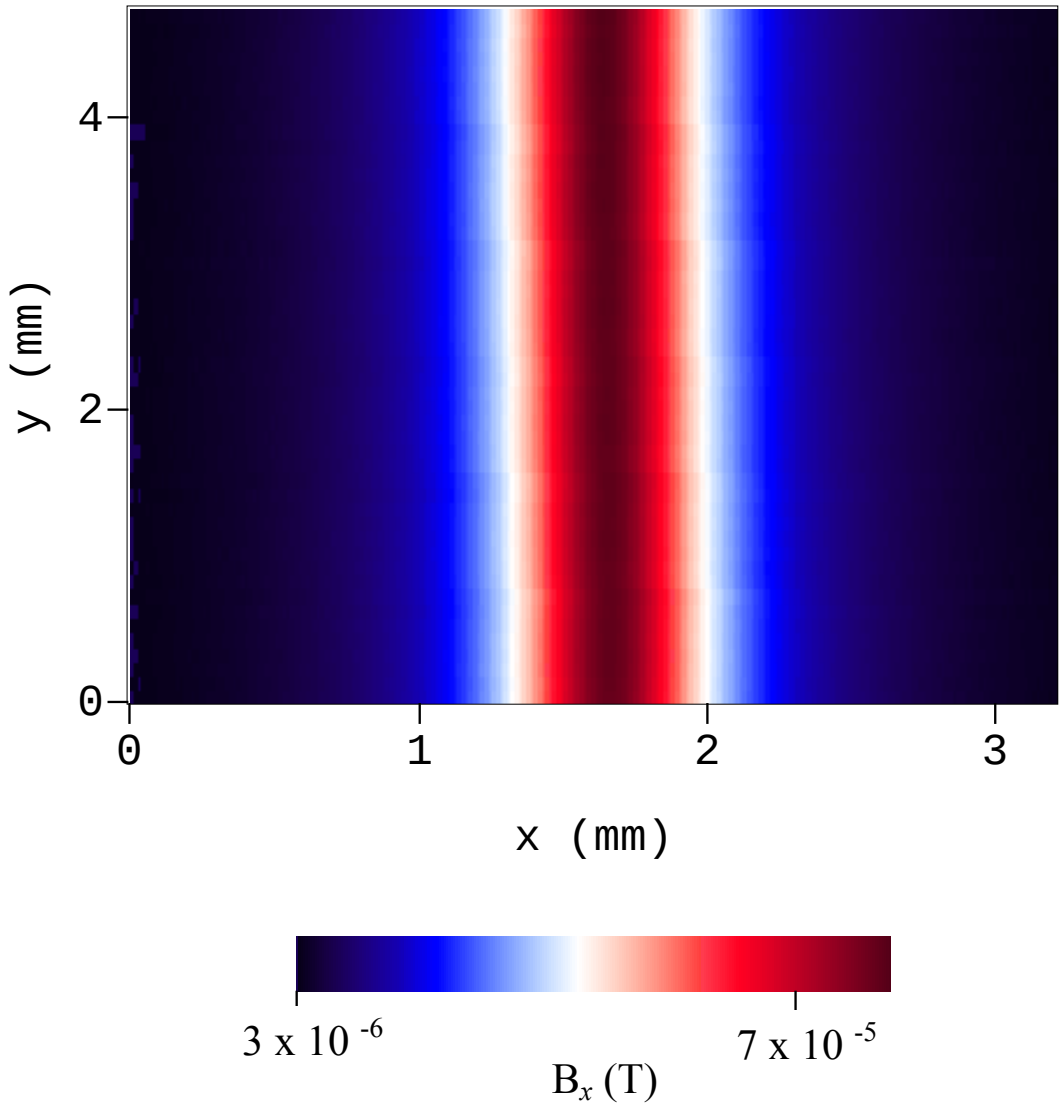

Figure 6.19: Combined magnetic image of straight wire carrying current I = 3.8 mA at z = 337 μm taken using four SQUIDs with height calibration, ϕ-calibration, and crosstalk correction applied (raw data: *m022807_0~3*, combined data: *m022807_angle_ct.hdf*).

output voltages by the mutual inductance matrix, the intensity difference between channels is reduced, as shown in Fig. 6.19. However, there is still a slight discontinuity visible. Since I couldn't make the distance between each SQUID and the sample plane exactly the same, I suspected that height variations were the cause.

6.5.4 **Another test scan**

To further test the multi-channel system, I made another test scan. The sample was a patterned mask with 2 μm line width (see Fig. 6.20). The patterned mask sample has 13 parallel lines carrying opposing currents. In this mask, the widths of parallel lines are 100, 50, 40, 35, 30, 25, 20, 15, 10, 8, 6, 5, and 4 μm from the left in Fig 6.20, respectively, and the distance between neighboring parallel lines is 1mm. I used two SQUIDs, channel 4 and channel 7, to generate a single image. The image in Fig. 6.21(a) was obtained by using one SQUID, and the image in Fig. 6.21(b) was obtained by using two SQUIDs. The two images are very similar, and it is hard to distinguish which one was made using two SQUIDs. One might think that because the image in Fig. 6.21 has a wider range than Fig. 6.19, any problem might be hidden. Figures 6.22(a) and (b) show the magnified images of the dotted box in Figs 6.21. The magnified images also look identical.

I note that the calibration of two SQUIDs is relatively easier than that of four SQUIDs. In addition the distance between the channels was 600 μm, therefore the crosstalk was much less. The elapsed time to scan the image for Fig 6.21(a) and Fig 6.21(b) were 174 minutes 34s and 86minutes 53s, respectively. Thus I could save approximately 88 minutes by using 2 SQUIDs.

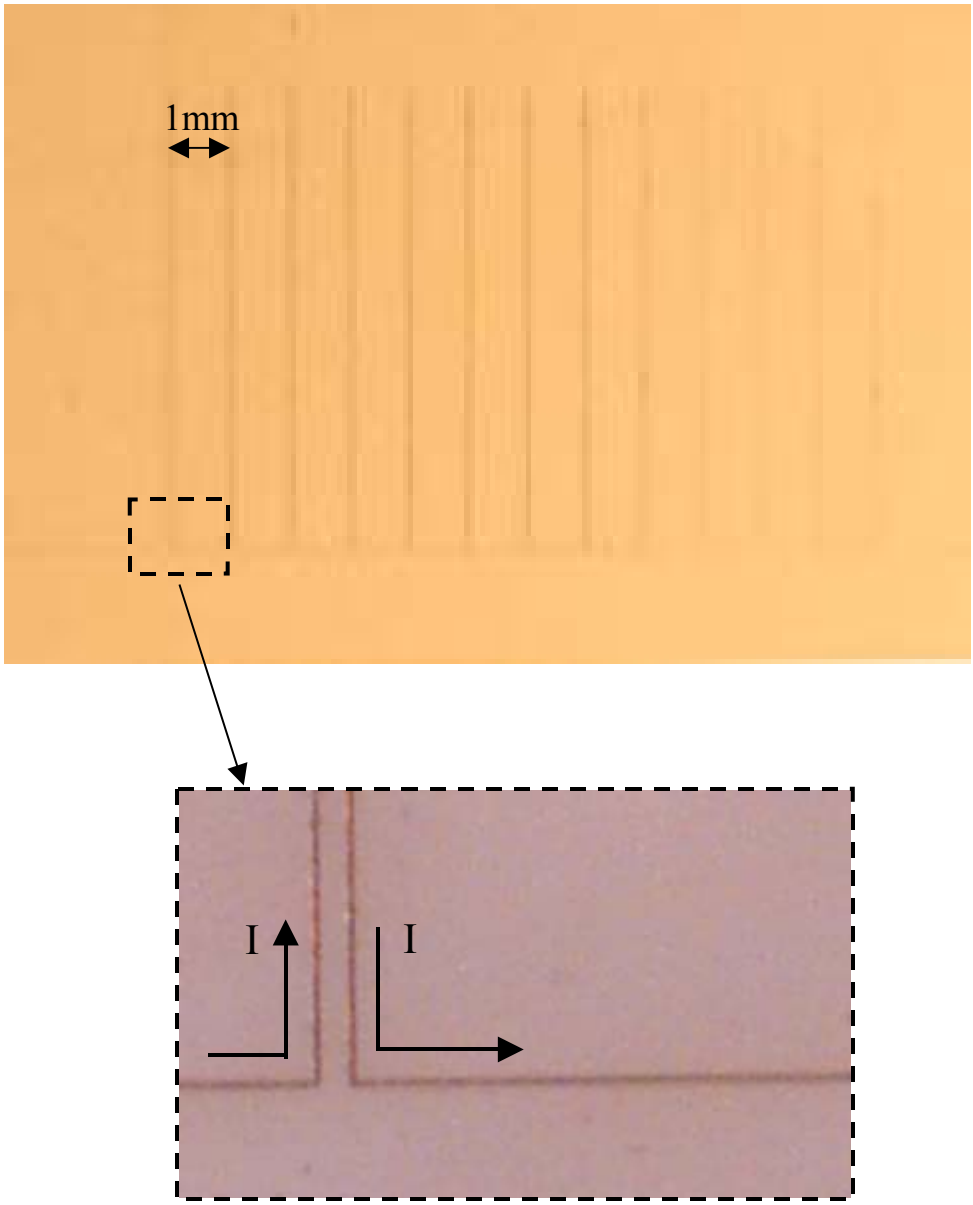

Figure 6.20: Photograph of patterned mask sample with 13 parallel lines carrying opposing currents. The line width is 2 μm. The distance between neighboring parallel lines is 1 mm.

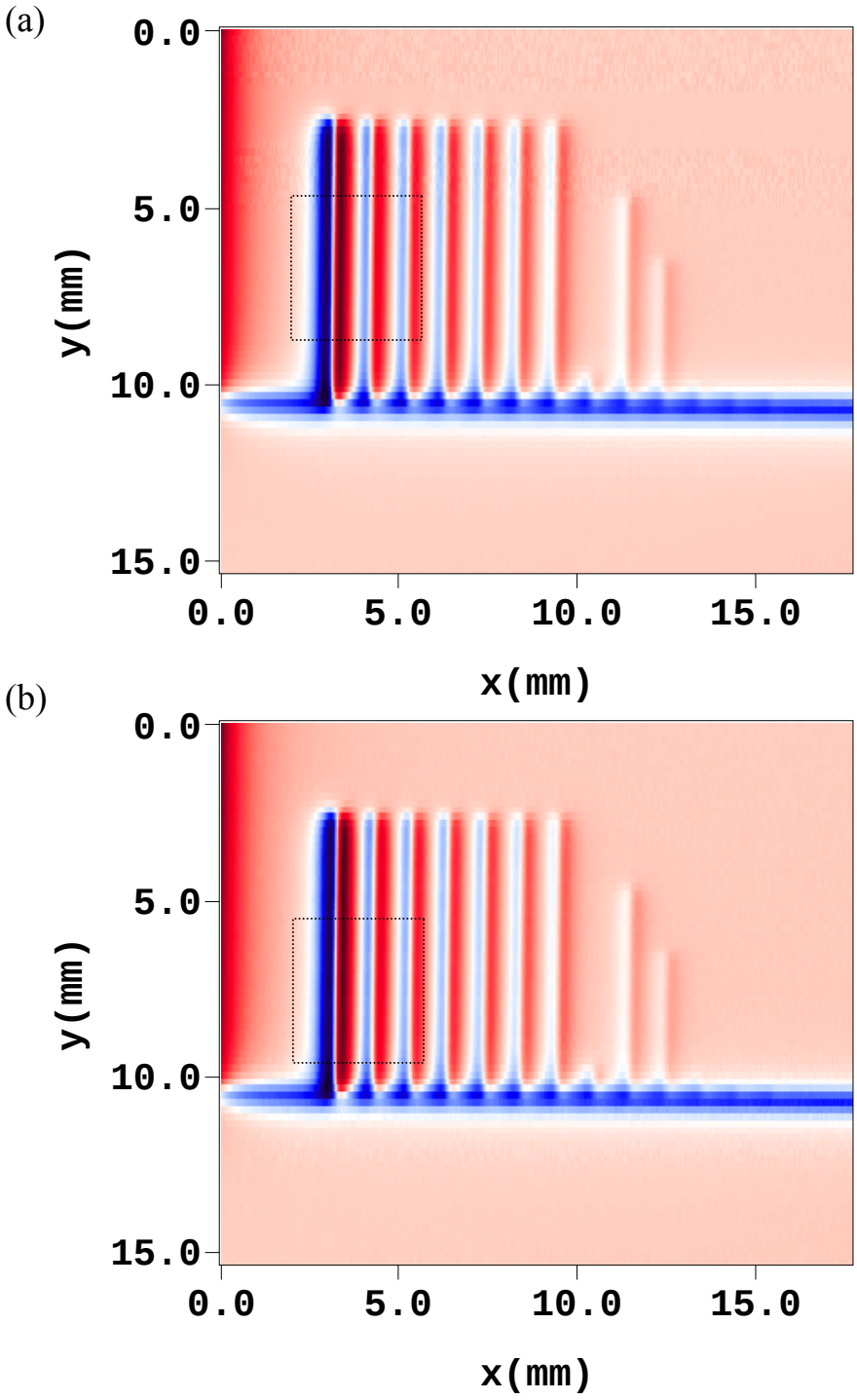

Figure 6.21: 2-dimensional test scan magnetic field image of patterned mask carrying I = 1.5 mA at z ~ 400 μm with (a) one SQUID and (b) two SQUIDs (combined to one image). Region in dotted box shown magnified in Fig. 6.22. Reds/Blues indicate +0.17/-0.2 μT. (file name (a)*:m100204.hdf,* (b)*: m100203.hdf*)

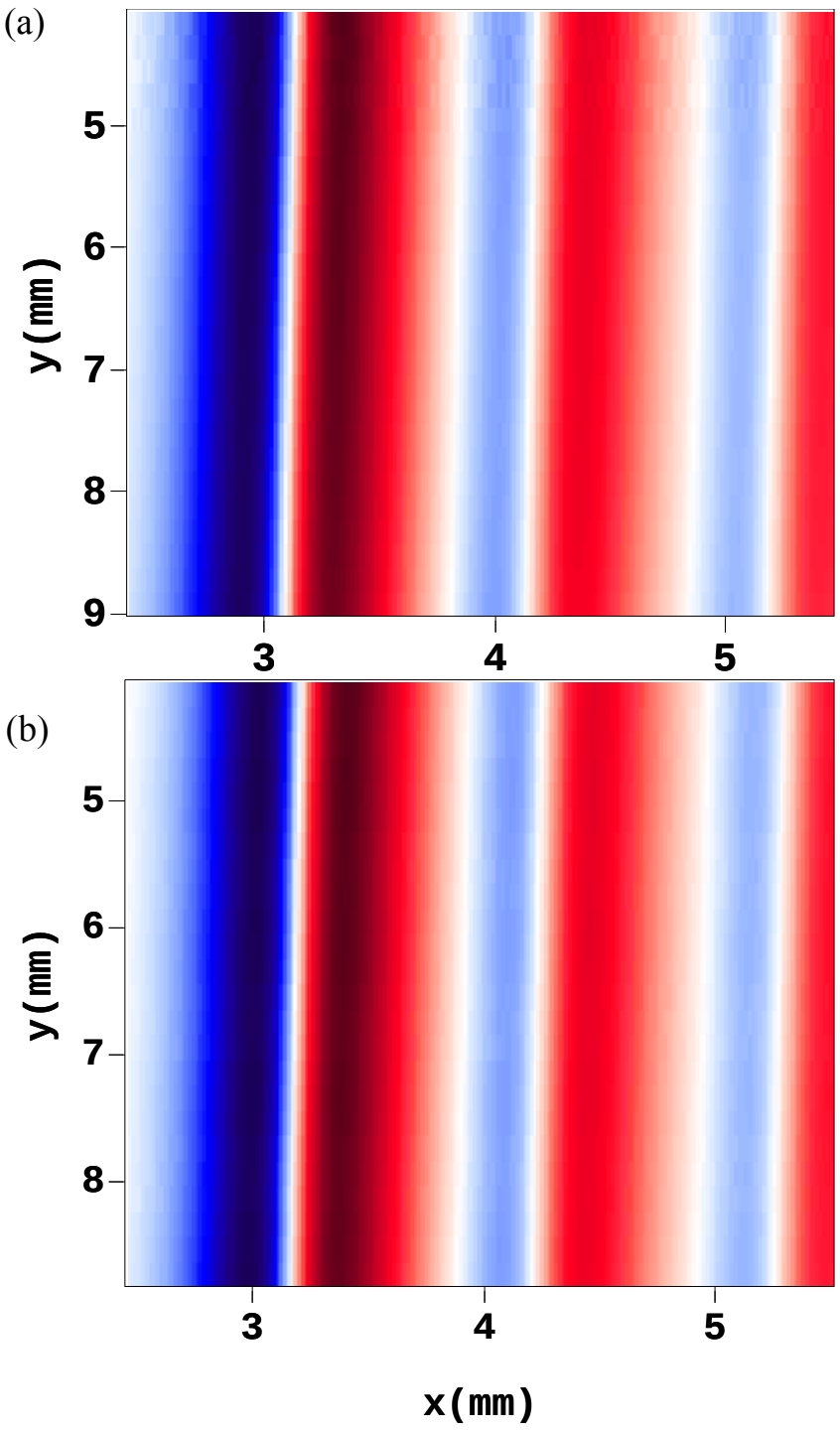

Figure 6.22: Magnified view of section of Figs. 6.21 with (a) one SQUID and (b) two SQUIDs (combined to one image). Reds/Blues indicate +0.17/- 0.2 μT.

6.6 Conclusion

I designed, fabricated, built, and tested an 8-channel high-T_c scanning SQUID microscope. I obtained the transfer function and the dynamic range ($\Phi_{max} \sim 11\Phi_0$) for each SQUID. At 1kHz, the slew rate is about 3000 Φ_0/s. I also found that he white noise level varied from 5 $\mu\Phi_0/\mathrm{Hz}^{1/2}$ to 20 $\mu\Phi_0/\mathrm{Hz}^{1/2}$ depending on the SQUID.

I also wrote a new data acquisition program that triggered on position and can collect data from up to eight SQUIDs. To generate a single image from the multi-channel system, I first calibrated the tilt of the *xy* stage and *z* stage manually. Finally I calculated the actual applied flux by multiplying the feedback signal by the mutual inductance matrix and showed that I could improve the image quality by doing so.

Chapter 7

The Effect of Position Noise on Imaging

Experimentally obtained images of magnetic field contain not only magnetic field noise, but also uncertainty in the position at which the data points are recorded. In this chapter, I discuss how position noise affects magnetic field images and find the position noise of my system. I show that the effect of position noise is largest where the magnetic field gradients are strongest.

7.1 Introduction

By scanning very close to the surface of a sample, good spatial resolution can be obtained in the resulting image. Recent research on room-temperature SQUID microscopy [1,2](the sample is at room temperature) has focused on improving the spatial resolution achieved under typical operating conditions either through hardware or software improvements [3,4]. For example, using a magnetic inverse transformation, it is possible to transform a magnetic image into an image of the source currents [5]. The spatial resolution of the resulting current density image can be up to 10 times better than the raw magnetic field image or up to 5 times smaller than the SQUID-sample separation z under typical conditions, limited by the strength of the magnetic signal and the noise in the SQUID [4]. This result is only possible because the data from a SQUID

is quantitatively very precise and accurate, allowing a complicated transformation to be reliably performed without introducing significant distortion.

I should remark that noise is not always immediately evident in many SQUID images. For example, when I scan a wire, the magnetic field can look very clear and strong as shown in Fig.7.1. However, by subtracting away the expected field I can easily see random magnetic field noise. In particular though, I always obtain strong noise near the wire (see Fig.7.2). The fact that strong noise tends to occur near a strong gradient in the signal is a symptom of position noise. In the next section, I analyze the effect of position noise on a magnetic field image and compare the results to data from a scanning SQUID microscope. I find that surprisingly small amounts of position noise during scanning can significantly degrade an image.

7.2 Theory of position noise

7.2.1 Non-accumulated position noise

In scanning SQUID microscopy, magnetic images are acquired by raster scanning a sample close to a SQUID while recording the output from the SQUID. The position of the sample with respect to the SQUID is controlled by a computer that is linked to motors that drive a scanning stage. The movement of the stage is usually driven by motors that are attached to a scanning stage. The position of the stage is usually determined by position encoders. Stage jitter, uncertainty in the encoder readout, and environmental vibrations cause random errors in the position at which the data is recorded. Thus, for a scan along the x-direction, if the recorded position of the i-th pixel is x_i, then the actual position of the i-th pixel will be

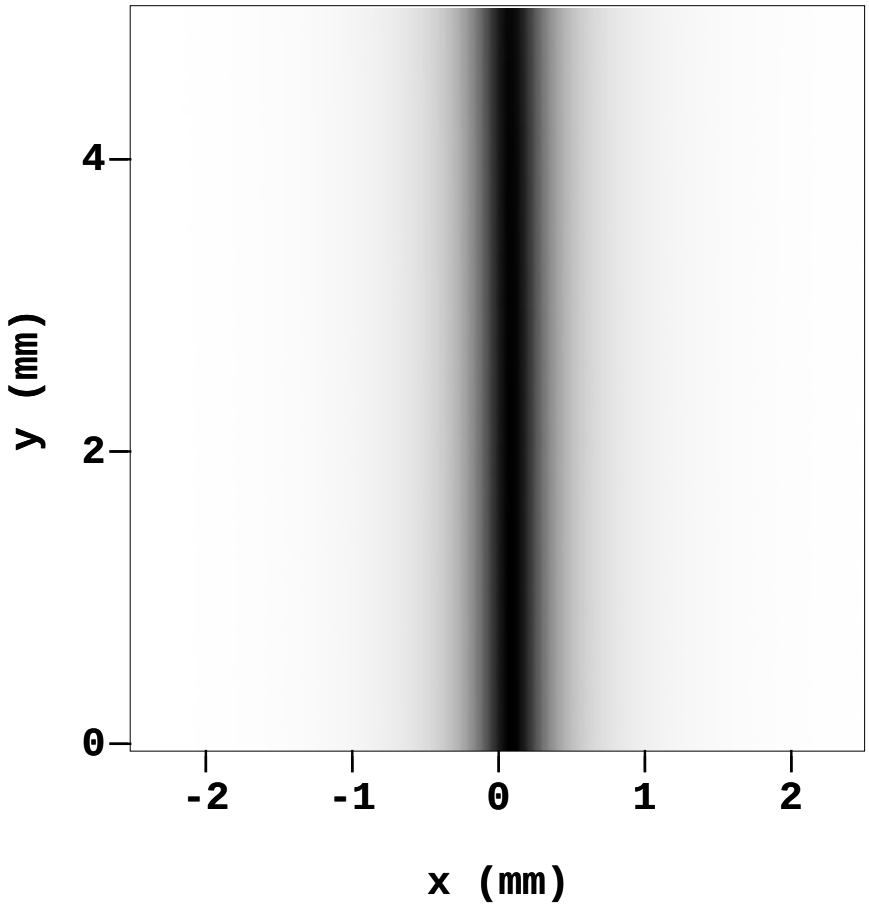

Figure 7.1: Measured 2-dimensional magnetic field B_x image of straight wire carrying current I = 2.3 mA using scanning SQUID microscope with z = 250 μm and Δx = 10 μm. Black/white indicates 2/0μT. (file # : m0927010)

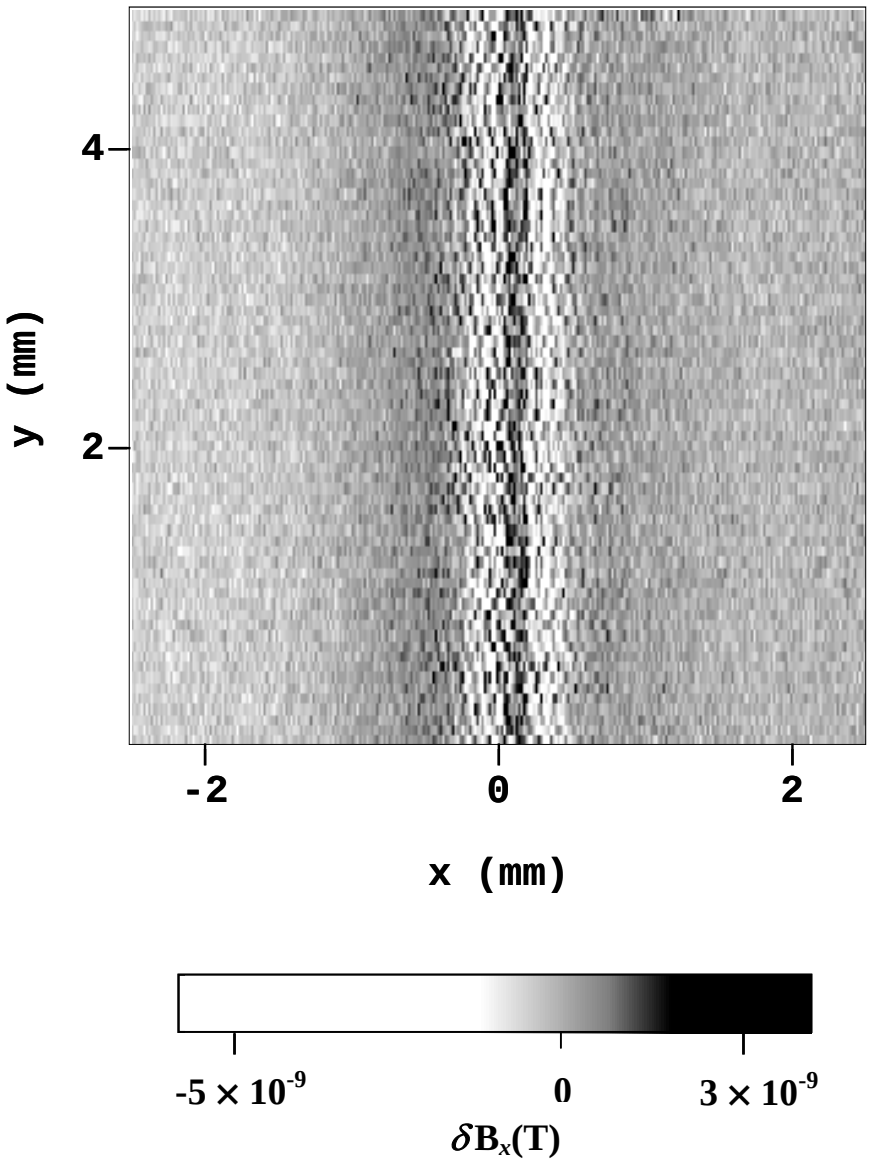

Figure 7.2: Magnetic field noise in Fig 7.1 found by taking the difference between measured magnetic field and fit to expected magnetic field from wire. (file # : m0927010).

$$x_i' = x_i + \delta x_i, \tag{7.1}$$

where δx_i is the error in the recorded position of the *i*-th pixel.

We will assume that the δx_i are uncorrelated and distributed randomly with standard deviation σ_x. For simplicity, we also assume that the only position error is along the scan direction *x* and that σ_x does not depend on position. For convenience, we can express σ_x as an effective r.m.s. uncertainty in the magnetic field,

$$\sigma_{B_i} = \left|\partial B_x / \partial x\right|_{x=x_i} \sigma_x \tag{7.2}$$

where $\left|\partial B_x / \partial x\right|_{x=x_i}$ is the derivative of the magnetic field B in the *x* direction at $x = x_i$. Including the random magnetic field noise σ_B from the SQUID sensor itself, the total effective r.m.s. magnetic field noise in the *i*-th pixel is thus :

$$\sigma_{B_i}^{Tot} = \sqrt{\sigma_{B_i}^{\ 2} + \sigma_B^{\ 2}} = \sqrt{\left|\frac{\partial B}{\partial x}\right|_{x=x_i}^2 \sigma_x^2 + \sigma_B^2} \tag{7.3}$$

As an example, Eq. (7.3) can be evaluated for the case of a straight wire which carries current *I* along the *y*-axis. With the SQUID loop oriented to detect the *x*-component of the magnetic field (an *x*-SQUID configuration, see Fig. 7.3(a)), then

$$B_x = \frac{\mu_0 I}{2\pi} \frac{z}{x^2 + z^2}, \tag{7.4}$$

where z is the distance between the center of the SQUID and the *x*-*y* plane. Figure 7.3(b) shows B_x for I = 2.3mA and z = 250 μm and also shows how the position uncertainty affects the magnetic field noise. The dotted line indicates the expected position and the

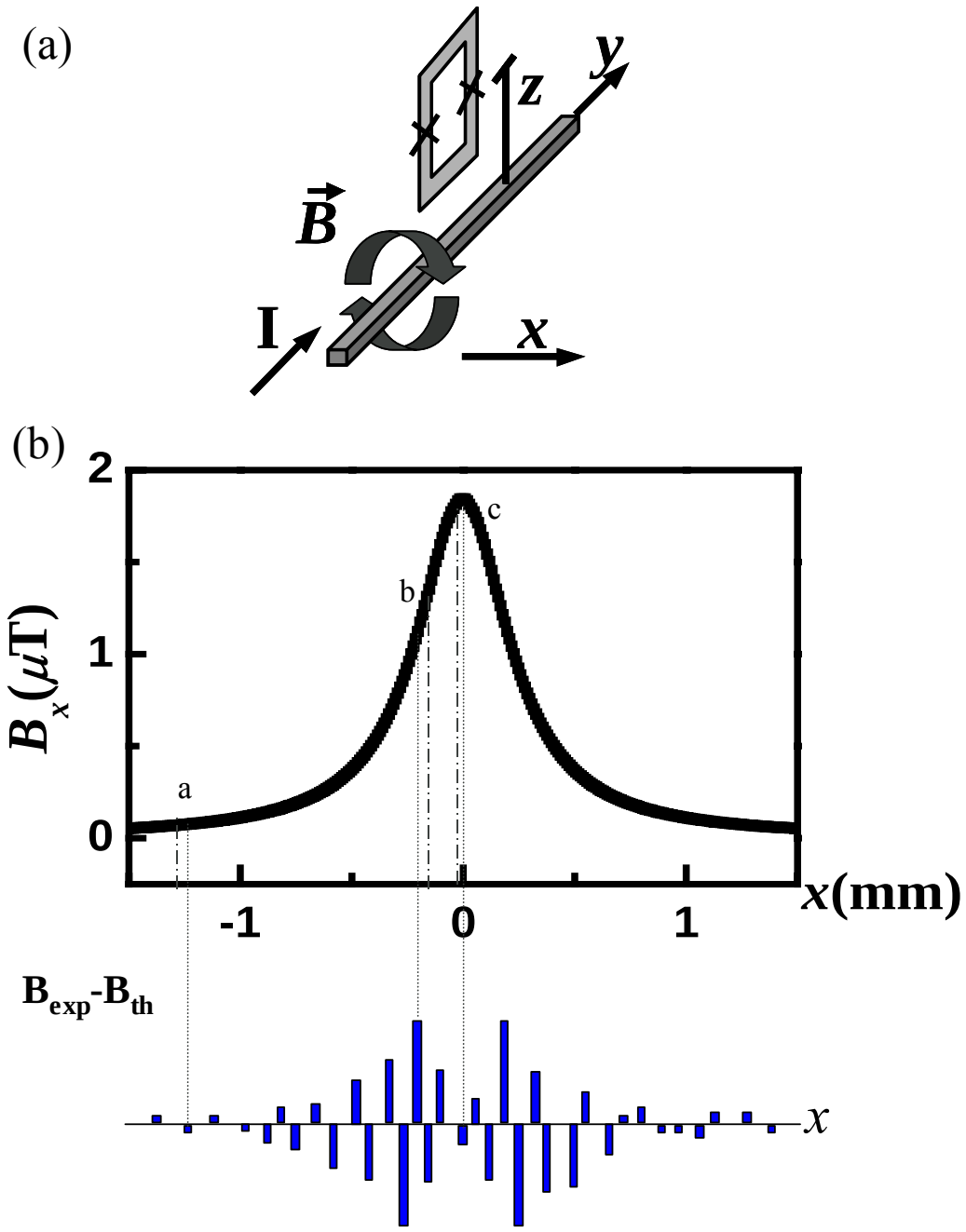

Figure 7.3: (a) *x*-SQUID configuration. (b) B_x for I = 2.3 mA and z = 250 μm from a wire with Gaussian position noise, showing why the effective field noise near the wire will be larger.

dashed line indicates the actual position. At "a", the magnetic field difference between the expected position and actual position is relatively small. However, at "b" the effect becomes large because the slope of the magnetic field signal is sharp. At "c", the difference again becomes small. I note that the noise is a maximum to both sides of the wire, where the derivative of the field with respect to x is a maximum.

Substituting Eq. (7.4) into Eq. (7.3), I find:

$$\sigma_{B_i}^{Tot} = \sqrt{\left(\frac{\mu_0 I}{2\pi} \frac{2xz}{(x^2 + z^2)^2} \sigma_x \right)^2 + \sigma_B^2} \qquad (7.5)$$

Figure 7.4 shows σ^{Tot}_{Bi} calculated for typical parameters I = 2.3mA, σ_B = 0.2 nT, z = 250 μm, and σ_x = 0.5 μm. Note that the peak r.m.s. noise of 1.2 nT in Fig. 7.4 is about 6 times larger than that due to the intrinsic SQUID noise σ_B = 0.2 nT (dashed line in Fig. 7.4).

I note that an insidious feature of the position noise is that its existence tends to be hidden in an image because it is only significant where there is a strong signal, yet it delivers its effect at the worst place, i.e. where the signal is. This behavior is somewhat analogous to the role of current noise in determining the total voltage noise when an amplifier is connected to a source with resistance $R = \partial V / \partial I$; the effect of current noise is only observable when a non-zero impedance R is connected across the amplifier input [6]. Thus instead of Eq. (7.5), one finds

$$\sigma_V^{Tot} = \sqrt{\left(\frac{\partial V}{\partial I} \right)^2 \sigma_I^2 + \sigma_V^2} \qquad (7.6)$$

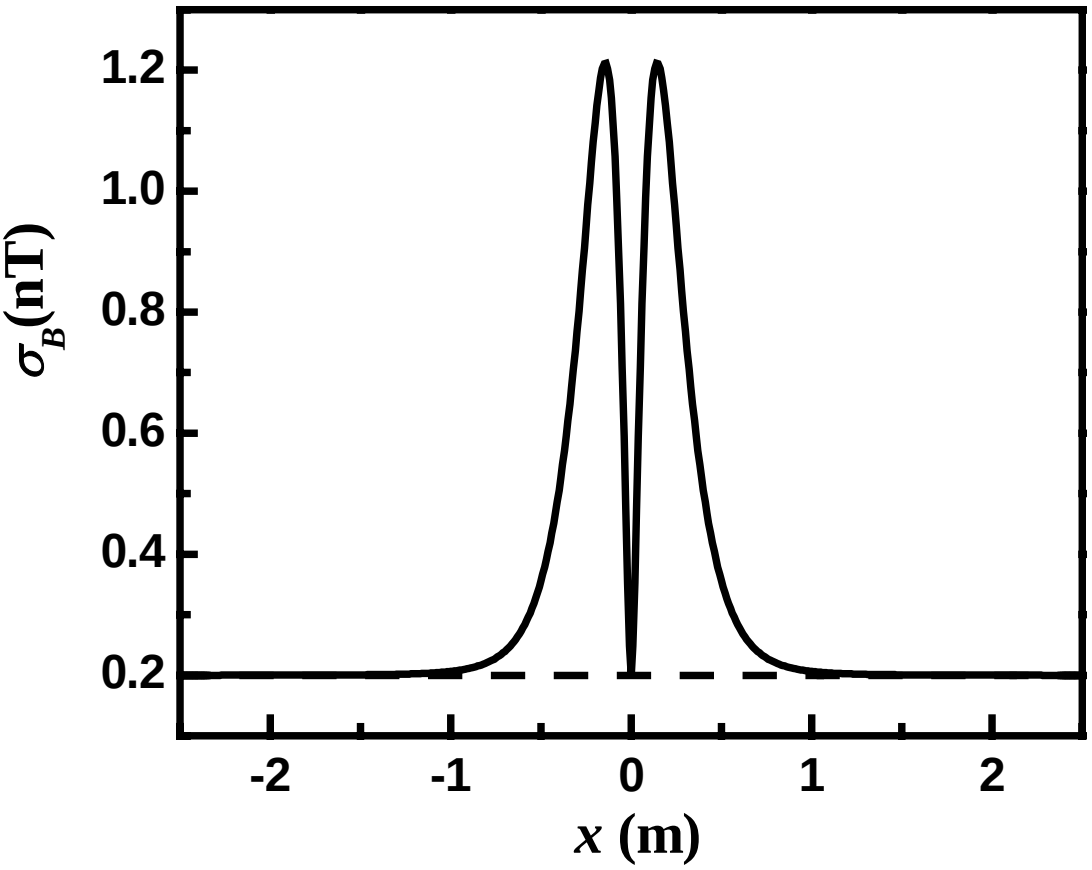

Figure 7.4: Predicted total root means square effective field noise from Eq. (7.5), including both position noise and intrinsic *x*-SQUID noise for $I = 2.3$ mA, $\sigma_B = 0.2$ nT, $z = 250$ μm, $\sigma_x = 0.5\mu$m. The dotted line indicates intrinsic SQUID noise level, $\sigma_B = 0.2$ nT.

For comparison, Fig. 7.5(a) shows a simulated 2D image of the difference between the field B_x with and without noise for a wire carrying 2.3 mA at z = 250 μm. Figure 7.5(b) shows a line section through Fig. 7.5(a). Figure 7.5(c) shows the corresponding difference between a measured field from a wire and theory for a real scan, as described below. Figure 7.5(d) is a line section through Fig. 7.5(c).

Examination of Eq. (7.5) reveals that at $x = \pm z/\sqrt{3}$ the effective field noise near a wire is a maximum,

$$\sigma_B^{\max} = \sigma_B \sqrt{\left(\frac{3\sqrt{3}\mu_0 I\, \sigma_x}{16\pi\, z^2 \sigma_B} \right)^2 + 1} = \sigma_B \sqrt{\left(\frac{z_0}{z} \right)^4 + 1} \qquad (7.7)$$

where we define a new parameter, $z_0 \equiv \sqrt{3\sqrt{3}\mu_0 I \sigma_x / (16\pi\sigma_B)}$. For $z \ll z_0$, the effect of position noise will dominate, while for $z \gg z_0$, the true magnetic noise σ_B is dominant. In addition, as z is reduced below z_0, we see from Eq. (7.7) that the effect of position noise increases rapidly. For I = 2.3 mA, σ_B = 0.2 nT and σ_x = 0.5 μm, we obtain z_0 = 864.3 μm, which is remarkably large compared to typical scanning separations. This implies that position noise is the dominant source of noise for typical situations in scanning SQUID microscopy, rather than the magnetic noise from the SQUID.

7.2.2 **Accumulated position noise**

In Eq. (7.1), we assumed that the position noise varied randomly, in an uncorrelated fashion from one pixel to the next. However, position noise can be correlated depending on the configuration of the motor controller and the position encoding mechanism. If the motor controller uses feedback and the data taking is triggered by position, then correlated position noise is minimized. This is the case with

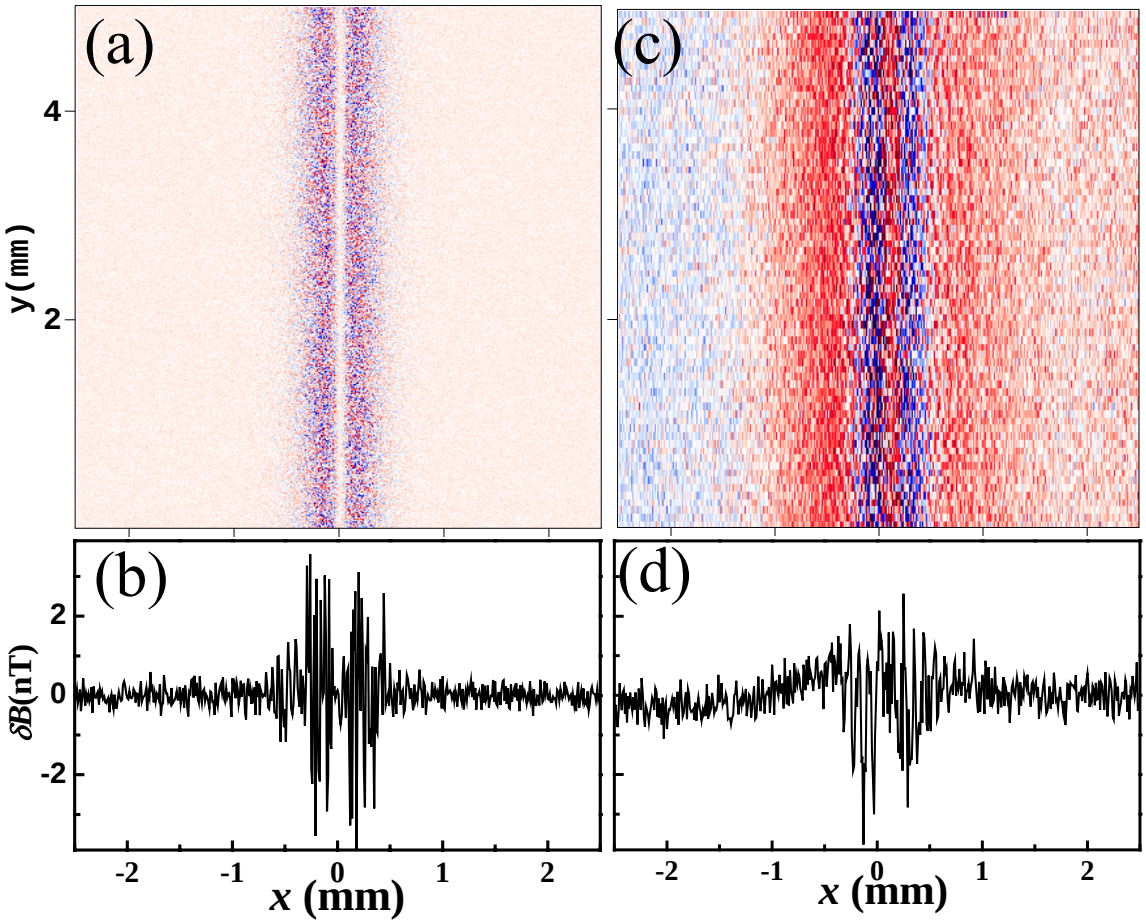

Figure 7.5: (a) Magnetic field noise from simulation with $\sigma_x = 0.5\mu$m, $\sigma_B = 0.2$ nT, I = 2.3 mA, and z = 250 μm. (b) Line-section through plot (a). (c) Noise from measured image showing effect of position noise (plot is difference between measured magnetic field and fitted magnetic field). (d) Line-section through plot (c).

the Newport stage I used, but was not the case for the earlier scanning systems used with my microscope. However, correlated position noise can be significant if, for example, the position is acquired at regular time intervals. In this case, the actual position, x_i', of the i-th pixel depends on the recorded point, x_i, of the i-th pixel and the sum of the errors, δx_n, from all previous steps. Thus:

$$x_i' = x_i + \sum_{n=1}^{i} \delta x_n \tag{7.8}$$

where x_i is the expected position. Then, the r.m.s. position error at the i-th pixel is

$$\sigma_{x_i} = \sqrt{\sum_{n=1}^{i} \left(\frac{\partial x_i'}{\partial \delta x_n} \delta x_n \right)^2} \cong \sqrt{i}\, \sigma_x \tag{7.9}$$

where we have assumed the δx_n are distributed randomly with standard deviation σ_x. For example, if we have 2000 pixels, then the magnetic field noise with accumulated position noise near the center of the image will be about $\sqrt{1000} \approx 31$ times larger than that without accumulated noise.

The gray solid line in Fig. 7.6 shows three simulated scans of magnetic field noise, including the effect of accumulated position noise, generated with the same parameters as Fig.7.4 with 2000 pixels. The black dashed line shows the standard deviation of 30 line scans. Comparing the maximum noise in Fig. 7.6 to Fig. 7.4, the standard deviation of the magnetic field noise including accumulated position noise is

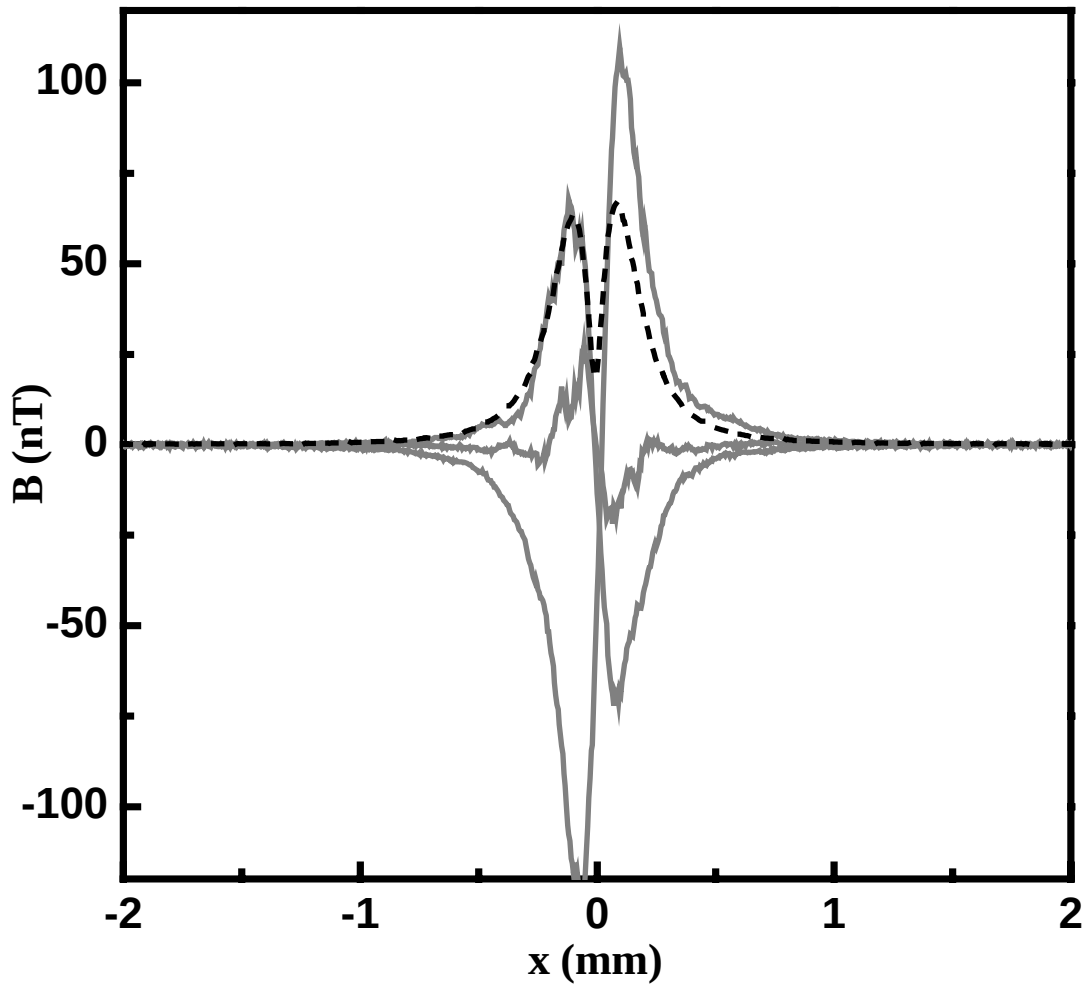

Figure 7.6: Solid lines show three examples of difference between simulated magnetic field with "accumulated" position noise and the field without any noise. Calculated for parameters, I = 500μA, σ_B = 0.2 nT, z = 150 μm, σ_x = 1μm, and n = 2000. The black dashed line shows the standard deviation of 30 such line scans. Note that the effect of σ_B is negligible on this scale.

60 nT, i.e. about $40 \approx \sqrt{2000}$ times larger than that without accumulated noise. From these results, we see that it is very important to eliminate accumulated position noise. This is a significant benefit of using the Newport stage, compared to out old home-made stage.

In Chapter 6.4.2, I described the difference between triggering in time and triggering on position. Figure 6.13(a) shows that the center positions from the data triggered in time shift left and right in subsequent scans. For the data triggered in position, there is no shift, as shown in Fig. 6.13(b). This data was taken using motor controllers with PID servo loops that are triggered by position [7]. I also note that there is no position noise evident in Fig. 6.13(b) because the sample-to-sensor distance was far (z = 1.6mm), so the magnetic field noise from the non-accumulated position noise was buried by intrinsic SQUID noise.

7.3 Measurement of position noise

7.3.1 Position noise results

To measure the position noise in my system, I scanned an Au-patterned mask that had a 5 cm long and 5 μm wide straight wire aligned along the *y*-direction. The wire was carrying about 5 mA of current. For this experiment, I used four *x*-SQUIDs (1, 3, 5 and 7th SQUIDs). Since the signal was almost identical, I used data only from the 1st SQUID for the position noise. For these measurements I took a 1 cm scan in the *x*-direction with a step size $\Delta x = 5$ μm.

The resulting data from the wire was fit to the expected magnetic field from a straight wire. For accurate fitting, I must consider the effect of the SQUID area and

allow for tilt of the SQUID sensor. Strictly speaking, the SQUID does not measure the field at a point, but rather the average field over the area of the SQUID loop. For an *x*-SQUID with a loop of width *w* and height *h*, the average field is

$$\langle B_x \rangle = \frac{1}{wh}\int_{z-h/2}^{z+h/2}\int_0^w \frac{\mu_0 I}{2\pi}\frac{z'}{x^2+z'^2}\,dz'\,dy = \frac{\mu_0 I}{4\pi h}\ln\left(\frac{x^2+(z+h/2)^2}{x^2+(z-h/2)^2}\right) \quad (7.10)$$

Secondly, since the alignment between the wire and the SQUID is not perfect, we need to allow for some coupling of the *z*-component of the magnetic field (there is no *y*-component for a straight wire running along the *y*-axis). Including the tilt θ of the SQUID from the perpendicular, the expected response of the *x*-SQUID will be,

$$\langle B_x \rangle = \frac{\mu_0 I}{4\pi h}\ln\left(\frac{x^2+(z+h\cos\theta/2)^2}{x^2+(z-h\cos\theta/2)^2}\,\frac{(x-h\sin\theta/2)^2+z^2}{(x+h\sin\theta/2)^2+z^2}\right) \quad (7.11)$$

From fits to the data, I found $\theta = 0.64\,^\circ$ and $h \cong 50\ \mu$m.

The difference between the experimental data and the fit reveals the total field noise, as shown in Fig. 7.7 for $z = 354\ \mu$m and $z = 858\ \mu$m. For $z = 858\ \mu$m (see Fig. 7.7(b)) the noise level does not depend on position, and I cannot distinguish any effect from position noise. However, for $z = 354\ \mu$m (see Fig. 7.7(a)), the position noise is obvious near $x = 0$. I note that there is some residual drift evident in the difference, probably due to a small systematic error in the fit. To eliminate this in a model independent way, and locally determine $\sigma_{B_i}^{tot}$, we further analyze the data by computing at each point the standard deviation of the neighboring 5 data points. Figure 7.8 shows the procedure to get rid of residual drift. Figure 7.9(a)-(c) show the results for a series of scans for z = 354 μm, z = 514 μm, z = 858 μm, and I note how the position noise is distinguishable only for small *z*.

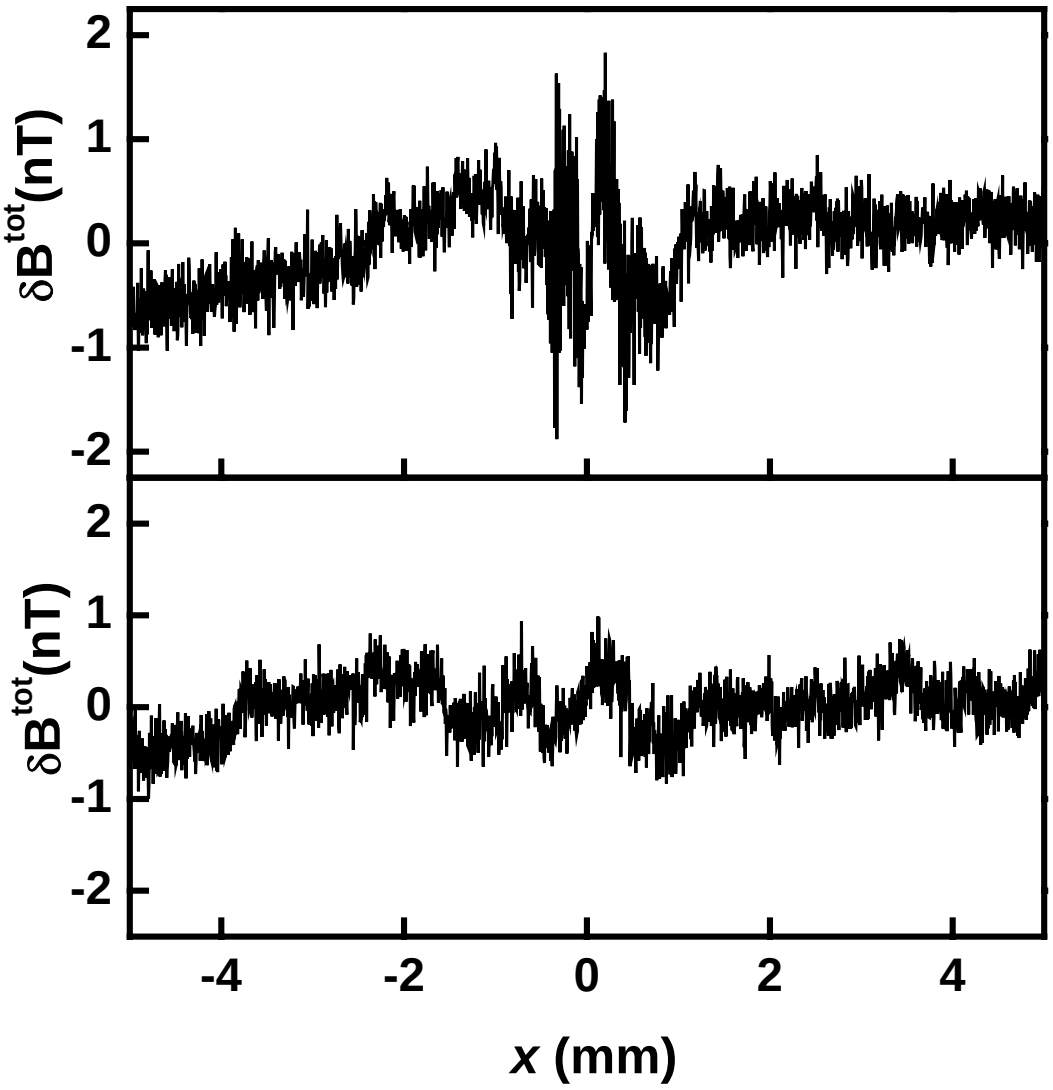

Figure 7.7: Difference between measured magnetic field and fitted magnetic field for wire carrying I = 4.8 mA at (a) z = 354 μm, and (b) z = 858 μm.

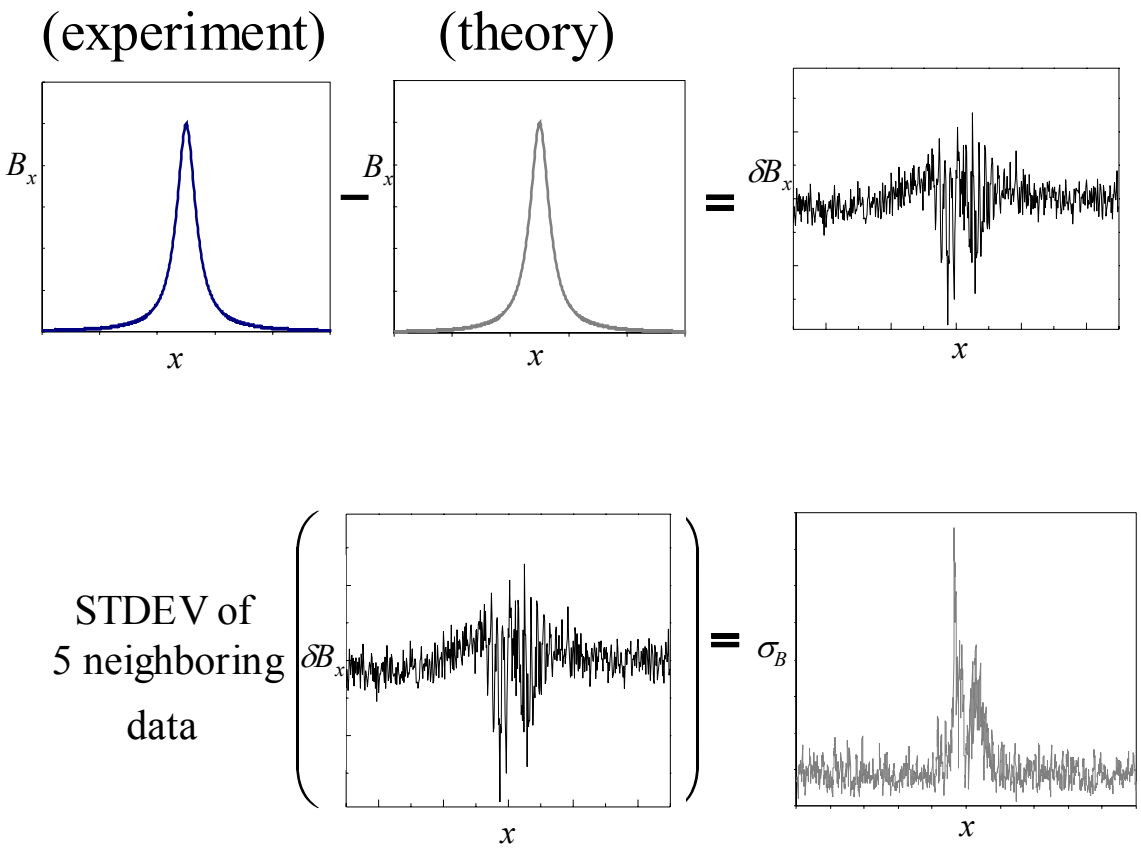

Figure 7.8: Procedure for obtaining position noise by taking standard deviation of 5 neighboring points of the difference between the measured field and fitted field.

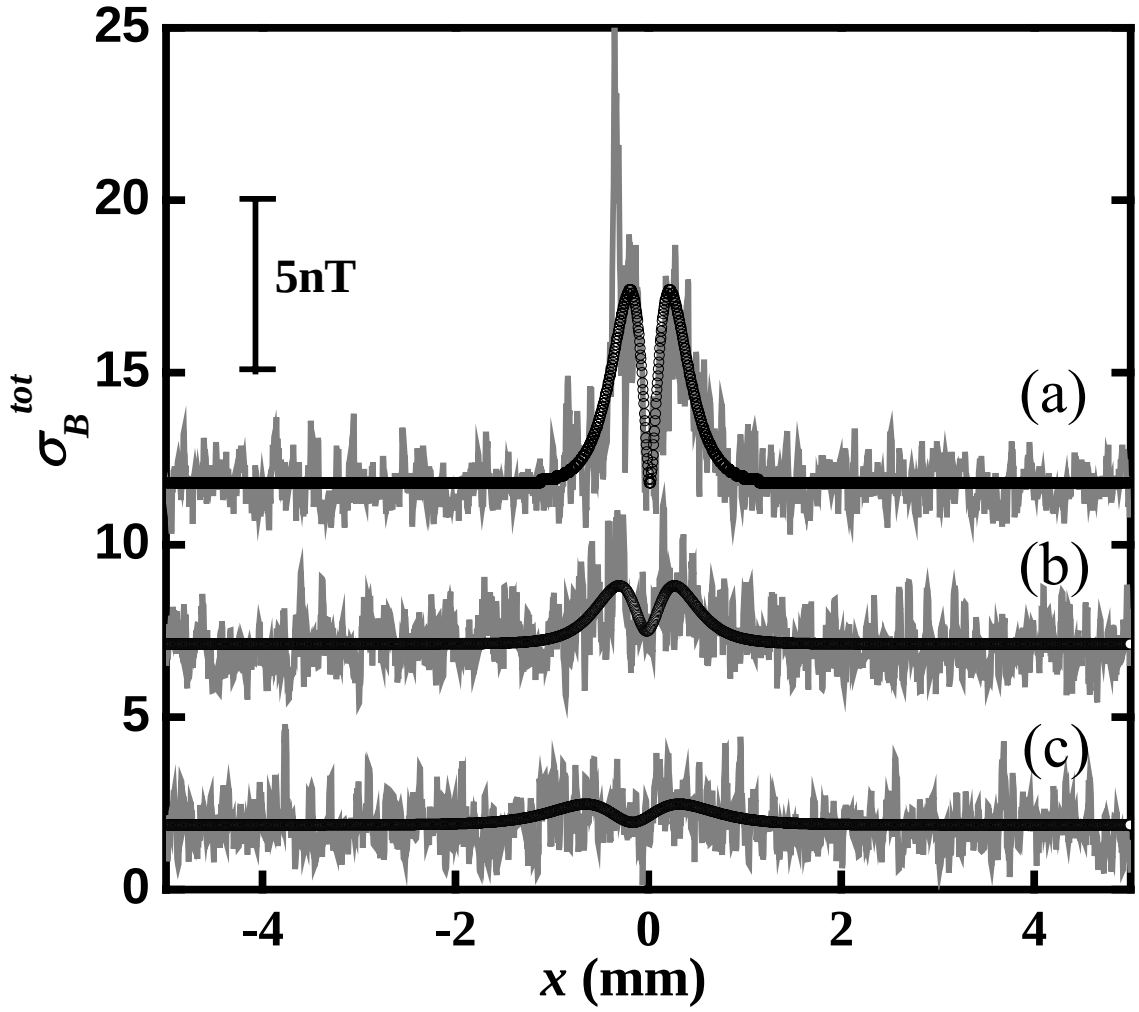

Figure 7.9: Measured $\sigma_{B_i}^{tot}$ for I = 4.8 mA and (a) z = 354 μm, (b) z = 514 μm, (c) z = 858 μm. Curves (a)-(b) have been offset by 10nT, and 5nT respectively for clarity. Here the plots were made by taking the standard deviation of 5 neighboring data points of the difference between the measured magnetic field and fitted magnetic field. Solid lines indicate fitted data using Eq. (7.5).

By fitting the data in Fig. 7.9 using Eq. (7.3), I obtain σ_B = 0.185 nT and σ_x = 0.145 μm (see solid lines in Fig. 7.9). From I, σ_x, and σ_B, I obtain z_0 = 700μm. As can be seen in Fig 7.9(c), when $z \gg z_0$, the position noise is buried by the intrinsic SQUID noise. I also note that the measured σ_x = 0.145 μm is somewhat larger than the nominal encoder resolution of 0.1 μm and that σ_B is reasonable for our SQUID.

7.3.2 Position noise criteria

The presence of position noise has an important implication for the design of scanning SQUID microscopes or other magnetic imaging systems. From Eq. (7.7), the criteria

$$\sigma_x \leq \sigma_B \left(\frac{16\pi z^2}{3\sqrt{3}\mu_0 I} \right) \tag{7.12}$$

will guarantee that the effect of position noise is no larger than the intrinsic magnetic noise σ_B when imaging a wire carrying current I at distance z. For example, if σ_B = 0.185 nT, I = 500 μA, and z = 150 μm, then Eq. (7.12) implies that we need σ_x < 62 nm. This is a remarkably strict requirement on the positioning, largely due to the very low noise in the SQUID compared to the signal strength. Use of a larger current, a smaller separation or a more sensitive SQUID would necessitate an even tighter requirement on positioning. Table 7.1 shows the position noise criteria for various scanning parameters.

7.4 How to reduce position noise

Since the position noise is random, in principle, I can reduce it by averaging. There are 2 kinds of position noise sources. When the stage moves with step size Δx,

Table 7.1: Position criteria $\sigma_x^{\max}$ for imaging a wire varying current I at sample-to-sensor distance z.

I (mA)	z (μm)	σ_x (μm)
0.1	10	0.0014
0.2	10	0.0007
0.5	10	0.0003
1	10	0.0001
0.1	100	0.1424
0.2	100	0.0712
0.5	100	0.0285
1	100	0.0142
0.1	150	0.3204
0.2	150	0.1602
0.5	150	0.0641
1	150	0.0320
0.1	200	0.5697
0.2	200	0.2848
0.5	200	0.1139
1	200	0.0570

the actual position is $x_i' = x_0 + i \cdot \Delta x \pm \delta x_i$. If the position noise δx_i is from a systematic error in the motor encoder, then averaging at one position doesn't help to reduce the position noise. However, if this error varies randomly from one scan to the next, then averaging scans reduces the position noise from encoder error. Another source of position noise is actual vibration of the stage or SQUID. Averaging at one encoder position can reduce this source. If more than one source of position noise is present, it can be hard to determine the root cause.

To see if I could reduce the effect of position, I made 70 scans in the *x*-direction at the same *y* position over a straight wire that was running along the *y*-direction. Figure 7.10 shows the result after averaging for 1, 8, and 70 times. Averaging clearly reduces both the magnetic field noise from intrinsic SQUID noise and the position noise. By fitting Eq. (7.5) to these measurements, I could get the relation between σ_x (see Fig. 7.11) and σ_B (see Fig. 7.12) and the number of scans averaged. If the noise is random and uncorrelated, the noise will be reduced by a factor of $N^{1/2}$ after averaging, where N is the number of scans. Therefore, if the averaged random noise is multiplied by $N^{1/2}$, one might expect a constant. As shown in Fig. 7.11 and 7.12, the intrinsic noise multiplied by $N^{1/2}$ is roughly constant until 10 to 20 scans are averaged, but it increases after that. For the position noise, the increase starts earlier after 4 or 5 scans. This behavior means that the source of both noises is not entirely uncorrelated. The cause of these correlations is unclear, but in the case of position noise, it may be that the encoder is making repeatable systematic mistakes in positioning, i.e. it is reliably inaccurate.

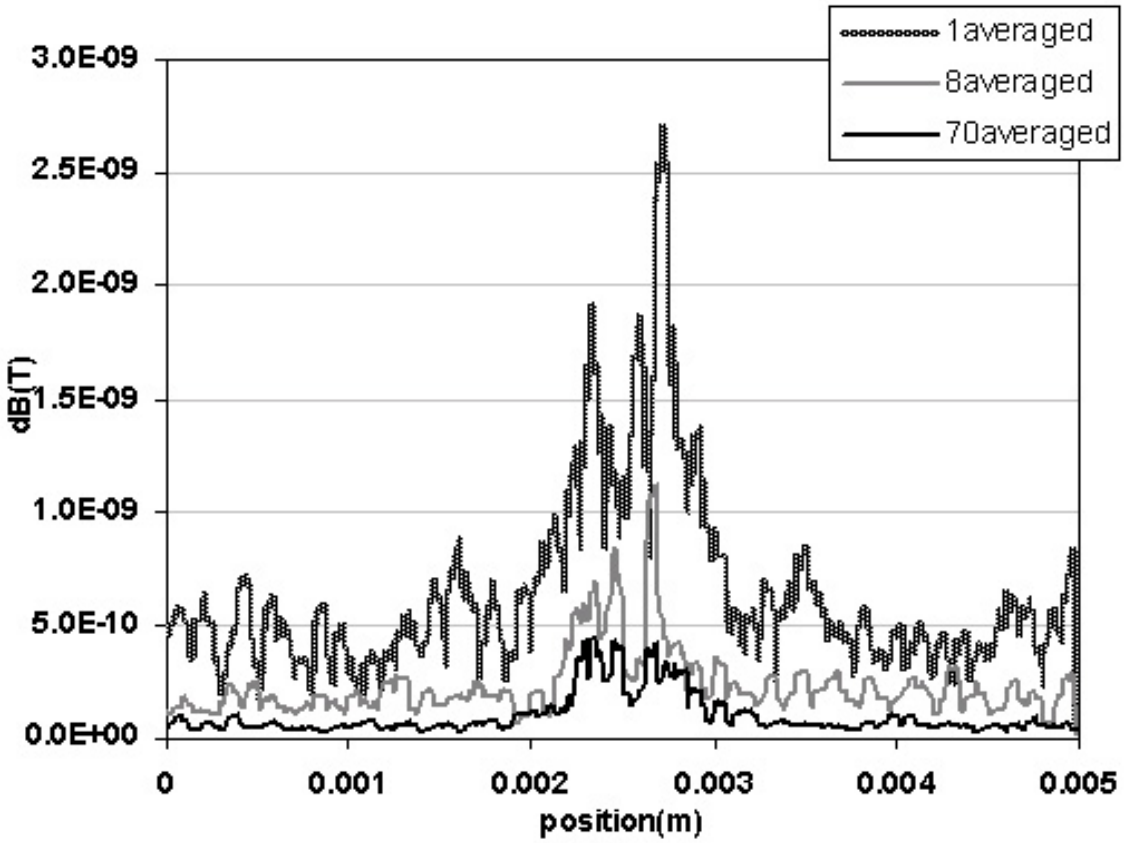

Figure 7.10: Measured total effective magnetic field noise $\sigma_{B_i}^{tot}$ for I = 2.32 mA and z = 250 μm after averaging 1, 8, and 70 scans following the procedure as shown in Fig.7.8.

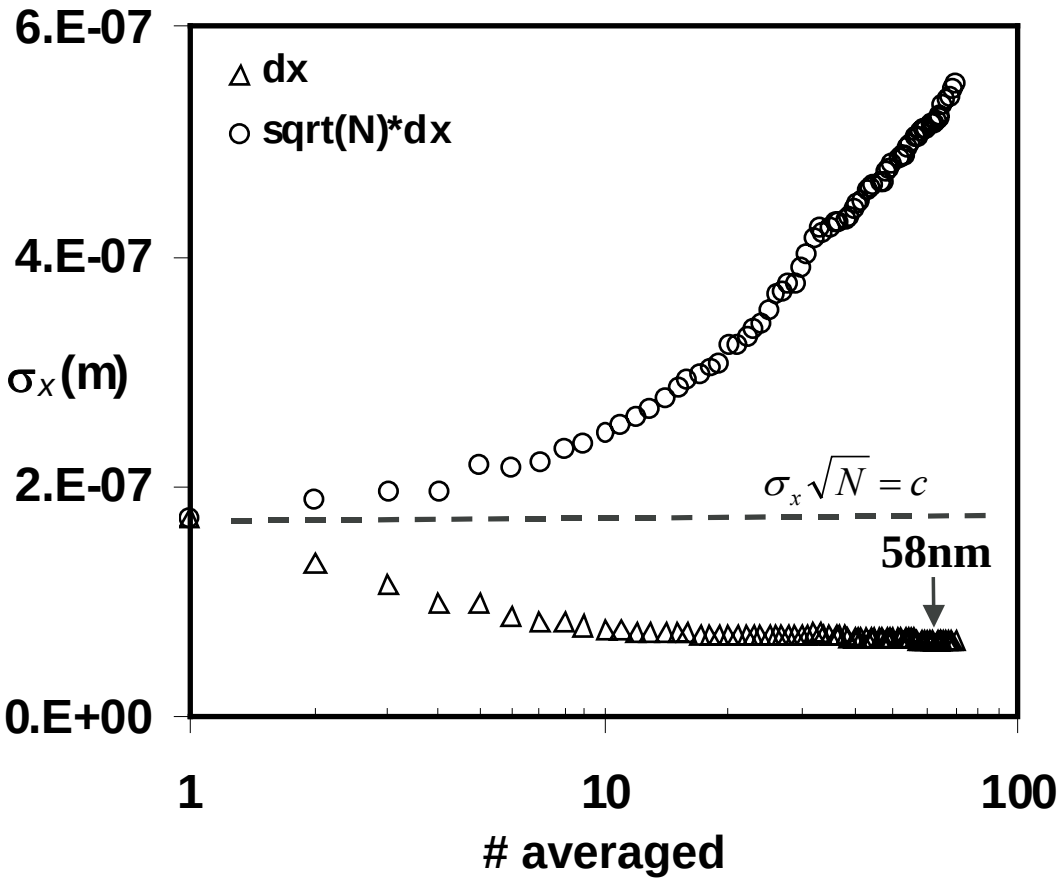

Figure 7.11: Relation between r.m.s. position noise and number of scans averaged. Points are obtained by fitting magnetic field noise (dataset in Fig. 7.10) to Eq. (7.5). Triangles are σ_x as function of # of averaging and circles are $\sigma_x\sqrt{N}$.

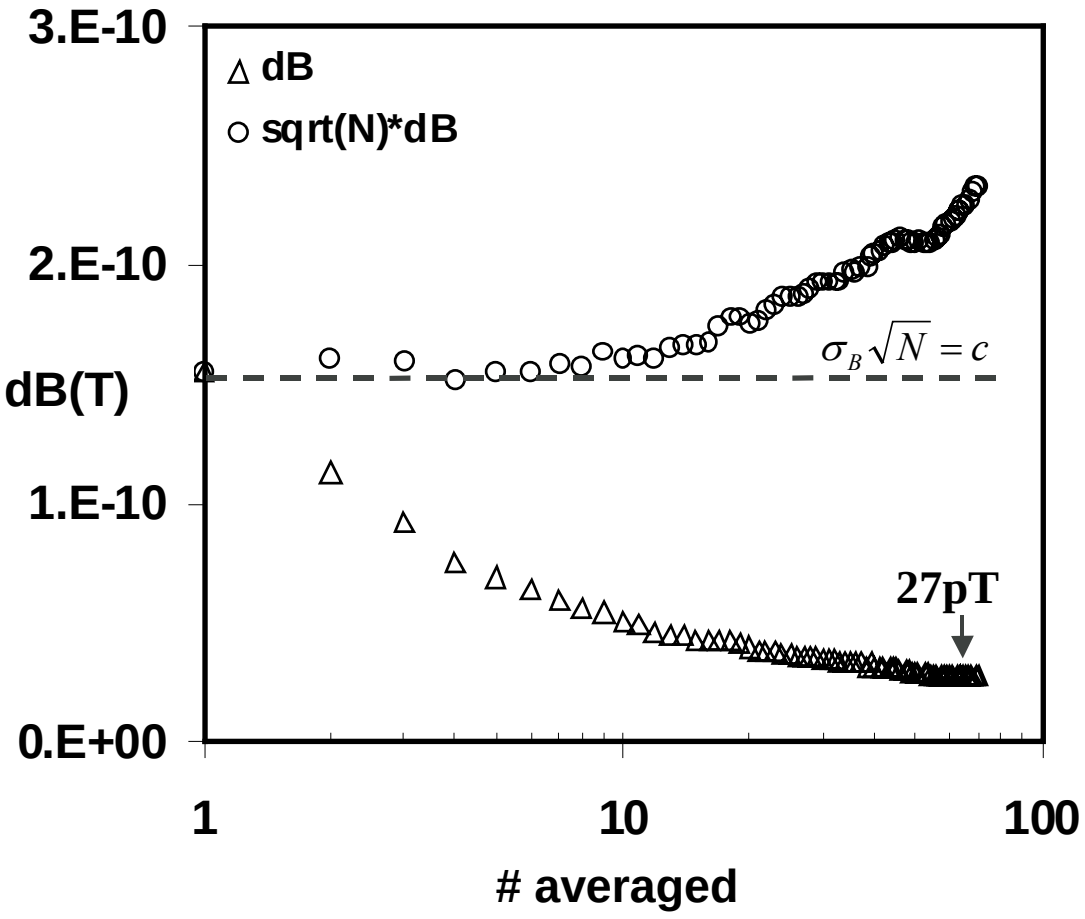

Figure 7.12: Relation between r.m.s. magnetic field noise and number of scans averaged. Results obtained by fitting magnetic field noise (dataset in Fig. 7.10) to Eq. (7.5). Triangles are σ_B as function of # of averages and circles are $\sigma_B\sqrt{N}$.

If the source of position noise is from stage vibration, I can reduce the effect of position noise by increasing the number of points averaged at each position. Figure 7.13 shows position noise and intrinsic SQUID noise after averaging at each position. Unlike the intrinsic SQUID noise, the position noise is not reduced noticeably. The condition for this experiment was that the time constant of the lock-in amplifier and DAQ sampling rate were 3 ms and the time period between one position and the next position was 100 ms. Since the motor is moving while I scan, 20 times averaged data at one position covers 60 % of Δx, therefore, it is not clear whether the position noise is not reduced or I am simply seeing the effect of B varying within Δx. None the less, by keeping the number of averages at one position fixed and varying the scanning speed, I obtained a reduction of the position noise, as shown in Fig. 7.14. However, the slower speed can also lead to less vibration and lower error in the encoder. Therefore, it is still hard to say what the source of the position noise correlation is. Although I could not definitively identify the source of the position noise, I found that averaging several scans and scanning slower both reduced its effect.

7.5 Applications of position noise results

The above results for an *x*-SQUID image of an infinite wire can be readily extended to other samples and SQUID arrangements. For example, the component of the magnetic field from an infinite wire measured by a z-SQUID configuration is given by,

$$B_z = \frac{\mu_0 I}{2\pi} \frac{x}{x^2 + z^2}. \qquad (7.13)$$

The maximum total magnetic field noise obtained by using Eq. (7.3) is

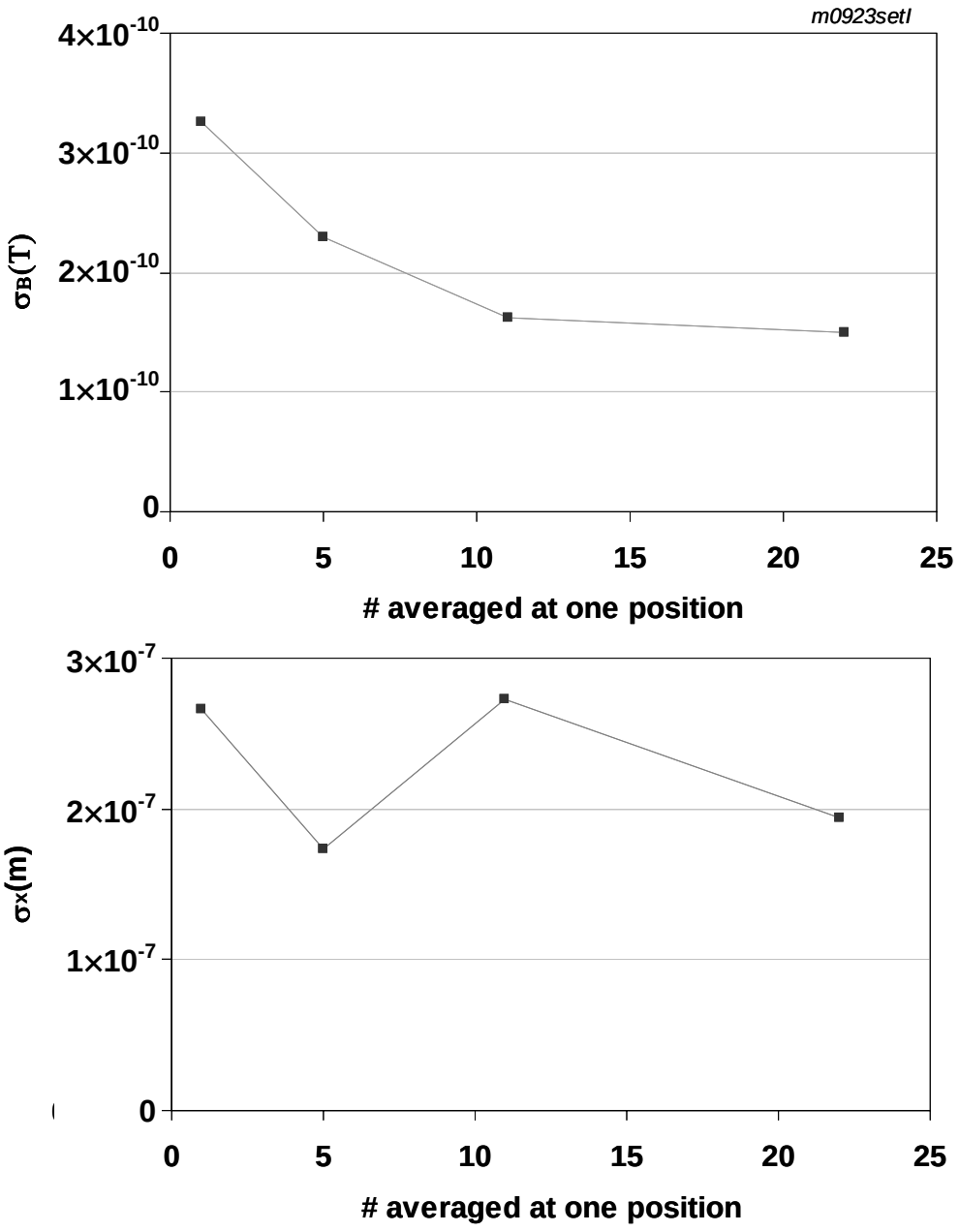

Figure 7.13: (a) SQUID noise σ_B and (b) position noise σ_x obtained from the total magnetic field noise by averaging at each x-position, plotted as a function of the number of averages.

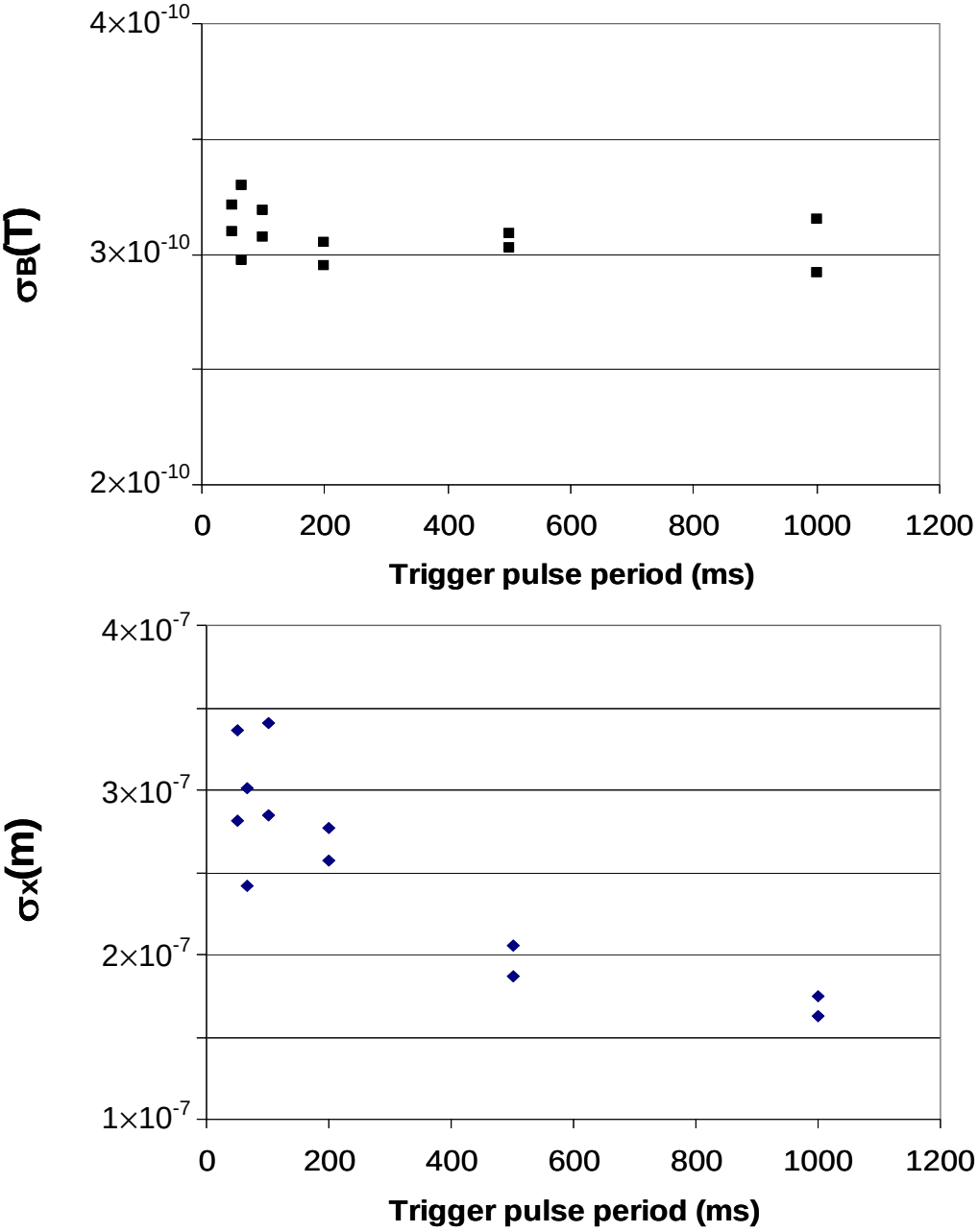

Figure 7.14: (a) Intrinsic SQUID noise and (b) position noise obtained from the magnetic filed noise by varying the trigger pulse period (time width between two pixles).

$$\sigma_B^{\max} = \sigma_B \sqrt{\left(\frac{\mu_0 I \, \sigma_x}{2\pi \, z^2 \sigma_B} \right)^2 + 1} \quad . \tag{7.14}$$

where the maximum occurs at $x = 0$. The criteria on the positioning will thus be

$$\sigma_x \leq \sigma_B \left(\frac{2\pi \, z^2}{\mu_0 I} \right), \tag{7.15}$$

which is quite similar, but not identical, to Eq. (7.12) which we found for the x-SQUID. I summarize the positioning requirement for some other common cases in Table 7.2. For example, for a magnetic flux line (vortex), the typical sensor-to-sample z is very close. If the z is 20 μm and σ_B is 0.2 nT, then the positioning requirement is 5.6 nm. This is a very tight requirement.

7.6 Conclusion

In conclusion, I have analyzed and observed the effect of position noise on magnetic field images and used these results to find the position noise in my scanning SQUID microscope. The smaller the sensor-sample separation, the greater the effect of position noise is on the total effective magnetic field noise. In particular, I have identified a parameter z_0 for which $z < z_0$ will lead to the noise in an image being dominated by position noise. Finally I note that the above results are not unique to SQUID microscope and analogous results will arise for raster scan imaging using other types of sensors at other length scales.

Table 7.2 Magnetic field and position noise limit for different sample and SQUID configurations. d is the distance between the two coils of a gradiometer, m is magnetic moment (m = I·area), c = 1.27, λ is the magnetic penetration depth [8] in a superconductor, and Δl is the length of a short current carrying wire. Last column gives value that σ_x must not exceed in order for the noise in the image to be dominated by the SQUID noise.

SQUID configuration	Sample	Magnetic signal	σ_x limit
x-SQUID	infinite wire	$\frac{\mu_0 I}{2\pi}\frac{z}{x^2+z^2}$	$\sigma_B\left(\frac{16\pi z^2}{3\sqrt{3}\mu_0 I}\right)$
z-SQUID	infinite wire	$\frac{\mu_0 I}{2\pi}\frac{x}{x^2+z^2}$	$\sigma_B\left(\frac{2\pi z^2}{\mu_0 I}\right)$
x-gradiometer	infinite wire	$\frac{\mu_0 I}{\pi}\frac{xz}{\left(x^2+z^2\right)^2}$	$\sigma_B\left(\frac{4\sqrt{2}\pi z^3}{\mu_0 I d}\right)$
z-SQUID	magnetic dipole	$\frac{3\mu_0 \mathrm{m}}{4\pi}\frac{y\,z}{\left(x^2+y^2+z^2\right)^{5/2}}$	$\sigma_B\left(\frac{1372\sqrt{35}\pi\, z^4}{1875\mu_0 \mathrm{m}}\right)$
z-SQUID	magnetic flux line	$\frac{\Phi_0}{2\pi}\frac{z+c\lambda}{\left(x^2+y^2+(z+c\lambda)^2\right)^{3/2}}$	$\sigma_B\left(\frac{50\sqrt{5}\pi(z+c\lambda)^3}{16\Phi_0}\right)$
x-SQUID	short current segment	$\frac{\mu_0 I}{4\pi}\frac{z\,\Delta l}{\left(x^2+y^2+z^2\right)^{3/2}}$	$\sigma_B\left(\frac{25\sqrt{5}\pi\, z^3}{12\mu_0 I\Delta l}\right)$

Chapter 8

The Effect of Position Noise on Spatial Resolution

In this chapter, I derive an analytical relationship between spatial resolution and position noise. I find that the closer the sample is to the sensor, the greater is the effect of position noise on the spatial resolution. In addition, I find how much the spatial resolution is improved by reducing position noise.

8.1 Introduction

After applying a magnetic inverse transformation [1] to typical SQUID images, one finds the spatial resolution in the resulting current density image can be improved by about 10 times compared to the raw magnetic field image [2]. For example, Figure 8.1 shows the improvement of spatial resolution in a simulation of an infinite straight wire with z = 250 μm. The black line is the simulated raw magnetic field and the gray line is the current density found by taking a magnetic inverse transformation of the simulated magnetic field. While the full width at half maximum (FWHM) of the magnetic field is 500 μm (= 2z), the FWHM of the current density (defined as "s") is 61 μm. The ratio is given by

$$\frac{\text{FWHM of magnetic field}}{\text{FWHM of current density}} = \frac{2z}{s} = 8.2\,. \qquad (8.1)$$

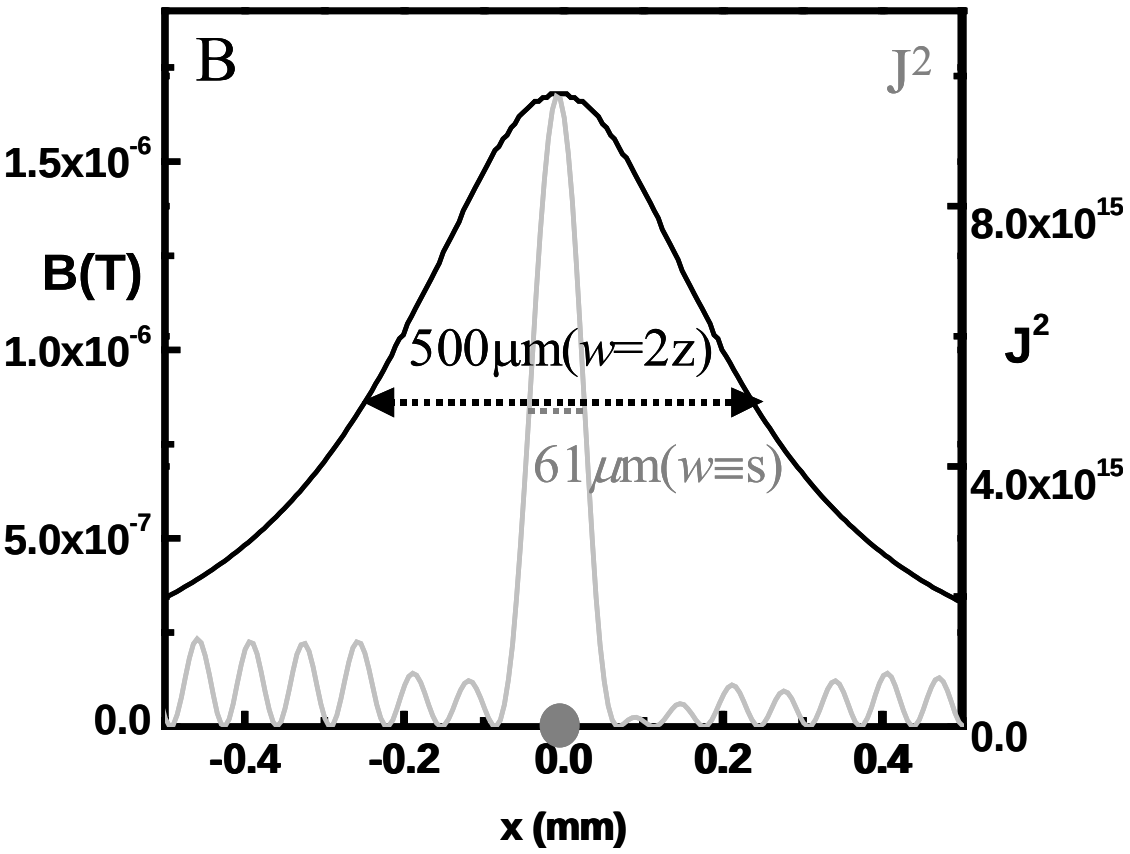

Figure 8.1: Full Width at Half Maximum (FWHM) of magnetic signal and current density image showing 8 times improvement of spatial resolution in current density domain obtained by using magnetic inverse technique. The FWHM in current density is defined as the spatial resolution "s".

Thus in this case the spatial resolution is improved by 8.2 times upon converting to a current density image. Chatraphorn *et. al*. found that one expects the maximum ratio of the sample-to-sensor distance z to spatial resolution s to be constant, determined only by the noise in the SQUID, the pixel size, and the current [3]. I note that this improvement is only possible because the data from a SQUID is quantitatively very precise and accurate, allowing a complicated transformation to be reliably performed without introducing significant distortion. However, this analysis did not include any effects from position noise. When the position noise is involved, the relationship needs to be modified.

8.2 Magnetic inverse technique

To make a current density image from a magnetic field image, one can use the "standard" magnetic inverse technique, as shown in Fig. 8.2. B. J. Roth, *et. al*. have described this technique in detail [4]. For completeness, I now describe this procedure briefly for the *x*-SQUID configuration I use [3].

From the Bio-Savart law, the *x*-component of the magnetic field produced by a current density is

$$B_x(x,y,z) \approx \frac{\mu_o d}{4\pi} z \int_{-\infty}^{\infty}\int_{-\infty}^{\infty} \frac{J_y(x',y')}{[(x-x')^2+(y-y')^2+z^2]^{3/2}}\, dx'\, dy', \qquad (8.2)$$

where $\mu_0 = 4\pi \times 10^{-7}\,\mathrm{T \cdot m / A}$ is the permeability of free space, $J_y(x,y)$ is the y component of the current density, and the approximation arises because I have assumed the current is confined to a thin non-magnetic conducting sheet with thickness d at z = 0. What I want to get is the current density, given that I have experimentally obtained

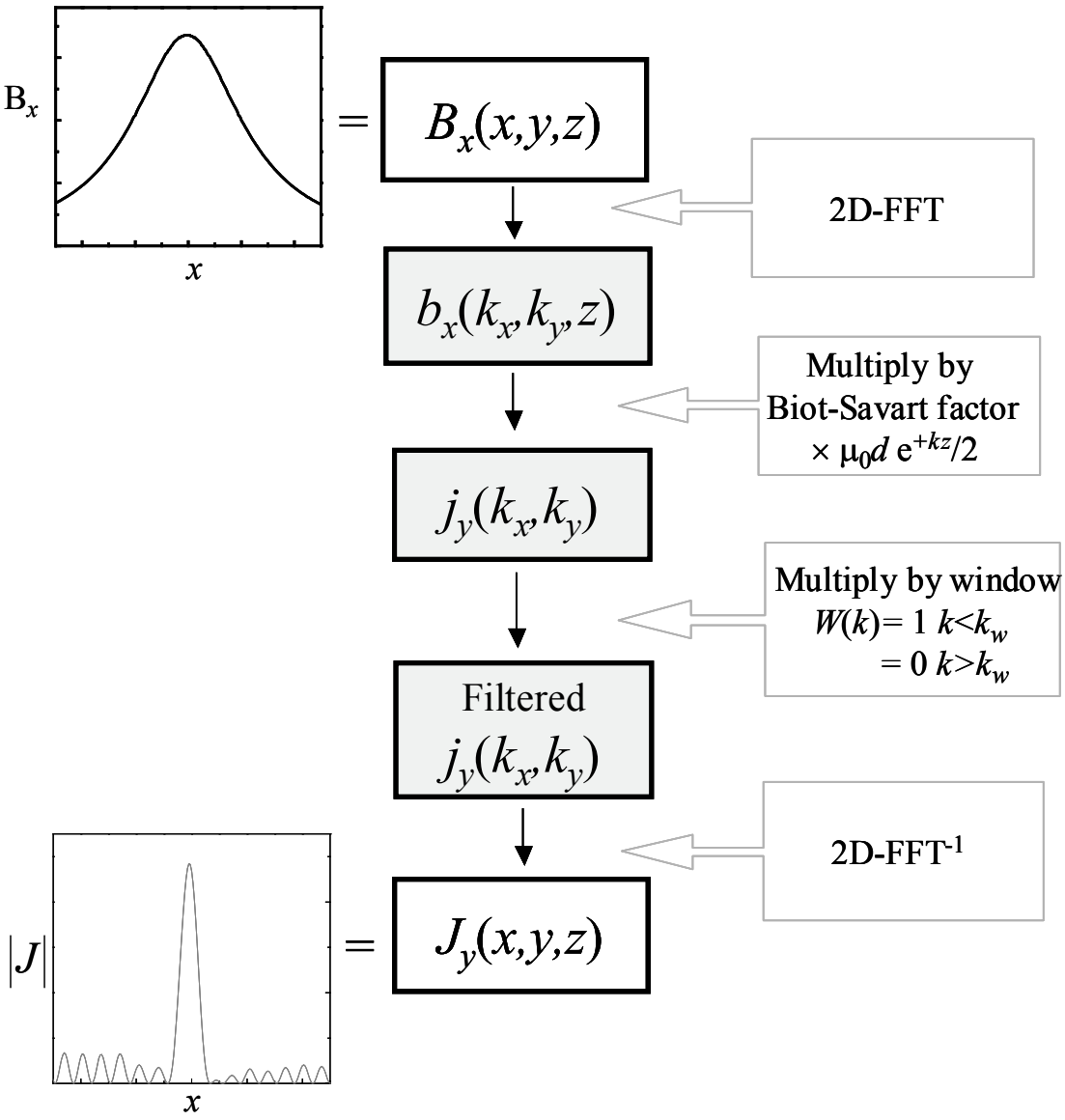

Figure 8.2: Summary of standard magnetic inverse technique [4].

magnetic fields. If I define the Green's function G(x-x', y-y', z) as

$$G(x-x', y-y', z) = \frac{\mu_0 d}{4\pi} \frac{z}{\left[(x-x')^2 + (y-y')^2 + z^2\right]^{3/2}}. \qquad (8.3)$$

Then, Eq.(8.2) can be rewritten as,

$$B_x(x,y,z) \approx \int_{-\infty}^{\infty}\int_{-\infty}^{\infty} G(x-x', y-y', z) J_y(x', y')\, dx'\, dy' \ . \qquad (8.4)$$

Applying a 2-D Fourier transform to both sides, one finds

$$b_x(k_x, k_y, z) = g(k_x, k_y, z) \cdot j_y(k_x, k_y), \qquad (8.5)$$

where $j_y(k_x, k_y)$ is the *y*-component of the current density in *k*-space and $g(k_x, k_y, z)$ is the Fourier transform of the Green's function. Fortunately, $g(k_x, k_y, z)$ has a simple analytical form :

$$g(k_x, k_y, z) = \frac{\mu_0 d}{2} e^{-kz}, \qquad (8.6)$$

where $k = (k_x^2 + k_y^2)^{1/2}$.

Using Eqs (8.5) and (8.6), the *y*-component of the current density in k-space can be written as:

$$j_y(k_x, k_y) = \frac{2e^{kz}}{\mu_0 d} b_x(k_x, k_y, z). \qquad (8.7)$$

I note that b_x can be obtained by taking a 2-D Fourier transform of the measured magnetic field data.

By taking an inverse Fourier transform of Eq.(8.7) , I can obtain the current density in real space. However there is another step to consider before the transform. In Eq. 8.7, notice that high spatial frequency magnetic field data is amplified by the exponential term e^{kz}. Since white noise from the SQUID will cause the field to vary

from pixel to pixel, it will appear in k-space as white noise that extends to a high spatial frequency. Therefore, the noise will be amplified at high k. To prevent too much noise from being amplified, a filter is required in k-space. To do this I apply filter function $f(k)$ to Eq. (8.7), and write :

$$j_y(k_x,k_y)=\frac{2e^{kz}}{\mu_0 d}b_x(k_x,k_y,z)\cdot f(\bar{k}), \qquad (8.8)$$

where I can define a cutoff k_w such that $f(k)$ is zero when $|\bar{k}| \geq k_w$. In practice I usually use a hard cutoff filter : $f(k) = 1$ when $k = |\bar{k}| \leq k_w$ and $f(k) = 0$ otherwise.

By taking an inverse Fourier transform of Eq.(8.8), I can obtain the current density in real space. Depending on the cutoff spatial frequency k_w, the current density looks different. If k_w is too large, the magnified white noise obscures the signal from the current source. If k_w is too low, the white noise is cut off, but so is signal from the current source, while it causes broadening of the peak.

To illustrate what happens, Figs 8.3(a)~(c) show J^2 for (a) $k_w = 8\times2\pi\times10^3$ m^{-1}, (b) $k_w = 10.1\times2\pi\times10^3$ m^{-1}, and (c) $k_w = 10.5\times2\pi\times10^3$ m^{-1}. In Fig. 8.3(c), the signal is hidden by "edge artifacts" that have been greatly amplified at high k_w. On the other hand, Figure 8.3(a) shows broadening of the FWHM of the peak compared with Fig. 8.3(b) due to use of a small k_w. In general, one wants good spatial resolution but not too much noise, and thus k_w can neither be too large or too small.

8.3 Analytical relation between z and s including position noise

To obtain an analytical relationship between z and s, I have to find an analytical form for the current density J and its noise ΔJ when position noise is present.

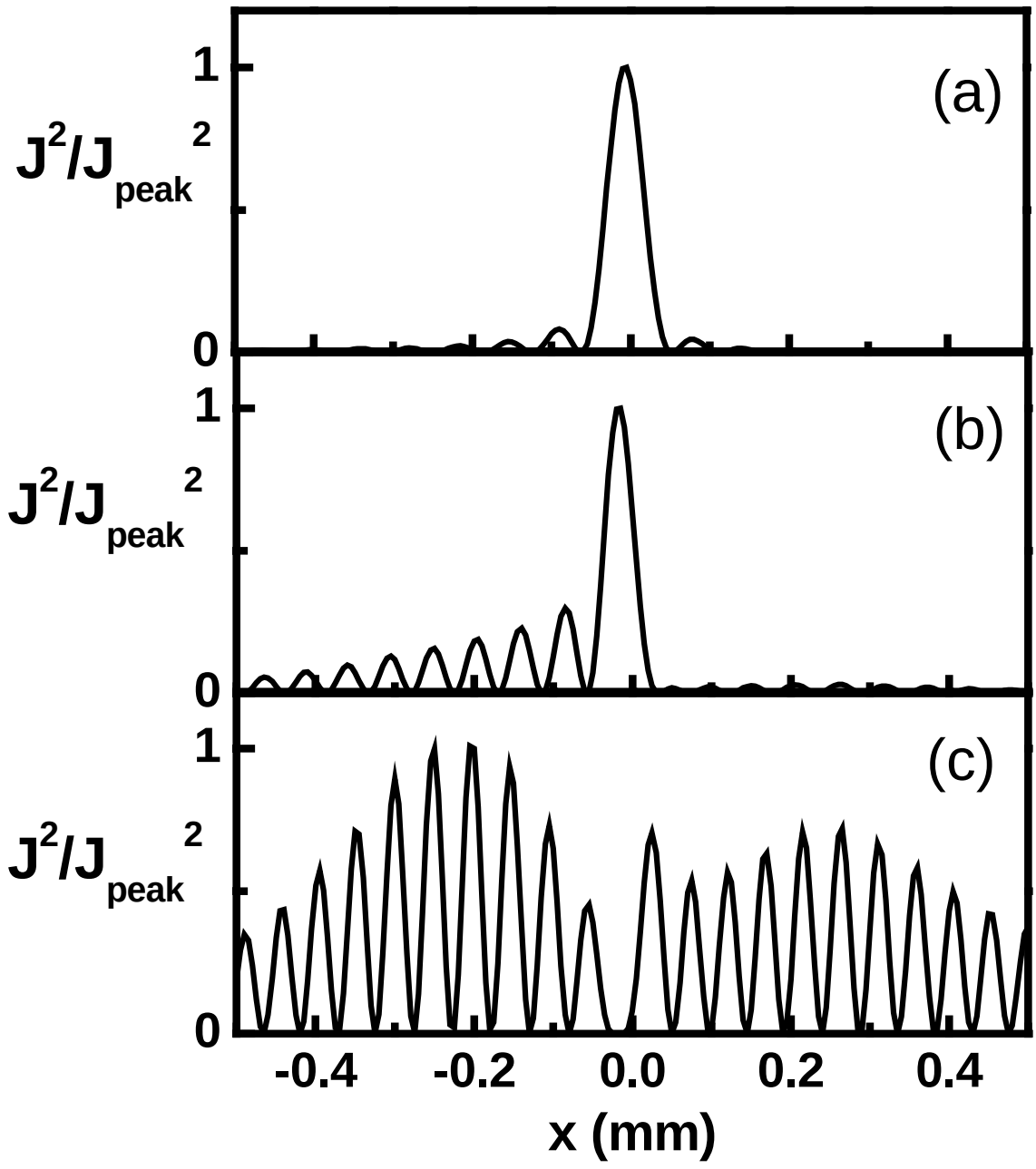

Figure 8.3: Squared current density for different cutoff spatial frequencies k_w. (a) $k_w = 8\times2\pi\times10^3$ m^{-1}, (b) $k_w = 9.5\times2\pi\times10^3$m^{-1}, (c) $k_w = 10.1\times2\pi\times10^3$ m^{-1}, and (d) $k_w = 10.5\times2\pi\times10^3$ m^{-1}.

8.3.1 **Current density noise with position error (ΔJ^2)**

For simplicity, I will assume that the spatial frequency k_x is always much smaller than the inverse of pixel length Δx, i.e. $k_x \Delta x \ll 1$. In order to understand how noise affects a magnetic field image, we consider a single pixel of noise B_0 at x_i and y_i with pixel size $A=\Delta x \Delta y$. Taking the Fourier transform of the magnetic field,

$$B_x(x,y) = \begin{cases} B_0 & \text{if } \dfrac{-\Delta x}{2} < x < \dfrac{\Delta x}{2} \text{ and } \dfrac{-\Delta y}{2} < y < \dfrac{\Delta y}{2} \\ 0 & \text{otherwise} \end{cases} \quad (8.9)$$

yields:

$$b_x(k_x,k_y) = \int_{-\Delta y/2}^{\Delta y/2}\int_{-\Delta x/2}^{\Delta x/2} e^{i(k_x x + k_y y)} B_0 \, A\, dx\, dy \approx B_0 A \,. \quad (8.10)$$

Substituting into Eq. (8.8), I can write the y-component of the current density in k-space as

$$j_y(k_x,k_y) = \frac{2e^{kz}}{\mu_0 d} B_0 A \cdot f(\bar{k}) \,. \quad (8.11)$$

Taking the inverse Fourier transform of the current density, the current density $J_y^F(x,y)$ in real space is.

$$\begin{aligned} J_y^F(x,y) &= \frac{1}{(2\pi)^2}\int \frac{2B_0 A}{\mu_0 d} e^{kz} e^{i\vec{k}\cdot\vec{r}} f(k) d\vec{k} \\ &= \frac{1}{(2\pi)^2}\frac{2B_0 A}{\mu_0 d}\int_0^{k_w} \left(\int_0^{2\pi} e^{ikr\cos\alpha} d\alpha\right) e^{kz} k dk \end{aligned} \quad . \quad (8.12)$$

where $r = (x^2+y^2)^{1/2}$ and α is angle between $\vec{k}$ and $\vec{r}$. Using integral table [5], Eq. (8.12) yields

$$J_y^F(x,y) = \frac{1}{(2\pi)^2}\frac{2B_0 A}{\mu_0 d}\int_0^{k_w} 2\pi J_0(kr) e^{kz} k dk \quad (8.13)$$

here J_0 is the zero order Bessel function of the first kind. Then the resulting square of the *y*-component of the current density due to the single pixel of magnetic field in real space is.

$$\left|J_y^F(x,y)\right|^2 = \left(\frac{B_0 A}{\pi\mu_0 d}\right)^2 \left(\int_0^{k_w} k e^{kz} J_0(kr)dk\right)^2 . \qquad (8.14)$$

Evaluating Eq. (8.14) numerically reveals that the current density $|J_y^F|^2$ decays as $1/r^3$ (see Fig. 8.4).

Now suppose that there is noise in every pixel in the image. Since we have N pixels in the scanning area and each pixel will have noise, the total current density due to the noise will be the superposition of N single pixel current densities, each centered at their respective pixel,

$$J_y(x,y) = \sum_{i=1}^{N} J_y^F(x-x_i, y-y_i)\frac{B_i}{B_0} . \qquad (8.15)$$

where B_i is the noise at *i*-th pixel.

The mean square deviation of the *y*-component of current density is,

$$\sigma_{Jy}{}^2 = [\Delta J_y(x,y)]^2 = \sum_{i=1}^{N} \left|\frac{\partial J_y(x-x_i, y-y_i)}{\partial B_i}\right|^2 (\sigma_{Btotal,i})^2 , \qquad (8.16)$$

where $\sigma_{Btotal,i}$ is the rms total effective field noise at *i*-th pixel. By substituting the total magnetic field noise $\sigma_{Btotal,i}$ from Eq. (7.5) into Eq. (8.16), I find ,

$$\sigma_{Jy}{}^2 = \sum_{i=1}^{N} \left|J_y^F(x-x_i, y-y_i)\right|^2 \left(\frac{\sigma_{B,i}}{B_0}\right)^2 \left(1 + \left\{\frac{\mu_0 I}{2\pi}\frac{2x_i z}{(x_i{}^2 + z^2)^2}\frac{\sigma_x}{\sigma_{B,i}}\right\}^2\right), \qquad (8.17)$$

If we assume a small pixel size, $\Delta x \ll 1/k_{w,}$ we can replace the discrete sum by an integral over *x* and *y*,

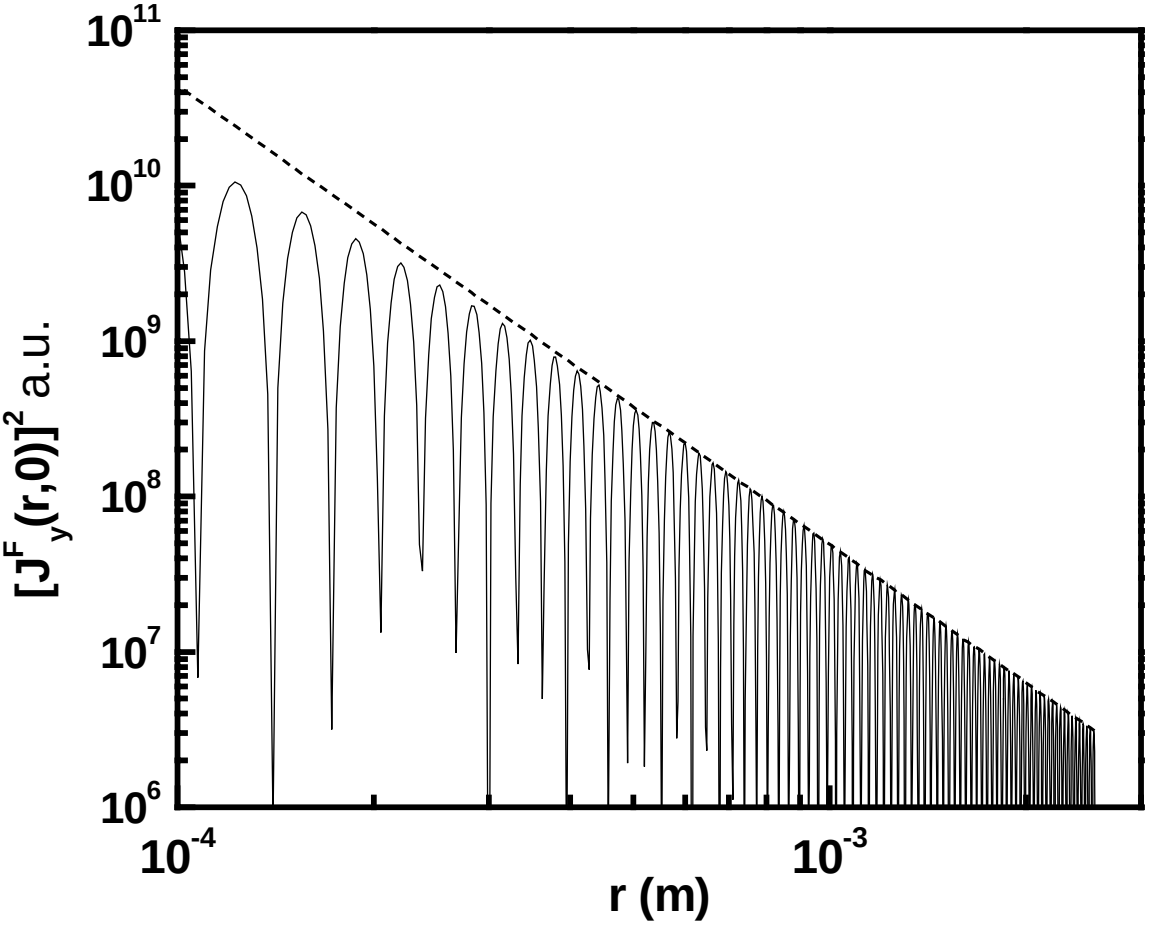

Figure 8.4: *r*-dependence of squared current density $\left|J_y\right|^2$ from single pixel field noise. The solid line is calculated numerically from Eq. (8.14) and the dashed line scales as $1/r^3$.

$$\sigma_{Jy}{}^2 \cong (\frac{\sigma_B}{B_0})^2 \int_{-L/2}^{L/2}\int_{-L/2}^{L/2} \left| J_y{}^F(x-x', y-y') \right|^2 \left(1 + \left(\frac{\mu_0 I}{2\pi} \frac{2zx'}{(x'^2+z^2)^2} \frac{\sigma_{x'}}{\sigma_B} \right)^2 \right) \frac{N}{L^2} dx'dy' ,$$

(8.18)

where N is the total number of pixels and L is the length of the scanned region, which is the same in the x and y directions. In addition, here we have assumed the intrinsic SQUID noise does not depend on position, and replaced $\sigma_{B,}$ by σ_B. Note that at $x' = z/\sqrt{3}$, the position noise term is maximum. To evaluate Eq. (8.18) approximately, we remove the dependence on x by assuming the troublesome term is constant and equal to its maximum value. The mean squared current density then becomes,

$$\sigma_{Jy}{}^2 \cong \left(\frac{\sigma_B}{B_0} \right)^2 \left(1 + \left\{ \frac{3\sqrt{3}}{16} \frac{\mu_0 I \sigma_x}{\pi z^2 \sigma_B} \right\}^2 \right) \int_{-L/2}^{L/2}\int_{-L/2}^{L/2} \left| J_y{}^F(x-x', y-y') \right|^2 \frac{N}{L^2} dx'dy' \quad (8.19)$$

The current noise should be random and the r.m.s. value should not depend on where we are in the position. Thus Eq. (8.19) should not depend on location, and we can set $x = 0$, and $y = 0$ for simplicity. Also, as can be seen in Fig. 8.4, $|J_y^F(x, y)|^2$ is only significant near the origin and decays as $1/r^3$, so we can extend the integration range to $\pm\infty$ provided L ≫ z. Therefore, the standard deviation of the current density is

$$\sigma_{Jy}^2 \cong \left(\frac{\sigma_B}{B_0} \right)^2 \left(1 + \left\{ \frac{3\sqrt{3}}{16} \frac{\mu_0 I \sigma_x}{\pi z^2 \sigma_B} \right\}^2 \right) \frac{N}{L^2} \int_{-\infty}^{\infty}\int_{-\infty}^{\infty} \left| J_y{}^F(x, y) \right|^2 dxdy . \qquad (8.20)$$

Using Parceval's theorem, we can write this equation as an integration in k-space:

$$\sigma_{Jy}^2 \cong \left(\frac{\sigma_B}{B_0} \right)^2 \left(1 + \left\{ \frac{3\sqrt{3}}{16} \frac{\mu_0 I \sigma_x}{\pi z^2 \sigma_B} \right\}^2 \right) \frac{N}{L^2} \frac{1}{(2\pi)^2} \int_{-\infty}^{\infty}\int_{-\infty}^{\infty} \left[\left| j_y^F(k_x, k_y) \right|^2 \right] dk_x dk_y \quad (8.21)$$

Using the result for j_y^F given in Eq. (8.8) and using a hard cutoff filter function $f(k)$ at $k = k_w$, we find :

$$\sigma_{Jy}^2 = \left(1+\left\{\frac{3\sqrt{3}}{16}\frac{\mu_0 I\sigma_x}{\pi z^2\sigma_B}\right\}^2\right)\left(\frac{2\sigma_B\Delta x}{\pi\mu_0 d}\right)^2\int_{-\infty}^{\infty}\int_{-\infty}^{\infty}e^{2kz}\,f(k)\,dk_x dk_y\,,$$

$$=\left(1+\left\{\frac{3\sqrt{3}}{16}\frac{\mu_0 I\sigma_x}{\pi z^2\sigma_B}\right\}^2\right)\left(\frac{2\sigma_B\Delta x}{\pi\mu_0 d}\right)^2\int_0^{k_w}e^{2kz}\,2\pi k dk\,,$$

$$=\left(1+\left\{\frac{3\sqrt{3}}{16}\frac{\mu_0 I\sigma_x}{\pi z^2\sigma_B}\right\}^2\right)\frac{1}{2\pi}\left(\frac{\Delta x\cdot\sigma_B}{\mu_0 d z}\right)^2\cdot\left[e^{2k_w z}(2k_w z-1)+1\right], \quad (8.22)$$

where we have used $NA=L^2$, and $A=(\Delta x)^2$ with Δx the width of a single pixel, assuming a square scanning area.

We define the mean squared current density without position noise as σ_{J0}^2 and find it by setting σ_x to zero in Eq. (8.22). Thus :

$$\sigma_{J0}^2 \equiv \frac{1}{2\pi}\left(\frac{\Delta x\cdot\sigma_B}{\mu_0 d z}\right)^2\cdot\left[e^{2k_w z}(2k_w z-1)+1\right]. \quad (8.23)$$

The mean squared current density including position noise is then simply,

$$\sigma_{Jy}^2 \cong \left(1+\frac{z_0^{\,4}}{z^4}\right)\sigma_{J0}^2, \quad (8.24)$$

where $z_0^{\,2} \equiv \frac{3\sqrt{3}}{16}\frac{\mu_0 I\sigma_x}{\pi\sigma_B}$.

To check this calculation, I generated sample magnetic field images without and with position noise. The magnetic field image shown in Fig. 8.5(b) is generated for σ_B = 0.18 nT, Δx = 5 μm, I = 4.8 mA, z = 200 μm and $k_w = 2\pi \times 11$ mm^{-1} without position noise. Figure 8.5(a) is a line-section through this image. The magnetic field image in

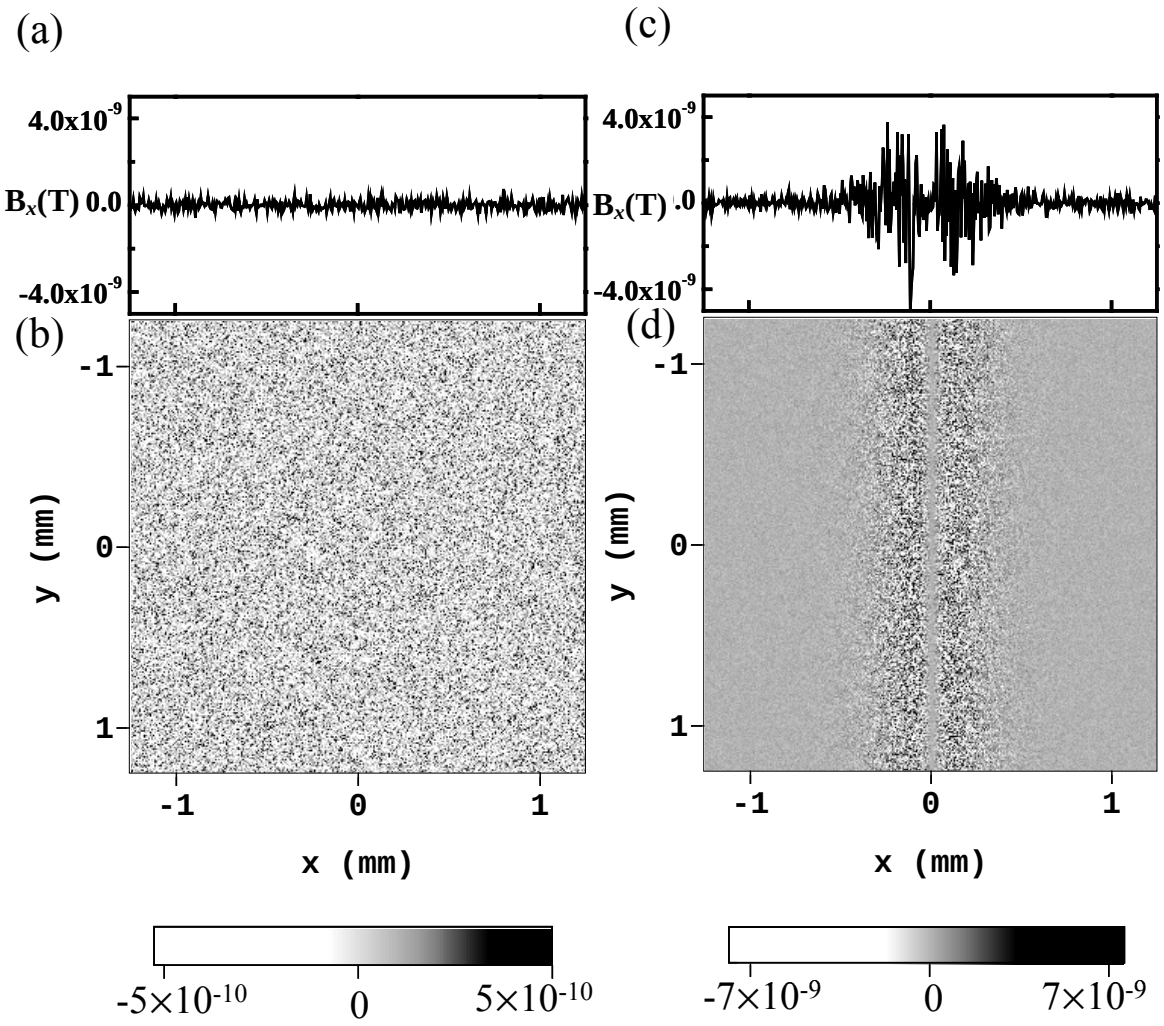

Figure 8.5: (a) and (b) Magnetic field noise without position noise generated randomly with σ_B = 0.1nT, z = 150 μm, I = 5 mA, Δx = 10 μm, and (c) and (d) magnetic field noise with position noise with σ_x=1μm. The line graphs on top are line-section through the lower images.

Fig. 8.5(d) uses the same parameters as Fig. 8.5(b) except that I have included position noise with σ_x = 0.145 μm. Fig. 8.5(c) is a line-section through Fig. 8.5(d). The current density image corresponding to Fig. 8.5(d) is shown in Fig. 8.6, obtained by the standard magnetic inverse technique [1,2]. The standard deviation of the current density (without position noise) in Fig. 8.6(b) is (2.168±0.501)×10^{12} A^2/m^4. The σ_{J0}^2 from Eq. (8.23) yields 2.184×10^{12} A^2/m^4, in good agreement with the simulated result.

When position noise is included, the standard deviation of the current density is a maximum near $x = \pm z/\sqrt{3}$ where it reaches (1.47±0.30)×10^{14} A^2/m^4 while the $\sigma_J(0,0)^2$ from Eq.(8.24) yields 3.45×$10^{14}$$A^2/m^4$, which is higher than the inverted current density deviation from the simulated B-field. Of course in Eq. (8.20), we overestimated the position noise by setting it equal to the maximum value, while the actual position noise is *x*-dependent and rolls off away from the wire. That is probably why the result from the calculation is larger than that from the full simulation. As a check when I filled all the area with the maximum field noise induced from the position noise at the center and inverted this to obtain a current density image, I obtained (3.41±0.742)× 10^{14} A^2/m^4 for the standard deviation of current density. This error in the calculation of ΔJ^2 with position noise is annoying but probably acceptable since the difference between the current density without position noise and the current density with position noise is 2 orders of magnitude.

8.3.2 **Spatial resolution with position noise**

Prior work in our group showed that the spatial resolution of the current density image using the inverse technique can be up to about 10 times better than that for the

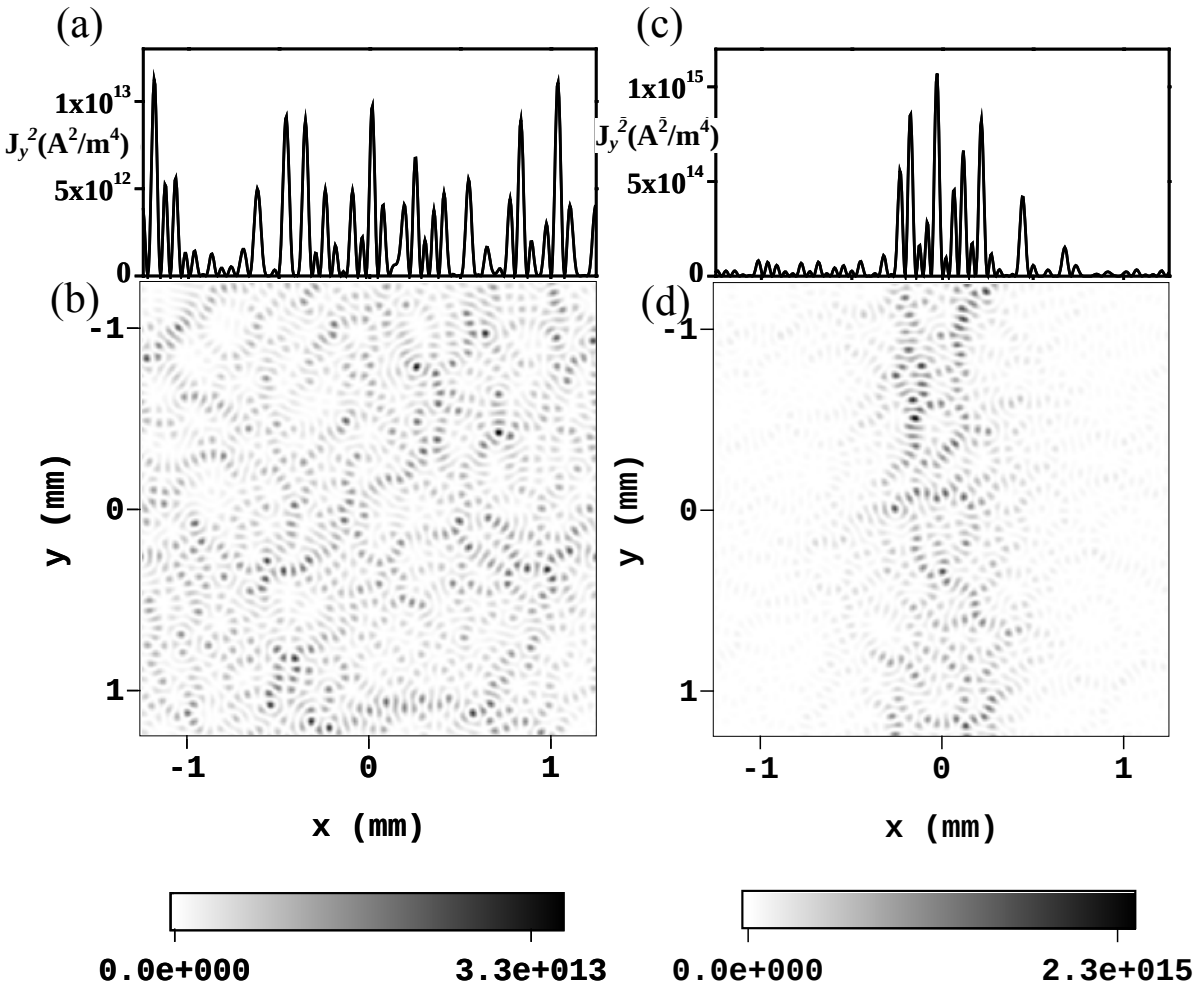

Figure 8.6: (b) Squared current density noise found by inverting the magnetic field noise in Fig. 8.5 (b) by using magnetic inverse transformation with $k_w = 10.5 \times 2\pi \times 10^3$ m^{-1}, and (d) current density noise found from Fig. 8.5(d) with $k_w = 10.5 \times 2\pi \times 10^3$ m^{-1}. The graphs (a) and (c) show the line section through the corresponding image.

raw magnetic field image. It was also found that z/s depends linearly on $\ln[I/\Delta x\cdot\sigma_B]$, so for a given I, Δx, and σ_B, z depends linearly on s [2]. This result did not include any effects from position noise.

To find the spatial resolution in a current density image when position noise is present, I consider the magnetic field generated by a current I flowing through a thin and infinitely long wire along the y-direction. The current density in the final image will just be :

$$J_x(x,y)=0\ , \qquad J_y(x,y)=\frac{I\,k_w}{\pi\,d}\frac{\sin(k_w x)}{k_w x}, \tag{8.25}$$

where d is the thickness of the wire and k_w is the cutoff spatial frequency used in the filter function. We define the spatial resolution s as the full width at half-maximum (FWHM) of the squared current density J_y^2. Plotting Eq (8.25), one finds that s is given by [2]

$$s = \frac{2.783}{k_w}. \tag{8.26}$$

From Eq. (8.24) and (8.25), we obtain the maximum signal to noise ratio, S/N, in the current density image including position noise at $x = 0$, $y = 0$,

$$S/N \equiv \frac{J_y^2(0,0)}{{\sigma_{Jy}}^2} = \frac{\left(\frac{Ik_w}{\pi d}\right)^2}{\left(1+\frac{{z_0}^4}{z^4}\right)\frac{1}{2\pi}\left(\frac{\Delta x\cdot\sigma_B}{\mu_0\,d\,z}\right)^2\cdot\left[e^{2k_w z}(2k_w z-1)+1\right]}. \tag{8.27}$$

Inserting k_w=2.783/s, we can eliminate k_w from Eq. (8.27) to find :

$$\frac{z}{s} = \frac{1}{2\times 2.783}\ln\left\{\frac{\frac{2\pi}{S/N(1+{z_0}^4/z^4)}\left[\frac{2.783\mu_0 I}{\pi\,\Delta x\cdot\sigma_B}\left(\frac{z}{s}\right)\right]^2-1}{2\times 2.783\left(\frac{z}{s}\right)-1}\right\}. \tag{8.28}$$

By substituting $z_0 = 0$ in Eq. (8.28), this reduces to the Chatraphorn *et al*. results for *z/s* without position noise. As described earlier, without position noise, z/s is a constant for a given I, Δx, $\sigma_{B,}$ and *S/N,* since z and s only enter in the ratio z/s. However, when position noise is included, *z/s* becomes z dependent, since now z no longer occurs just in z/s terms. The solid line in Fig. 8.7 shows z/s vs. z with I = 2.1 mA, Δx = 5 μm, *S/N* = 1, and $\sigma_B = 1$ pT. I obtained z_0 = 6.43 mm using $z_0 \equiv \sqrt{3\sqrt{3}\mu_0 I\sigma_x/(16\pi\sigma_B)}$ in Ch. 7. The upper solid trace is calculated with no position noise and the lower solid trace is calculated with $\sigma_x = 0.15$ μm. I note that the spatial resolution s is still reduced if z is reduced even when position noise is present, but the relation is not linear in z when z < z_0 (see Fig. 8.8).

8.4 Results

8.4.1 z/s vs. z (simulation)

To check the calculation I used generated random magnetic field noise and took a magnetic inverse transformation. By changing k_w, I can obtain different spatial resolution in the current density image. Since noise extends to high spatial frequency, a large k_w makes the noise exponentially large in the current density image (see Eq. (8.7)). However, if k_w is too small, the spatial resolution becomes worse. In fact, when large k_w is used, one also can run into problems with discontinuity at the edge (see section 8.4.2). We can reduce this edge effect by using a Manhattan filter [2] or a π-2π filter [6].

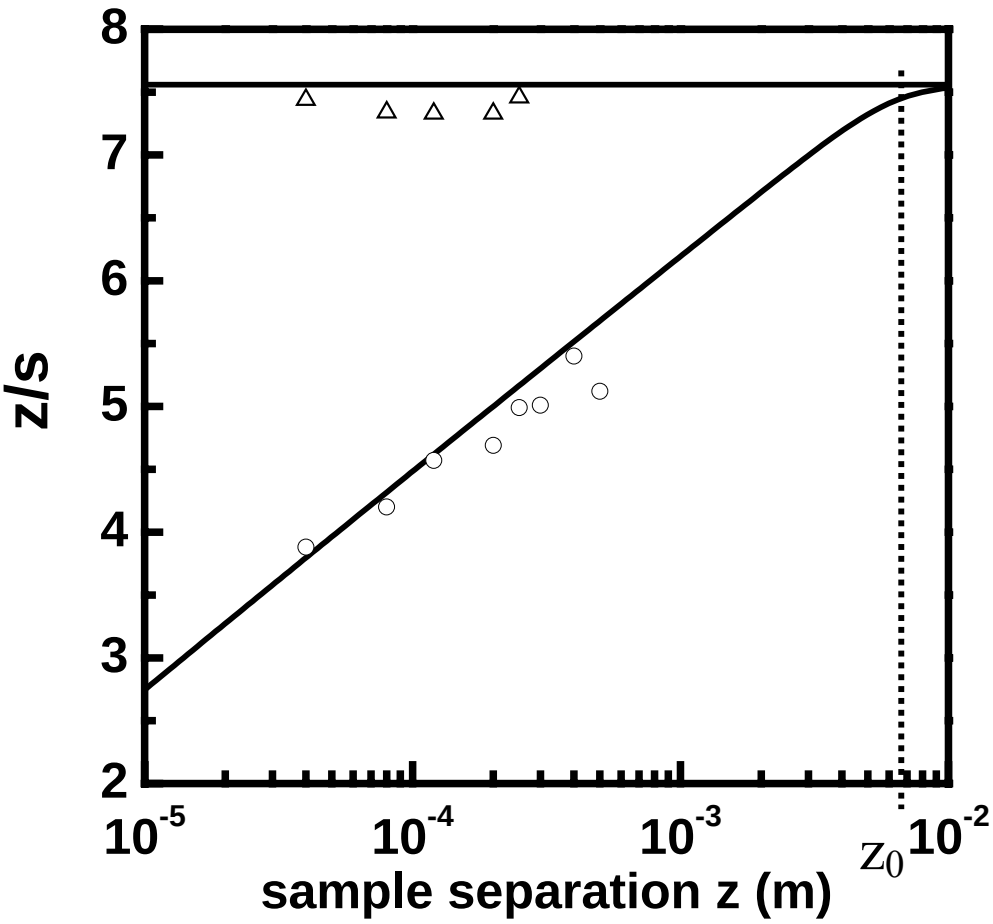

Figure 8.7: Ratio of sample separation z to spatial resolution s as a function of z, where I = 5mA, Δx = 5 μm, S/N = 1, σ_x = 0.15 μm, and σ_B = 1 pT (z_0 = 6.41 mm). The lines indicate numerically calculated z/s and symbols are obtained by optimizing k_w from simulated magnetic field noise. The upper trace is for no position noise and the lower trace is when position noise is included. (raw data: sim10101~14)

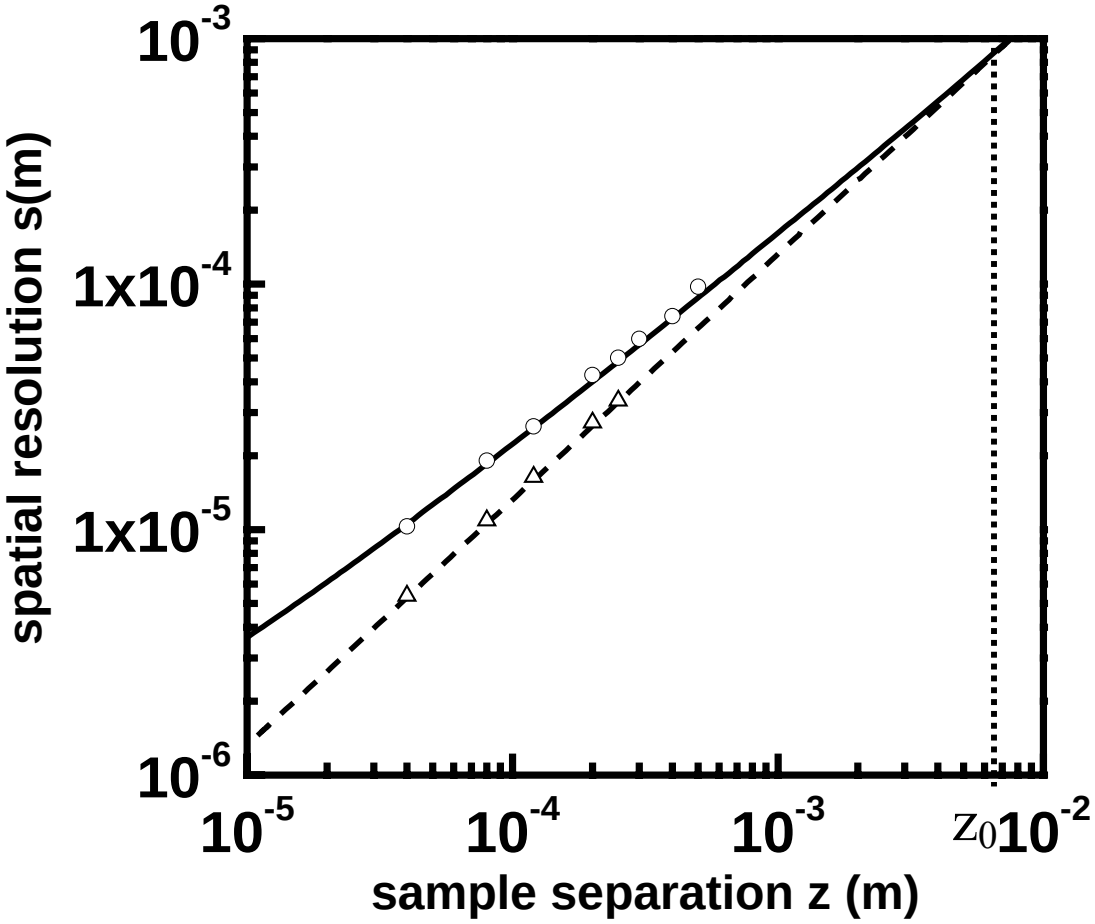

Figure 8.8: Spatial resolution s versus sample separation z for I = 5mA, Δx = 5 μm, S/N = 1, and σ_B = 0.1nT (z_0 = 6.41 mm). The solid line indicates numerically calculated z/s and symbols are values obtained by optimizing k_w from simulated magnetic field noise. The upper trace is for σ_x = 0.15 μm position noise and lower trace is for σ_x = 0. Note that s always decrease with z, even when position noise is present.(raw data: sim10101~14)

As we vary k_w, we can find the k_w which makes a specific signal to noise ratio S/N in a current density image. We could choose a fixed value of, for example, 1 for the S/N. Figure 8.3(a) shows that if we choose a smaller k_w, the signal in the center is very clear, but the FWHM is larger. Figure 8.3(c) shows that the signal is buried by edge effects for larger k_w. In this way, I found $k_w \cong 65$ mm^{-1} in Fig. 8.3(b) and (c) for S/N = 1. The squared current density in Fig 8.3 was normalized by dividing all values by the maximum value. The spatial resolution is found for the optimized k_w from $s = 2.783/ k_w$. The symbols in Figs. 8.7 and 8.8 are from this procedure. The triangles indicate the result without position noise and circles indicate the result with position noise. Both of them are in good agreement with the curves calculated using Eq. (8.28).

8.4.2 z/s vs. z (experiment)

The above results were all on simulated magnetic field data with simulated noise. For comparison, I also measured the magnetic field from a straight wire carrying I = 4.8 mA at different z. These results were presented in Ch. 7.4. The x scanning step size was 20 μm, and the position noise and intrinsic magnetic field noise were σ_x = 0.144 μm and σ_B = 0.179 nT. The solid line in Fig 8.9 is calculated using Eq. (8.28). The data points in Fig. 8.9 were found using the procedure described in section 8.4.1 applied to the measured magnetic field data.

In the actual experiment, the z was limited by a crack in my multi-channel SQUID chip (see Ch 5.4.1). (For this position noise experiment, there is no need to use

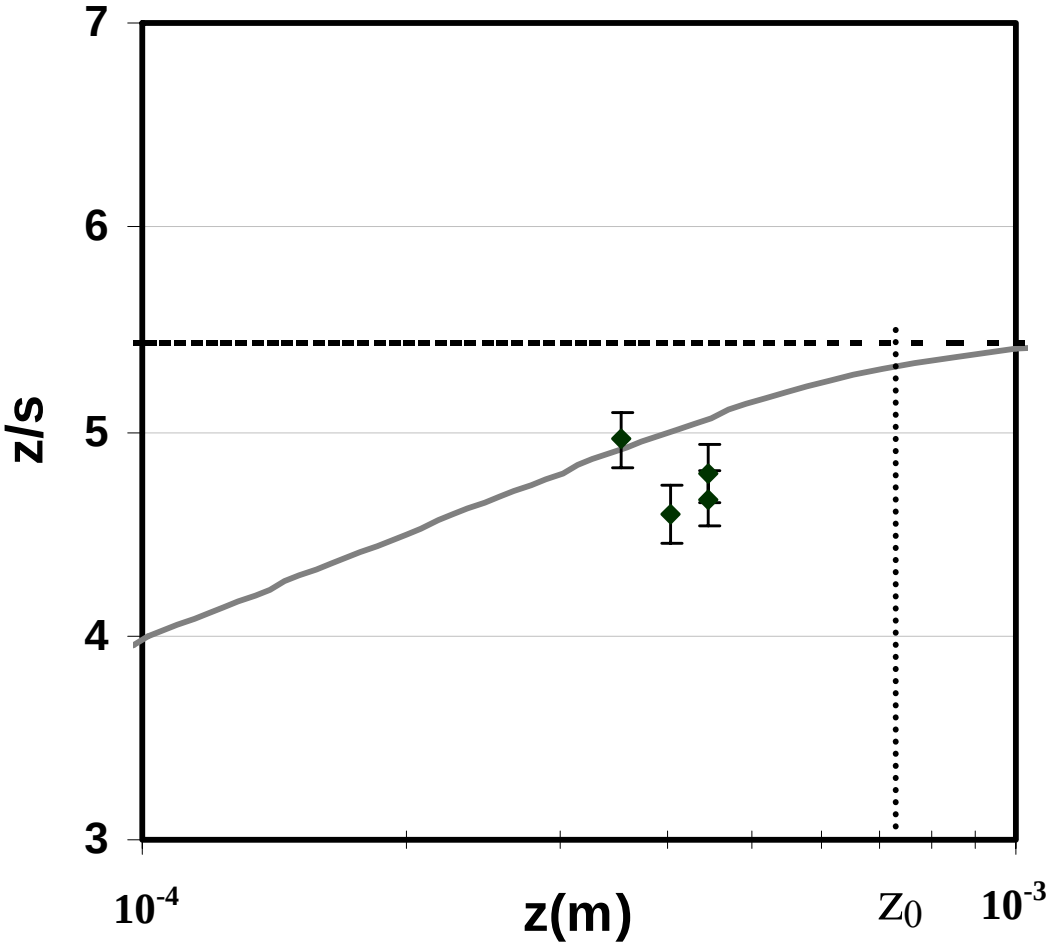

Figure 8.9: Ratio of sample separation z to spatial resolution s as varying z where I = 4.8mA, Δx = 20μm, S/N = 1, and σ_B = 0.178nT (z_0 = 711 μm). The lines indicate numerically calculated z/s and symbols is obtained by optimizing k_w from measured magnetic field. The upper trace is for no position noise and the lower trace is for position noise existence.(raw data: m042812~20)

the multi-channel system, but it was available.) That is why I did not take data below z = 330 μm. Above 500 μm, another limitation is involved. Since the scanning area is limited and signal at the edge is not completely zero, a large artifact is generated due to the discontinuity in the field at the edge. If the maximum signal is strong compared with the field at the edge and the signal at the edge is at the white noise level, as shown in Fig. 8.10, the optimized k_w will be what I expect from the above discussion. However, if the field at the edge is not negligible compared with the signal of the wire and the field discontinuity at the edge is much larger than the white noise level, as shown in Fig. 8.10, then the optimized k_w will be some k_{w2}, which is lower than what one would expect without an edge effect.

Figure 8.11(a) shows the current density at optimized k_w without edge effect. Figure 8.11(b) shows the current density when the edge effect is significant. The lower value of k_w means a smaller z/s because s = 2.783/k_w (Eq. (8.26)). That is why I have underestimated z/s above z = 400 μm in Figs 8.7 and 8.9. Even if I use additional filters to minimize the edge effect [6], I still face problems above z = 400 μm.

Nevertheless, the experimental results at between z = 300 μm and z = 500 μm agree reasonably well with the analytical form in Eq. (8.28).

8.4.3 **Reducing position noise**

In Ch. 7.5 I showed that the position noise can be reduced by averaging several scans and by reducing scanning speed. In this section, I analyze the effect of the reduced position noise on the spatial resolution. To compare the result without

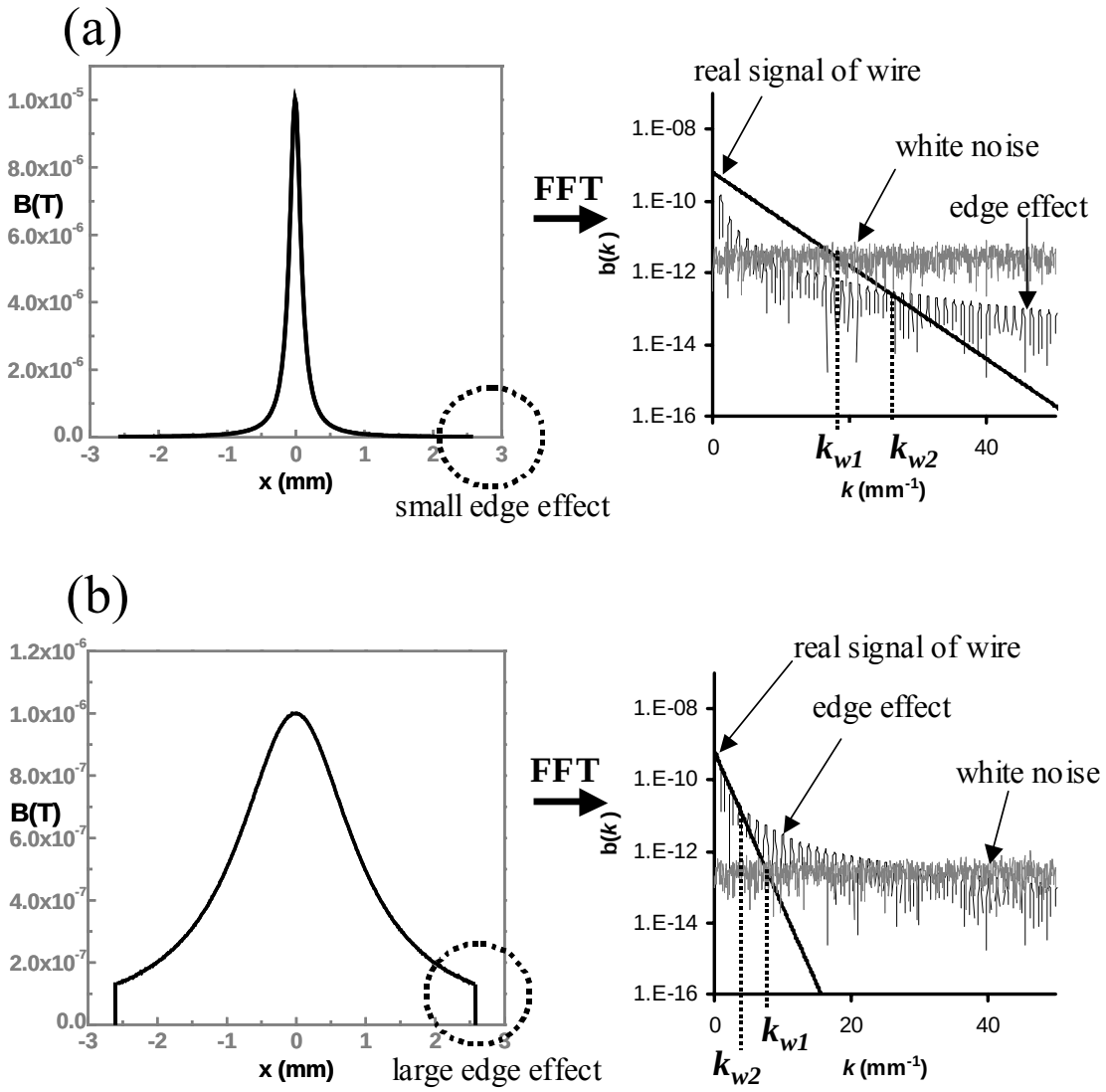

Figure 8.10: Sketch of magnetic field data for a current injected wire in real space and k-space. For (a) the white noise is dominant at z ~ 0.1 mm and for (b) the edge effect is dominant at z ~ 1 mm.

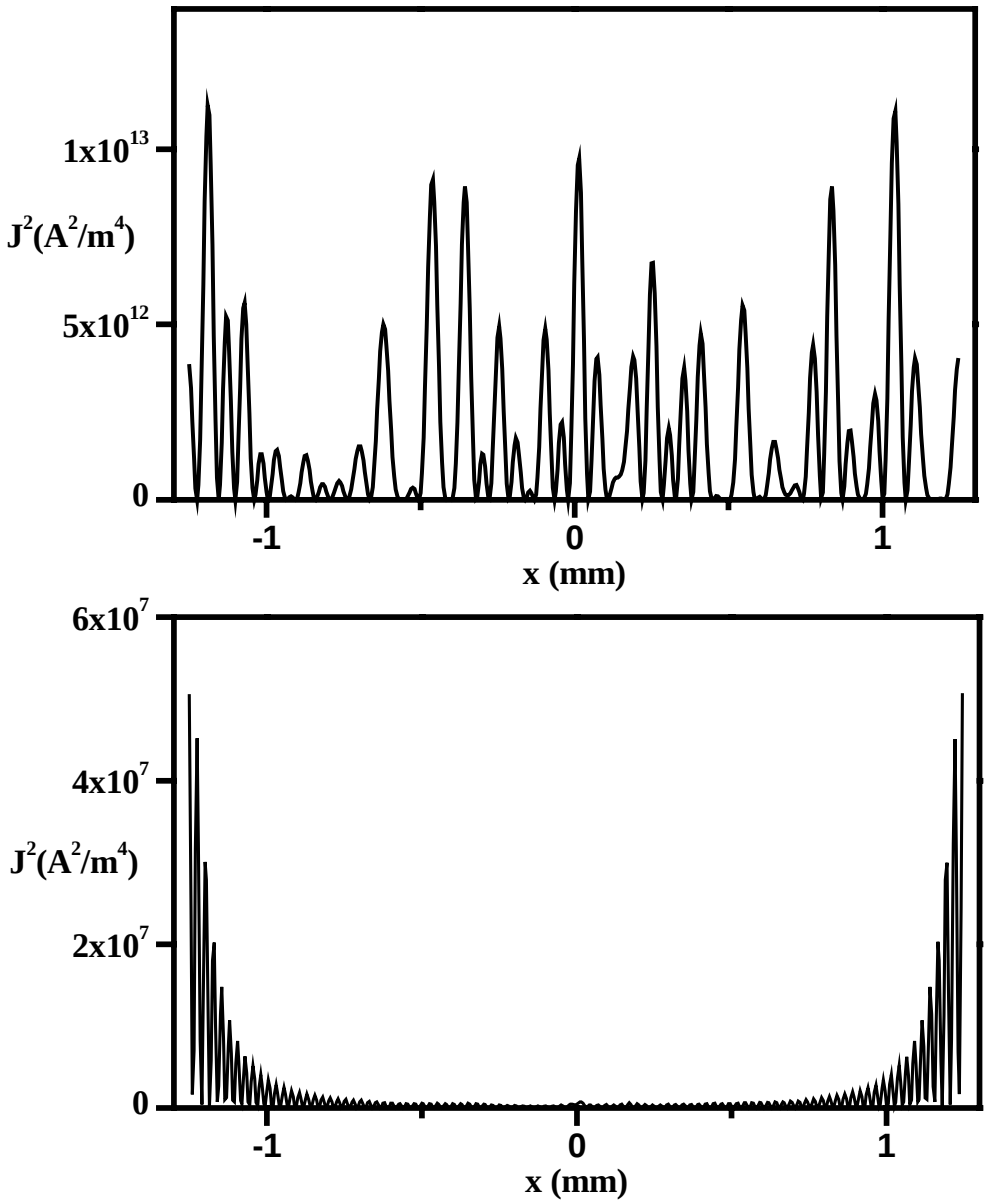

Figure 8.11: Squared current density (a) when white noise obscures the signal from a wire and (b) when edge effect obscures the signal from the wire.

averaging to with averaging, I assume the noise is random and uncorrelated. In this case $\sigma_x^{avg} = \sigma_x / \sqrt{n}$ and $\sigma_B^{avg} = \sigma_B / \sqrt{n}$ where n is the number of scans that are averaged. Of course as I noted in Ch 7, the real noise doesn't follow $1/\sqrt{n}$ beyond about 5~20 averages.

Eq. (8.28) with averaged position noise and SQUID noise then becomes:

$$\frac{z}{s} = \frac{1}{2 \times 2.783} \ln \left\{ \frac{\frac{2\pi \cdot n}{S/N(1+z_0^{\,4}/z^4)} \left[\frac{2.783 \mu_0 I}{\pi \Delta x \cdot \sigma_B} \left(\frac{z}{s} \right) \right]^2 - 1}{2 \times 2.783 \left(\frac{z}{s} \right) - 1} \right\} . \quad (8.29)$$

I note that z_0 does not change with average number n since both σ_x^{avg} and σ_B^{avg} decrease simultaneously. Setting $\sigma_x = 1.44 \times 10^{-7}$ μm, $\sigma_B = 0.179$ nT, I = 4.8 mA, $\Delta x = 20$ μm, and n = 8, I plot Eq. (8.29) in Fig. 8.12. For 8 times averaging I find that the spatial resolution improves from 46.6 μm to 42.8 μm at z = 200 μm. This improvement is relatively small. This happens because s and z are only logarithmic function of the noise. If we were able to correct for correlated errors in x, then averaging several scans could become another tool to significantly improve spatial resolution without modifying the system.

I note that one can also effectively vary the ratio of σ_x to σ_B by averaging. For example. If we keep the total imaging time constant but average N scans, we will still get $\sigma_x / \sqrt{n}$ improvement in position noise but the σ_B will be unaffected, since it is just determined by the total averaging time.

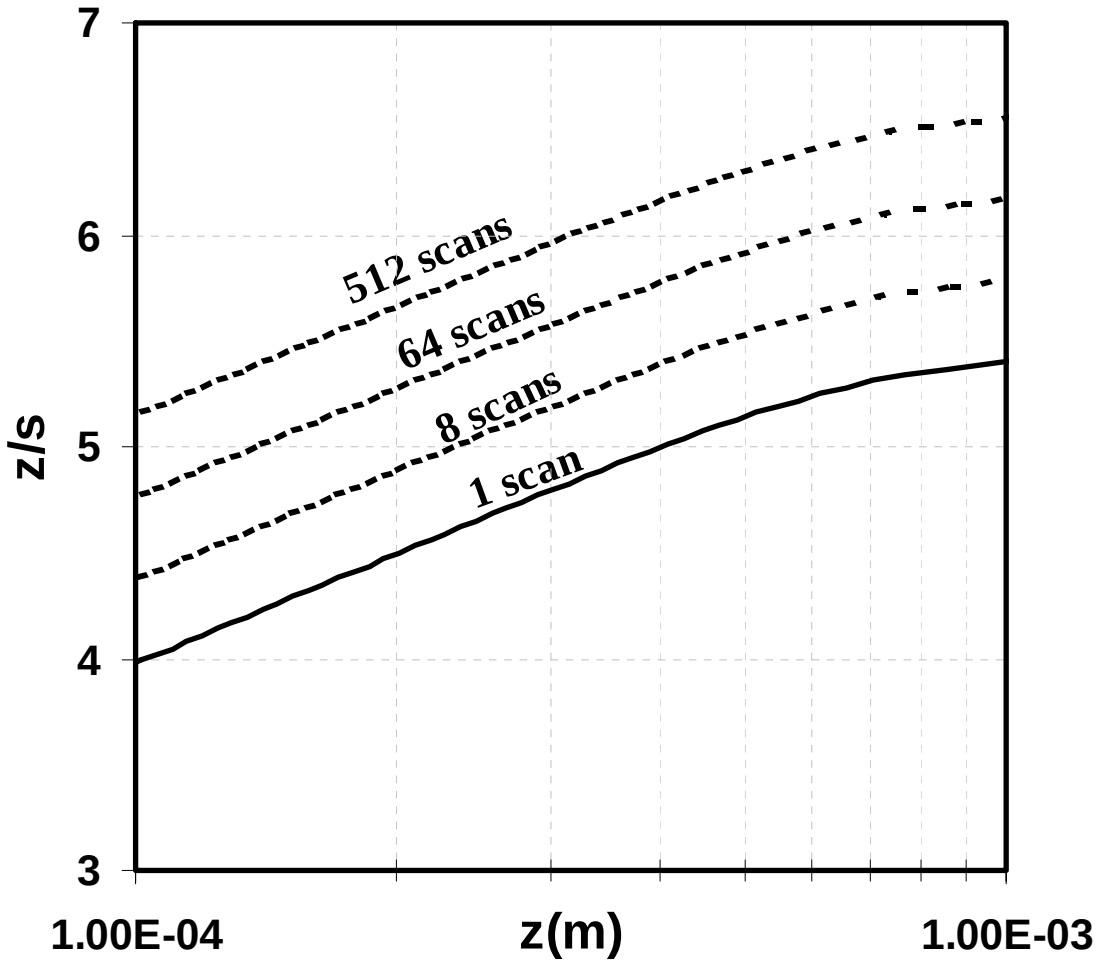

Figure 8.12: Ratio of sample separation z to spatial resolution s versus z for I = 4.8mA, Δx = 20 μm, S/N = 1, σ_x = 0.15 μm, and σ_B = 0.178nT. The solid line indicates numerically calculated z/s with no average, and dashed lines indicate numerically calculated z/s for 8~512 scans.

8.5 Conclusion

In conclusion, I have found that the spatial resolution *s* is limited by position noise as well as separation *z,* field noise σ_B, and source current I. With position noise present, the relation between s and z is no longer linear. To minimize spatial resolution, we must still reduce the sample separation z. However, the closer we approach our sample to the sensor, the greater the effect of position noise on spatial resolution. Therefore, the position noise from stage, motor, or other source should be considered if one wants to improve spatial resolution. By averaging several scans, my analysis shows that the spatial resolution can be improved somewhat.

Chapter 9

Fault Detection in MRI Wires Using Scanning SQUID Microscopy

9.1 Superconducting magnet wire

Nb-Ti superconducting wire is used to make the coils for high-field magnets used in Magnetic Resonance Imaging (MRI) systems. Magnets made from superconducting wire are far more efficient than those made from copper wire when supplying large magnetic fields. Typical construction of the superconducting wires involves embedding a large number of fine filaments of Nb-Ti in a copper matrix by means of repeated drawing operations (see Fig. 9.1). The solid copper jacket gives thermal stability and provides an alternative path for the large currents in case the superconducting state is lost.

For a typical MRI system, kilometer long sections of wire are used to wind the coils. If a single defect occurs, it can limit the current carrying capacity of the entire coil. Defects such as broken Nb-Ti filaments can occur deep inside wire, making them difficult to detect visually. If a superconducting magnet is wound and then cooled down and fails to operate properly, the entire system may need to be thrown away. Thus, it is useful to be able to detect defects reliably without damaging the wire and before winding the magnets.

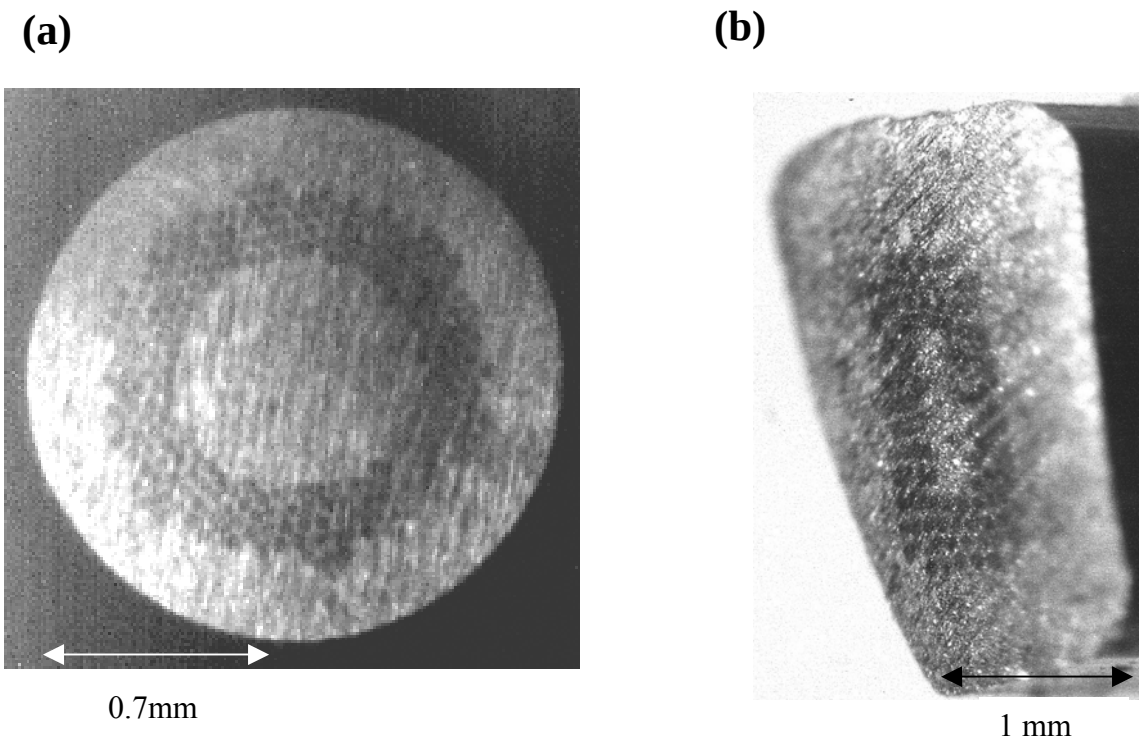

Figure 9.1: Photograph of Nb-Ti superconducting wire showing outer copper cladding and embedded Nb-Ti filaments with (a) round and (b) rectangular cross-section. Wires from IGC Inc. [1].

There are 4 main types of defects that arise in the manufacturing process [2];

(a) **Yields**: If the wire is stretched too much during the drawing process, filaments can break which are then filled by Cu.

(b) **Occlusions**: Non-conducing grains can be incorporated into core or cladding during the drawing process.

(c) **Seams**: the wire has been folded over, leaving an internal poorly-conducting plane running down the length of the wire.

(d) **Bare spots**: the insulating jacket around the wire is missing or has been rubbed off.

My wire samples are commercial Cu-clad Nb-Ti magnetic wire from IGC Advanced Superconductors, Inc. [1]. The ratio of copper to superconductor is up to about 7 to 1. It varies depending on application. The superconducting wires have 1~3 mm diameter with round or rectangular cross-section (see Fig. 9.1). To prevent electrical shorts, the outside copper is coated with an insulating material. I measured several samples:

i. Sample A has round cross-section (1.45 mm diameter) with a "yield" defect.

ii. Sample B has rectangular cross-section (2.29×1.55 mm^2) with a "seam" defect.

iii. Sample C has round cross-section (1.45 mm diameter) with a "yield" defect.

iv. Sample D is a 3.15 mm diameter home-made Brass test sample with four through holes and four half-through holes with different sizes [see Fig. 9.14(a)].

9.2 Prior fault detection methods using SQUID

9.2.1 Eddy Current Method

The use of eddy currents to find defects in superconducting wires is fairly well-known. Usually, however, one employs simple normal metal coils and senses the voltage induced by the changing flux from the eddy currents. Figure 9.2 shows the basic idea using a SQUID as the detector. The coil induces a drive field. The drive field induces eddy currents in the metal sample. The magnitude and direction of the field is different depending on the sample geometry. If there is a void inside the sample, the current will flow around the void, resulting in a different B-field being generated. Since the SQUID is a very sensitive flux meter, it can detect very small changes in the field.

One of the key factors in the eddy current technique is that the induced eddy currents only flow within about one penetration depth of the surface. The relation between the penetration depth and frequency is given by [3],

$$d = \sqrt{\frac{1}{\pi f \mu_0 \sigma}} \tag{9.1}$$

where μ_0 is the permeability of free space, σ is the conductivity of the sample, and f is the frequency of the applied current. Thus the penetration depth for low frequency current is long, while the penetration depth for high frequency current is short.

In previous work, Erin Fleet showed that defects could be detected with a z-SQUID (SQUID loop parallel to sample plane). He imaged a test sample with an artificial defect and also examined Cu-clad Nb-Ti wire using the eddy current method [4]. Erin showed that he could localize the defect in test samples, but that real defects in superconducting wire didn't appear in the eddy current method without further analysis. There were several factors that cause problems. To obtain a reasonable

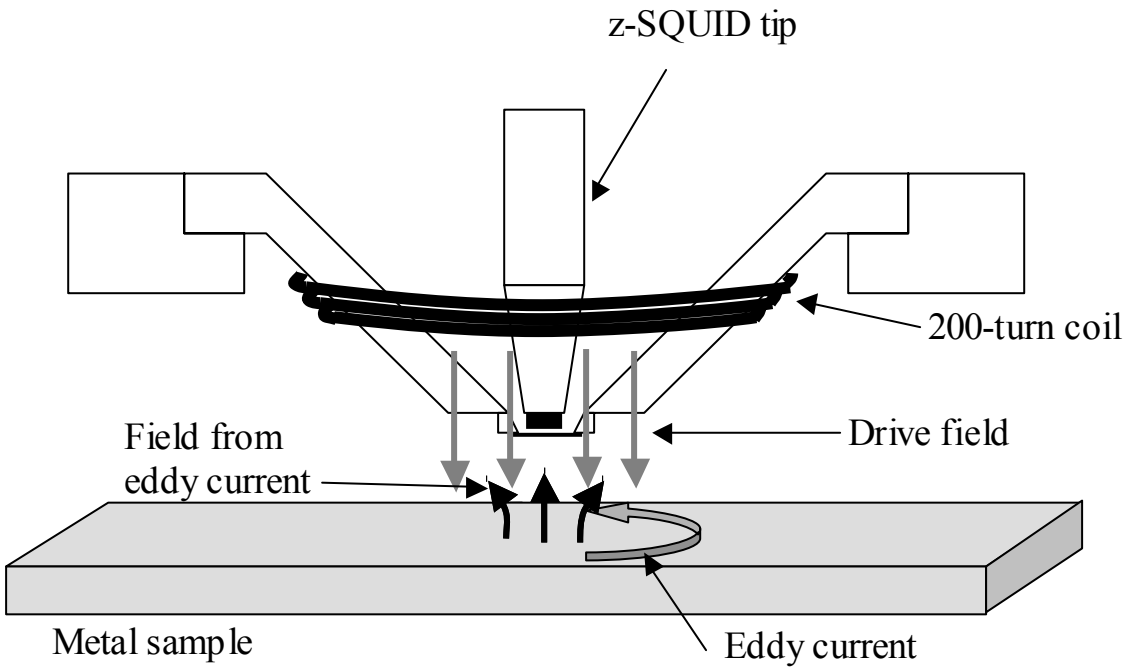

Figure 9.2: Experimental set-up for eddy current imaging using a SQUID microscope (modified from [4])

signal, a large drive coil carrying a current with relatively high amplitude and high frequency was required. The large coil tends to lead to relatively poor spatial resolution. Also, he could not apply too large of an amplitude and frequency because it caused the SQUID to unlock. Low frequency current in the drive coil causes very weak eddy currents. However, because of the penetration depth, high frequencies only provide information about surface regions of a sample. In general, one must also deal with the fact that the induced field is usually small compared with the drive field and the signal from the wire itself is much stronger than the signal from the defect.

9.2.2 **Current injection method with z-SQUID**

In addition to eddy current detection, Erin also tried injecting current through the wire and measuring the resulting field using a z-SQUID microscope [4]. One test sample he tried had a cylindrically asymmetric defect and the other had a cylindrically symmetric defect. Since the raw magnetic field B_z from the wire itself was very strong, he took a derivative with respect to y to get dB_z/dy and to pull out magnetic features produced by the defect [4,5]. The asymmetric defect in the test sample and defects in superconducting wires appeared in the derivative images. However, the symmetric defect didn't show up because of symmetry.

Figure 9.3 shows the magnetic field and field gradient image of a superconducting wire. The darkest red and blue indicate the maximum and minimum B_z values, respectively. As marked with the dashed line in Fig. 9.3(b), the defect appeared as a dipolar feature in just the derivative image. There are also strong signals at the top

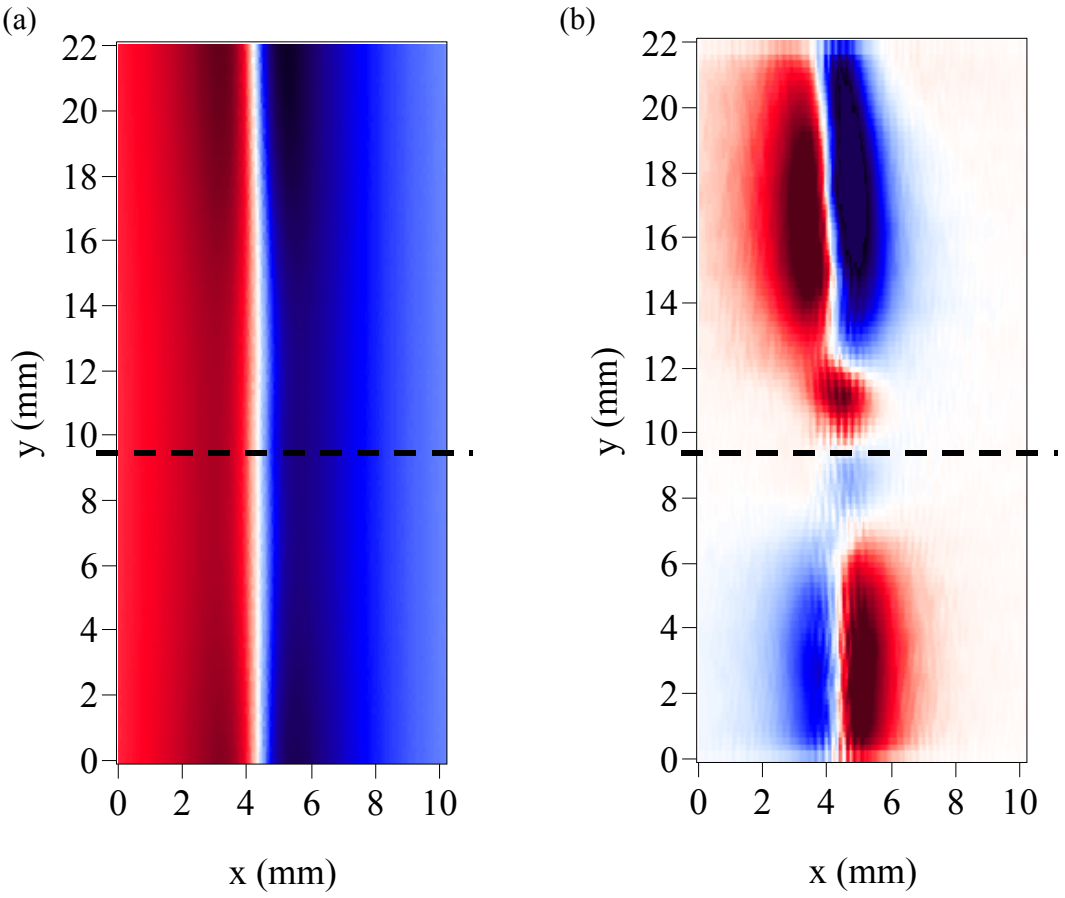

Figure 9.3: (a) Raw magnetic field (B_z) image of current injected superconducting wire using z-SQUID. Reds/Blues indicate +/- 840nT. (b) dB_z/dx calculated from (a) showing feature produced by defect in the wire. Reds/Blues indicate +25/- 50nT/mm. Images taken by Erin Fleet [4].

and bottom produced in Fig. 9.3(b) by bending of the wire. Thus, we can see that the current injection method using a z-SQUID is very sensitive to defects, but at the same time it is also sensitive to bending. Since real superconducting wires will have small bends in them, we need to do something else to separate signals produced by bending from signals produced by defects.

9.3 Current injection method with *x*-SQUID

The main problem with trying to find defects in wires using the current injection method with a z-SQUID is that the wire itself produces a very strong field which tends to hide the signal from the defect. Unlike for a z-SQUID, the alignment of the wire is very important for an *x*-SQUID. If a perfect wire is aligned exactly perpendicular to the *x*-SQUID loop (i.e. the loop normal, which is in the x-direction, is parallel to the axis of the wire), then no signal is detected by the *x*-SQUID. On the other hand, if there is a defect in the wire, then the flow of current is perturbed, resulting in an *x*-component of the magnetic field, which can be detected by the *x*-SQUID. Thus if the *x*-SQUID is closely aligned with the wire, the signal from the defect will be visible in the raw magnetic field data.

For this experiment, I used a cylindrical Nb-Ti superconducting wire from IGC with a "yield" defect (sample A) [1]. I injected 95 mA of current at 20 kHz. Figures 9.4(b)-(d) show raw magnetic field images from the *x*-SQUID. For these images, the *x*-SQUID loop is not perfectly aligned to the *x*-scan direction. In fact, the tilt angle ϕ of the SQUID loop from the *y*-scan direction (see Fig 6.15 and Ch 6.5.2) is about 7.5°.

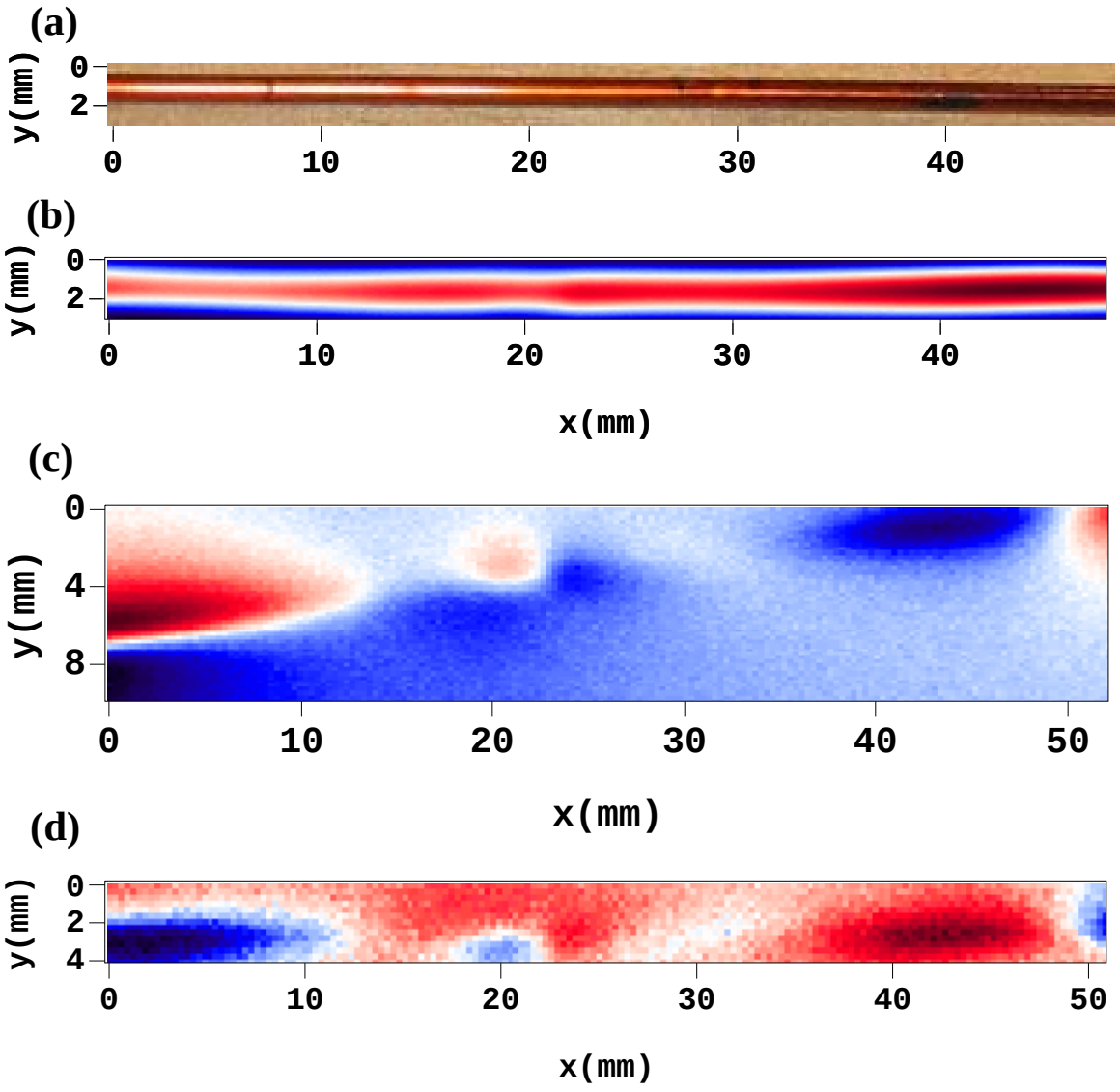

Figure 9.4: Raw magnetic field (B_x) image using current injection method with (b) normal scanning method and wire aligned along x-scan direction, (c) normal scanning method and wire aligned along the direction of SQUID loop (7.5° tilted), and (d) scanning along the direction of SQUID loop and wire aligned along the direction of SQUID loop. (a) Photograph of superconducting wire sample A with yield defect.(raw data: m121602, m121607, m121702)

Thus, the magnetic field image of a wire that is aligned along the *x*-scan direction shows a strong signal from the wire itself, as shown in Fig. 9.4(b). For this image, red/blue indicates +0.6/+0.240 μT, respectively.

To reduce the signal from the wire itself, it is necessary to align the wire to the direction of the SQUID loop. Figure 9.5 shows the scanning direction and wire direction corresponding to the images in Figs. 9.4. Figure 9.4(c) shows the magnetic field image after aligning the SQUID direction with the wire direction [see Fig 9.5(b)]. Red/blue in Fig. 9.4(c) indicates +0.4/-0.3 μT. In this image, the defect appears as a red spot in the center (see Figure 9.4(b)). Since the wire is tilted compared with the scanning direction, one needs to use a larger scanning area to cover the wire.

To reduce the scanning time, I modified the scanning program to move the stage along the tilted wire direction, as shown in Fig. 9.5(c). I kept the scanning direction and wire direction as shown in Fig. 9.5(c) for all experiments after this. Thus, for this set-up the wire is tilted by 7.5 ° from the *x*-direction and scanning is along the x' direction, which required moving the *x* and *y* stages at the same time. Figure 9.4(d) shows the result after modifying the scanning program. Red/blue indicates +80.3/-160.6 nT, respectively.

I note that this procedure helps to reduce the scanning time but also allows me to use dB_x/dx to find defects (see section 9.5). As shown in Fig. 9.4(c)-(d), there is a strong signal in the left and right sections of the images. This is the same problem that Erin Fleet found for the current injection method with the *z*-SQUID (see section 9.2.2), i.e. bending of the wire causes a strong signal in the *x*-SQUID also.

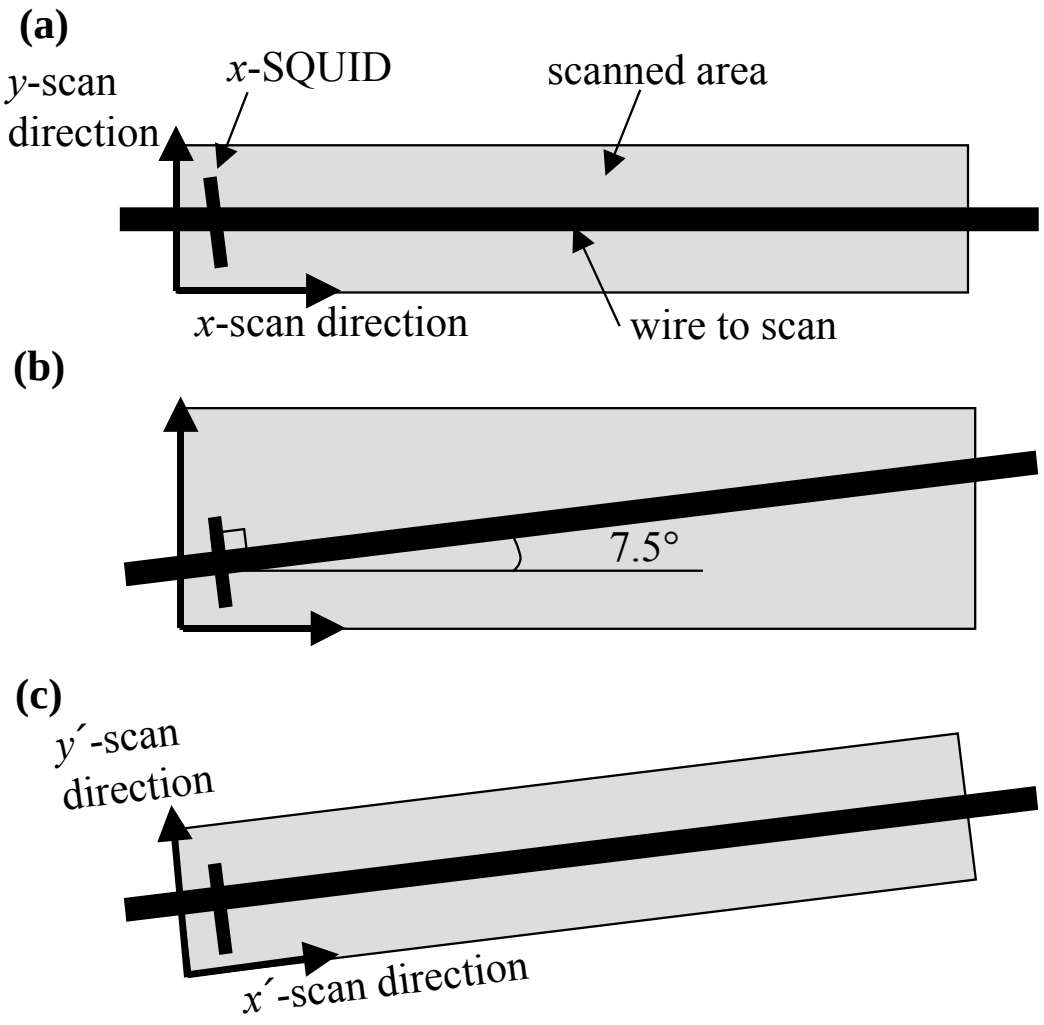

Figure 9.5: Sketch of different scanning set-ups. (a) Normal scanning direction with wire aligned along *x*-scan direction, (b) normal scanning direction with SQUID tilted so that wire is perpendicular to the SQUID loop area, and (c) set-up with scanning direction, tilted wire, and SQUID aligned.

9.4 current injection using high-low frequency image subtraction

To distinguish bending from defects, I use a high-frequency low-frequency image subtraction technique that was first proposed by Dr. Harold Weinstock [5] and first demonstrated by Anders Gilbertson in our group [6].

The idea is to use the fact that the penetration depth in a metal depends on frequency, as shown in Eq. (9.1). Using this property, I can separate interior defects from bends. Applying high frequency current gives information about the surface of the metal, while low frequency current gives information about both the surface and interior because of the longer penetration depth. Table 9.1 shows the penetration depth in copper and brass at several different frequencies. The signal from bending of the wire will be the same at high frequencies as at low frequencies because the entire cross-section of the wire has to follow a bend. Thus by appropriately subtracting a high-frequency magnetic field image from a low-frequency image, the signal from bending will be canceled out but the signal from a defect deep inside the wire will not be.

Table 9.1 Penetration depth of copper and brass for different frequencies.

Frequency (Hz)	δ_Cu (mm)	δ_Brass (mm)
500	2.917	4.211
1×10^3	2.063	2.978
2×10^3	1.459	2.105
5×10^3	0.923	1.332
1×10^4	0.652	0.942
2×10^4	0.461	0.666
5×10^4	0.292	0.421

9.4.1 **Sample B ("seam" defect)**

To test the high-low subtraction technique, I tried imaging a Cu-clad Nb-Ti wire with a rectangular cross-section and a "seam" defect (sample B). The wire was 29 cm long and I applied about 95 mA of current and used a distance between the sensor and the surface of sample z ~ 800 μm. Figure 9.6(b) and (c) show the raw magnetic field image at 1kHz (Red/blue indicate +91.5/-53 nT) and 50 kHz (Red/blue indicate +225/-129 nT), respectively. A large dipole structure is clearly visible. Seam defect tends to run the entire length of a wire. So, the defect I found might be place where the seam defect changed in some way. So it is not surprising that the signal is very broad and unlocalized. Figure 9.6(d) shows the difference between 50 kHz and 1 kHz images (Red/blue indicate +120.5/-120.5 nT). As shown in Table 9.1, the penetration depth at 50 kHz and 1 kHz are 0.29 mm and 2.062 mm, respectively. This means that the current at 1 kHz can penetrate all the way through the wire, while the 50 kHz current flows mainly in the surface of the wire. By subtracting these data, I could find whether this signal was from the surface, from bends, or from the interior. To do the subtraction I had to multiply the low-frequency data by 0.44 (it is different depending on data) before doing the subtraction. This is necessary because the system gain at high frequency and low frequency is different.

To confirm whether the defect signal was coming from inside or from the surface of the sample, I subtracted images taken at various frequencies. Figures 9.7(a)~(c) are the differences between 50kHz and 1kHz, 50kHz and 10kHz, and 10kHz and 1kHz, respectively. Figures 9.7(a) and (b) look very similar, showing a signal in the center of the wire. However, in Fig. 9.7(c) the defect is not apparent. This is probably

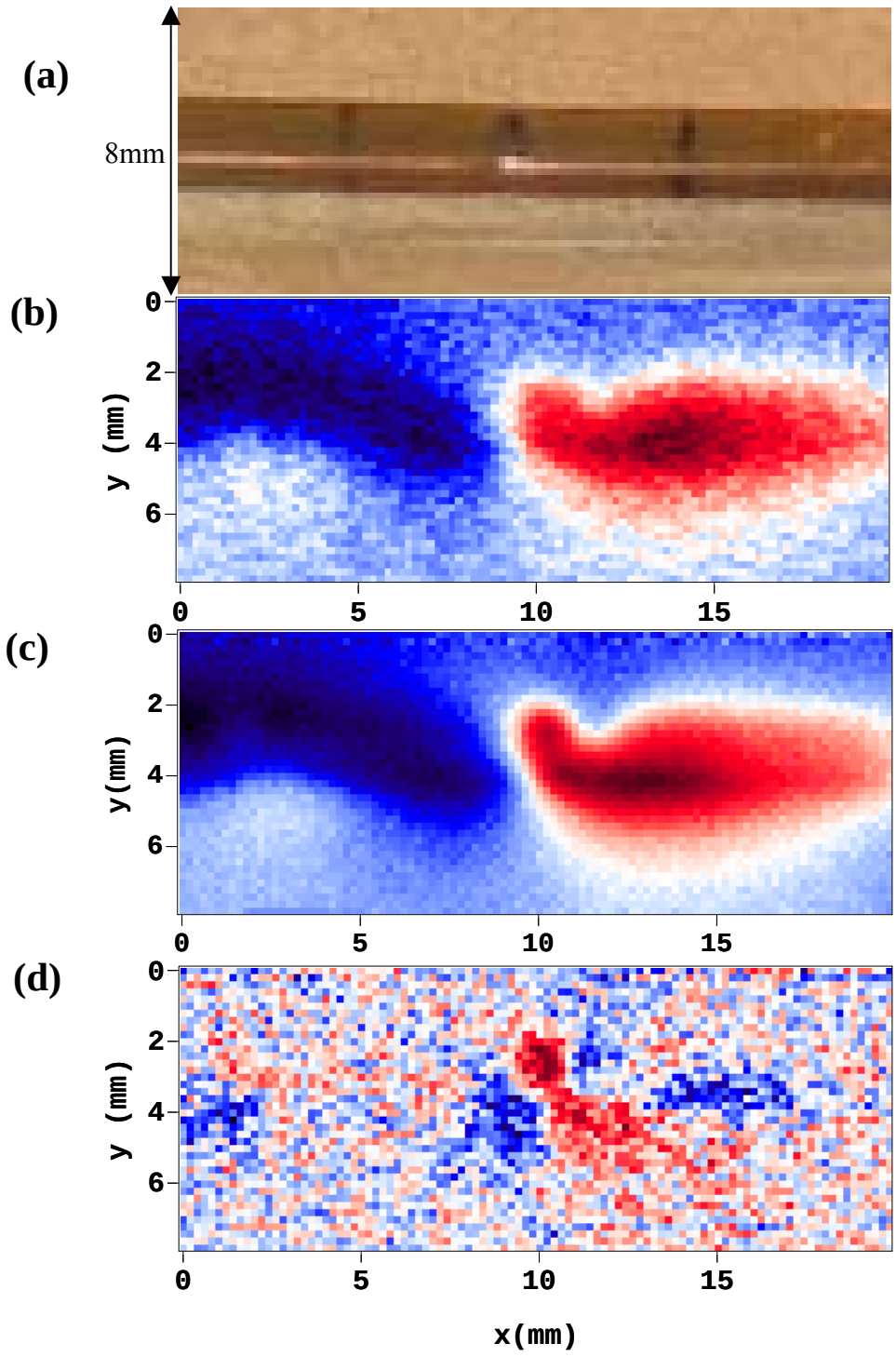

Figure 9.6: (a) Photograph of wire sample B with "seam" defect, (b) Magnetic field image B_x of sample B at 1kHz, (c) magnetic field image B_x at 50 kHz, (d) the difference between B_x with 50kHz current and B_x with 1kHz current (raw data : (b) m122210, (c) m12208, (d) m12208-(m12210)×0.44)

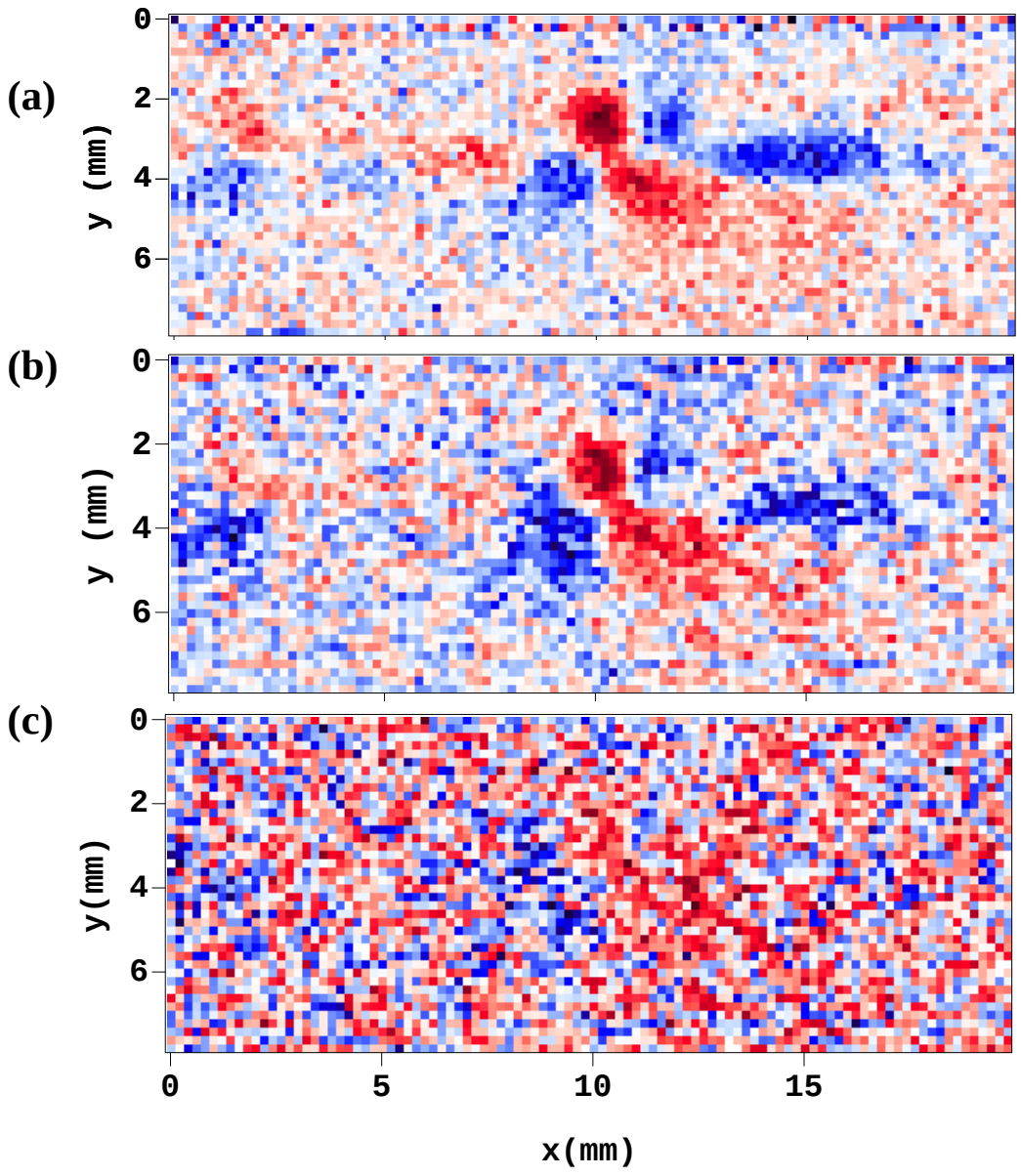

Figure 9.7: (a)-(c) The magnetic field differences between 50kHz and 1kHz, 50kHz and 10kHz, and 10kHz and 1kHz, respectively, of the current injected superconducting wire sample B with the "seam" defect. Reds/blues indicate +120.5/-120.5 nT (a), 84.3/-105.2 nT (b), and 184.7/-168.6 nT (c) field respectively.

because the 10 kHz current (δ = 0.653 mm) and 1 kHz (δ = 2 mm) current both penetrate to the inside the wire, causing the defect signal to cancel out. This suggests the defect signal comes from inside the wire, rather than some artifact of the high-frequency subtraction process.

9.4.2 Sample C ("yield" defect)

Figure 9.8 shows magnetic field images of superconducting wire sample C which has a "yield" defect. I used I = 125 mA and z ~ 800 μm. Figure 9.8(b) shows the raw magnetic field (B_x). The defect is in the center of image. By applying the same high-low subtraction for sample B, I found again that there is a signal from inside the wire, as shown in Figs. 9.8(c)-(d).

I scanned a few more "yield" defects and one "seam" defect. Although I could detect defects, I was not able to use these images to classify the types of defects.

9.5 Current injection using dB_x/dx

By taking a derivative of B_z with respect to x, Erin Fleet showed that he could find defects in supercoducting wires. However, this method could not distinguish defects from bending. For an x-SQUID, the signal from the wire itself along the direction of the x-SQUID is negligible provided the SQUID and wire are correctly aligned. In the x-SQUID configuration, the detected signal is only from the bends or defects. Since the bending occurs on a size scale that is large compared with typical defects (except for seams, which tend to run through large sections), I can get rid of the signal from bending by taking the derivative of B_x with respect to x.

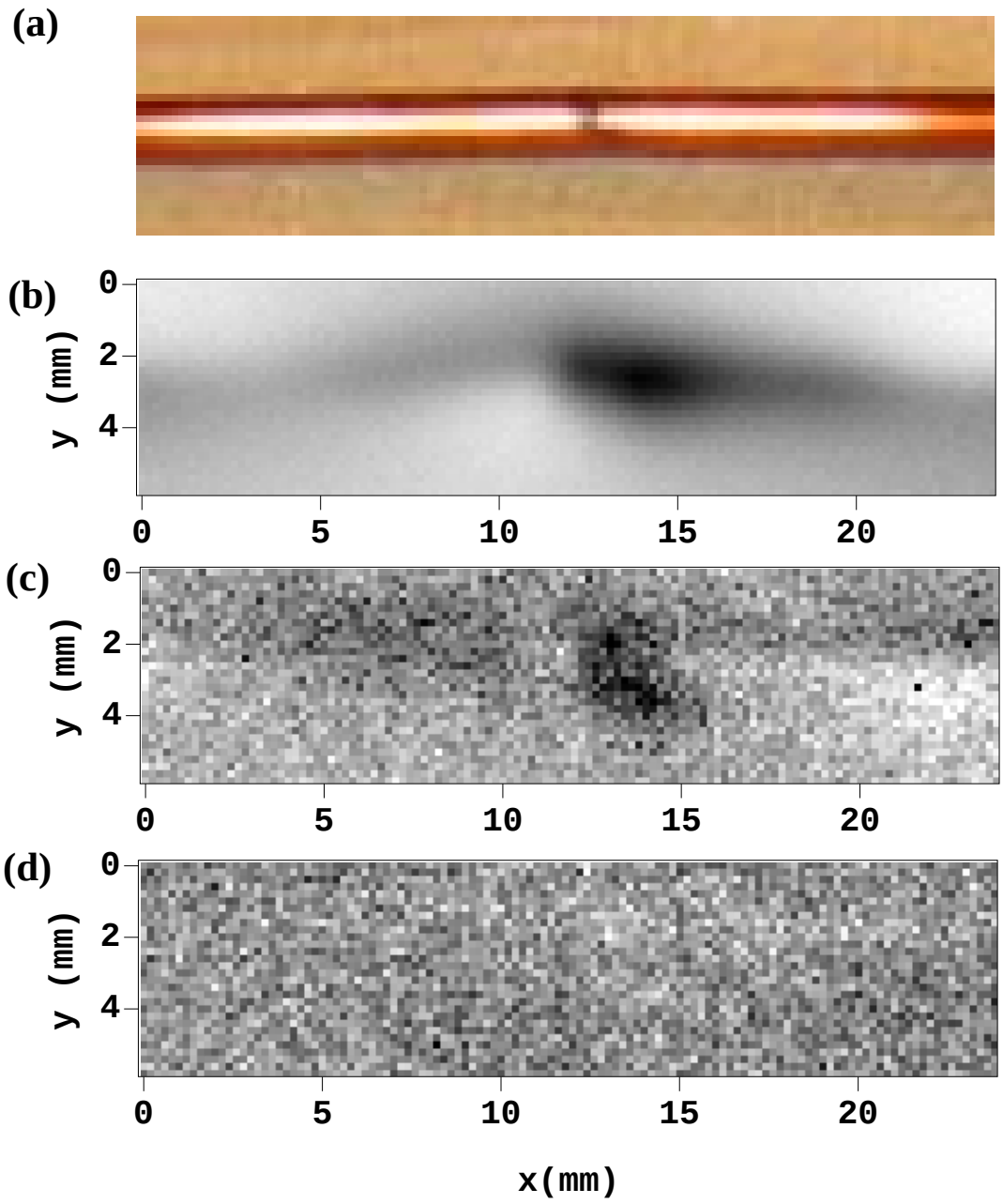

Figure 9.8: (a) Photograph of wire sample C with the "yield" defect, (b) magnetic field image B_x, (c) the difference between B_x with 50kHz and 10kHz, and (d) the difference between B_x with 10kHz and 1kHz of sample C. Blacks/whites indicate (b) +91.5/-16.1 nT, (c) 321.2/-56.2 nT, and (d) 80.3/-112.4 nT, respectively.

9.5.1 **Sample A ("yield" defect)**

Figure 9.9(a) and (b) show the raw magnetic field image B_x of sample A with a current of 95 mA at 20 kHz. The difference between Fig. 9.9(a) and Fig. 9.9(b) is just how flat the wire was. After I scanned Fig. 9.9(a), I flattened the wire and rescanned to produce Fig. 9.10(b) using the same conditions. The two images look different, and it is hard to say where the defect is. However, when I took the derivative of B_x with respect of x, I could locate a defect in both images, as shown in Figs. 9.9(c) and (d), and the position of the defect in Figs. 9.9(c) and (d) is the same.

9.5.2 **Sample C ("yield" defect)**

Figures 9.10 shows a comparison between different images of sample C ("yield" defect) found using different methods. Figure 9.10(a) is a raw magnetic field image of B_x using the current injected method with about 95 mA at 50 kHz, Fig. 9.10(b) shows dB_x/dx found from the image in Fig. 9.10(a), and Fig. 9.10(c) shows the result of a (B_x'(50kHz)-0.275·B_x"(1kHz)) subtraction. The defect appears in the raw magnetic field image in Fig. 9.10 (a), but the area of the defect is very wide (about 9 mm), so it is hard to localize. The signal in Figs. 9.10 (b) and (c) is more localized, to within about ±2 mm. The position of the defect in Figs. 9.10 (b) and (c) is at x =11~14 mm and x = 12~15 mm, respectively. Thus, the position of the signal from the defect in Fig. 9.10 (b) is about 1 mm off from that in Fig. 9.10 (c), but it is negligible compared with the wide range of the signal from the defect by other methods. I note that for these three images, z ~800 μm from the surface of the wire, so it is not surprising that the features are 2~3mm wide.

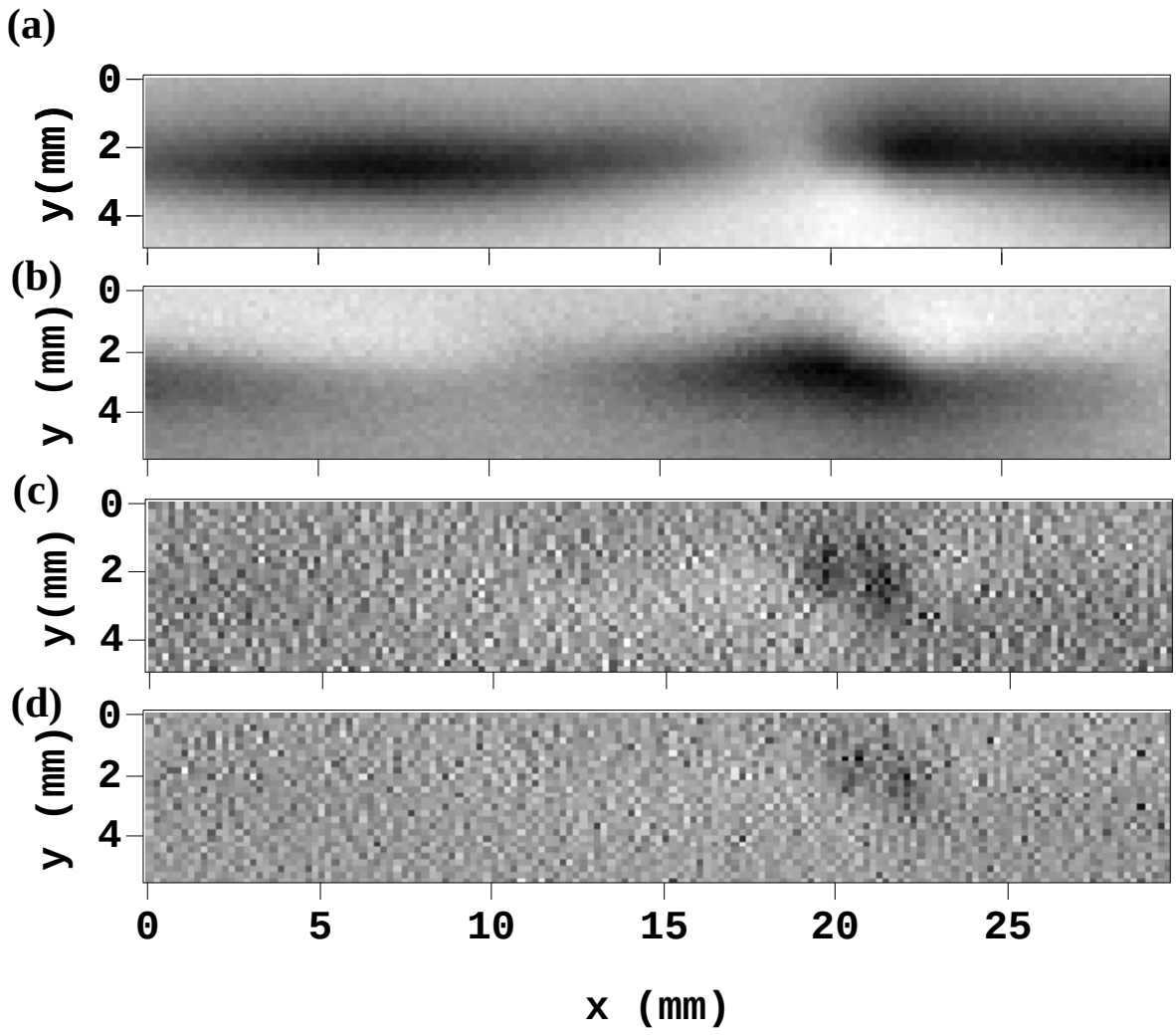

Figure 9.9: (a)-(b) Raw magnetic field B_x of current injected sample A with "yield" defect with different flatness of same wire. Images taken at 20kHz, with I = 95 mA at z~800 μm. (c)-(d) Gradient dB_x/dx of (a) and (b), .

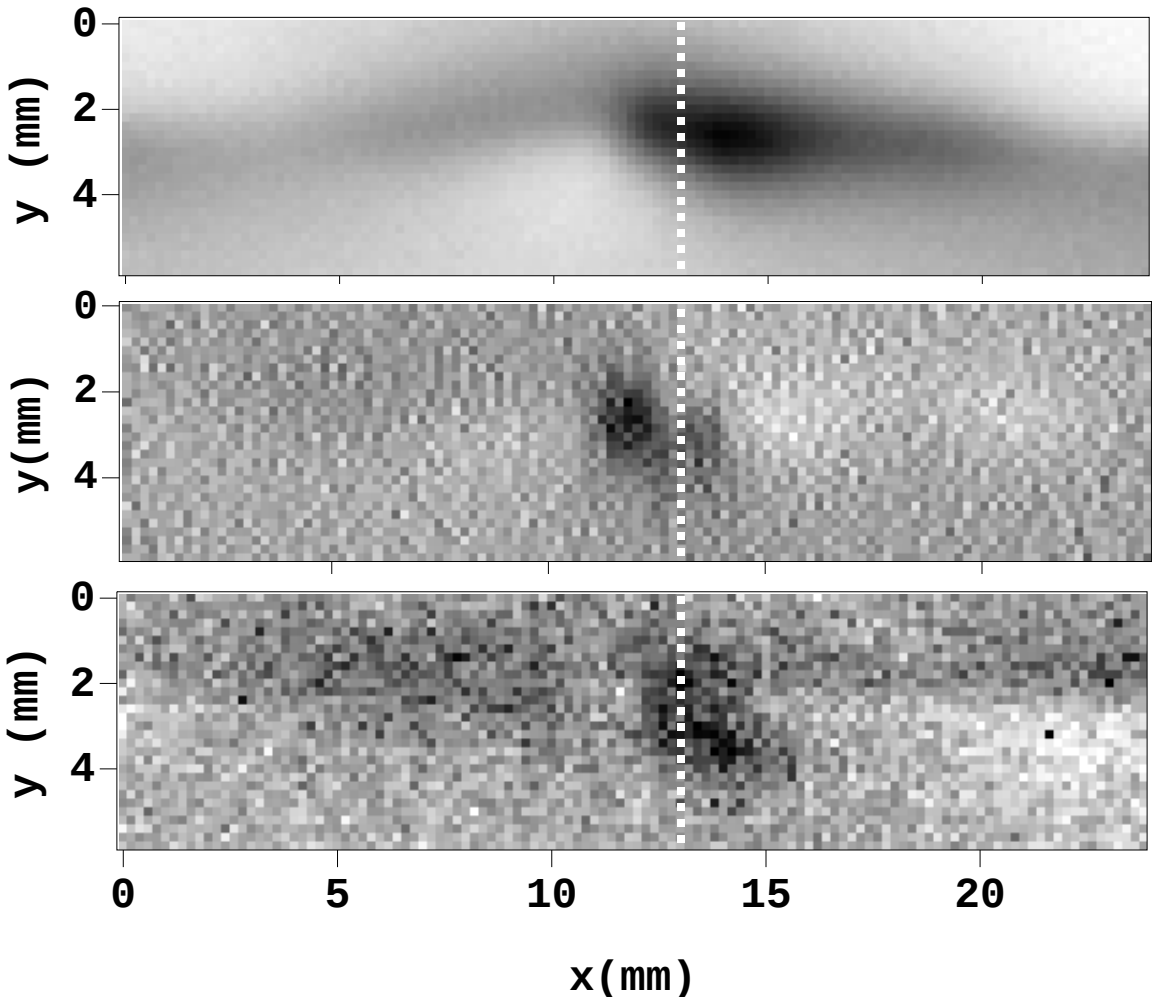

Figure 9.10: (a) Raw magnetic field B_x of 50kHz current injected sample C with a "yield" defect, (b) gradient dB_x/dx of (a), and (c) magnetic field difference between with 50 kHz and with1 kHz frequency current injected. I ~ 125 mA and z~ 800 μm for all images. ((a)~(b):m122404, (c):m122404-(m122406)×0.275)

9.5.3 Sample B ("seam" defect)

Similarly, I took the derivative of the magnetic field data shown in Fig. 9.6(a) which was for the "seam" defect. Figure 9.11(a) shows the raw magnetic field B_x using for 95 mA at f = 50 kHz. Figure 9.11(b) shows dB_x/dx of the image in Fig. 9.11(a), and Fig. 9.11(c) shows the result of a (B_x(50kHz)-0.44·B_x(1kHz)) subtraction. As with sample C, the signal from the defect in Fig. 9.11(a) is not localized while the defect signal in Fig. 9.11(b) and (c) is more localized. In sample B, the defect signal in Figs. 9.11(b) and (c) are both at 9~11 mm. There is no obvious offset. I note that the dB_x/dx image (Fig. 9.11(b)) is less noisy than that from the high-low frequency subtraction method (Fig. 9.11(c)). I note that since seams generally run the length of the wire, the dB_x/dx technique would tend to pick out regions of the seam where the seam direction changed. If this happened inside the wire, this would show up in the high-low subtraction.

9.6 Fault detection in MRI wires with the multi-channel SQUID microscope

Since a useful section of MRI wire can be 1 km-long, it takes too long to check where the defect is by scanning back and forth under a SQUID microscope. The elapsed time will be important if the SQUID system is used commercially for fault detection. Figure 9.12 shows how one could arrange things to measure such a long section; the wire is centered under the SQUID and moved with a motor. The idea is then to detect the fault by line scanning the sample once with multi-SQUID system rather than raster scanning. However, the thickness of the wire is more than 2mm D. One could increase the SQUID size in order to cover the

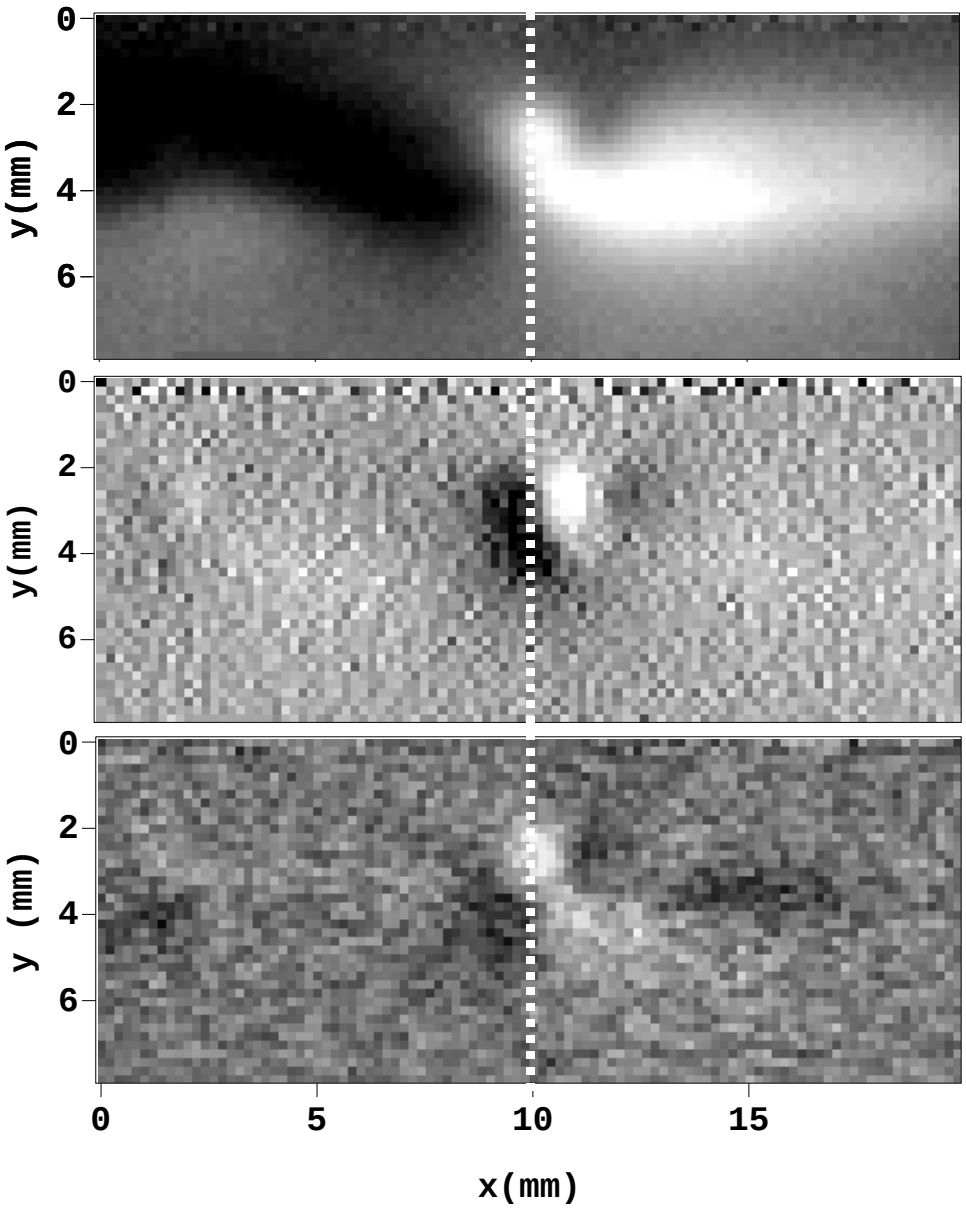

Figure 9.11: (a) Raw magnetic field image B_x from 50kHz current injected in sample B with "seam" defect, (b) gradient dB_x/dx of (a), and (c) the difference between 50 kHz and 1 kHz images. I ~ 95 mA and z~ 800 μm for all images. (file name (a)~(b):m122208, (c):m122208-(m122210)×0.44)

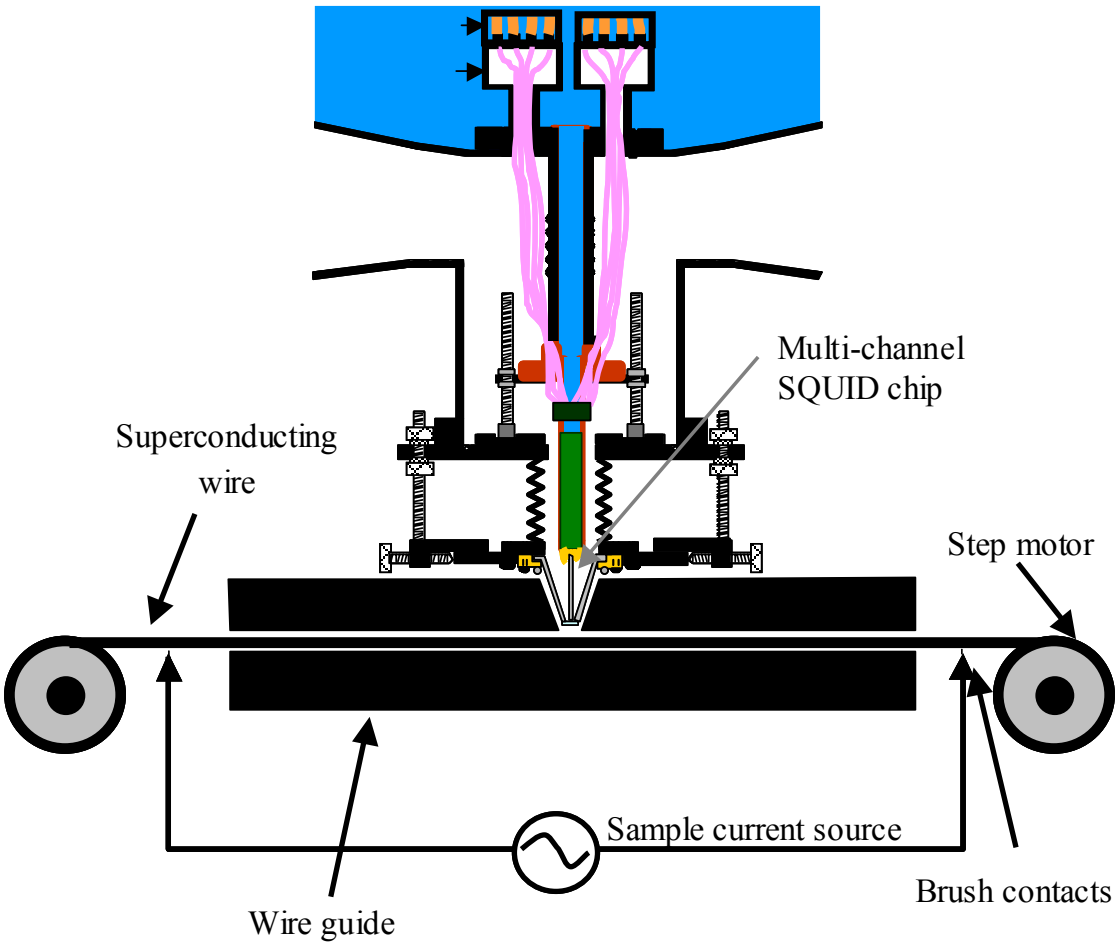

Figure 9.12: Schematic of multi-channel SQUID microscope used for detecting faults in MRI wire. (modified from Ref. [5])

entire area, but then one will lose the spatial resolution. On the other hand, a multi-channel SQUID could cover the entire area of the wire and keep good spatial resolution.

Although I did not set up my system as shown in Fig. 9.12, I can check the merit of using the multi-channel SQUID system to detect faults using single line scans. For this experiment, I used the 4-channel *x*-SQUID system described in Chapters 3~6. First I set up sample B (with the "seam" defect) along the x' direction (7.5° tilted from *x*-scan direction) and made a line scan along x' as shown in Fig. 9.5(c). Since I have 4 channels and the distance between channels is 200 μm, a single line scan produces an area scan which is 20 mm (length of line scan) × 0.6 mm, as shown in Fig. 9.13 (a). Examination of Fig. 9.13(a) shows that a signal from the defect is evident as a dipole structure that is spread out over a wide area. Taking the derivative of B_x with respect to *x*, a feature was localized as shown in Fig. 9.13 (b). The range of y is only 0.6 mm in this result, so I couldn't localize the defect in the *y*- direction. However by using more than 4 channels or a larger distance between channels, in principle I should be able to localize the defect in the *y*-direction also.

9.7 Brass test sample with different size holes

Using the methods described in the previous sections, I can find where a defect is. It would also be useful to be able to estimate the size of the defect from the magnetic field data. To see how the defect size affects the signal, I made a 3.15mm diameter Brass test sample with known artificial defects; 4 through-holes and 4 half-through-holes with different diameters [see Fig. 9.14(a)]. Since the test sample D is very flat, the current injection method produced clear signals from the defects. With known defect

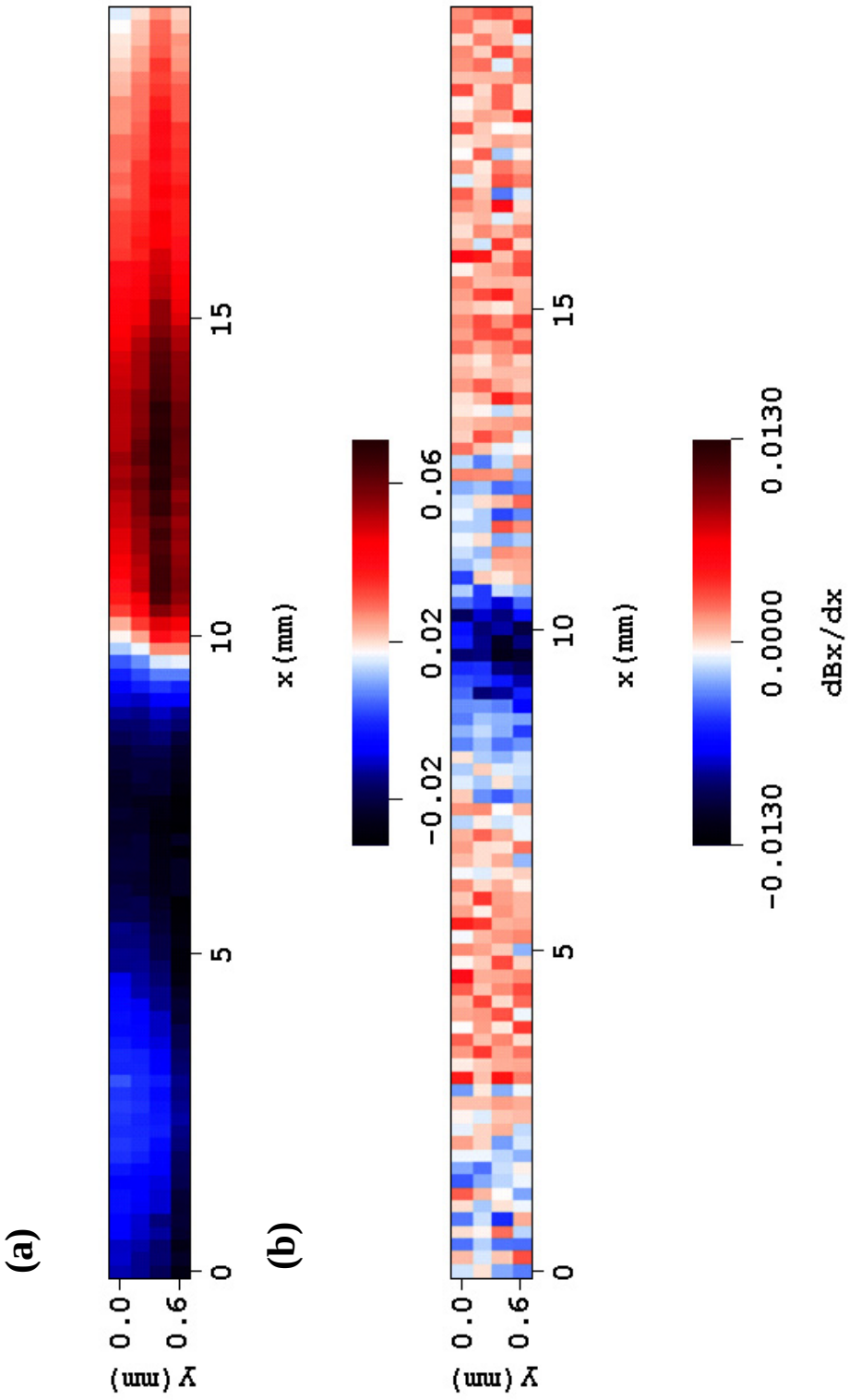

Figure 9.13: (a) Line scan of current injected sample B ("seam" defect) using one line scan of 4-channel SQUID system. (b) Gradient of (a).

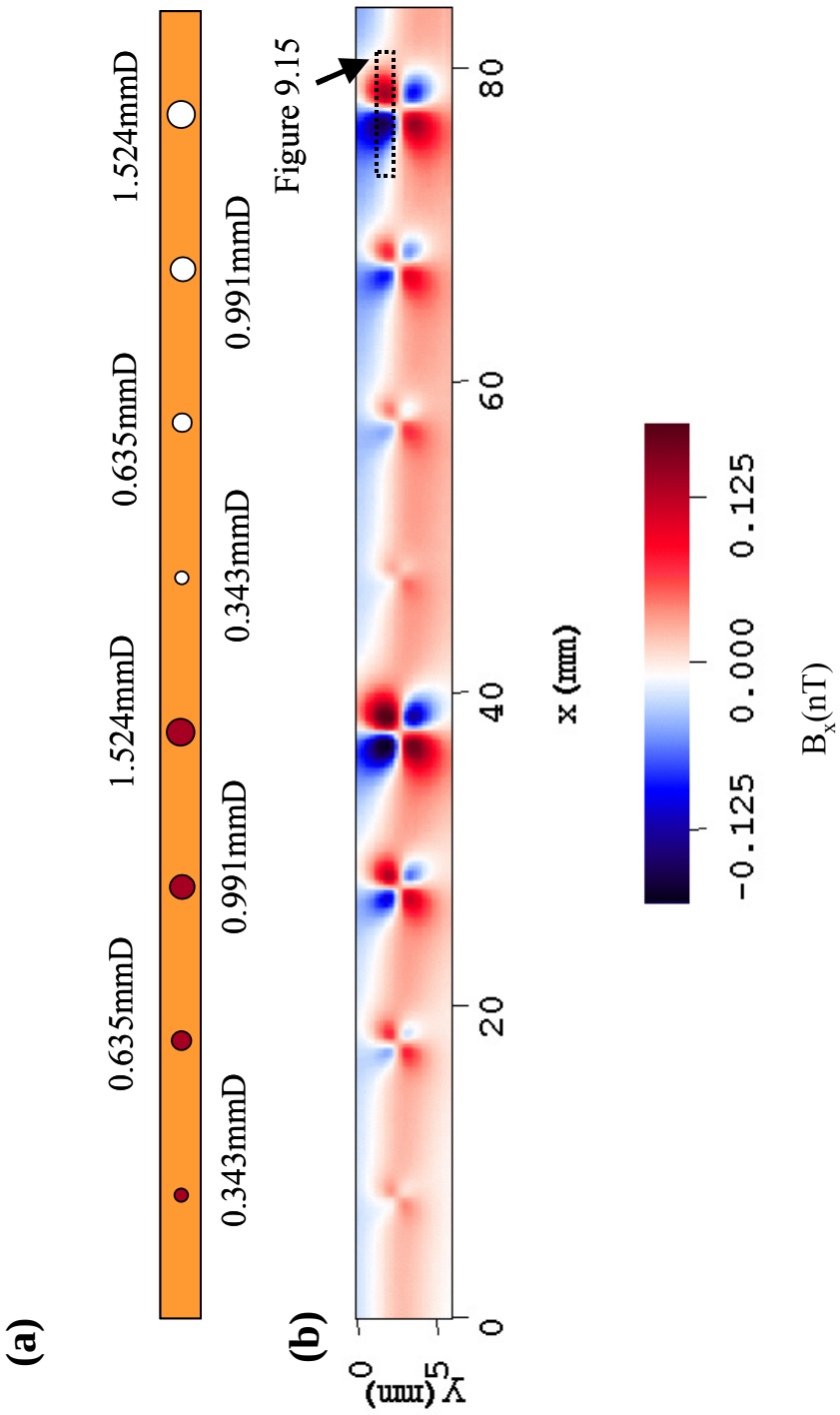

Figure 9.14: (a) Sketch of 3.15 mm diameter brass test sample D with 4 half-through holes and 4 through holes having various hole sizes. (b) Raw magnetic field image for I = 125 mA and z ~800 μm at 50 kHz .

size, I can find the relation between the measured size from the magnetic field image and the actual defect size at fixed z ~ 800 μm.

Figure 9.14(b) shows a raw magnetic field image of the test sample using 125 mA of current at z ~ 800 μm. The current flows around the holes, causing an *x*-component of the magnetic field near the holes. The result is a cloverleaf shaped pattern at each hole. By taking a line section through the strongest magnetic field at each hole (see Fig. 9.14(b)), I can obtain the peak-to-trough distance *w* as shown in Fig. 9.15. Figures 9.16(a) and (b) show the actual diameter d of the hole vs. *w* for the half-through-holes and through-holes. The diamond shaped points in Fig. 9.16(a) and the square shaped points in Fig. 9.16(b) are the averaged experimental results. The dashed lines indicate a fit to the function,

$$w = \sqrt{w_0^2 + d^2} \tag{9.2}$$

The relation between the actual hole size and *w* is not linear. Even though I have just one fitting parameter w_0, the fit agrees with the experimental results in both cases. The best fit is w_0 = 1.47 mm for the half-through holes, while w_0 = 1.21 mm for the through holes. I note that the half-through holes are more asymmetric than the through holes. This might lead to a larger w_0. Physically, I expect w_0 to have information about the geometry of the defect and the sensor-to-sample distance.

We know that if the sensor-to-sample distance z $\ll$ d, then we expect *w* ~ d. From the fitting equation, when $w_0 \ll$ d, then *w* ~ d. Thus, I expect w_0 is related to z. Therefore, if I scan far away from the sample, I expect w_0 will be large and directly related to spatial resolution. If z was accurately known, then I might be able to extract d

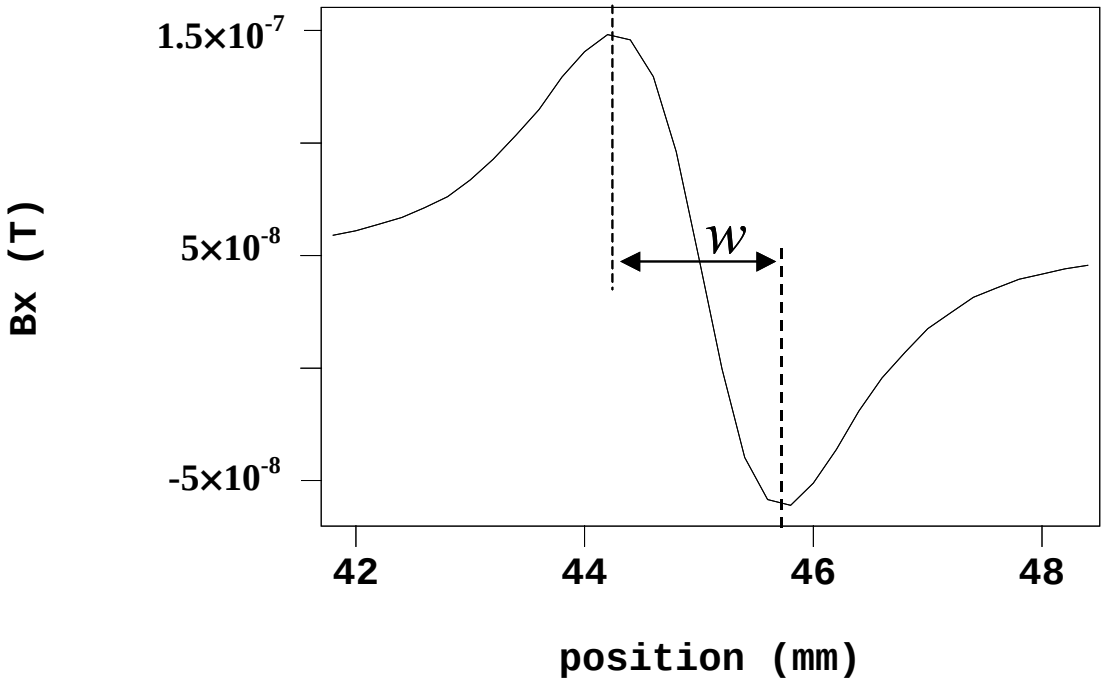

Figure 9.15: Line section through Fig. 9.14 along dashed line, showing how I define "peak-to-tough" distance *w*.

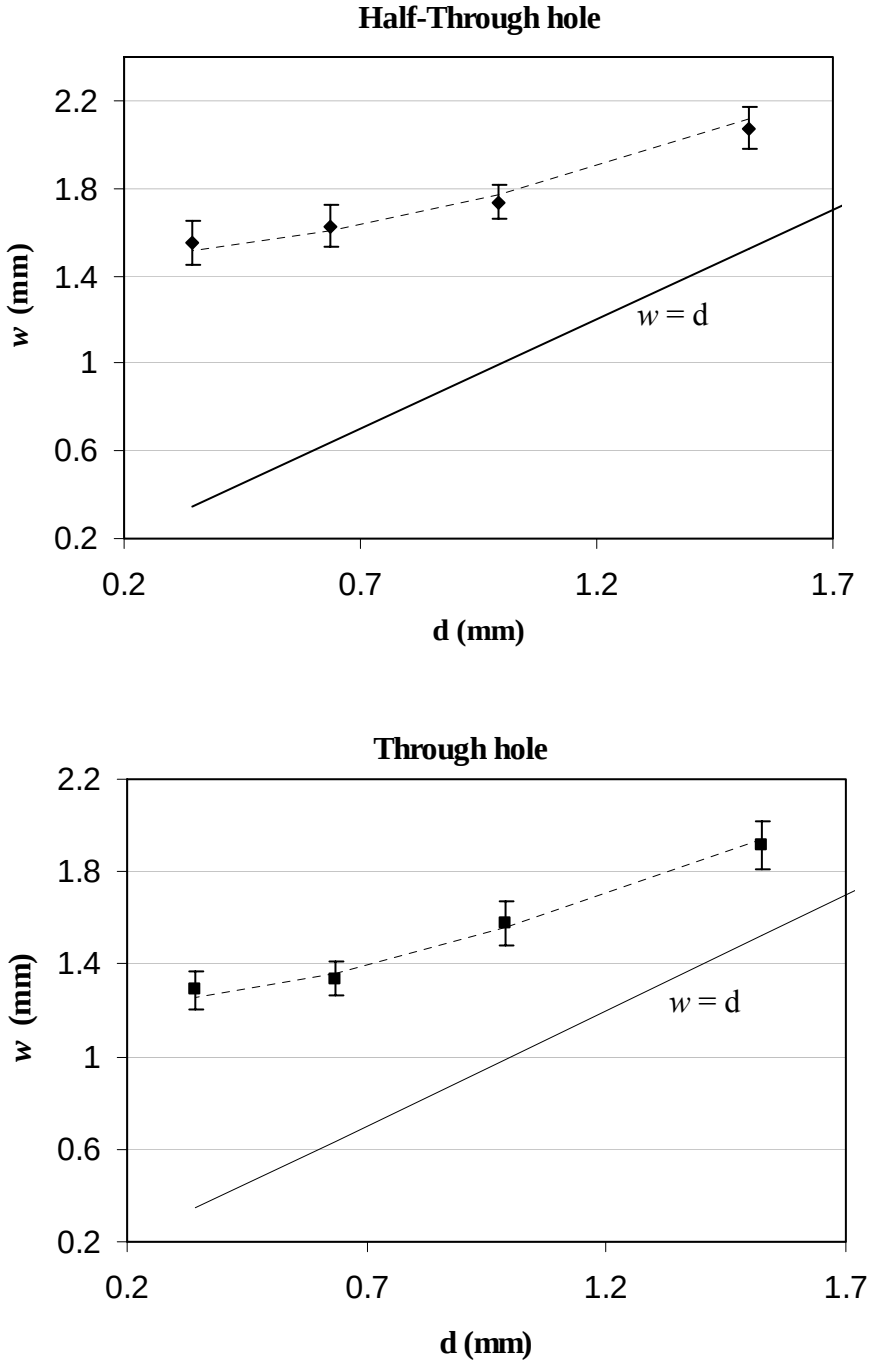

Figure 9.16: Measured hole size *w* from magnetic field image vs. actual hole diameter d for (a) half-through holes and (b) through holes, for z ~ 800 μm. Solid line is *w* = d.

by measuring w. Some additional information is available in the strength of the signal. This might allow us to classify the type and size of defects. Clearly I would need to scan the test sample for different z and do more analysis, but this is left for future work.

9.8 Conclusion

Using the current injection method with an *x*-SQUID, I showed that I could find defects in MRI wires. However the signal from the defect is spread over a relatively wide area. In addition, the B_x signal was also sensitive to bends in the wire. To solve these problems, I used a high-low frequency subtraction technique and also computed the derivative of the magnetic field B_x with respect to *x*. These two methods produced the same position for the defect and localized the defect to within 2-3 mm. By adding more SQUID channels, I showed I could achieve fast fault detection without losing spatial resolution. Finally I found that the defect size d agrees with the phenomenological equation $w = \sqrt{w_0^2 + d^2}$ with just one parameter w_0, where w_0 for half-through and through holes is 1.47 mm and 1.21 mm, respectively for z ~ 0.8 mm.

APPENDIX

Using Hooke's law, I can obtain the bending depth of the thin window under the air pressure [1]. Suppose I bend a rod like that in Fig. A.1, then different parts of the rod will be either stretched, compressed, or neutral. If I assume that the neutral surface is along the center of axis of rod, then the relation between longitudinal stretch Δl and height y is given by,

$$\frac{l}{l+\Delta l} = \frac{R}{R+y} \quad , \quad \frac{y}{R} = \frac{\Delta l}{l} \tag{A.1}$$

From Hooke's law, stress (force per unit area) is a product of the Young's modulus Y and the strain, which is

$$\frac{F}{A} = Y * \frac{\Delta l}{l} = Y * \frac{y}{R} \tag{A.2}$$

where A is the cross-sectional area, and R is the radius of curvature for the bending. At radial distance y from the axis of the rod, the moment due to a force dF is $dm = ydF$.

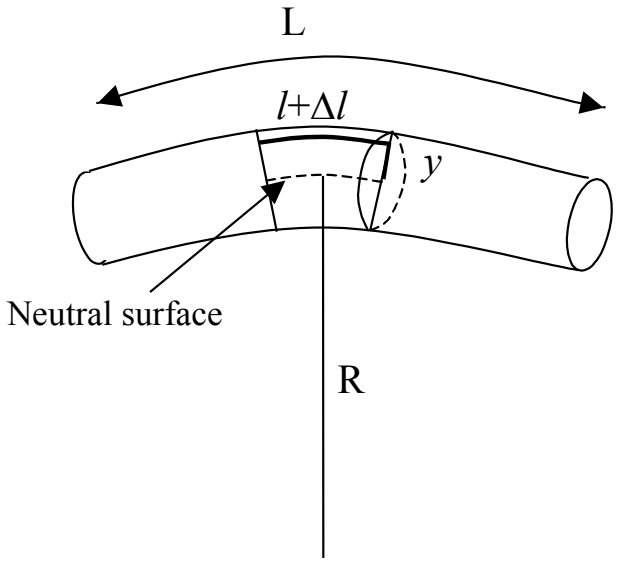

Figure A.1 Bent rod by force with compressed or stretched curve.

Therefore the total moment over one face of the segment is given by,

$$m = \int y \, \mathrm{d}F = \int y^2 \mathrm{d}A \frac{Y}{R} = \frac{YI}{R} \ , \tag{A.3}$$

where the center of mass $I \equiv \int y^2 dA$. Using the equation of a circle in the *x*-*z* plane with radius R, $z^2 = \mathrm{R}^2 - x^2$ and taking the first and second derivatives with respect *x*, 1/R can be written as

$$\frac{1}{R} = \frac{d^2 z / dx^2}{\left[1 + (dz/dx)^2\right]^{3/2}} \, . \tag{A.4}$$

In the large radius limit, the *dz/dx* term is negligible. Then the moment becomes

$$m = \frac{YI}{R} = YI \frac{d^2 z}{dx^2} \tag{A.5}$$

However I want to know is the bending depth , z. Eq (A.5) can be rearranged as,

$$z = \frac{1}{YI} \int dx \int m dx \tag{A.6}$$

BIBLIOGRAPHY

Chapter 1:

1. H. Kamerlingh Onnes, *Leiden Comm*. **120b, 122b, 124c** (1911).

2. W. Meissner and R. Ochsenfeld, "Ein Neuer Effekt bei Eintritt der Supraleitfahigkeit", *Naurwissenschaften* **21**, 787 (1933).

3. F. London, Superfluids, Wiley, New York (1950).

4. J. Bardeen, L.N. Cooper, and J. R. Schrieffer, "Theory of Superconductivity", *Phys. Rev*. **108**, 1175 (1957).

5. B. D. Josephson, "Possible new effects in superconductive tunneling", *Phys. Lett*. **1**, 251 (1962) ; "Supercurrents through barriers", *Adv. Phys*. **14**, 419 (1965).

6. R. C. Jaklevic, J. Lambe, A. H. Silver, and J. E. Mercereau, "Quantum interference effects in Josephson tunneling", Phys. Rev. Lett. **12**, 159-160 (1964).

7. J. E. Zimmerman, P. Thiene, and J. T. Harding, "Design and operation of stable rf-biased superconducting point-contact quantum devices, and a note on the properties of perfectly clean metal contacts", *J. Appl. Phys*. **41**, 1572-1580 (1970).

8. J. E. Mercereau, "Superconducting magnetometers", *Rev. Phys. Appl*. **5**. 13-20 (1970); M. Nisenoff, "Superconducting magntetometers with sensitivities approaching 10-10 gauss", *Rev. Phys. Appl*. **5**, 21-24 (1970).

9. G. Bednorz and K. A. Muller, Z. Phys, **B64**, 189 (1986).

10. A. M. Chang, H. D. Hallen, L. Harriott, H. F. Hess, H. L. Kao, *et al*. "Scanning Hall probe microscopy", *Appl. Phys. Lett.* **61**, 1974 (1992).

11. S. Y. Yamamoto, S. Schultz, "Scanning magnetoresistance microscopy", *Appl. Phys. Lett.* **69**, 3263 (1996).

12. D. Rugar, H. J. Mamin, P. Guethner, S.E. Lambert, J.E. Stern, *et al.* "Magnetic force microscopy: General principles and application to longitudinal recording media", *J. Appl. Phys,* **68**, 1169 (1990).

13. S. Gotoh, N. Koshizuka, *Phys .C,* **176**, 300 (1991).

14. L. N. Vu, and D. J. Van Harlingen, *IEEE Trans. Appl. Supercond.* **3**, 1918, (1993).

15. A. Mathai, D. Song, Y. Gim, and F. C. Wellstood, *IEEE Trans. Appl. Supercond.* **3**, 2609, (1993).

16. C. C. Tsuei, J. R. Kirtley, C. C. Chi, L. S. Yu-Jahnes, A. Gupta, T. Shaw, J. Z. Sun, and M. B. Ketchen, "Pairing Symmetry and Flux Quantization in a Tricrystal Superconducting Ring of $YBa_2Cu_3O_{7-delta}$", *Phys. Rev. Lett.* **73**, 593 (1994).

17. A. Mathai, Y. Gim, R. C. Black, A. Amr, F. C. Wellstood, "Experimental Proof of a Time-Reversal-Invariant Order Parameter with a *pi* shift in $YBa_2Cu_3O_{7-delta}$", *Phys. Rev. Lett*. **74**, 4523 (1995).

18. L. N. Vu, M. S. Wistrom, and D. J. Van Harlingen, "Imaging of magnetic vortices in superconducting networks and clusters by scanning SQUID microscopy", *Appl. Phys. Lett.* **63**, 1693 (1993).

19. R. C. Black, F. C. Wellstood, E. Dantsker, A. H. Miklich, J. J. Kingston, D. T. Nemeth, and J. Clarke, "Eddy current microscopy using a 77-K superconducting sensor", *Appl. Phys. Lett*. **64**, 100 (1994).

20. W. G. Jenks, S. S. H. Sadeghi, J. P. Wikswo Jr., "SQUIDs for nondestructive evaluation", *J. Phys. D*, **30**, 293 (1997).

21. F. C. Wellstood, Y. Gim, A. Amar, R.C. Black, and A. Mathai, "Magnetic microscopy using SQUIDs", *IEEE Trans. Appl. Supercond.* **7**, 3134 (1997).

22. S. Chatraphorn, "Room-Temperature Magnetic Microscope Using High-T_c SQUID", *Ph. D. Thesis,* University of Maryland, College Park (2000).

23. E. Fleet, "Design and Applications of a Cryocooled Scanning SQUID Microscope", *Ph. D. Thesis*, University of Maryland, College Park (2000).

24. A. Cochran, J. C. Macfarlane, L. N. C. Morgan, J. Kuznik, R. Weston, Hao Ling, R. M. Bowman, G. B. Donaldson, "Using a 77 K SQUID to measure magnetic fields for NDE", *IEEE Trans. Appl. Supercon*. **4**, 128 (1994).

25. L. N. Morgan, C. Carr, A. Cochran, D. McAMcKirdy, G. B. Donaldson, "Electromagnetic nondestructive evaluation with simple HTS SQUIDs: measurements and modeling", *IEEE Trans. Appl. Supercond*, **5**, 3127 (1995).

26. T. S. Lee, Y. R. Chemla, E. Dantsker, and J. Clarke, "High-T_c SQUID microscope for room temperature samples", *IEEE Tans. Appl. Supercon*. **7**, 3147 (1997).

27. F. Baudenbacher, N. T. Peters, and J. P. Wikswo Jr, "High resolution low-temperature superconductivity superconducting quantum interference device microscope for imaging magnetic fields of samples at room temperature", *Rev. Sci. Insrum. Phys*. **73**, 1247 (2002).

28. J. Dechert, M. Mueck, and C. Heiden, “A scanning SQUID microscope for samples at room temperature**”**, *IEEE Trans. Appl. Supercon*, **9**, 4111(1999).

29. S. Chartraphorn, E. F. Fleet, F. C. Wellstood, L. A. Knauss, and T. M. Eiles, “Scanning SQUID microscopy of integrated circuits”, *Appl. Phys. Lett*, **76**, 2304 (2000).

30. L. A. Knauss, Superconductor & Cryoelectronics, pp 16-22, Summer (2000).

31. Gudoshnikov, S.A.; Liubimov, B.Ya.; Deryuzhkina, Yu.V.; Matveets, L.V. “HTS scanning SQUID microscope with high spatial resolution for room temperature samples”, *Physica C,* **372-376**, 166-9 (2002).

32. S. Chatraphorn, E. F. Fleet, and F. C. Wellstood, “Relationship between spatial resolution and noise in scanning superconducting quantum interference device microscopy”, *J. Appl. Phys*., **92(8)**, 4731 (2002).

33. L. A. Knauss, A. B. Cawthorne, N. Lettsome, S. Kelly, S. Chatraphorn, E. F. Fleet, F. C. Wellstood, W. E. Vanderlinde, “Scanning SQUID microscopy for current imaging”, *Microelectronics Reliabilty*, **41**, 1211 (2001).

Chapter 2:

1. B. D. Josephson, “Possible new effects in superconductive tunneling”, *Phys. Lett*. **1**, 251(1962) ; “Supercurrents through barriers”, *Adv. Phys*. **14**, 419 (1965).

2. W. C. Stewart, “Current-voltage characteristics of Josepson junctions.” *Appl. Phys. Lett.* **12**, 277 (1968).

3. D. E. McCumber, “Effect of ac Impedance on dc Voltage-Current Characteristics of Superconductor Weak-Link Junctions.” *J. Appl. Phys.* **39**, 3113 (1968).

4 .C. A. Hamilton, R. C. Kautz, R. L. Steiner, and F. L. Loyd, *IEEE Elctron Device Lett.* **EDL6**, 623 (1985).

5. D. Haviland, and P. Agren “Introduction to Josephson Tunneling”, http://www.nanophys.kth.se (2001).

6. M. R. Spiegel, “Schaum’s Mathematical Handbook”, McGraw-Hill (1994).

7. A. J. Berkeley, H. Xu, R. C. Ramos, M. A. Gubrud, F. W. Strauch, P. R. Johnson, J. R. Anderson, A. J. Dragt, C. J. Lobb, and F. C. Wellstood, “Entangled Macroscopic Quantum States in Two Superconducting Qubits”, *Science,* **300**, 1548 (2003).

8. C. D. Tesche “Noise and Optimization of dc SQUID”, *Thesis,* (1978).

9. J. Clarke, “SQUIDs Fundamentals, *SQUID Sensors: Fundamentals, Fabrication and Applications”*, *Kluwer Academic Publishers*, pp. 1-62 , (1996).

10. R. H. Koch, J. Clarke, W. M. Goubau, J. M. Martinis, C. M. Pegrum, and D. J. Van Harlingen, “Flicker(1/f) noise in tunnel junction dc SQUIDs”, *J. Low. Temp. Phys*. **51**, 207, (1983).

11. P. Dutta, and P. M. Horn, “Low-frequency fluctuations in solids: 1/f noise”, *Rev. Mod. Phys.* **53**, 497 (1981).

12. R. H. Koch, W. Fidelloth, B. Oh, R. P. Robertazzi, S. A. Andrek, and W. J. Gallagher, “Identifying the source of 1/*f* noise in SQUIDs made from high-temperature superconductors.” *Appl. Phys. Lett*. **60**, 507, (1992).

13. V. Foglietti, W. J. Gallagher, M. B. Ketchen, A. W. Kleinsasser, R. H. Koch, S. I. Raider, and R. L. Sandstrom, "Low-frequency noise in low 1/*f* noise dc SQUID's." *Appl. Phys. Lett.* **49**, 1393, (1986).

14. D. Koelle, R. Kleiner, F. Ludwig, E. Dantsker and J. Clarke, "High-transition-temperature superconducting quantum interference devices" *Rev. of Modern Physics*, Vol. **71**, No. 3, 631-686, (1999).

15. M. J. Ferrari, M. Johnson, F. C. Wellstood, J. Clarke, A. Inam, X. D. Wu, L. Nazar, T. Venkatesan, "Low magnetic flux noise observed in laser-deposited *in situ* films of $YBa_2Cu_3O_y$ and implications for high-T_c SQUIDs", *Nature*, **341**, 723-725, (1989).

16. E. Dantsker, S. Tanaka, P.A. Nilsson, R. Kleiner, and J. Clarke, "Reduction of 1/*f* noise in high-T_c dc superconducting quantum interference devices cooled in an ambient magnetic field." *Appl. Phys. Lett.* **69**, 4099, (1996).

17. C. D. Tesche and J. Clarke, "dc SQUID: noise and optimization", *J. Low Temp. Phys*, **27**, 301 (1977).

18. M. J. Ferrari, M. Johnson, F. C. Wellstood, J. Clarke, P. A. Rosenthal, R. H. Hammond, and M. R. Beasley, "Magnetic flux noise in thin-film rings of $YBa_2Cu_3O_{7-\delta}$", *Appl. Phys. Lett.* **53**, 695, (1988).

19. T. J. Shaw, J. Clark, R. B. van Dover, L. F. Shneemeyer, and A. E. White, "Effects of 3.1-MeV proton and 1-GeV Au-ion irradiation on the magnetic flux noise and critical current of $YBa_2Cu_3O_{7-\delta}$.", *Phys. Rev. B*, **54**, 15411 , (1996).

20. M. Tinkham, "Introduction to Superconductivity", chapter 6.

21. J. J. P. Bruines, V. J. de waal, and J. E. Mooij, "Comment on 'DC SQUID :Noise and Optimization' by Tesche and Clarke", *J. Low Temp. Phys*, **46**, 383 (1982)

22. K. Enpuku, G. Tokita, T. Maruo, and T. Minotani, "Parameter dependencies of characteristics of a high-T_c dc superconducting quantum interference device." *J. Appl. Phys.* **78**, 3498 (1995).

23. B. J. Roth, N. G. Sepulveda, and J. P. Wikswo, "Using a magnetometer to image a two-dimensional current distribution", *J. Appl. Phys*. **65**(1), 361 (1989).

24. S. Chatraphorn, "Room-temperature magnetic microscopy using a high-T_c SQUID." *Ph. D. thesis,* University of Maryland, Physics Department (2001).

25. D. Li, Y. Ma, W.F. Flanagan, B.D. Lichter and J.P. Wikswo Jr., "Detection of Hidden Corrosion of Aircraft Aluminum Alloys by Magnetometry Using a Superconducting Quantum Interference Device", *Tri-Service Conference on Corrosion,* Orlando, Florida, (June 21-23 1994).

26. J. O. Gaudestad, "HTS SQUID Determination of Corrosion on Aluminum" *M. S. thesis,* University of Maryland, Physics Department (2000).

27. H. Hattori, T. Yamano, T. Tsutada, N. Tsuyuguchi, H. Kawawaki, and M. Shimogawara, "Magnetoencephalography", *Brain & Develoment*, **23**, 528 (2001).

28. M. Tanosaki, A. Suzuki, R. Takino, T. Kimura, Y. Iguchi, Y. Kurobe, Y. Haruta, Y. Hoshi, and I. Hashimoto, "Neural mechanisms for generation of tactile interference effects on somatosensory evoked magnetic fields in humans." *Clin. Neurophysiol*, **113**, 672 (2002).

29. D. Embick, M. Hackl, J. Schaeffer, M. Kelepir, and A. Marantz, "A magneto-encephalographic component whose latency reflects lexical frequency." *Brain Res. Cogn. Brain Res*. **10**, 345 (2001).

30. R. T. Wakai , M. Wang, S. L. Pedron, D. L. Reid, C. B. Martin, "Spectral analysis of antepartum fetal heart rate variability from fetal magnetocardiogram recordings", *Early Human Development,* **35**, 15 (1993).

31. G. Stroink, M. J. R. Lamothe, and M. J. Gardner, " SQUD Sensors: Fundamentals, Fabrication and Applications", *Kluwer Academic Publishers,* p413 (1996).

32. J. Clarke, "Geophysical applications of SQUIDs." *IEEE Trans. Magn.* **19**, 288 (1983).

33. H. Paik, "SQUIDs Fundamentals, *SQUID Sensors: Fundamentals, Fabrication and Applications"*, *Kluwer Academic Publishers*, pp. 1-62 , (1996).

Chapter 3:

1. http://superdevices.phys.strath.ac.uk/prgs.html.

2. A. J. Millar, E. J. Romans, C. Carr, A. Eulenburg, G. B. Donaldson, P. Maas and C. M. Pegrum, "High-T_c gradiometric superconducting quantum interference device and its incorporation into a single-layer gradiometer", *Appl. Phys. Lett*. **76**, 2445-2447 (2000).

3. L. P. Lee, J. Longo, V. Vinetskiy, and R. Cantor, "Low-noise $YBa_2Cu_3O_{7-d}$ direct-current superconducting quantum interference device magnetometer with direct signal injection", *Appl. Phys. Lett*, **66**(12), 1539 (1995).

4. J. Beyer, D. Drung, and F. Ludwig, T. Minotani and K. Enpuku, "Low-noise YBCO single layer dc superconducting quantum interference device (SQUID) magnetometer", *Appl. Phys. Lett.* **72**(2), 203 (1998).

5. M. B. Ketchen, and J. M. Jaycox, "Ultra-low noise tunnel junction dc SQUID with a tightly coupled planar input coil", *Appl. Phys. Lett,* **40**, 736 (1982).

6. J. R. Kirkley, J. P. Wikswo, Jr. "Scanning SQUID Microscopy." *Annu. Rev. Mater. Sci*. **29**, 117 (1999).

7. S. Gudoshnikov, Y. V. Deryuzhkina, P. E. Rudenchik, Y. S. Sitnov, S. I. Bondarenko, A. A. Shablo, P. P. Pavlov, A. S. Kalabukhov, O. V. Snigirev, P. Seidel, "Magnetic flux guide for high-resolution SQUID microscope", *IEEE Trans. Appl. Supercon.* **11**, 219 (2001)

8. F. Baudenbacher, N.T.Peters, and J.P.Wikswo, Jr., "High resolution low-temperature superconducting quantum interference device microscope for imaging magnetic fields of samples at room temperatures", *Rev. Sci. Insrum. Phys*. **73**(3), 1247 (2002).

9. S. Chatraphorn, E. F. Fleet, and F. C. Wellstood, "Relationship between spatial resolution and noise in scanning superconducting quantum interference device microscopy", *J. Appl. Phys*. **92**(8), 4731 (2002).

10. PFL-100(FLL electronics) and PCI-1000(PFL controller), Star Cryoelectronics, http://www.starcryo.com.

Chapter 4:

1. R. G Humphreys, J. S. Satchell, N.G. Chew, J. A.Edwards, S. W. Goodyear, S. E. Blenkinsop, O.D. Dosse and A.G. Cullis, "Physical vapour deposition techniques for the growth of $YBa_2Cu_3O_7$ thin films", *Superconductor Sci. Technol.* **3**, 38 (1990).

2. S. Chatraphorn, " Room-Temperature Magnetic Microscopy Using a High-T_c SQUID", Ph. D. Thesis, University of Maryland (2000).

3. Earth Chemical Co., Ltd. Inorganic Division, New Awajimchi Bldg. 6F, 3-14, 1-Chome, Awajimachi, Chuo-ku, Osaka 541-0047, Japan. Tel 06-6221-2275, Fax. 06-6203-3143.

4. Lambda Physik model LPX300 excimer lase with KrF gas mixture, λ = 248 nm, pulse width ~ 15ns, and 600mW of power.

5. Neocera, Inc., 10000 Virginia Manor Road, Belitsville, MD 20705 USA.

6. Jeonggoo Kim, "Growth Mode Transition of $YBa_2Cu_3O_{7-\delta}$ Thin Films on Planar and Vicinal (100) $SrTiO_3$ Substrates"**,** *Ph. D. Thesis*, George Washington University (2000).

7. C. D. Tesche, J. Clarke, "dc SQUID: noise and optimization", *J. Low Temp. Phys*. **29**, 301 (1977).

8. K. Enpuku, G. Tokita, T. Maruo, and T. Minotani, "Parameter dependencies of characteristics of a high-T_c dc superconducting quantum interference device." *J. Appl. Phys.* **78**, 3498 (1995).

9. M. N. Keene, J. S. Satchell, S. W. Goodyear, R. G. Humphreys, J. A. Edwards, N. G. Chew, and K. Lander, "Low noise HTS gradiometers and magnetometers constructed from $YBa_2Cu_3O_{7-x}/PrBa_2Cu_3$ O_{7-y} thin films", *IEEE Trans. Appl. Supercond.* **5**, 2923 (1995).

Chapter 5:

1. R. C. Black, "Magnetic Microscopy Using a Superconducting Quantum Interference Device." Ph.D. Thesis, University of Maryland, College Park, 1995.

2. Y. Gim, Ph.D. Thesis, University of Maryland, College Park, 1996.

3. S. Chatraphorn, "Room-Temperature Magnetic Microscopy Using a High-T_c SQUID", Ph.D Thesis, University of Maryland, College Park, 2000.

4. E. Fleet, "Design and Applications of a Cryo-cooled Scanning SQUID Microscope." Ph.D Thesis, University of Maryland, College Park, 2000.

5. T. S. Lee, Y. R. Chemla, E. Dantsker, and J. Clarke, "High-T_c SQUID microscope for room temperature samples", *IEEE Tans. Appl. Supercon.* **7**, 3147 (1997).

6. Feyman, Leighto, Sands, "The Feyman Lectures on Physics.Volume II" Addision Wesley. 38-1~38-12 (1964).

7. DATAKOAT matte clear protective spray, CAT.NO 04178, DATAK Co.

8. Master Bond EP30FL. Ratio of part A to part B = 4:1. The hardening time is about 24 hours at room temperature. Master Bond, Inc. Hackensack, NJ, USA.

9. Micro Automation, Inc., Dicing saw model 1006.

10. Fiber Optics Products Polish film, Alum. Oxide, 9x13, 1m, P/N:F1-0109-1, Fiber intrument sales, Inc., 24 Clear Road, Oriskany, NY 13424.

11. Neocera, Inc., 10000 Virginia Manor Road, Beltsville, MD 20705 USA.

12. West Bond Model 1200D, West Bond Inc. 1551 Gene Autry Way, Anaheim, California, 92805.

13. LakeShore Pt-sensor, Model : PT-111, Serial #: P8475, LakeShore Cryotronics. Inc. www.lakeshore.com.

14. PCP0002, solid 10 pin male connector, Oxford Instruments, 130A Baker Ave. Concord, MA, 01742.

15. DATAKOAT clear protective gloss coating kit, CAT.NO 04176, DATAK Co.

16. CBL-C2-1 cryo-cable for ½" Bulkhead fitting, 1m long with 10 pin warm LEMO receptacle and 10 pin cold LEMO plug. STAR Cryoelectronics, 25-A Bisbee Court, Santa Fe, NM 87508-1338.

Chapter 6:

1. S. Chatraphorn, "Room-Temperature Magnetic Microscopy using a High-T_c SQUID", *Ph.D. Thesis*, University of Maryland (2000).

2. PFL-100(FLL electronics) and PCI-1000(PFL controller), Star Cryoelectronics, http://www.starcryo.com.

3. Physics Department, Electronics Development Group, Work Order Number 9539.

4. Manual for PFL-100 and PCI-1000, Star Cryoelectronics http://www.starcryo.com.

5. R. H. Koch, J. Clarke, W. M. Goubau, J. M. Martinis, C. M. Pegrum, and D. J. Van Harlingen, "Flicker(1/f) noise in tunnel junction dc SQUIDs", *J. Low. Temp. Phys*., **51**, 207 , (1983)

6. Intelligent Motor Controller, PC34 Family and MD10A microstepping motor drive module, Oregon Micro Sytem, Inc., Beaverton, OR, USA.

7. ESP 6000 UNIDRIVE 6000 Motion Controller, TSP 150 stage, Newport, 1791 Deere Avenue, Irvine, CA USA.

8. User's manual for ESP 6000 UNIDRIVE 6000 Motion Controller, Newport, 1791 Deere Avenue, Irvine, CA USA.

9. R. C. Black "Magnetic Microscopy Using a Superconducting Quantum Interference Device." Ph D thesis, University of Maryland (1995).

10. C. P. Vlahacos, R. C. Black, S. M. Anlage, A. Amar, F. C. Wellstood, **"**Near-field scanning microwave microscope with 100 μm resolution", *Appl. Phys. Lett.* 69, 3272 (1996).

11. LabVIEW 6*i*, NATIONAL INSTRUMENTS, www.ni.com/labview.

12. DAQ, PCI 6052 E, NATIONAL INSTRUMENTS, www.natinst.com.

13. DAQ, PCI 6052 E, NATIONAL INSTRUMENTS, www.natinst.com.

Chapter 7:

1. A. Mathai, D. Song, Y. Gim, and F. C. Wellstood, "One-dimensional magnetic flux microscope based on the dc superconducting quantum interference device", *Appl. Phys. Lett*. **61**, 598-600, (1992).
2. F. C. Wellstood, Y. Gim, A. Amar, R. C. Black, and A. Mathai, "Magnetic Microscopy Using SQUIDs", *IEEE Trans. Appl. Supercond.*, **7**(2), 3134 (1997).
3. S. A. Gudoshnikov, B.Ya.Liubimov, Yu.V.Deryuzhkina, L.V. Matveets, "HTS scanning SQUID microscope with high spatial resolution for room temperature samples", *Physica C*, **372-376**, pt.1, 1, 166-9 (2002).
4. S. Chatraphorn, E. F. Fleet, and F. C. Wellstood, "Relationship between spatial resolution and noise in scanning superconducting quantum interference device microscopy", *J. Appl. Phys*. **92** (8), 4731 (2002).
5. B. J. Roth, N. G. Sepulveda, and J. P. Wikswo, "Using a magnetometer to image a two-dimensional current distribution", *J. Appl. Phys*. **65** (1), 361 (1989).
6. P. Horowitz, W. Hill, in The Art of Electronics (second edition) 7.14, 438.
7. ESP6000 UNIDRIVER6000 Motion Controller Manual, Newport Corporation, 1791 Deere Ave. Irvine, CA 92606.
8. P. E. Goa, H. Hauglin, A. A. F. Olsen, M. Baziljevich, and T. H. Johanson, "Magneto-optical imaging setup for single vortex observation", *Rev. Sci. Instrum.* **74** (1), 141 (2003).

Chapter 8:

1. B. J. Roth, N. G. Sepulveda, and J. P. Wikswo, "Using a magnetometer to image a two-dimensional current distribution", *J. Appl. Phys*. **65**(1), 361 (1989).
2. S. Chatraphorn, E. F. Fleet, and F. C. Wellstood, "Relationship between spatial resolution and noise in scanning superconducting quantum interference device microscopy", *J. Appl. Phys*. **92**(8), 4731 (2002).
3. S. Chatraphorn, "Room-temperature magnetic microscopy using a high-T_c SQUID." *Ph. D. thesis,* University of Maryland (2001).
4. B. J. Roth, N. G. Sepulveda, and J. P. Wikswo, "Using a magnetometer to image a two-dimensional current distribution", *J. Appl. Phys*. **65**(1), 361 (1989).
5. http://mathworld.wolfram.com/BesselFunctionoftheFirstKind.html.
6. C. F. Busko, J. Matthews and F. C. Wellstood, "A novel technique for eliminating edge artifacts in magnetic microscopy: the π-2π filter technique." (2003) unpublished.

Chapter 9:

1. Wire samples were provided by IGC Advanced Superconductors, 1875 Thomaston Ave., Waterbury, CT 06704.
2. E. Fleet, A. Gilbertson, S. Chatraphorn, N. Tralshawala, H. Weinstock, and F. C. Wellstood, "Imaging Defects in Cu-clad NbTi Wire Using a High-T_c Scanning SQUID Microsocpe." *IEEE. Trans. Appl. Supercon.* **11**, 215, 2001.

3. David J. Griffiths, “Introduction to electrodynamics. 3rd edition”, Prentice Hall, 394.

4. E. F. Fleet, “Design and Applications of a cryo-cooled scanning SQUID microscope”, *Ph. D. Thesis of University of Maryland*, (2000).

5. H. Weinstock, N. Tralshwala, and J.R. Claycomb, “Nondestructive evaluation of wires Using High-Temperature SQUIDs”, *IEEE Trans. Appl. Supercond.* **9**, 3797 (1999).

6. A.F. Gilbertson and F.C. Wellstood, “Detection of wire defects using high-low frequency image subtraction” (unpublished).

Appendix :

1. Feyman, Leighto, Sands, “The Feyman Lectures on Physics.Volume II” Addision Wesley. 38-1~38-12 (1964).